

Multi-order Vector Finite Element Modeling of 3D Magnetotelluric Data Including Complex Geometry and Anisotropy

Aixa M. Rivera Ríos

Thesis submitted for the degree of
Doctor of Philosophy
in
The University of Adelaide
School of Earth and Environmental Sciences
June, 2014

For the life.

Contents

List of Figures	v
List of Tables	vi
List of Symbols and Acronyms	x
Abstract	xi
Statement of Originality	xiii
Acknowledgments	xiv
Introduction	xv
1 Magnetotelluric Method	1
1.1 Introduction	1
1.2 Energy Sources and Measurements	1
1.2.1 Sources	1
1.2.2 Measurements	2
1.3 EM Induction in the Earth	3
1.3.1 EM Induction in the Air	5
1.3.2 EM Induction in a Homogeneous Earth	6
1.3.3 EM Induction in a Layered Earth	8
1.3.4 2D Earth EM Induction	11
1.3.5 3D Earth EM Induction	13
1.4 Galvanic Distortion	14
1.5 Dimensionality Analysis	15
1.5.1 WAL Invariants	15
1.5.2 Phase Tensor	16
1.5.3 WALDIM	16
1.6 Electrical Anisotropy	17
2 3D MT Modeling and Inversion	18
2.1 Introduction	18
2.2 Problem Statement	19
2.3 Finite Difference Method	21
2.4 Integral Equation Method	22
2.5 Finite Element Method	23
2.5.1 Galerkin Method	24

2.5.2	Domain Discretization	24
2.5.3	Nodal FEM	25
2.5.4	Vector FEM	26
2.6	System of Equations Solvers	28
2.7	3D Inversion	29
2.7.1	Unconstrained Nonlinear Optimization	29
2.7.2	Newton Iterations	30
2.7.3	Constrained Optimization	31
3	Multi-order Vector Finite Element Method	32
3.1	Introduction	32
3.2	Magnetotelluric Problem	33
3.2.1	Secondary Field Formulation	33
3.2.2	Primary Fields	35
3.2.3	Boundary Conditions	35
3.3	Vector Finite Elements	39
3.3.1	Domain Discretization	39
3.3.2	Nodal Basis Functions	41
3.3.3	Vector Basis Functions	42
3.3.4	Local Problem: Numerical Integration	44
3.3.5	Assembly and Solution	46
4	Validation: Homogeneous Earth	49
4.1	Introduction	49
4.2	Resistive Earth	50
4.2.1	Input Model and MT Problem	50
4.2.2	hp-Convergence Analysis	50
4.2.3	Model Discretization	52
4.2.4	Dirichlet Results	53
4.2.5	GPML (Fang, 1996) Results	56
4.2.6	GPML (Zhou et al., 2012) Results	58
4.2.7	Frequency Range Validation	60
4.3	Conductive Earth	62
4.3.1	Input Model and MT Problem	62
4.3.2	hp-Convergence Analysis	62
4.3.3	Model Discretization	63
4.3.4	Dirichlet Results	64
4.3.5	GPML (Fang, 1996) Results	65
4.3.6	GPML (Zhou et al., 2012) Results	67
4.3.7	Frequency Range Validation	67
4.4	General Remarks	69
5	Applications: Complex Models	71
5.1	Introduction	71
5.2	COMMEMI 3D-1A	72
5.3	COMMEMI 3D-2	75
5.4	Topography Effect for Homogeneous Earth	78
5.5	Anisotropic Homogeneous Earth	81

5.6	Three Layers with Complex Interfaces: Isotropic Case	83
5.7	Three Layers with Complex Interfaces: Anisotropic Case	86
5.8	General Remarks	88
6	Conclusions	90
6.1	Future Work	91
A	Finite Element Method	93
A.1	Sobolev Space	93
A.2	Isoparametric Elements	95
A.2.1	Coordinate Transformation	95
B	MoVFEM Algorithm	97
B.1	MT Problem	97
B.1.1	Maxwell's Equations with Secondary Field Formulation	97
B.1.2	Homogeneous Earth	97
B.1.3	Layered Earth	98
B.1.4	MT Governing Equations with GPML	98
B.2	Complete Nodal Basis Functions	100
B.3	Complete Multi-Order Vector Basis Functions	101
B.4	Covariant Basis Vectors	104
B.5	Curl of Basis Vector	105
B.6	Assembly	106
C	Fortran Program	108
	References	112

List of Figures

1.1	MT field layout	2
1.2	Faraday's and Ampere's Law	3
1.3	Skin-depths for different resistivities and periods	7
1.4	Apparent resistivity and phase plots for a layered Earth	10
1.5	2D conductivity model with vertical contact	11
2.1	Staggered grid	22
2.2	Multigrid scheme	22
2.3	IE discretization	23
2.4	Tetrahedral edge-elements	26
2.5	Hexahedral edge-elements	27
3.1	GPML scheme	37
3.2	GPML stretching factor graphs	39
3.3	Computational domain discretization	40
3.4	Nodal numbering in element	41
4.1	Convergence plots of resistive model	51
4.2	Domain discretization for resistive Earth model	52
4.3	MT responses of Dirichlet boundaries	53
4.4	Surface resistivities from Dirichlet boundaries	55
4.5	MT responses from GPML (Fang) boundaries	56
4.6	Surface resistivities from GPML (Fang) boundaries	58
4.7	MT responses from GPML (Zhou) boundaries	59
4.8	Surface resistivities from GPML (Zhou) boundaries	60
4.9	MT responses on frequency range with linear elements	61
4.10	MT responses on frequency range with quadratic elements	61
4.11	MT responses on frequency range with Lagrangian elements	62
4.12	Convergence for conductive half-space	63
4.13	Conductive half-space discretization grids	64
4.14	MT responses of Dirichlet boundaries for conductive half-space	65
4.15	Conductive model: MT responses from GPML (Fang) boundaries	66
4.16	Conductive model: MT responses from GPML (Zhou) boundaries	67
4.17	Conductive model: MT responses on frequency range with linear-order edge-elements	68
4.18	Conductive model: MT responses on frequency range with quadratic elements	68

4.19	Conductive model: MT responses on frequency range with Lagrangian elements	69
5.1	COMMEMI model 3D-1A	72
5.2	COMMEMI model 3D-1A computational grid	73
5.3	Apparent resistivity and phase results for the model COMMEMI 3D-1A	74
5.4	Surface resistivity values for the model COMMEMI 3D-1A	75
5.5	Input model of COMMEMI 3D-2	75
5.6	Computational grid for the model COMMEMI 3D-2	76
5.7	Apparent resistivity and phase results for the model COMMEMI 3D-2	77
5.8	Apparent resistivity on the surface of the COMMEMI 3D-2 model	78
5.9	2D topography input model	79
5.10	2D topography computational grid	79
5.11	Apparent resistivity and phase results for the homogeneous model with 2D topography	80
5.12	Surface resistivities from the homogeneous model with 2D topography	81
5.13	Anisotropic homogeneous computational grid	82
5.14	Apparent resistivity and phase plots for the anisotropic homogeneous model	82
5.15	Apparent resistivity on the surface of the homogeneous model with transverse anisotropy	83
5.16	Input model for the layered model with complex interfaces	83
5.17	Computational grid for the layered model with complex interfaces	84
5.18	Apparent resistivity and phase results for the layered model with complex interfaces: isotropic case	85
5.19	Surface resistivity for the layered model with complex interfaces: isotropic case	86
5.20	Apparent resistivity and phase results for the layered model with complex interfaces: anisotropic case	87
5.21	Surface resistivity for the layered model with complex interfaces: anisotropic case	88
A.1	De Rham Complex	94
A.2	Tonti diagram	94
A.3	Hexahedral isoparametric element	95
B.1	Linear edge-elements numbering scheme.	101
B.2	Quadratic edge-elements numbering scheme	102
B.3	Lagrangian edge-elements numbering scheme	103
C.1	Fortran program flowchart	108
C.2	Fortran program sub-flowcharts	110

List of Tables

2.1	Interface conditions in MT modeling	20
2.2	EM fields in staggered grids	22
4.1	Resistive model: time & memory with Dirichlet boundaries	54
4.2	Resistive model: Time & memory with GPML (Fang) boundaries . . .	56
4.3	Resistive model: time & memory with GPML (Zhou) boundaries . . .	59
4.4	Conductive model: time & memory with Dirichlet boundaries	65
4.5	Conductive model: time & memory with GPML (Fang) boundaries . .	66
4.6	Conductive model: Time & memory with GPML (Zhou) boundaries . .	67

List of Symbols and Acronyms

List of Symbols	This list presents the definition of most used symbols in this thesis.
(ξ, η, ζ)	Isoparametric coordinates
(x, y, z)	Cartesian coordinates in m or km
$\boldsymbol{\nu}, \boldsymbol{\kappa}$	General 3×3 EM model tensors
δ	Skin-depth in m
Γ	Surface boundary of a domain
$\langle \mathbf{a}, \mathbf{b} \rangle$	Vector inner product
$\hat{\mathbf{n}}$	Unit normal vector
$\tilde{\mathbf{s}}^F$	Modified source field with GPML
$\mathbf{B} = (B_x, B_y, B_z)$	Magnetic induction in T
\mathbf{B}_0	Magnetic induction on a reference point on the surface
\mathbf{D}	Displacement currents in Cm^{-2}
$\mathbf{E} = (E_x, E_y, E_z)$	Electric field in Vm^{-1}
\mathbf{E}_0	Electric field on a reference point on the surface
$\mathbf{F} = (F_x, F_y, F_z)$	General field
\mathbf{F}_0	General field on a reference point on the surface
$\mathbf{H} = (H_x, H_y, H_z)$	Magnetic field in Am^{-1}
\mathbf{I}	3×3 Identity matrix
\mathbf{j}	Current density in Am^{-2}
\mathbf{r}	$\mathbf{r} = (x, y, z)$ is a point with Cartesian coordinates
\mathbf{s}	General source vector
$\mathbf{v}_i(\xi, \eta, \zeta)$	Vector basis function (edge-element)

\mathbf{w}	Weighting vector function for the Galerkin method
$\mathcal{C}(\Omega)$	Differentiability class of continuous and differentiable functions
$\mathcal{H}(\Omega)$	Sobolev space
$\mathcal{H}_0(\Omega)$	Sobolev space in terms of the boundary of the domain
C	Schmucker-Weidelt transfer function in km
$D(\mathbf{m})$	Differential operator with an EM model \mathbf{m}
$e^x = \exp(x)$	Exponential function
Ω	A 3D domain
$\omega = 2\pi f$	Angular frequency in Hz
Ω_e	Hexahedral element of the domain Ω
ϕ	MT phase in degrees
$\rho = 1/\sigma$	Resistivity in Ωm
ρ_a	Apparent resistivity in Ωm
a_0, b_0	GPML stretching factor parameters of Fang (1996)
$a_{min}, a_{max}, b_{min}, b_{max}$	GPML stretching factor parameters of Zhou et al. (2012)
$c(\omega)$	MT transfer function for layered Earth
C_Γ	Defines the boundary integration in the Galerkin method
$e(z)$	Plane wave propagation within layers
f	Frequency in Hz
$f(z)$	Plane wave characteristic of EM fields in a homogeneous Earth
$h_{x_m} = h_{x_m}(x_m)$	GPML stretching factor
$i = \sqrt{-1}$	Imaginary number
$k = \sqrt{i\omega\mu\sigma}$	Propagation constant or wave number
m_e	Number of edges in the hexahedral element
n_e	Number of nodes in the hexahedral element
$N_i(\xi, \eta, \zeta)$	Nodal basis function
t	Time in s
$\boldsymbol{\sigma}$	3×3 Conductivity tensor in Sm^{-1}
σ	Scalar conductivity in Sm^{-1}

$\mu = \mu_0 \mu_r$	Scalar magnetic permeability in Hm^{-1}
$\mu_0 = 4\pi \times 10^{-7}$	Magnetic permeability of a vacuum in Hm^{-1}
$\mu_r \approx 1$	Relative magnetic permeability of a medium
$\varepsilon = \varepsilon_0 \varepsilon_r$	Electric permittivity in Fm^{-1}
$\varepsilon_0 = 8.854 \times 10^{-12}$	Electric permittivity of a vacuum in Fm^{-1}
ε_r	Relative electric permittivity of a medium
$\nabla = (\partial_x, \partial_y, \partial_z)$	Nabla operator
$\partial_x = \frac{\partial}{\partial x}$	Partial derivative with respect to x variable
\mathbf{Z}	2×2 Impedance tensor in VA^{-1}
Z	1D MT impedance in VA^{-1}
$\partial_{\tilde{x}_i} = \frac{1}{h_{x_i}} \frac{\partial}{\partial x_i}$	GPML modified partial derivative
$\tilde{\nabla} = (\partial_{\tilde{x}_1}, \partial_{\tilde{x}_2}, \partial_{\tilde{x}_3})$	Modified differential operator with GPML
q	Electric charge
\Im	Imaginary part
\Re	Real part
Acronyms	This list presents the definition of most used acronyms in this thesis.
1D	One-Dimensional
2D	Two-Dimensional
3D	Three-Dimensional
EM	Electromagnetic
FD	Finite Difference
FEM	Finite Element Method
GPML	Generalized Perfect Matched Layers
IE	Integral Equation
MoVFEM	Multi-order Vector Finite Element Method Algorithm
MT	Magnetotelluric
PDE	Partial Differential Equation
PML	Perfect Matched Layer

TE	Transverse Electric
TM	Transverse Magnetic
VFEM	Vector Finite Element Method

Abstract

This thesis presents the development of a computational algorithm in Fortran, to model 3D magnetotelluric (MT) data using a Multi-order Vector Finite Element Method (MoVFEM) to include complex geometry (such as topography, and subsurface interfaces). All the modules in MoVFEM have been programmed from the beginning, unless specified by referencing the libraries used. The governing equations to be solved are the decoupled electromagnetic (EM) partial differential equations for the secondary electric field, or the secondary magnetic field, with a symmetric conductivity tensor to include anisotropy. The primary fields are the solution of a plane-wave within the air domain.

Two boundary conditions are implemented, namely the Generalized Perfect Matched Layers method (GPML) and Dirichlet boundary conditions. Three Dirichlet boundary schemes are applied, first considering zero EM fields at the boundaries of the computational domain; secondly, considering the boundaries as homogeneous Earth; and finally, considering the boundaries as a layered Earth. Two formulations of GPML are implemented in this algorithm, firstly the original GPML formulation and secondly, the GPML parameters are modified for the MT and Controlled Source Electromagnetic (CSEM) problem.

High-order edge-elements are defined based on covariant projections, and mixed-order edge-elements for hexahedra. The vector basis functions are defined for linear elements (12 edge-elements), quadratic elements (36 edge-elements), and Lagrangian elements (54 edge-elements). By this definition, the vector basis will have zero divergence in the case of rectangular elements and relatively small divergence in the case of distorted elements.

The validation of this computational algorithm is performed with a homogeneous Earth, where the analytic solution of the MT problem is known. In the validation, the convergence of the solution is analyzed for different grid spacing and for different element-orders with Dirichlet boundary conditions. High-order elements produce accurate solutions with larger spacing than the fine grid needed for linear-order elements.

After the convergence analysis, the solution obtained with all the proposed boundary conditions, and edge-element orders are compared for one frequency, and for a frequency range. In the homogeneous Earth, Dirichlet boundary condition presents backward reflections from the boundaries of the computational domain to the center of the model. Both GPML formulations produce more stable solutions, where no boundary reflections are present. However the MT responses fluctuate within a small range close to the values for the homogeneous Earth. The GPML formulation for MT and CSEM produce more accurate results and stabilize the MT responses over a frequency range.

This algorithm is applied to synthetic examples with complex conductivity struc-

tures. Some of these synthetic examples have been published previously, thus the results of this algorithm are compared qualitatively. In the case of anisotropy and complex geometry, the proposed synthetic examples have not been published, and a discussion of how the MT responses behave for these Earth examples is presented.

This computational algorithm could be extended with the use of an adaptive method, and it could be implemented in an algorithm for 3D inversion of MT data.

Statement of Originality

I certify that the work presented in this thesis is original and has not been accepted for the award of any other degree or diploma in any university or other tertiary institution and, contains no material previously published or written by another person, except where due reference has been made in the text.

I give consent for this thesis to be made available for loan and photocopying after it has been deposited in the University Library, subject to the provisions of the Copyright Act 1968.

I also give consent for the digital version of the thesis to be made available on the web, via the University's digital research repository, the Library catalogue and also through web search engines, unless permission has been granted by the University to restrict access for a period of time.

Aixa M. Rivera-Ríos

Acknowledgments

I would like to thank my supervisors Bing Zhou, Graham Heinson and Stephan Thiel for their guidance during this time. Special thanks to Bing Zhou for helping me on the development of the computational algorithm, and giving me feedback about the methodology. Graham Heinson and Stephan Thiel, thanks for helping me understanding the theory behind the MT method.

I wish to thank my colleagues in the MT group, fellow PhD students and staff of Geology and Geophysics. I am grateful to Jenny Reiners for opening the doors of Australia for me, thanks for giving me a place to stay in the first weeks! Thanks to Jared Peacock for allowing me to be part of his field work, and gain experience applying the MT method. Special thanks to Lars Krieger, and Kate Robertson for taking the time to read my thesis to correct the English and writing format.

I am grateful to Andrew Hill and Paul Coddington of eResearch, SA for their support in the use of high performance computing facilities.

This research was supported by the Australian Research Council with the Discovery Project (DP20106713). Special thanks to Kinesis, PR Foundation for their scholarship to help pay for my studies in Adelaide. Thanks to the School of Earth and Environmental Sciences for providing a scholarship to live in Adelaide.

Personally, I wish to thank Adalexix, Pedro, Sasha, Alexis, Dorian, and Julia for their love, support and encouragement, and for being an awesome family! Thanks to Veronica for being there listening and helping me to get through the good and bad times. Marcelo and Alejandro, you have been like my brothers here, thanks for everything! Meryn, thanks for being there when I needed to clear my mind. Thanks Michael Juttner, your care and support over these years was necessary, thanks for reviewing my writing! Special thanks to Tim Wong, Lisa Farrell and Emma Watson for being great housemates, understanding my moments of stress and cloister, and being like a family.

Introduction

The magnetotelluric (MT) method is a passive electromagnetic (EM) sounding method that measures the variation of EM fields at Earth's surface. It is used to image the electrical conductivity of the subsurface, which may be interpreted geologically. This geophysical technique is governed by Maxwell's partial differential equations with the quasi-stationary approximation, which describes EM induction in Earth (Weaver, 1994). Natural EM fields are the source signal of the MT method. These natural fields are described by a plane-wave with harmonic time-dependence (Weaver, 1994). The penetration depth of natural EM fields depends on the frequency of the inducing source field and conductivity of Earth materials, and allows the MT method to obtain information from the near-surface of hundred meters or less, to mantle scales of hundreds of kilometers.

Inversion is a numerical framework for obtaining a conductivity distribution of the subsurface from the measured EM data. An important aspect of MT data is in terms of its sensitivity to how the conductivity varies in different orientations in Earth. A dimensionality analysis provides information about the subsurface structures in terms of conductivity varying in one-dimension (1D), two-dimensions (2D) or three-dimensions (3D) (Martí, 2014). With this analysis it is also possible to obtain information about the electrical anisotropy of the subsurface, in which the conductivity varies within any single unit (Martí, 2014). The importance of the dimensionality analysis is that it imposes a framework for which inversion scheme should be applied for the measured MT data, and whether anisotropy in the inversion should be included.

Forward modeling is the critical hub of inversion methods by parameterizing the subsurface in terms of resistivity (inverse of conductivity) and generating synthetic MT data. Such forward models are obtained by numerically solving the EM partial differential equations. Three-dimensional MT modeling and inversion has become a significant area of research with the increase of large-scale MT surveys and the availability of high performance computing strategies (Newman, 2014). The primary numerical methods for 3D MT modeling are integral equation, finite difference and finite element methods (Avdeev, 2005).

Finite difference methods are well developed, but the current emphasis is on finite element methods because it may account for the topography, bathymetry, and complex geometry of subsurface structures more accurately (Newman, 2014). In 3D finite element methods the domain is discretized with hexahedral or tetrahedral elements, which can fit any complex geometry. Vector finite element method defines the EM problem on the edges of the elements, and takes into consideration the continuity of EM fields among shared elements in the computational domain (Jin, 2002). Vector finite element method is mostly implemented in 3D EM modeling with linear-order edge-elements (Farquharson & Miensopust, 2011; Han et al., 2009; Mitsuhata & Uchida, 2004; Shi

et al., 2004).

Objectives The primary objective of this research is to develop a forward modeling algorithm in Fortran, called ‘Multi-order Vector Finite Element Method’ (MoVFEM) to model 3D MT data. This forward model can simulate EM fields in a 3D anisotropic subsurface with complex geometry, such as topography, bathymetry and non-planar interfaces. The computational domain is discretized with hexahedral elements, and three types of vector basis functions are defined. These basis functions are defined for linear, quadratic and Lagrangian hexahedrals, to analyze the behavior of the solution for different element orders.

Boundary conditions are important in EM modeling in order to restrain the values of EM field on the boundaries of the computational domain. Two boundary conditions are applied in the MoVFEM program, namely Dirichlet boundaries and Generalized Perfect Matched Layers. Dirichlet boundaries assign EM field values tangential to the boundary locations. These values can be considered as zero, as homogeneous Earth or layered Earth. Generalized Perfect Matched Layers boundary conditions defines the EM field so that these fields decrease to zero on the Perfect Matched Layer zone. The main idea of these boundary conditions is that the fields are ‘absorbed’ on the Perfect Matched Layer zone and no reflection of EM fields are expected to be present in the inner model (Fang, 1996; Zhou et al., 2012).

The MT problem is presented by the secondary field formulation, in which the primary fields are the EM field propagating in the air. Anisotropy is included by defining a symmetric conductivity tensor in the EM partial differential equations. The MT data are presented as standard responses, in terms of the apparent resistivity and phase of the MT impedances.

In this thesis, MoVFEM is validated with a homogeneous Earth for which an analytic solution and MT responses are known. The analysis of convergence of the solution is obtained in two ways; one is the spacing convergence (h-convergence) in which the solution is analyzed for different hexahedral size; the second convergence analysis is the element order convergence (p-convergence) in which the solution is analyzed for the three different element-order schemes. In the validation of MoVFEM, a comparison of the effect of Dirichlet and GPML boundary conditions is presented.

This program is applied to models containing complex conductivity structures. Some of the models presented have been previously published, therefore the solution obtained can be compared (Mackie et al., 1994; Nam et al., 2007; Wannamaker et al., 1986; Zhdanov et al., 1997; Mitsuhashi & Uchida, 2004). The solution of models that have not been published, including anisotropic models, and models with complex geometry, are presented with a discussion and description of the MT responses obtained.

Outline This thesis is organized as follows. In Chapter 1, the MT theory is reviewed. Chapter 2 contains the theory of forward modeling, a literature review of numerical methods to solve the MT problem with a particular emphasis on the finite element method. Additionally, Chapter 2 presents a brief review of MT inversion to show the importance of forward modeling in the inversion process. Chapter 3 contains the theory and approach of the MoVFEM algorithm, where the governing equations, boundary conditions and edge-elements are described. Chapter 4 presents the validation of this program with homogeneous Earth, and Chapter 5 contains the application to syn-

thetic examples. Chapter 6 concludes this thesis and provides ideas for future work. Complementary sections of some of these Chapters are included in the Appendices.

Chapter 1

Magnetotelluric Method

1.1 Introduction

The MT method is a geophysical technique that measures the variation of electric and magnetic fields at Earth's surface. It is used to study the EM properties of subsurface structures. This geophysical method uses natural EM fields as the source signal, which penetrate Earth's surface and are modified by different geological structures in the subsurface.

Measured EM field fluctuations depend principally on the electrical properties of the subsurface, and on the frequency of the source signal. The dominant property for the MT method is the conductivity σ , defining the ability of subsurface structures to conduct electrical currents. In the MT method, this property may also be presented as resistivity ρ (inverse or reciprocal of conductivity, $\rho = 1/\sigma$). It is then interpreted and correlated with specific geological structures. For the frequency range of induction, the MT method may obtain information from tens of meters to hundreds of kilometers depth. Consequently, this method is one of few geophysical techniques that can obtain information about the deep continental crust and the upper mantle (Boerner, 1992).

The basis of the MT method was first proposed by Tikhonov (1950) and Cagniard (1953) for a simple (1D) Earth model. Vozoff (1972, 1991) provided an extended description of MT method theory applied to other Earth model dimensions. More recently, Simpson & Bahr (2005) and Chave & Jones (2012) have reviewed the full theory and application aspects of the MT method.

1.2 Energy Sources and Measurements

1.2.1 Sources

In MT applications, the source of interest are natural EM fields with periods ranging from 10^{-3} to 10^5 s or with an equivalent frequency range of 10^{-5} to 10^3 Hz. The power spectral densities of these EM fluctuations decay around 0.5 to 5 Hz, which is called the MT *dead-band*. Within this band the power spectrum reaches its minimum around 1 Hz and is recognized by a reduction of EM data quality (Simpson & Bahr, 2005, Chap.1). The main source regions within this frequency range of interest are the magnetosphere and the atmosphere.

Natural EM source fields with frequencies lower than 1 Hz are caused by interactions of solar wind with Earth's magnetosphere. When the solar wind reaches the Earth's magnetic field, ionospheric currents build up electric charges and generate a secondary electric field, which causes secondary electric currents (Viljanen, 2012). These electric

currents establish magnetic fields that travels to the Earth's surface (Simpson & Bahr, 2005, Chap.1). In most parts of the Earth, this source field reaches the surface in a vertical propagation, as a horizontally polarized plane-wave with harmonic time-dependence. According to Weaver (1994) this signal can be approximated by an infinite current sheet over the surface. Close to polar zones and to the magnetic equator, the source fields are polarized in a different way and weaken very rapidly (Viljanen, 2012). In these regions, the sources are known as ionospheric electrojets, and can be approximated by a superposition of fields for a distribution of infinite current lines of different strengths (Weaver, 1994, Chap.1).

Source fields with frequencies higher than 1 Hz are caused by electrical storms which originate in the atmosphere. These signals are known as spherics. Electrical storms are larger on summer afternoons in tropical areas (Viljanen, 2012). The EM fields propagate to the Earth's surface in three different types of polarization (Simpson & Bahr, 2005, Chap.1). First, the electric field may be polarized horizontally, thus the orthogonal magnetic field propagates vertically to the surface. In the second polarization, the magnetic field propagates horizontally and the electric field travels vertically to the Earth surface. The last polarization of spherics describes both the electric and magnetic fields traveling horizontally, so both an electric field and a magnetic field are expected to reach the surface. Regardless of the atmospheric propagation direction and polarization, the EM version of Snell's law shows that the direction of EM fields propagation turns to vertical when entering the relatively conductive Earth (Ward & Hohmann, 1988). For that reason, these EM fields can be described by an infinite current sheet over the surface, for MT modeling purposes (Weaver, 1994, Chap.1).

1.2.2 Measurements

EM field components $\{E_x, E_y, B_x, B_y, B_z\}$ are measured over a period of time at the Earth's surface, obtaining the EM time series which are used to study the electrical properties of the subsurface. Measured electric field components $\{E_x, E_y\}$ consist of the voltage variation between two grounded electrodes (Figure 1.1).

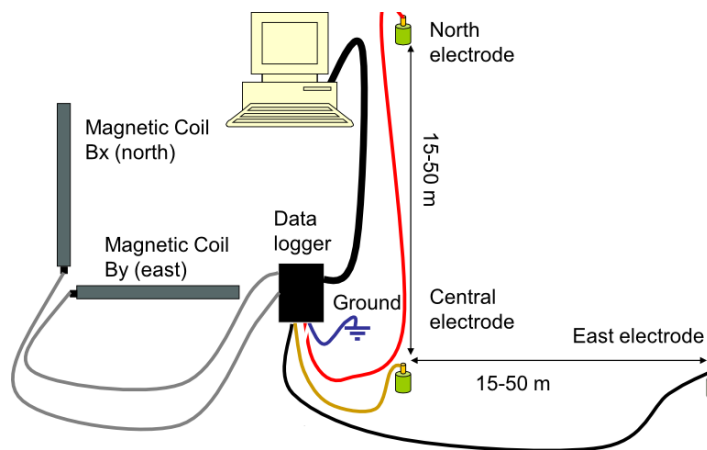


Figure 1.1: Scheme of MT deployment on the field.

Therefore, two dipoles are placed perpendicular to each other, usually, one in the North-South x direction and the other in the East-West direction y . Vertical component of electric field E_z is only measured occasionally in marine MT applications.

The magnetic induction components $\{B_x, B_y, B_z\}$ are measured as a function of

time. Two types of magnetometers are used in EM method applications, and these are induction coils, or fluxgate magnetometers. Induction coils consist of a loop of wires that produce a voltage proportional to the change of magnetic induction over time. These induction coils rely on using a highly permeable magnetic core to gather the local magnetic flux, which gives amplification factors of 100 to 1000 times over that of an equivalent air-cored coil (Tumanski, 2007). Three induction coils are placed perpendicular to each other in each site, e.g. in North x , East y , and vertical z directions (Figure 1.1). Fluxgate magnetometers are used to measure long-period (low-frequency) magnetic induction variations, in this case the three sensors are on the same plate and perpendicular to each other (Simpson & Bahr, 2005).

1.3 EM Induction in the Earth

The EM fields within a medium (Earth's subsurface) are described by Maxwell's equations in differential form:

$$\nabla \times \mathbf{E} = -\frac{\partial \mathbf{B}}{\partial t} \quad (1.1a)$$

$$\nabla \times \mathbf{H} = \mathbf{j} + \frac{\partial \mathbf{D}}{\partial t} \quad (1.1b)$$

$$\nabla \cdot \mathbf{B} = 0 \quad (1.1c)$$

$$\nabla \cdot \mathbf{D} = q. \quad (1.1d)$$

These equations relate the electric field to the orthogonal magnetic field. Faraday's Law (1.1a) states that the variation with time of the magnetic induction \mathbf{B} will generate a voltage or electric field variation \mathbf{E} in a closed loop and orthogonal to \mathbf{B} (Figure 1.2a). Ampere's Law (1.1b) relates the magnetic field \mathbf{H} with the current density \mathbf{j} and displacement current \mathbf{D} (Figure 1.2b). Gauss's Law for the magnetic induction (1.1c) indicates that magnetic induction always form a loop, while Gauss's Law for the electric field (1.1d) states that the electric displacement on a closed surface is equal to the charge q enclosed by that surface.

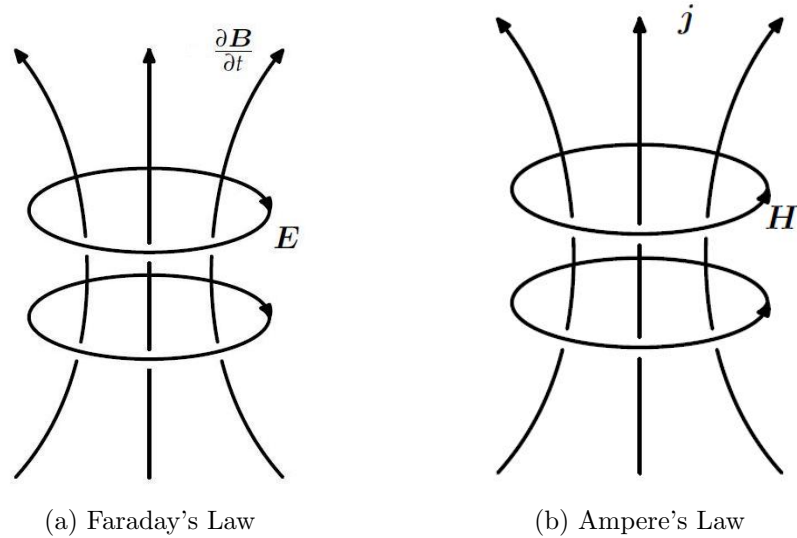


Figure 1.2: Graphical description of the behavior of electric and magnetic fields from Maxwell's equations.

The constitutive relationships describe the EM fields behavior according to the EM properties of the medium, and they are

$$\mathbf{j} = \sigma \mathbf{E} \quad (1.2a)$$

$$\mathbf{B} = \mu \mathbf{H} \quad (1.2b)$$

$$\mathbf{D} = \varepsilon \mathbf{E}. \quad (1.2c)$$

These properties are conductivity σ , magnetic permeability μ and electric permittivity ε . The conductivity is a measure of the medium's ability to transport (or conduct) electrical charge, and relates the current density with the electric field by Ohm's Law (1.2a). This parameter is the primary target for MT applications, and in its most general case (3D) it consists of a 3×3 symmetric tensor ($\boldsymbol{\sigma}$) in Cartesian coordinates.

The magnetic permeability is $\mu = \mu_0 \mu_r$, where $\mu_0 = 4\pi \times 10^{-7} \text{ Hm}^{-1}$ is the magnetic permeability of a vacuum, and μ_r is the relative value for a specific material. This property is defined as the ability of the medium to accommodate magnetic induction lines, or alternatively the magnetization degree of a material. The magnetic permeability, defined by Equation (1.2b), relates the magnetic induction with the magnetic field of the medium. For most of geological materials that are not iron-rich $\mu_r \approx 1$, and it is common to use only the value of μ_0 in MT applications. The electric permittivity is defined as $\varepsilon = \varepsilon_0 \varepsilon_r$, where the free-space value is $\varepsilon_0 = 8.854 \times 10^{-12} \text{ Fm}^{-1}$ and the relative value for a specific material is ε_r . This parameter is defined by Equation (1.2c) as the ability of the medium to store or retain charges. In other words, the electric permittivity is a measure of the material ability to polarize in response to an applied electric field \mathbf{E} and establishes the displacement current \mathbf{D} inside the material.

In order to solve the partial differential equations (PDEs) and describe the EM induction within a medium, Maxwell's equations have to be decoupled to define them in terms of only \mathbf{E} or \mathbf{B} . As MT measures the magnetic induction, it is important to modify Ampere's Law (1.1b) in terms of \mathbf{B} . In addition, for the frequency range used in EM applications, the EM fields satisfy the quasi-static condition. This condition means that the distribution of EM fields through space, at any instant of time, change sufficiently slow to behave as quasi-static fields (Weaver, 1994, Chap.1). The quasi-static assumption can be described in the Amperes's Law by neglecting the displacement current variation within the medium, because $\mathbf{j} \gg \frac{\partial \mathbf{D}}{\partial t}$ for the frequency range used in MT applications (Weaver, 1994, Chap.1). Therefore, Ampere's Law (1.1b) at low frequencies typically less than 10^4 Hz can be written as

$$\nabla \times \mathbf{H} = \mathbf{j} \implies \nabla \times \mathbf{B} = \mu \sigma \mathbf{E} \quad (1.3)$$

by including the Ohm's Law (1.2a) and the relationship (1.2b). The electrical permittivity can be considered as constant within the medium.

An important aspect that arises from neglecting displacement currents is that the current density will satisfy $\nabla \cdot \mathbf{j} = 0$, because $\nabla \cdot (\nabla \times \mathbf{B}) \equiv 0$. This means that the current density is solenoidal, so all conduction currents flow in closed circuits (Weaver, 1994, Chap.1). With this in mind, it is possible to obtain the volume charge density in a conductive medium as

$$q = -\frac{\nabla \sigma \cdot \mathbf{E}}{\sigma} \varepsilon. \quad (1.4)$$

This equation describes those charges that accumulate on small inhomogeneities causing a distortion of the electric field. Equation (1.4) is obtained by calculating $\nabla \cdot \mathbf{j}$ using Ohm's Law (1.2a) and Gauss's Law (1.1d).

The general diffusion PDE for the electric field is obtained by taking the curl of Faraday's Law (1.1a), as

$$\nabla \times (\nabla \times \mathbf{E}) = -\frac{\partial}{\partial t}(\nabla \times \mathbf{B}). \quad (1.5)$$

The definition of the vector Laplacian states that $\nabla \times (\nabla \times \mathbf{E}) \equiv \nabla(\nabla \cdot \mathbf{E}) - \nabla^2 \mathbf{E}$. Applying this definition in Equation (1.5), substituting Equation (1.3) and the volume charge definition (Equation (1.4)) from Gauss's Law (1.1d), the PDE governing the diffusion process of the electric field within a medium is (Weaver, 1994, Chap.1):

$$\nabla^2 \mathbf{E} + \nabla \left[\frac{\nabla \sigma \cdot \mathbf{E}}{\sigma} \right] = \mu \sigma \frac{\partial \mathbf{E}}{\partial t}. \quad (1.6)$$

In the same way, the PDE governing the diffusion process of the magnetic induction within a medium, can be obtained by taking the curl of Ampere's Law (1.3) as

$$\nabla \times (\nabla \times \mathbf{B}) = \mu \nabla \times (\sigma \mathbf{E}) \quad (1.7)$$

Expanding the curl of the product $\sigma \mathbf{E}$ by the product rule of differentiation, the following equation is obtained:

$$\nabla \times (\nabla \times \mathbf{B}) = \mu \sigma (\nabla \times \mathbf{E}) + \mu \nabla \sigma \times \mathbf{E} \quad (1.8)$$

In Equation (1.8), $(\nabla \times \mathbf{E})$ is Faraday's Law (1.1a), and using Ohm's Law (1.2a) in $\mu \nabla \sigma \times \mathbf{E}$, the second term of the sum will be $\nabla \sigma \times \mu \mathbf{j} / \sigma$. Consequently, Ampere's Law (1.3) can be substituted in Equation (1.8). Applying the definition of vector Laplacian, and considering Gauss's Law (1.1c) (Weaver, 1994, Chap.1), the PDE for the magnetic induction is:

$$\nabla^2 \mathbf{B} + \nabla \sigma \times (\nabla \times \mathbf{B}) / \sigma = \mu \sigma \frac{\partial \mathbf{B}}{\partial t}. \quad (1.9)$$

Equations (1.6) and (1.9) are the general governing equations that describe the diffusion process of the EM fields within a medium. The procedure to numerically approximate these PDEs is the basis of forward modeling.

1.3.1 EM Induction in the Air

Source fields for the MT method travel through the atmosphere as a uniform and plane-wave with harmonic time dependence of $e^{i\omega t}$, where $\omega = 2\pi f$ is the angular frequency, and f is the frequency in Hz. To understand the EM induction within Earth, it is important to know how the EM fields behave in air. Such EM fields are polarized in horizontal directions while propagating in $\hat{\mathbf{z}}$ direction towards the Earth's surface.

Consider the electric field \mathbf{E} polarized in the x direction and propagating in $\hat{\mathbf{z}}$ direction only, $E_x(z)$. The conductivity of air is very low and is usually taken as $\sigma = 0$ S/m, so the PDE for the electric field (Equation (1.6)), in frequency domain, reduces to

$$\frac{\partial^2 E_x}{\partial z^2} = 0. \quad (1.10)$$

From Faraday's Law (1.1a), the magnetic induction B_y , in the frequency domain, is given by

$$B_y = i/\omega \frac{\partial E_x}{\partial z}. \quad (1.11)$$

The solution of Equation (1.10) will be a linear function of z , and the solution of Equation (1.11) is a constant (Cagniard, 1953). Therefore, the electric field and the magnetic induction in air are

$$E_x = E_0 + i\omega B_0 z \quad (1.12a)$$

$$B_y = B_0. \quad (1.12b)$$

From this procedure, and similarly for the magnetic field PDE (1.9), one can conclude that only horizontal components of EM fields travel through the air, and no vertical components (E_z or B_z) reach the Earth's surface. The change of field intensity and energy density is associated with a flow of energy from or toward the source, the intensity of energy flow at a point in the field is defined by the Poynting vector $\mathbf{S} = \mathbf{E} \times \mathbf{H}$ in watts/meters² (Stratton, 2007).

1.3.2 EM Induction in a Homogeneous Earth

A homogeneous Earth contains a constant σ value, thus $\nabla\sigma = 0$. Therefore the PDEs (1.6) and (1.9) reduce to

$$\nabla^2 \mathbf{E} = \mu\sigma \frac{\partial \mathbf{E}}{\partial t} \quad (1.13)$$

$$\nabla^2 \mathbf{B} = \mu\sigma \frac{\partial \mathbf{B}}{\partial t}. \quad (1.14)$$

Both Equations (1.13) and (1.14) have the same form, thus a general field $\mathbf{F} \in \{\mathbf{E}, \mathbf{B}\}$ can be defined to satisfy the Maxwell's equations. Away from equatorial and polar zones, EM fields reach the Earth surface as uniform, plane-waves with surface value \mathbf{F}_0 . In addition, to satisfy Maxwell's equations within the half-space, \mathbf{F} will have a sinusoidal depth (z) variation that decays exponentially with depth (e^{-ikz}) (Vozoff, 1991), as

$$\mathbf{F} = \mathbf{F}_0 e^{-ikz} e^{i\omega t}, \quad (1.15)$$

where k is the propagation constant or wave number.

Taking the partial derivative of Equation (1.15) with respect to time, the PDE for each EM field (Equation (1.13) or (1.14)) is reduced to

$$\nabla^2 \mathbf{F} = i\omega\mu\sigma \mathbf{F} \quad (1.16a)$$

$$\frac{\partial^2 \mathbf{F}}{\partial z^2} = k^2 \mathbf{F} \quad (1.16b)$$

$$k = \sqrt{i\omega\mu\sigma} = \sqrt{\frac{\mu\omega\sigma}{2}} - i\sqrt{\frac{\mu\omega\sigma}{2}}. \quad (1.16c)$$

The solution (Equation (1.15)) does not vary in x and y directions, so the Laplacian of \mathbf{F} is reduced in terms of the z direction only (Equation (1.16b)). From this equation, the propagation constant k is defined as Equation (1.16c), using $\sqrt{i} = \frac{i+1}{\sqrt{2}}$.

Skin-Depth The sinusoidal depth variation is related to the real part of k , and the exponential decay with depth relates to the imaginary part of Equation (1.16c). The depth where the EM fields are reduced to 1/e of its initial values (\mathbf{F}_0) is known as the skin-depth. From the definition of k (Equation (1.16c)), the skin-depth is obtained by

$$\delta = \frac{1}{\Re(k)} = \sqrt{\frac{2}{\mu\omega\sigma}}. \quad (1.17)$$

This parameter is inversely proportional to the square root of frequency, so high-frequency signals penetrate much less than low-frequency ones. It is also inversely proportional to the square root of conductivity, such that signals penetrate further in low conductivity (resistive) regions.

Considering that it is rare to encounter large magnetizable bodies (and thus $\mu_r \approx 1$), $\mu = \mu_0$ is used in Equation (1.17). In practice, it is common to use: $\delta \approx 500\sqrt{\rho T}$, where $\rho = 1/\sigma$ is the resistivity of the half-space and T is the period (s). Figure 1.3 presents the range of skin-depth for the range of periods in MT applications. Thus, in theory, a single MT site can be sensitive to conductivity structures over ranges of tens of meters to hundreds of kilometers in depth.

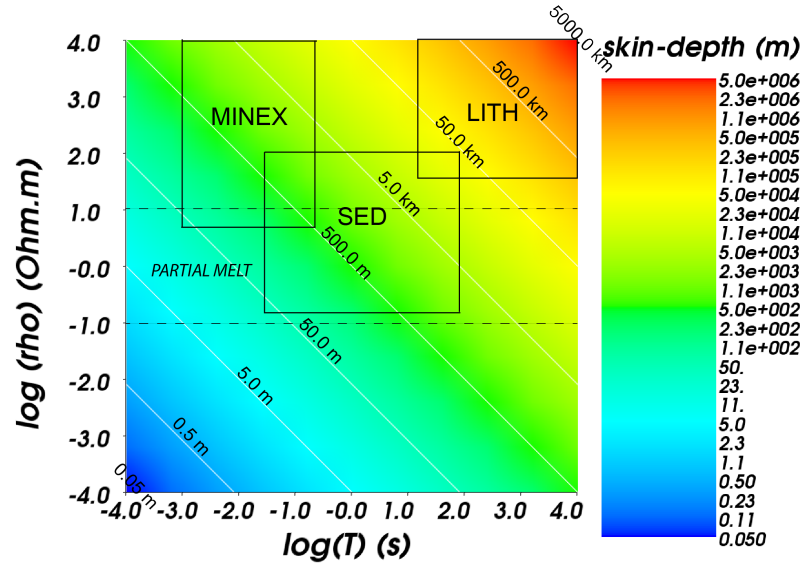


Figure 1.3: Skin-depths (meters) for typical range of periods (T) used in MT applications and typical resistivity values. The main MT applications are bounded by squares: mineral exploration (MINEX), energy resource exploration (SED), lithospheric studies including mantle studies (LITH). The dashed lines enclose the applications to quantify partial melt (PARTIAL MELT) in volcanic regions and in the mantle.

The relationship of each measured electric field component with its orthogonal induced magnetic induction can be obtained by expanding the curl of Faraday's Law (1.1a) and calculating the partial derivatives in terms of the field solution (Equation (1.15)) (Simpson & Bahr, 2005). This relationship is reduced in terms of z direction only, within the homogeneous half-space:

$$\begin{pmatrix} kE_y \\ -kE_x \end{pmatrix} = \begin{pmatrix} -i\omega B_x \\ -i\omega B_y \end{pmatrix}. \quad (1.18)$$

Impedance From Equation (1.18) it is possible to define the impedance Z , which relates the orthogonal electric field and magnetic induction (Simpson & Bahr, 2005) as:

$$\begin{aligned} Z &= \frac{E_x}{B_y} = \frac{i\omega}{k} = \sqrt{\frac{\omega}{\mu\sigma}} \sqrt{i} \\ Z &= \sqrt{\frac{\omega\rho}{2\mu}} + i\sqrt{\frac{\omega\rho}{2\mu}}. \end{aligned} \quad (1.19)$$

Although the magnetic induction is measured in MT applications, most of MT practitioners use the impedance with units of VA^{-1} , which is defined in terms of the magnetic field. In this case, Equation (1.19) becomes

$$\begin{aligned} Z &= \frac{E_x}{H_y} = \frac{i\omega\mu}{k} = \sqrt{\frac{\omega\mu}{\sigma}}\sqrt{i} \\ Z &= \sqrt{\frac{\omega\mu\rho}{2}} + i\sqrt{\frac{\omega\mu\rho}{2}}. \end{aligned} \quad (1.20)$$

The Schmucker-Weidelt (Weidelt, 1972; Schmucker, 1973) transfer function is

$$C = \frac{1}{k} = \frac{1}{i\omega\mu}Z. \quad (1.21)$$

Equation (1.21) is a function that represents the Earth subsurface as a linear system relating the orthogonal EM fields (Simpson & Bahr, 2005).

From the magnitude of the impedance (Equation (1.20)), the resistivity of the homogeneous half-space is defined by

$$\rho = \frac{1}{\mu\omega} |Z|^2 = \mu\omega |C|^2. \quad (1.22)$$

The phase of a complex number $c = a + ib$ is defined as $\tan^{-1}(b/a)$. By the definition of Z in Equation (1.19), the associated impedance phase is defined as

$$\phi = \arg(Z) = \tan^{-1}(1) = 45^\circ. \quad (1.23)$$

Therefore, the impedance phase of any homogeneous half-space is always 45° (Simpson & Bahr, 2005).

1.3.3 EM Induction in a Layered Earth

The Earth model contains N layers with thickness $d = \{d_1, d_2, \dots, d_N\}$, and conductivities $\sigma = \{\sigma_1, \sigma_2, \dots, \sigma_N\}$, where the conductivity of each layer does not change horizontally. Thus, it is possible to assume a homogeneous solution for the diffusion equations (Equations (1.13) and (1.14)) within each n -layer ($n = 1, 2, \dots, N$). The orthogonal field solutions for each n -layer are defined as

$$E_{xn}(k_n, \omega) = E_{1n}e^{i\omega t - ik_n z} + E_{2n}e^{i\omega t - ik_n z} \quad (1.24)$$

$$B_{yn}(k_n, \omega) = B_{1n}e^{i\omega t - ik_n z} + B_{2n}e^{i\omega t - ik_n z} \quad (1.25)$$

(Simpson & Bahr, 2005).

The Schmucker-Weidelt transfer function for each n -layer is defined by the ratio between Equations (1.24) and (1.25), following the definition in Equation (1.21). This function now depends on z , as the propagation constant $k_n = \sqrt{i\omega\mu\sigma_n}$ depends on the conductivity of the layers, that vary with depth. Also, the fields components (Equations (1.24) and (1.25)) must be continuous at layer contacts, that is, the field component at the top of the $n + 1$ layer must be equal to that at the bottom of n layer, where n increases downward in the z direction (Simpson & Bahr, 2005).

Wait's recursion formula (Wait, 1954) is

$$\begin{aligned} C_n(z_{n-1}) &= \frac{1}{k_n} \frac{k_n C_{n+1}(z_n) + \tanh(k_n l_n)}{1 + k_n C_{n+1}(z_n) \tanh(k_n l_n)}, \\ C_N &= \frac{1}{k_N}; \quad l_n = z_n - z_{n-1}. \end{aligned} \quad (1.26)$$

This formula is used to calculate the transfer function C on top of n layer if the top of $n+1$ layer value is known (Simpson & Bahr, 2005). With Equation (1.26) it is possible to calculate C_n , starting from C_N that is the value at the top of the deepest layer, assuming that the EM fields decay exponentially with depth. The calculation is made recursively until the top layer transfer function is found.

Apparent Resistivity From this Earth model, to more complex ones, the resistivity is defined as a depth-weighted resistivity within each half-space, now being the apparent resistivity ρ_a . The apparent resistivity and phase of each layer n are

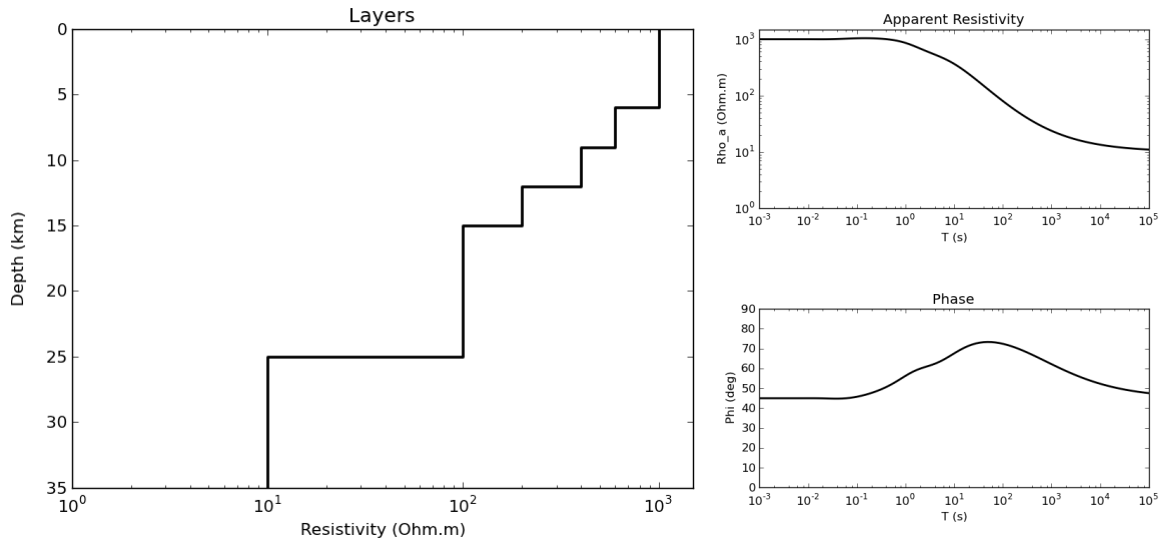
$$\begin{aligned}\rho_{a_n}(\omega) &= \frac{1}{\mu\omega} |Z_n(\omega)|^2 \\ \phi_n &= \tan^{-1} \left[\frac{\Im Z_n}{\Re Z_n} \right].\end{aligned}\tag{1.27}$$

In this case ρ_a is the resistivity of a layer as a uniform half-space. When plotted against frequency, this parameter oscillates and reaches asymptotic values according to the value of the layer related to the frequency (Figure 1.4).

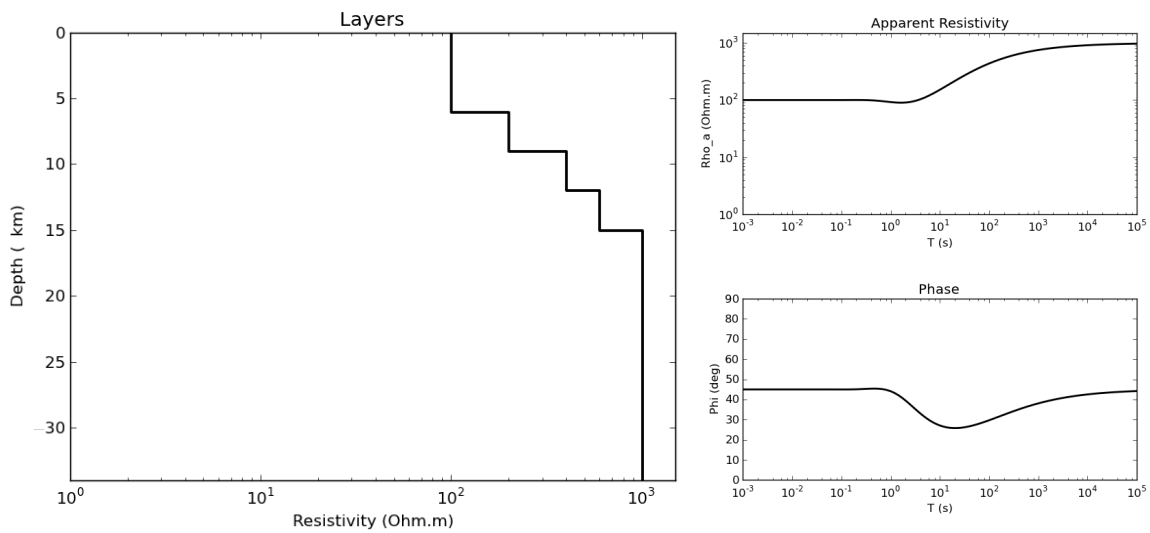
Therefore, for higher frequencies ρ_a is asymptotic to ρ_1 (i.e. the resistivity of the first layer), and for low frequencies ρ_a is asymptotic to ρ_N . Within intermediate frequencies the apparent resistivity curve oscillates approximating resistivity values at intermediate layers (Figure 1.4). These values depend also on the thickness of the layer and cannot always be completely determined. In addition, resistive layers between conductive layers have no effect, thus ρ_a does not approximate a small resistive layer.

On the other hand, the impedance phase anticipates the behavior of ρ_a , because it is always asymptotic to 45° within each layer as a homogeneous body. Simpson & Bahr (2005) describe this behavior as follow:

- If $\phi > 45^\circ$, ρ_a decreases with depth and the layer thickness can be determined (Figure 1.4a).
- If $\phi < 45^\circ$, ρ_a increases with depth and the layer conductance ($\tau = \sigma l$) can be determined, where l is the layer thickness defined in Equation (1.26) (Figure 1.4b).



(a) Apparent resistivity plot (top right panel) and phase plot (bottom right panel) for a layered earth where resistivity decreases with depth (left panel).



(b) Apparent resistivity plot (top right panel) and phase plot (bottom right panel) for a layered earth where resistivity increases with depth (left panel).

Figure 1.4: Behavior of apparent resistivity and phase plots obtained from Wait's Recursion for two layered Earth models. Based on Simpson & Bahr (2005).

1.3.4 2D Earth EM Induction

When Earth's subsurface also presents lateral variation of structures, the conductivity, currents, and EM fields vary in x and z directions, e.g. $\sigma = \sigma(x, z)$ (Vozoff, 1991). In its more general (3D) case, the conductivity varies in x , y , and z directions, as $\sigma = \sigma(x, y, z)$. In consequence \mathbf{E} , and \mathbf{B} are usually not orthogonal to each other (Vozoff, 1991).

Impedance Tensor The impedance \mathbf{Z} is now a 2×2 tensor relating the 'orthogonal' components of the horizontal EM fields, and is defined as

$$\begin{pmatrix} E_x \\ E_y \end{pmatrix} = \begin{pmatrix} Z_{xx} & Z_{xy} \\ Z_{yx} & Z_{yy} \end{pmatrix} \begin{pmatrix} B_x \\ B_y \end{pmatrix}. \quad (1.28)$$

From Equation (1.18), the impedance tensor \mathbf{Z} has an anti-diagonal form with $Z_{xy} = -Z_{yx}$ in the 1D case.

The simplest 2D model can be considered as a lateral discontinuity in Earth's subsurface, with a strike considerably longer than the penetration depth (Simpson & Bahr, 2005, Chap.2), and assuming that the strike is parallel to the x direction (Figure 1.5).

Figure 1.5: Simple 2D conductivity model with a vertical contact, ($\sigma_1 \neq \sigma_2$). The \mathbf{E} field orthogonal to the contact is discontinuous, but the currents \mathbf{j} are continuous across the contact. Two field polarizations (TE mode and TM mode) are obtained when each of the EM fields are parallel to the strike direction. Redrawn from Simpson & Bahr (2005).

If the current density (\mathbf{j}) and the electric field (\mathbf{E}) are applied across the lateral contact (in the y direction), electrical charges (q) will build up at this contact (Figure 1.5). These electrical charges along the strike direction generate a secondary electric field in order to satisfy the boundary condition, which is the continuity of current density across the boundary. Vozoff (1991) described the effect of this secondary electric field as making the conductor appear more conductive and the resistive region appear more resistive. Therefore, in this case the apparent resistivity curve, when plotted against horizontal distance across the lateral contact, will show an abrupt jump of the ρ_a value on the contact location. This kind of field polarization is known as \mathbf{B} -polarization or Transverse Magnetic (TM) mode, because when the electric field is polarized across the lateral contact, the magnetic induction will be aligned parallel to the strike direction (Figure 1.5).

Another field polarization is the Transverse Electric (TE) mode or **E**-polarization, where **B** is polarized across the lateral contact while **E** is polarized parallel to strike (x) direction (Figure 1.5). In this case, charges are not strong enough to be sensed because the boundary condition requires only the continuity of the electric field across the boundary (Vozoff, 1991). Consequently, two independent polarizations are obtained when each EM field is aligned parallel to the strike direction.

Transverse Magnetic mode Calculating the curl of both Faraday's and Ampere's Law, and considering that in this polarization the only field components are $\{B_x, E_y, E_z\}$, the **B**-polarization can be described by the following equations:

$$\frac{\partial B_x}{\partial z} = \mu\sigma E_y \quad (1.29a)$$

$$-\frac{\partial B_x}{\partial y} = \mu\sigma E_z \quad (1.29b)$$

$$\frac{\partial E_z}{\partial y} - \frac{\partial E_y}{\partial z} = -i\omega B_x. \quad (1.29c)$$

Transverse Electric mode The field components in this case are $\{E_x, B_y, B_z\}$, therefore, the equations derived from Faraday's and Ampere's Law that describe this polarization are:

$$\frac{\partial E_x}{\partial y} = i\omega B_z \quad (1.30a)$$

$$\frac{\partial E_x}{\partial z} = -i\omega B_y \quad (1.30b)$$

$$\frac{\partial B_z}{\partial y} - \frac{\partial B_y}{\partial z} = \mu\sigma E_x. \quad (1.30c)$$

From Ampere's Law in the TM mode (Equation (1.29a)) and Faraday's Law in the TE mode (Equation (1.30b)), it is evident that Z_{xy} and Z_{yx} components of the impedance tensor are related to the field polarizations. Therefore, in a 2D Earth, where the strike of the lateral discontinuity is long enough and the fields are parallel to this strike, the impedance tensor takes an anti-diagonal form as

$$\begin{pmatrix} 0 & Z_{xy} \\ Z_{yx} & 0 \end{pmatrix} = \begin{pmatrix} 0 & Z_{TE} \\ Z_{TM} & 0 \end{pmatrix}. \quad (1.31)$$

In the general case of lateral discontinuity (previously described) the impedance tensor has the general form described in Equation (1.28). However, it is possible to rotate the coordinate system (x, y, z) in order to mathematically obtain the same representation as Equation (1.31). The new coordinate system (x', y', z) can be found by looking for the optimal angle θ (e.g. Swift, 1967) that anti-diagonalize the **Z** tensor as

$$\mathbf{Z}' = \mathbf{R}\mathbf{Z}\mathbf{R}^T \quad (1.32)$$

$$\mathbf{R} = \begin{pmatrix} \cos \theta & \sin \theta \\ -\sin \theta & \cos \theta \end{pmatrix} \quad (1.33)$$

where **R** is the rotation matrix (Equation 1.33), and **R**^T is its transpose. According to Vozoff (1991) θ is the angle between the measurement orientation and the strike in positive clockwise direction.

Tipper Vector If the polarization of the source field is in TE mode, from Faraday's Law (1.30a) and Ampere's Law (1.30c) a vertical magnetic induction component B_z will be obtained. This magnetic induction component B_z is related to the horizontal components (B_x, B_y) by the Tipper vector \mathbf{T} (Simpson & Bahr, 2005). In other words, the vector \mathbf{T} relates the horizontal magnetic induction into its vertical component for a given frequency ω , as

$$B_z = T_x B_x + T_y B_y. \quad (1.34)$$

The graphical representations of the tipper vectors are known as induction arrows. These arrows infer the presence or absence of lateral conductivity variations. Simpson & Bahr (2005) discussed two types of induction arrows that differentiate between them by the way they point towards the conductivity variation. Parkinson induction arrows point from the resistive region towards the region with high conductivity (Parkinson, 1959). These arrows have a real (in phase) and imaginary (out of phase) parts with magnitude M_r , and M_q , respectively (Parkinson, 1959). These magnitudes are defined as

$$M_r = (\Re T_{zx} + \Re T_{zy})^{1/2} \quad (1.35)$$

$$M_q = (\Im T_{zx} + \Im T_{zy})^{1/2}. \quad (1.36)$$

The orientation of these induction vectors are θ_r for the real part, and θ_q for the imaginary part (Parkinson, 1959). These angles are defined as

$$\theta_r = \tan^{-1} \left(\frac{\Re T_{zx}}{\Re T_{zy}} \right) \quad (1.37)$$

$$\theta_q = \tan^{-1} \left(\frac{\Im T_{zx}}{\Im T_{zy}} \right). \quad (1.38)$$

Other induction arrows follow the Wiese convention that points away from the high conductivity region toward the more resistive one (Simpson & Bahr, 2005, Chap.2).

1.3.5 3D Earth EM Induction

When there is no predominant 2D strike, a rotation angle θ cannot be found to align the coordinate system to any strike direction. This means that the Earth subsurface contains 3D geological structures, so the conductivity varies in all directions (x, y, z) . In this case the diffusion PDEs for either electric and magnetic fields must be solved for all of its field components. Considering that a solution exist for both electric and magnetic fields, and assuming that these solutions also have a harmonic time and depth dependence, the impedance tensor will be a complex tensor described as

$$\begin{pmatrix} Z_{xx} & Z_{xy} \\ Z_{yx} & Z_{yy} \end{pmatrix} = \begin{pmatrix} X_{xx} & X_{xy} \\ X_{yx} & X_{yy} \end{pmatrix} + i \begin{pmatrix} Y_{xx} & Y_{xy} \\ Y_{yx} & Y_{yy} \end{pmatrix} \quad (1.39)$$

(Simpson & Bahr, 2005).

In the same manner, both the resistivity and phase of this impedance tensor are matrices with indexes $\{i, j\}$ belonging to any of the directions $\{x, y\}$, as:

$$\begin{aligned} \rho_{a_{ij}}(\omega) &= \frac{1}{\mu\omega} |Z_{ij}(\omega)|^2 \\ \phi_{ij} &= \tan^{-1} \left[\frac{\Im Z_{ij}}{\Re Z_{ij}} \right]. \end{aligned} \quad (1.40)$$

To deal with the full impedance tensor, Romo et al. (2005) introduced a transformation of this tensor into what they called serial and parallel components, that behave similarly to the concepts of TM and TE in 2D, respectively. This means that the flow of electric current in the earth can be obtained to be either along or across 3D boundaries. Therefore, these authors considered a rotation of the horizontal electric field by $\mathbf{R}_e(\theta_e)$, and another for the magnetic field by $\mathbf{R}_h(\theta_h)$. The basis of this transformation is that the impedance tensor can be represented as $\mathbf{Z}' = \mathbf{R}_e \mathbf{Z} \mathbf{R}_h^T$, so the values of θ_e and θ_h can be obtained to anti-diagonalize \mathbf{Z} . The serial estimator depends on the higher principal impedances, while the parallel estimator is more sensitive to lower principal impedances (Romo et al., 2005).

Another way to deal with 3D MT data, is to interpret it with 2D processes (Ledo, 2005). Ledo (2005) provided some general situations where it is possible to interpret 3D data with 2D techniques, and determined which data subset (TE or TM mode) is the best to obtain the resistivity model of the subsurface. The aim of this interpretation is to obtain the information of the 3D targets, such as location, geometry, size, resistivity and depth, from measured data. The interpretation of 3D data from 2D techniques depends on the scale of the problem. For large scale problems, a 2D model of the subsurface is affected to a small degree by medium-scale 3D structures. On the other hand, in small scale problems the information of the 3D conductive body can be obtained from measured data (Ledo, 2005).

1.4 Galvanic Distortion

When the electric field is orthogonal to the boundary of an inhomogeneity, charges build up at this contact and are described by Equation (1.4) in the conductive medium. These charges produce a secondary electric field in order to satisfy the boundary condition of the current density \mathbf{j} . Shallow subsurface inhomogeneities produce two types of distortion to the electric field depending on the frequency of the applied signal, and the size of the anomaly. For high frequency signals, and when the size of the anomaly is sufficiently larger than the skin-depth, this inhomogeneity has an inductive effect on the electric field. The secondary electric field is frequency-dependent, so this induction effect is seen in both apparent resistivity and phase (Vozoff, 1991).

In contrast, at low frequencies and when the size of the inhomogeneity is small compared to the skin-depth, the induction effect vanishes (Vozoff, 1991). The presence of electric charges, at the boundaries of inhomogeneities, influence the observed electric field and also alter the magnetic field when the charges deflect regional electric currents (Chave & Smith, 1994). This effect is known as galvanic distortion. In a similar way to the description of TE and TM modes, charges build up only when the electric field is applied perpendicular to the boundary. Therefore, the TM mode present a weak inductive distortion and the TE model will be affected by galvanic distortion (Ledo, 2005).

Two effects of galvanic distortions are present in MT data, these are the phase mixing, and static shift (Ogawa, 2002). Phase mixing is the distortion of telluric orthogonality, while static shift is the distortion of telluric amplitudes (Ogawa, 2002). Therefore, static shift is seen in MT data as a movement of the resistivity curve by a time independent multiplicative factor at a station.

Galvanic distortion can be removed by an impedance tensor decomposition into an undistorted tensor and a distorted part (e.g. Chave & Smith, 1994; Groom & Bahr, 1992; Groom & Bailey, 1989, 1991; Utada & Munekane, 2000). The most used

technique is the Groom-Bailey (1989) decomposition, which decomposes the observed impedance tensor Z_{obs} as

$$Z_{\text{obs}} = R(gTSAZ_{2D})R^{-1}. \quad (1.41)$$

In Equation (1.41), R is the rotation matrix that transforms between the observed and regional coordinate systems, g is the site gain, T is the twist tensor, S is the shear tensor, A is the anisotropy tensor, and Z_{2D} is the 2D impedance tensor with off-diagonal components (Groom & Bailey, 1989). In this decomposition method, twist and shear tensors describe the orthogonality of EM fields (Ogawa, 2002). The site gain and anisotropy describe the static shift, so the static shift contaminated impedance Z'_{2D} is

$$Z'_{2D} = gAZ_{2D}. \quad (1.42)$$

From the Groom-Bailey (1989) decomposition, one can only determine Z'_{2D} , thus static shift cannot be removed with an impedance tensor decomposition (Ogawa, 2002).

According to Tournerie et al. (2007), static shift effect can be removed on MT data by spatial filtering. The spatial filtering of \mathbf{E} can be applied on field by the use of dipoles (e.g. Torres-Verdín & Bostick, 1992) or on MT data processing by spatial low-pass filters (e.g. Zhang et al., 1995). The use of other geophysical (or geological) information about the inhomogeneity with methods that are not affected by static shift (such as Transient EM method, TEM) can be another alternative for static shift removal (Tournerie et al., 2007).

The consideration of static shift as an unknown for the inversion of MT data can also be used to remove the static shift effect (e.g. deGroot Hedlin, 1991; Rodi & Mackie, 2001; Smith & Booker, 1991). The relationship between the original (uncorrected) EM data with the correct one can be obtained by adding a weighted matrix of static shift values at appropriate locations, and include this in the inversion process (deGroot Hedlin, 1991).

Tournerie et al. (2007) argued that both ρ_a and phase ϕ are uncorrelated because near surface inhomogeneities only affect the apparent resistivity data. Consequently, ρ_a data can be corrected in order to obtain an adequate spatial correlation between ϕ and ρ_a using the Cokriging method (Tournerie et al., 2007).

1.5 Dimensionality Analysis

The dimensionality analysis of EM data is an important step in data processing because it provides information of the dimension (1D, 2D or 3D) of subsurface structures and can provide some information about shallow subsurface anomalies that distort the data. For these reasons, this step is used to select an appropriate dimension and static shift parameters for the modeling and inversion of EM data.

As described in Section 1.3.4 of 2D EM induction, the coordinate system can be rotated in order to obtain EM fields aligned to the strike of the main subsurface structure. By rotating the coordinate system, the impedance tensor is also rotated. Since Swift (1967), the study of some components of the rotated impedance tensor that are invariants to the coordinate system rotation, has been used to obtain the dimensionality of the subsurface structures (e.g. Bahr, 1988; Groom & Bailey, 1989; Martí et al., 2009; Weidelt, 1972).

1.5.1 WAL Invariants

Weaver et al. (2000) introduced seven mutually independent invariants $\{I_1, I_2, \dots, I_7\}$ based on Fischer & Masero (1994) and Szarka & Menvielle (1997), and another invari-

ant Q that reflects the dependence on the rotational angle. These invariants provide information about the subsurface medium, and are calculated from the components of the complex impedance tensor in the rotated coordinate system. The interpretation of these invariants yields a classification in three main categories (Weaver et al., 2000). According to Weaver et al. (2000), the ‘fundamental pair’ (I_1, I_2) provides information about 1D structures, and is used to obtain the values of ρ_a and ϕ when the subsurface is 1D. The second pair of invariants (I_3, I_4) contains information about 2D Earth and anisotropy. These invariants provide information about a 2D region, or 3D inhomogeneities on a 2D or 1D region from which the angle of rotation θ can be obtained (Weaver et al., 2000). The remaining invariants contain information about 3D structures, and galvanic distortion.

1.5.2 Phase Tensor

Caldwell et al. (2004) decomposed the phase tensor Φ of the impedance into 3 invariants and an angle α that express the tensor dependence on the coordinate system. They defined the invariants of Φ as its maximum Φ_{\max} , its minimum Φ_{\min} , and its skew angle β . All these invariants are functions of the following phase tensor components: trace, determinant and skew which are also invariants to coordinate rotation (Caldwell et al., 2004).

To describe the behavior of these invariants for the different dimensional cases on the subsurface, Caldwell et al. (2004) plotted this components as an ellipse. In their plots, major and minor axis of the ellipse are Φ_{\max} , and Φ_{\min} respectively, with the orientation of major axis specified by the angle $(\alpha - \beta)$, where α includes the tensor’s dependence on the coordinate system. The geometry of this ellipse will provide information about the dimensionality of subsurface structures. In the 1D case, a homogeneous half-space is represented by a circle of unit radius for all frequencies. In a layered Earth, the radius of circle varies with frequency reflecting the variation of resistivity with depth (Caldwell et al., 2004). In a 2D Earth, the orientation of the major axis will be aligned parallel or perpendicular to the strike of regional 2D structure, and the skew angle β will be zero unless 3D structures are relevant (Caldwell et al., 2004).

According to Caldwell et al. (2004), in a 3D subsurface, the observed MT response will reflect the influence of a near-surface body only for short periods. The direction of the major axis will indicate the preferred flow direction of induction currents in near surface structures. For intermediate periods, alignment of the major axis of ellipses will reflect the effect of both near-surface and deep resistivity structures. Finally, for long periods, deep structures dominate in the phase tensor, so alignment of major axis indicate the preferred flow of inductive currents associated with deep resistivities.

1.5.3 WALDIM

The dimensionality analysis using the phase tensor does not provide information about EM field distortion by local inhomogeneities. For this reason, Martí et al. (2009) preferred the WAL dimensionality analysis, because it is the most suitable to obtain information of either regional and local (inhomogeneities) structures. Based on the WAL invariants, these authors developed a computational program to obtain a dimensionality analysis of subsurface structures. The main features of this program is that the dimensionality analysis can be performed within a band of frequencies, and that it solves inconsistencies when the real and imaginary strike angle are different, in a 2D region. By calculating the dimensionality within a band of frequencies for each station, this program yields a more stable estimate by taking the lowest dimension when more

than one dimensionality is present (Martí et al., 2009). In addition the 2D inconsistencies are solved by changing the dimensionality into a 3D inhomogeneity over a 2D region, and assigning the strike direction and distortion parameters respectively (Martí et al., 2009).

1.6 Electrical Anisotropy

Electrical anisotropy is a property of subsurface structures in which the conductivity depends on direction of measurement for any given unit of rock. This property causes currents to depart from the direction of exciting electric field (Wang & Fang, 2001). In geologic structures, electrical anisotropy has a microscopic or macroscopic origin. An example of microscopic anisotropy is when the conductivity has different directions within crystals (Martí, 2014). Examples of macroscopic anisotropy can be found in fractured formations with voids filled with conductive fluids, thin layers of sediments with different electrical properties, or variation in water saturation (Wang & Fang, 2001; Weiss & Newman, 2002). According to Martí (2014), macroscopic anisotropy is recognized by the lack of ability of EM methods to resolve structures at scales beyond instrument resolution.

In its more general (3D) case, the conductivity σ is a positive definite and symmetric 3×3 tensor in Cartesian coordinates with components in (x, y, z) directions. It is defined in Ohm's Law (1.2a) as

$$\begin{pmatrix} j_x \\ j_y \\ j_z \end{pmatrix} = \begin{pmatrix} \sigma_{xx} & \sigma_{xy} & \sigma_{xz} \\ \sigma_{yx} & \sigma_{yy} & \sigma_{yz} \\ \sigma_{zx} & \sigma_{zy} & \sigma_{zz} \end{pmatrix} \begin{pmatrix} E_x \\ E_y \\ E_z \end{pmatrix}.$$

This means that the conductivity will be a second-rank tensor instead of a scalar as in isotropic media.

As with the impedance tensor, the conductivity can be diagonalized into its three principal components by Euler's rotation (Martí, 2014). Three angles of rotation are obtained, and named as strike, dip and slant angles.

The number of different conductivity values in the principal directions defines two types of anisotropy. Biaxial or triaxial anisotropy is defined when the three principal directions have different values. If two of these principal directions have the same value, then uniaxial anisotropy is defined (Martí, 2014).

The geometry of anisotropy is defined by the values of rotation angles. Azimuthal anisotropy occurs when the strike angle is non-zero and the other angles are zero. If dip angle is the only non-zero, then, dipping anisotropy is present. If all angles are zero, vertical (or transverse) anisotropy occurs in the subsurface (Martí, 2014).

Anisotropy can be detected with MT method. The dimensionality analysis or modeling and inversion gives information about the possibility of electrical anisotropy in the subsurface (Martí, 2014).

Chapter 2

3D MT Modeling and Inversion

2.1 Introduction

In geophysics, EM modeling is the numerical solution of Maxwell's PDEs in order to obtain the EM fields behavior within a specific subsurface model. The physical properties of interest are ε , σ and μ . Maxwell's PDEs are modified according to the source and conditions required for each geophysical EM method. In MT modeling, Maxwell's PDEs will include the quasi-static condition, and the source field will be a uniform plane-wave with harmonic time dependence (Weaver, 1994). In this limit, the only EM property of the subsurface will be the conductivity σ , because ε is removed by the quasi-static condition, and $\mu \approx \mu_0$ for most geological structures. In view of geophysical applications, forward modeling is the simulation of the MT method application on a specific EM model (σ), to generate synthetic EM data.

The main numerical techniques applied for 3D EM modeling problem are finite difference (FD), integral equation (IE), and finite element (FEM) methods. These methods differ from each other by the discretization scheme applied to the model domain, and by the discretized version of governing EM equations.

MT inversion is the application of a numerical scheme to obtain the subsurface EM model (σ or ρ) from measured data. Usual approaches to inversion are made by optimization methods, in order to obtain successive models that yields synthetic MT data that replicate observed data. Consequently, MT inversion requires an efficient and accurate forward modeling algorithm to predict the model responses (Avdeev, 2005).

Avdeev (2005) and Börner (2010) presented a literature review of the main numerical methods used in 3D forward modeling. Avdeev (2005) extended the review to the inversion of geophysical EM methods. Han et al. (2009) compared the numerical accuracy and computational time of four different forward modeling algorithms for the 3D MT problem.

This chapter contains the theory of 3D MT modeling by defining the governing equations to be solved, and the boundaries and interface conditions used for this geophysical method. A literature review of the main methods to solve the forward modeling problem will be presented, with emphasis on the finite element method. In addition, a brief review of inversion methods are discussed to show the importance of forward modeling solution on inversion schemes.

2.2 Problem Statement

The 3D modeling problem consists of a governing PDE

$$\mathbf{D}(\mathbf{m})\mathbf{F}(\mathbf{r}) = \mathbf{s}(\mathbf{r}), \mathbf{r} \in \Omega \quad (2.1a)$$

$$\frac{\partial \mathbf{F}(\mathbf{r})}{\partial \hat{\mathbf{n}}} + \nu \mathbf{F}(\mathbf{r}) = g, \mathbf{r} \in \Gamma, \quad (2.1b)$$

where \mathbf{D} is a differential operator with an EM model \mathbf{m} , $\mathbf{F}(\mathbf{r})$ is an unknown vector function and $\mathbf{s}(\mathbf{r})$ a known source function. This problem is defined in a domain Ω , such that $\mathbf{r} = (x, y, z) \in \Omega$, and $\Omega \in \mathbb{R}^3$. In order to obtain a full solution, the PDE problem is completed by assigning specific values of the unknown function \mathbf{F} on the boundary Γ of the domain. These values are obtained by the Robin boundary conditions (Equation (2.1b)), which is a linear combination of Neumann and Dirichlet boundary conditions. In Equation (2.1b), the term $\frac{\partial \mathbf{F}(\mathbf{r})}{\partial \hat{\mathbf{n}}}$ is the Neumann condition, and $\nu \mathbf{F}(\mathbf{r})$ is the Dirichlet boundary condition.

Governing Equations MT PDEs are usually solved in frequency domain for $\mathbf{E}(\mathbf{r}, \omega)$ or $\mathbf{H}(\mathbf{r}, \omega)$. Hence, all the fields components have a harmonic time dependence $e^{i\omega t}$. The frequency domain governing equations are obtained by applying the Fourier transform to time domain PDEs:

$$\nabla \times (\mu^{-1} \nabla \times \mathbf{E}) + i\omega \sigma \mathbf{E} = -i\omega \mathbf{s}_E(\mathbf{r}, \omega) \quad (2.2a)$$

$$\nabla \times [\sigma^{-1} (\nabla \times \mathbf{H})] + i\omega \mu \mathbf{H} = -i\omega \mu \mathbf{s}_M(\mathbf{r}, \omega). \quad (2.2b)$$

From the similarity of Equations (2.2a) and (2.2b), a general MT governing equation can be written as

$$\nabla \times [\boldsymbol{\nu}^{-1} \cdot (\nabla \times \mathbf{F})] + i\omega \boldsymbol{\kappa} \cdot \mathbf{F} = \mathbf{s}_F, \quad (2.3)$$

where $\mathbf{F} \in \{\mathbf{E}, \mathbf{H}\}$, $\boldsymbol{\nu} \in \{\boldsymbol{\mu}, \boldsymbol{\sigma}\}$, and $\boldsymbol{\kappa} \in \{\boldsymbol{\sigma}, \boldsymbol{\mu}\}$ for the electric field problem, or the magnetic field problem, respectively. The general MT governing equation includes the 3×3 anisotropic tensors. For the isotropic case, these tensors are defined as $\boldsymbol{\nu} = \nu \mathbf{I}$, and $\boldsymbol{\kappa} = \kappa \mathbf{I}$, where \mathbf{I} is the 3×3 identity matrix. In MT modeling, the magnetic permeability is $\mu \approx \mu_0$, then, in the general governing equation the tensor $\boldsymbol{\mu} \approx \mu_0 \mathbf{I}$. Known source fields are represented by an external current density \mathbf{s}_E for the electric field, and by a magnetic source density \mathbf{s}_M for the magnetic field (Equations (2.2a) and (2.2b)). In the case of naturally occurring EM fields, such as with the MT method, the primary field (\mathbf{F}_p) can be included as part of the total field as: $\mathbf{F} = \mathbf{F}_p + \mathbf{F}_s$ (Weaver, 1994). In this case, the external current density and magnetic source density are treated as zero because the source fields will be implicitly present in the solution of the PDE by the primary field. The secondary field \mathbf{F}_s represents the field behavior in the conducting medium, and is the unknown field value to be obtained by numerical methods.

Away from polar and equatorial zones, these primary fields can be represented in terms of the impressed current density $\mathbf{j}(\omega)$, as

$$\mathbf{H}^p = -\frac{1}{2} \mathbf{j}(\omega) \text{sign}(z) \hat{\mathbf{y}} \quad (2.4)$$

for the magnetic field \mathbf{H} , and

$$\mathbf{E}^p = \mathbf{E}_0^p - \frac{1}{2} \mu_0 \mathbf{j}'(\omega) (|z| - |z_0|) \hat{\mathbf{x}} \quad (2.5)$$

for the electric field \mathbf{E} (Weaver, 1994, Chap.1). According to Weaver (1994), these fields represent an infinite current sheet that is obtained from a distribution of infinite current lines with a sinusoidal variation in horizontal directions $(\hat{\mathbf{x}}, \hat{\mathbf{y}})$. A field \mathbf{E}_0^p on a reference point z_0 is added to the primary field \mathbf{E}^p .

Other definitions of the governing equations are also used. The governing equations can be represented by a Helmholtz decomposition of EM fields into a magnetic vector potential \mathbf{A} and a scalar electric potential ϕ , such that $\mathbf{B} = \nabla \times \mathbf{A}$ and $\mathbf{E} = -\nabla\phi - i\omega\mu\mathbf{A}$ (Haber et al., 2000b). Mitsuhashi & Uchida (2004) also used a Helmholtz decomposition, but in their case the EM fields are decomposed into an electric vector potential \mathbf{T} and a scalar magnetic potential Ω , such that $(\sigma\mathbf{E}) = \nabla \times \mathbf{T}$ and $\mathbf{H} = \mathbf{T} - \nabla\Omega$. Another definition of these governing equations are integral forms of Maxwell's equations by Mackie et al. (1993):

$$\begin{aligned} \oint \mathbf{H} \cdot d\mathbf{l} &= \iint \sigma \mathbf{E} \cdot d\mathbf{S} \\ \oint \mathbf{E} \cdot d\mathbf{l} &= \iint i\omega\mu \mathbf{H} \cdot d\mathbf{S} \end{aligned} \quad (2.6)$$

Boundary and Interface Conditions In order to obtain a realistic EM solution, boundary and interface conditions of the EM fields have to be considered.

Interface Conditions At the contact of two conducting mediums with different conductivities ($\sigma_1 \neq \sigma_2$), the electric field polarized orthogonal to this contact will be discontinuous in order to satisfy the continuity of current density $\mathbf{j}_1 = \mathbf{j}_2$. Therefore, this electric field discontinuity is proportional to the surface charge density (Equation (1.4)). The orthogonal magnetic field is not affected by those surface charge densities and is continuous. On the other hand both electric and magnetic field traveling parallel to the interface contact will be continuous. These interface conditions are defined in terms of the normal vector ($\hat{\mathbf{n}}$) to the contact and are presented in Table 2.1.

Normal	Tangential
$\hat{\mathbf{n}} \cdot (\mathbf{E}_2 - \mathbf{E}_1) = q/\varepsilon$	$\hat{\mathbf{n}} \times (\mathbf{E}_2 - \mathbf{E}_1) = 0$
$\hat{\mathbf{n}} \cdot (\mathbf{H}_2 - \mathbf{H}_1) = 0$	$\hat{\mathbf{n}} \times (\mathbf{H}_2 - \mathbf{H}_1) = 0$
$\hat{\mathbf{n}} \cdot (\sigma_2 \mathbf{E}_2 - \sigma_1 \mathbf{E}_1) = 0$	

Table 2.1: Interface Conditions for the orthogonal (normal) and the parallel (tangential) EM fields Weaver (1994).

At the air-earth contact, the interface condition is that no current density travels outside from the conducting medium, so $\hat{\mathbf{n}} \cdot \mathbf{j} = 0$.

Dirichlet Boundary Conditions The common assumption to assign boundary conditions on Γ is that these boundaries are far away from inhomogeneities. In a 3D model domain Ω , the boundaries are considered at: side boundaries $(\pm\infty, y, z)$ and $(x, \pm\infty, z)$, top $(x, y, +\infty)$ and bottom boundaries $(x, y, -\infty)$.

According to Börner (2010), this condition is applied by assigning the tangential fields at these boundaries:

$$\begin{aligned} \hat{\mathbf{n}} \times \mathbf{E} &= \hat{\mathbf{n}} \times \mathbf{E}_0 \text{ on } \Gamma \\ \hat{\mathbf{n}} \times \mathbf{H} &= \hat{\mathbf{n}} \times \mathbf{H}_0 \text{ on } \Gamma. \end{aligned} \quad (2.7)$$

In Equation (2.7), the values of \mathbf{E}_0 and \mathbf{H}_0 could be that from a homogeneous or layered Earth solution (e.g. Nam et al., 2007), or in the case of assuming the model as a perfect conductor these values are zero (e.g. Shi et al., 2004; Mitsuhata & Uchida, 2004; Puzyrev et al., 2013). The EM field values at the side boundaries can also be obtained by solving their respective 2D EM problem (Weaver et al., 2000, Chap.6). That is, the values at $(\pm\infty, y, z)$ will be obtained by solving a 2D Transverse Magnetic problem, and the side boundary $(x, \pm\infty, z)$ by solving a 2D Transverse Electric problem (e.g. Mackie et al., 1993). Another approach to boundary conditions, is the assumption of an asymptotic behavior of the secondary fields when reaching the boundaries (Mogi, 1996).

At the bottom boundary, the EM fields can be assumed as zero because they decrease exponentially as $z \rightarrow \infty$ (Mitsuhata & Uchida, 2004). The EM fields values at the surface boundary can be obtained by including several air layers on top of the earth model, to take into consideration the perturbations of the magnetic fields from lateral current gradients (Mackie et al., 1993).

Absorbing Boundary Conditions In the application of Dirichlet boundary conditions, the domain should be extended until the reflections from the boundaries are negligible, leading to a large computational domain (Zyserman & Santos, 2000). The purpose of absorbing boundary conditions is that the EM fields normally arriving to the boundaries of the domain will be ‘absorbed’, reducing the computational domain, thus using less computational time and memory (Zyserman & Santos, 2000). Zyserman & Santos (2000) applied first order absorbing boundaries that simulates the vanishing EM fields at infinity in the modeling of 3D MT data.

Berenger (1994) designed a method that absorbs EM waves without any reflection from the boundaries of the domain. This method is applied on a boundary zone called Perfect Matched Layer (PML) where the EM fields will gradually decrease to zero on to the boundary of the domain (Berenger, 1994). This type of absorbing boundary condition is implemented by transforming the coordinates into a complex coordinate system in the PML zone. Alumbaugh et al. (1996) applied PML boundary conditions for the 3D wideband EM modeling. Newman & Alumbaugh (1997) applied the PML boundary conditions for 3D MT modeling. An application for 3D time-domain MT forward modeling is the use of a Convolutional-PML by de la Kethulle de Ryhove et al. (2013a). Most recently, for the 2D MT modeling, Alvarez-Aramberri et al. (2014) modified the PML formulation in order to automatically adjust the PML parameters for high contrast in subsurface properties.

2.3 Finite Difference Method

In finite difference method, the differential operator of each governing equation is discretized by approximating the partial derivatives with numerical differentiation (e.g. forward, backward or central differences). The most common discretization approach for FD methods are staggered grids introduced by Yee (1966) (Figure 2.1). In this case, the positions of EM fields are defined according to the definitions of Ampere’s and Faraday Laws as in Table 2.2. In addition, σ takes discretized values at each cell. For example, Mackie et al. (1993) considered the conductivity as being isotropic within each Yee cell.

This discretization scheme yields a system of linear equations $\mathbf{A}^{\text{FD}}\mathbf{x} = \mathbf{b}$, whose matrix \mathbf{A}^{FD} is complex valued, large, sparse and symmetric (Avdeev, 2005). Considering that the EM fields have components in $(\hat{\mathbf{x}}, \hat{\mathbf{y}}, \hat{\mathbf{z}})$ directions, the matrix \mathbf{A}^{FD} is $3M \times 3M$,

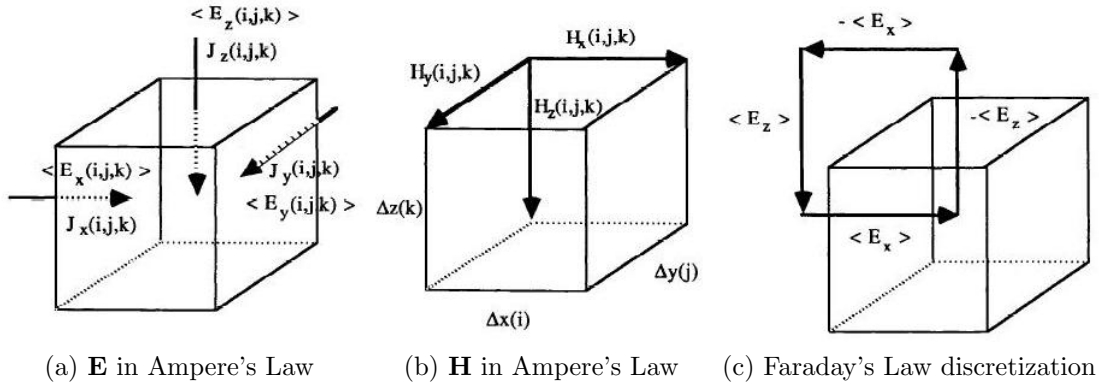


Figure 2.1: Description of a Yee Cell which form the staggered grid (Mackie et al., 1993)

EM Fields	Ampere's Law	Faraday's Law
E	Average across block surface (Figure 2.1a)	Average along contour (Figure 2.1c)
H	Average along block edges (Figure 2.1b)	Average across surface outlined by contours

Table 2.2: Discretized EM fields definitions in staggered grids (Mackie et al., 1993).

where M is the number of fields unknowns defined by the domain discretization. The unknown vector \mathbf{x} and known vector \mathbf{b} have size of $3M$.

The earliest FD application to 3D MT modeling is that of Jones & Pascoe (1972). Weiss & Newman (2002, 2003) applied the FD method considering fully 3D anisotropy, to solve the 3D EM induction problem. More recently, Weiss & Constable (2006) used this numerical method to solve the 3D EM problem of CSEM. In order to overcome the computational loads, Haber & Heldmann (2007) applied a multigrid method, known as OcTree, to solve the 3D MT induction problem with FD. The multigrid technique discretizes a model domain with finer cells around inhomogeneities while having coarser grids in more homogeneous regions (Figure 2.2).

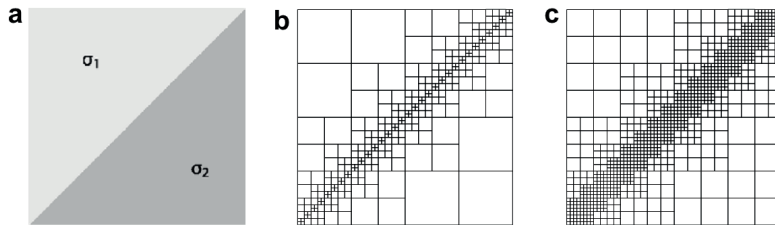


Figure 2.2: Multigrid refinement from coarse grid (b) to finer grid (c), scheme from Haber & Heldmann (2007).

2.4 Integral Equation Method

The basis of Integral Equation method is to represent the PDE (2.1a) in terms of a fundamental solution (Carey & Oden, 1983). When $\mathbf{s}(\mathbf{r})$ is a unit point source, the

fundamental solution will be a Dyadic Green's function at a point $\boldsymbol{\xi}$ satisfying

$$D\mathbf{G}(\mathbf{r}; \boldsymbol{\xi}) = \delta(\mathbf{r} - \boldsymbol{\xi})\bar{\mathbf{I}}, \text{ in } \Omega \quad (2.8a)$$

$$\mathbf{G}(\mathbf{r}; \boldsymbol{\xi}) = 0, \text{ on } \Gamma \quad (2.8b)$$

where δ is the Dirac delta function, and $\bar{\mathbf{I}}$ is the unit Dyad.

Equation (2.1a) can be solved by expressing the unknown function as $\mathbf{F}(\mathbf{r}) = \mathbf{F}_0(\mathbf{r}) + \delta\mathbf{F}(\mathbf{r})$. In this representation, the primary function $\mathbf{F}_0(\mathbf{r})$ is the response over a reference model $\mathbf{m}_0 = (\boldsymbol{\nu}_0, \boldsymbol{\kappa}_0)$, such that $D(\mathbf{m}_0)\mathbf{F}_0 = \mathbf{s}_0$. The secondary function $\delta\mathbf{F}(\mathbf{r})$ is the response due to a change in the model from \mathbf{m}_0 to $\mathbf{m} = \mathbf{m}_0 + \delta\mathbf{m}$ (Zhou et al., 2009).

If this principle is applied to the EM problem, the PDEs are reduced to a Fredholm integral of the second kind (e.g. for \mathbf{E}):

$$\mathbf{E}(\mathbf{r}) = \mathbf{E}_0(\mathbf{r}) + \int_{\Omega} G_{=0}(\mathbf{r}; \boldsymbol{\xi})(\boldsymbol{\sigma} - \boldsymbol{\sigma}_0) \cdot \mathbf{E}(\boldsymbol{\xi})d\Omega. \quad (2.9)$$

This Equation (2.9) considers the conductivity difference $(\boldsymbol{\sigma} - \boldsymbol{\sigma}_0)$ between the inhomogeneous medium and the background, and $G_{=0}$ is the Dyadic Green's function for the 1D reference (or background) medium (Avdeev, 2005).

Common domain discretization with this approach are rectangular prismatic cells (Figure 2.3), and the fields are considered at the center of each cell (Hohmann, 1983, 1975; Wannamaker, 1991).

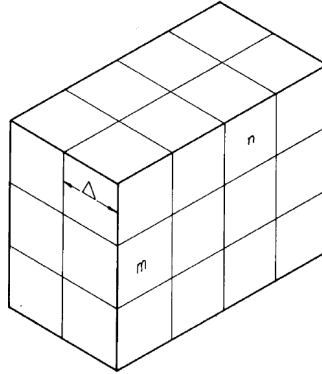


Figure 2.3: Rectangular grid for the IE discretization of the domain, from Hohmann (1975)

The system of linear equations $\mathbf{A}^{\text{IE}}\mathbf{x} = \mathbf{b}$ is obtained by the numerical integration of Equation (2.9). The matrix \mathbf{A}^{IE} is complex valued, dense but more compact than \mathbf{A}^{FD} (Avdeev, 2005).

A main feature of this methodology is that only the scattering volume (subsurface) has to be discretized, but the computation of the matrix \mathbf{A}^{IE} is tedious and nontrivial (Avdeev, 2005). This technique has been applied to EM modeling since Hohmann (1975). Based on Hohmann (1983, 1975), Wannamaker (1991) applied this technique to model 3D MT data. Zhdanov et al. (2006) presented a modification of the IE method to be able to consider inhomogeneous reference models in the 3D EM induction problem.

2.5 Finite Element Method

The algorithm proposed in this thesis is based on the finite element method, therefore a detailed description of this method will be included in this subsection, and in Appendix A.

2.5.1 Galerkin Method

The most applied FEM technique for 3D EM modeling is the Galerkin method (Shi et al., 2004; Nam et al., 2007; Farquharson & Miensopust, 2011; Puzyrev et al., 2013; Ren et al., 2013), which is based on a weak formulation of the PDEs. The weak formulation presents the PDE (2.1a) in terms of its inner product with a weighting function $\mathbf{w} \in \mathcal{C}(\Omega)$ that minimizes the residual $\mathbf{r} = \mathbf{D}(\mathbf{m})\mathbf{F} - \mathbf{s}$ (Jin, 2002), as

$$\begin{aligned}\langle \mathbf{w}, \mathbf{D}(\mathbf{m})\mathbf{F} - \mathbf{s} \rangle &= 0 \\ \langle \mathbf{w}, \mathbf{D}(\mathbf{m})\mathbf{F} \rangle &= \langle \mathbf{w}, \mathbf{s} \rangle.\end{aligned}\tag{2.10}$$

For the general MT governing equation (Equation (2.3)), these inner products (Equation (2.10)) are:

$$\langle \mathbf{w}, \mathbf{D}(\mathbf{m})\mathbf{F} \rangle = \int_{\Omega} \mathbf{w} \cdot (\nabla \times \boldsymbol{\nu}^{-1} \cdot \nabla \times \mathbf{F}) d\Omega + \int_{\Omega} i\omega \mathbf{w} \cdot \boldsymbol{\kappa} \cdot \mathbf{F} d\Omega \tag{2.11a}$$

$$\langle \mathbf{w}, \mathbf{s} \rangle = \int_{\Omega} \mathbf{w} \cdot \mathbf{s} d\Omega. \tag{2.11b}$$

The divergence theorem can be rephrased by using the vector identity:

$$\nabla \cdot (\mathbf{A} \times \mathbf{B}) = \mathbf{B} \cdot (\nabla \times \mathbf{A}) - \mathbf{A} \cdot (\nabla \times \mathbf{B}),$$

where $\mathbf{A} = \mathbf{w}$, $\mathbf{B} = \boldsymbol{\nu}^{-1} \cdot (\nabla \times \mathbf{F})$, and $\mathbf{C} = \hat{\mathbf{n}}$. This theorem states that

$$\begin{aligned}\int_{\Omega} [\mathbf{B} \cdot (\nabla \times \mathbf{A}) - \mathbf{A} \cdot (\nabla \times \mathbf{B})] d\Omega \\ = \int_{\Gamma} (\mathbf{A} \times \mathbf{B}) \cdot \hat{\mathbf{n}} d\Gamma.\end{aligned}\tag{2.12}$$

By applying this theorem (Equation (2.12)) to the inner product (Equation (2.11a)), and modifying the boundary Γ integral with

$$\mathbf{C} \cdot (\mathbf{A} \times \mathbf{B}) = \mathbf{A} \cdot (\mathbf{B} \times \mathbf{C}),$$

the Galerkin formulation is obtained as

$$\begin{aligned}\langle \mathbf{w}, \mathbf{D}(\mathbf{m})\mathbf{F} \rangle &= \int_{\Omega} [(\nabla \times \mathbf{w}) \cdot \boldsymbol{\nu}^{-1} \cdot (\nabla \times \mathbf{F}) + i\omega \mathbf{w} \cdot \boldsymbol{\kappa} \cdot \mathbf{F}] d\Omega \\ &\quad - \int_{\Gamma} \mathbf{w} \cdot \boldsymbol{\nu}^{-1} \cdot \nabla \times \mathbf{F} \times \hat{\mathbf{n}} d\Gamma\end{aligned}\tag{2.13a}$$

$$\langle \mathbf{w}, \mathbf{s} \rangle = \int_{\Omega} \mathbf{w} \cdot \mathbf{s} d\Omega. \tag{2.13b}$$

2.5.2 Domain Discretization

The domain Ω is discretized into n elements Ω_e , such that

$$\Omega = \bigcup_{e=1}^n \Omega_e.$$

Two types of elements are commonly used in FEM, which are tetrahedrals and hexahedral elements. According to Yilmaz & Kuzuoglu (2008), tetrahedral meshes are used

more often because of the availability of mesh generation schemes. In 3D EM modeling tetrahedral elements have been used by Liu et al. (2010), Ren et al. (2013), and Puzyrev et al. (2013). However, hexahedral meshes are commonly used (Mogi, 1996; Zyserman & Santos, 2000; Mitsuhashi & Uchida, 2004; Shi et al., 2004; Nam et al., 2007; Farquharson & Miensopust, 2011). The main advantages of hexahedral elements are (Yilmaz, 2007):

1. They provide basis functions with more terms (degrees of freedom) that can increase the accuracy of the solution.
2. Directional sizing without losing accuracy (i.e. thin tetrahedron can cause error in the interpolation).
3. They decrease the total number of elements.

The main feature of FEM discretization is that it accurately accounts for complex surface and subsurface geometries (Avdeev, 2005; Newman, 2014). The idea of this discretization is that it is possible to define a coordinate transformation from the Cartesian coordinates (x, y, z) to Isoparametric coordinates (ξ, η, ζ) . Therefore, it is possible to define the Galerkin formulation for this type of elements, and locally apply the numerical integration. Appendix A.2 presents the mathematical description of this coordinate transformation.

2.5.3 Nodal FEM

Within each element, the unknown solution \mathbf{F} is approximated by a set of nodal basis functions N defined in the Sobolev space $\mathcal{H}_0(\Omega) := \{N \in \mathcal{H}(\Omega); N = 0 \text{ on } \Gamma\}$. Appendix A.1, contains a description of Sobolev spaces used in FEM. If the e -th element contains n_e nodes, the field is approximated in terms of the nodal basis functions $N_i(\xi, \eta, \zeta)$ by

$$\mathbf{F}(\mathbf{r}) \approx \sum_{i=1}^{n_e} \mathbf{F}_i N_i(\xi, \eta, \zeta). \quad (2.14)$$

The Galerkin method uses this set of basis functions $N(\xi, \eta, \zeta)$ as weighting functions on the weak formulation (Jin, 2002). Hence, the MT problem consists of solving the following integral equation:

$$\begin{aligned} & \int_{\Omega} [(\nabla \times N) \cdot \boldsymbol{\nu}^{-1} \cdot (\nabla \times \mathbf{F}) + i\omega N \cdot \boldsymbol{\kappa} \cdot \mathbf{F}] d\Omega \\ & - \int_{\Gamma} N \cdot \boldsymbol{\nu}^{-1} \cdot \nabla \times \mathbf{F} \times \hat{\mathbf{n}} d\Gamma \\ & = \int_{\Omega} N \cdot \mathbf{s} d\Omega. \end{aligned}$$

At the e -th element, the Galerkin problem is proposed by choosing the N_m basis functions ($m = 1, 2, \dots, n_e$) as weighting functions, and the integration is calculated within each element as

$$\sum_{n=1}^{n_e} \mathbf{F}_n \int_{\Omega_e} [(\nabla \times N_m) \cdot \boldsymbol{\nu}^{-1} \cdot (\nabla \times N_n) + i\omega \boldsymbol{\kappa} N_m \cdot N_n] d\Omega_e = \int_{\Omega_e} \mathbf{s} \cdot N_n d\Omega_e.$$

The field interpolation with nodal basis functions (Equation (2.14)) leads to a $3n_e \times 3n_e$ matrix for the e -th element. The global solution is obtained by the sum of all local integrations. This numerical method yields also a linear system of equations $\mathbf{A}^{\text{FE}} \mathbf{x} = \mathbf{b}$, whose matrix \mathbf{A}^{FE} is complex valued, large, and sparse (Avdeev, 2005).

Since Reddy et al. (1977), nodal FEM has been applied to solve the forward EM modeling problem. Mogi (1996) used standard nodal elements with brick like form, for the secondary electric field formulation of the 3D MT problem. More recently, Puzyrev et al. (2013) applied standard nodal elements with the $\mathbf{A} - \phi$ Helmholtz decomposition to the 3D anisotropic Controlled Source EM (CSEM) problem. They applied the FEM scheme in parallel computation by subdividing recursively the elements with a mesh multiplication strategy (Puzyrev et al., 2013). According to Börner (2010) nodal basis functions force the EM fields to be continuous across element boundaries, and it becomes difficult to impose boundary conditions. It is more common to obtain spurious (non-physical) solutions, because of the lack of applying the divergence free condition (Jin, 2002, Chap.8).

2.5.4 Vector FEM

To overcome these problems, vector basis functions have been defined on the edge of elements, known as edge-elements (Börner, 2010). In this case, the vector basis function \mathbf{v} is defined in the Sobolev space $\mathcal{H}_0(\Omega, \text{curl}) := \{\mathbf{v} \in \mathcal{H}(\Omega, \text{curl}); \mathbf{v} \times \hat{\mathbf{n}} = 0 \text{ on } \Gamma\}$. By defining these vector functions, the divergence free condition is automatically satisfied, see the EM Tonti Diagram in Appendix A.1. In this case the field interpolation on the e -th element will be

$$\mathbf{F} = \sum_{i=1}^{m_e} F_i \mathbf{v}_i(\xi, \eta, \zeta),$$

where m_e is the total number of edge-elements on Ω_e

The construction and importance of edge-elements for EM problems was first introduced by Nédélec (1980) for a tetrahedron (Figure 2.4) and rectangular bricks.

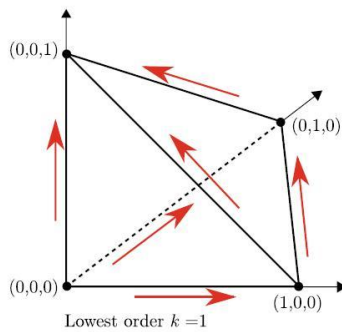


Figure 2.4: Nédélec Elements for FE approximation of Maxwell's equations on tetrahedral (Börner, 2010).

Hano (1984) introduced linear edge-elements for 2D rectangular elements. These edge-elements are defined by using mixed-order polynomials, i.e. polynomials of $(p-1)$ -order on the direction of the edge-element, and p -order on other directions. By using mixed-order polynomials, the degree of freedom within the element is reduced to the number of edges of the element (m_e), instead of $(3n_e)$. The main feature of using mixed-order vector basis functions is that the divergence of the field (within the element) will be

zero for rectangular elements and very small for distorted elements (Jin, 2002). The divergence free condition is satisfied and EM fields are (by construction) continuous across element boundaries, thus no spurious solutions are obtained (Jin, 2002).

Kameari (1990) introduced the linear-order (8 nodes, 12 edge-elements) hexahedral element, and high-order edges for the quadratic element (20 nodes, 36 edge-elements), see Figures 2.5a and 2.5b. Crowley et al. (1988) presented a formulation for high-order edge-elements on hexahedra, called covariant projection element (Figure 2.5c).

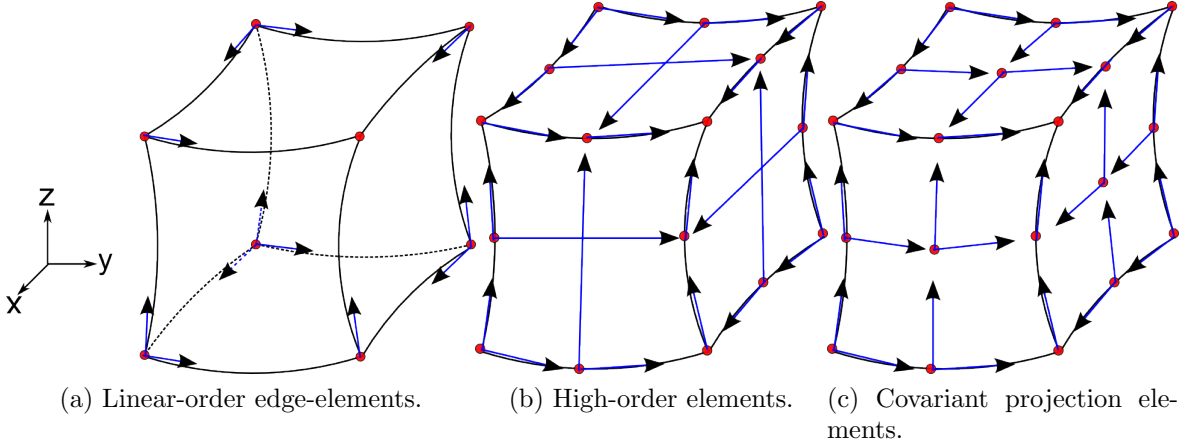


Figure 2.5: Vector Basis functions on hexahedral elements. a) Linear-order edge-elements on Hexahedral, $n_e = 8$, $m_e = 12$ (Kameari, 1990). b) High-order edge-elements on hexahedral, $n_e = 20$, $m_e = 36$ (Kameari, 1990). c) High-order covariant projection elements on hexahedral, e.g. $n_e = 27$, $m_e = 54$ with mixed-order polynomials (Crowley et al., 1988).

The formulation of Crowley et al. (1988) can construct edge-elements on each node (as in Nodal-FEM) by defining the covariant projection as $F_\xi = \mathbf{F} \cdot \frac{\partial \mathbf{r}}{\partial \xi}$, where $\mathbf{r} = (x, y, z)$ and $\frac{\partial \mathbf{r}}{\partial \xi}$ is obtained from the Jacobian matrix of transformation (Equation (A.7) in the Appendix). The basis function (N_ξ) could be the same basis function used in Nodal-FEM. However, Crowley et al. (1988) also argued that mixed-order polynomials will remove spurious solutions because the calculation of the divergence of the edge-element is zero for rectangular elements and very small for distorted elements (Crowley, 1988).

Zyserman & Santos (2000) defined non-conforming vector basis functions for the 3D MT problem, by solving the coupled Maxwell's equations (i.e. Faraday's and Ampere's Laws) on a rectilinear mesh with a domain decomposition method. For the electric field, the vector basis functions are defined on the mid-point of each hexahedral face, therefore twelve vector functions are obtained. For the magnetic field, nine edge-elements are defined as the curl of the spanned functions for the electric field (Zyserman & Santos, 2000). Mitsuhashi & Uchida (2004) used linear-order edge-elements and nodal basis functions to model MT data with $\mathbf{T} - \Omega$ Helmholtz decomposition on rectilinear elements, obtaining an asymmetrical system of equations. Shi et al. (2004) incorporated a divergence correction technique into Vector-FEM (VFEM) for 3D MT modeling using linear-order edge-elements on hexahedral mesh. By using the electric field formulation, and mixed-order elements the system of equations will give a large, sparse, banded and symmetric matrix (Shi et al., 2004). Farquharson & Miensopust (2011) also applied a divergence correction to 3D MT forward modeling, and used piecewise linear functions

to define the vector basis functions on a rectilinear mesh. The first to apply distorted hexahedrals, in order to include surface topography for 3D MT modeling were Nam et al. (2007), who used linear-order edge-elements.

A technique that has become of interest for EM modeling recently, are the adaptive methods. This technique adapts or changes either the element size (h-adaptive) or the polynomial order (p-adaptive) according to an error estimator, or both (hp-adaptive) (Pardo et al., 2007). Franke et al. (2007) applied the h-adaptive FEM for the 2D MT problem using triangular elements. Key & Weiss (2006) presented a goal-oriented h-adaptive FEM for 2D MT modeling, and Li & Key (2007) applied a similar technique for 2.5D CSEM modeling. Key & Oval (2011) presented a parallel goal-oriented h-adaptive FEM for 2.5D EM modeling. In the 3D MT modeling case, Liu et al. (2010) applied the h-adaptive method using linear-order edge-elements on tetrahedral mesh. More recently, Ren et al. (2013) developed a ‘goal-oriented’, h-adaptive method for the 3D MT and Radio-MT forward modeling. These authors used linear-order edge-elements for tetrahedron, and defined an element error estimator to obtain an automatic refinement of the mesh (Ren et al., 2013).

2.6 System of Equations Solvers

All the numerical methods yield a linear system of equations $\mathbf{Ax} = \mathbf{b}$, so the unknown EM field (\mathbf{x}) is found by solving this system. According to Avdeev (2005), this system of equations is commonly solved iteratively by preconditioned Krylov methods.

Krylov subspace methods If the complex matrix \mathbf{A} is Hermitian, it is possible to obtain successive solutions by an initial solution \mathbf{x}_0 (Avdeev, 2005). The new approximation is obtained in terms of the previous solution by means of residuals $\mathbf{r} = \mathbf{b} - \mathbf{Ax}$, and the iteration is stopped when the Euclidean norm of this residual is minimized. In order to enhance the convergence of the solution, a preconditioner can be applied in this method (Börner, 2010). The preconditioning is applied by solving a new system of equations $(\mathbf{AM}^{-1})\mathbf{y} = \mathbf{b}$, where $\mathbf{y} = \mathbf{Mx}$.

For the solution of EM modeling problem, the most common Krylov methods are Conjugate Gradients (CG), Quasi-minimum Residual (QMR) and Lanczos (Avdeev, 2005). Mitsuhata & Uchida (2004) applied a stabilized Bi-CG with incomplete LU decomposition as preconditioner. Newman & Alumbaugh (2000) and Siripunvaraporn et al. (2005) used QMR for the solution of the forward modeling in their inversion algorithms.

Multigrid method is a recent technique that makes iterative solvers a viable option for large-scale EM problems (Börner, 2010). This method solves the EM problem in a hierarchy of spatial discretizations (Börner, 2010).

Direct Methods These methods solve the system of linear equations as $\mathbf{x} = \mathbf{A}^{-1}\mathbf{b}$. Therefore the direct inversion of the matrix \mathbf{A} is calculated and the solution is obtained without iterations. According to Börner (2010), there has been a resurgence of direct methods to solve sparse matrices. These techniques are of Gauss’s elimination type, and have been highly optimized in terms of computational speed and memory (Börner, 2010). The optimization is applied by factorizing the matrix \mathbf{A} employing graph models (Börner, 2010), e.g. LU decomposition in MUMPS (Amestoy et al., 2006).

2.7 3D Inversion

In this thesis, an algorithm for MT forward modeling based on FEM is developed. This section presents a literature review of inversion methods, in order to show the importance of forward modeling in the inversion of MT data. 3D EM inversion is commonly applied using unconstrained nonlinear optimization. The basis of these optimization techniques are Newton's iterations to obtain successive EM models.

2.7.1 Unconstrained Nonlinear Optimization

The measured EM data are limited because it is not possible to apply the method on enough sites to cover all the study area. These data are noisy, so each datum has an associated error. For these reasons, the EM inversion problem is non-linear, and ill-posed, thus many solutions can fit the data (Avdeev, 2005). In 3D inversion, the optimization technique is applied by minimizing a penalty functional in terms of data misfit $\phi_d(\mathbf{m})$ or goodness of fit

$$\phi_d(\mathbf{m}) = ||W_d[\mathbf{d}_0 - F(\mathbf{m})]||^2, \quad (2.15)$$

and the model norm $\phi_m(\mathbf{m})$ which is a measurement of smoothness

$$\phi_m(\mathbf{m}) = ||W_m[\mathbf{m} - \mathbf{m}_0]||^2. \quad (2.16)$$

In the previous equations, \mathbf{m} corresponds to the obtained EM model, \mathbf{m}_0 is the previous or reference model, $F(\mathbf{m})$ is the forward modeling solution, \mathbf{d}_0 the measured data, and W are weighting matrices. According to Greenhalgh et al. (2006), the least squares norm is most applied in geophysical inversion due to its simple computation. Commonly, the values for the matrices W_d and W_m are the inverse covariance matrices C_d^{-1} and C_m^{-1} , respectively (Greenhalgh et al., 2006).

A typical definition of the penalty functional is that of the Tikhonov regularization method (Tikhonov & Arsenin, 1977):

$$\varphi(\mathbf{m}) = \phi_d(\mathbf{m}) + \lambda\phi_m(\mathbf{m}). \quad (2.17)$$

This penalty functional (Equation (2.17)) uses the Lagrange multiplier λ as regularization parameter. The Lagrange multiplier trades off between the misfit (Equation (2.15)) and the model smoothness (Equation (2.16)). Therefore, if λ is small, the penalty functional will emphasize the misfit, and a large λ increases the smoothness. The optimization technique is accomplished by an iterative procedure to minimize $\varphi(\mathbf{m})$. Equation (2.15) needs the calculation of the forward model, thus in the minimization of $\varphi(\mathbf{m})$ several forward models have to be obtained.

Constable et al. (1987) presented another optimization approach, called OCCAM, that considers the associated error to datum, and the diffusive nature of EM methods. The diffusive propagation of EM signals cannot resolve sharp boundaries of subsurface structures. Thus, the measured data will be that from a "smoother" version of the subsurface.

If the inversion is applied without considering these factors, the resulting model will probably contain spurious structures. Spurious structures are present when more emphasis is given to $\phi_d(\mathbf{m})$. Hence, conductivity models with structures that are not physically present in the subsurface can minimize $\varphi(\mathbf{m})$.

The unconstrained functional is defined in terms of roughness, as

$$\varphi_u(\mathbf{m}) = \phi_m(\mathbf{m}) + \lambda^{-1}(\phi_d(\mathbf{m}) - X_*^2), \quad (2.18)$$

which is minimized according to a pre-defined level of misfit X_*^2 (Constable et al., 1987). The roughness (inverse of smoothness) describes the amount of structures present in the obtained conductivity model.

Therefore, the minimization problem consists of finding the EM model that minimize the model norm, while the misfit achieves a desirable value (Constable et al., 1987). This minimization scheme can be considered in two phases. Phase I consists of minimizing the misfit to an X_*^2 , and phase II is to keep the misfit, and vary the Lagrange multiplier to minimize the model norm (Siripunvaraporn & Egbert, 2000).

2.7.2 Newton Iterations

Newton's iterative techniques are commonly used to solve nonlinear problems. As mentioned in the previous section, the unconstrained nonlinear optimization is solved by minimizing a penalty functional, such as the Tikhonov functional or the OCCAM functional. A necessary condition to minimize the penalty functional, is to find its stationary points that satisfy $\frac{\partial \varphi}{\partial \mathbf{m}} = 0$, which is the gradient of the penalty functional (Avdeev, 2005; Rodi & Mackie, 2012). According to Siripunvaraporn & Egbert (2000), the unconstrained functional φ_u and the penalty functional φ have the same stationary points with respect to model variations, when λ is fixed: $\frac{\partial \varphi_u}{\partial \mathbf{m}} = \frac{\partial \varphi}{\partial \mathbf{m}}$.

In the gradient of the penalty functional, $\frac{\partial F(\mathbf{m})}{\partial \mathbf{m}}$ is calculated, and is known as the sensitivity matrix. If there are N observed data and M model vectors, the sensitivity matrix is $N \times M$. This matrix is equivalent to the Fréchet derivatives of synthetic EM data $F(\mathbf{m})$ with respect to the model \mathbf{m} (Greenhalgh et al., 2006). In other words, it describes perturbations in the data due to changes in the model \mathbf{m} (Siripunvaraporn & Egbert, 2000). Consequently, an accurate and reliable forward modeling technique is necessary for the inversion of MT data.

If the k -th model $\mathbf{m}^{(k)}$ is found, the iteration for the model update $\delta \mathbf{m}^{(k)} = \mathbf{m}^{(k+1)} - \mathbf{m}^{(k)}$ satisfy

$$H^{(k)} \cdot \delta \mathbf{m}^{(k)} = -\frac{\partial \varphi^{(k)}}{\partial \mathbf{m}} \quad (2.19)$$

where the Hessian matrix $H = \frac{\partial^2 \varphi}{\partial \mathbf{m}^2}$, and the gradient of the penalty functional are determined for the k -th model (Avdeev, 2005). The advantage of this method is its fast local convergence, but this does not guarantee that the solution converges to the minimum of φ (Avdeev, 2005).

Based on Rodi & Mackie (2001), Siripunvaraporn et al. (2005) applied a Gauss-Newton technique for the inversion of 3D EM data (Avdeev, 2005; Rodi & Mackie, 2012). Their method, called DASOCC, is based on linearizing the forward modeling solution by Taylor series expansion, where the sensitivity matrix is defined in terms of the model update. The main attribute of their work is the application of the OCCAM optimization technique in the data space, instead of using the larger model space. The solution of DASOCC method is a linear combination of 'representers' of the linearized data misfit functional (Siripunvaraporn et al., 2005). Therefore, this problem consists of finding the N 'representers', instead of the M model vectors, where $N \ll M$ (Siripunvaraporn & Egbert, 2000). Moreover, the inverse of the model covariance matrix C_m^{-1} does not have to be calculated, only the inverse data covariance C_d^{-1} has to be obtained for the penalty functional. Consequently, the DASOCC method reduces the computational time and memory required for inversion significantly.

The 'representers' in DASOCC correspond to a single data element and vary slowly

with period and site location for a given response and model (Siripunvaraporn et al., 2005). This parameter is highly redundant, so it is possible to select a subset $L \subset N$, reducing the computational time and memory even more (Siripunvaraporn et al., 2005). In this case, the reduced sensitivity matrix is $L \times M$ and is obtained by interpolation. The same Gauss-Newton procedure is applied to find the reduced representers in the L dimensional subset of data, and Siripunvaraporn et al. (2005) named this method as REBOCC. Finally, both DASOCC and REBOCC algorithms follow the phases I and II of the OCCAM approach.

The model update in the Newton method is obtained by inverting the Hessian matrix. The Quasi-Newton method generates successive matrices to replace the Hessian inverse (Avdeev, 2005). These matrices are obtained by a recursion formula in terms of the model update and the gradient of the penalty functional. Avdeev & Avdeeva (2006) applied a Limited Memory Quasi-Newton technique, that requires the storage of the gradient only, while avoiding the second derivatives, when dealing with the Hessian matrix.

Madden & Mackie (1989) applied a Conjugate Gradient relaxation method within the Gauss-Newton technique to parameterize models in a coarse manner for the inversion of 3D MT data, therefore M remains relatively small. Newman & Alumbaugh (2000) applied a Nonlinear Conjugate Gradients (NLCG) method for the 3D inversion of MT data, defining the objective functional in terms of the observed (\mathbf{Z}_d) and predicted (\mathbf{Z}_m) impedance tensors and its associated error. The main feature of NLCG is that it requires only the computation of the gradient of the penalty functional instead of the sensitivity matrix.

Most recent applications of NLCG to MT data are that of Mackie et al. (2001), Newman & Alumbaugh (2000), and Zhdanov et al. (2000). Newman et al. (2003) applied this methodology for the inversion of 3D Radio-MT data. Commer & Newman (2008) applied a NLCG technique to 3D CSEM data with two levels of parallelization. The first parallelization corresponds to the forward modeling and the second level to what they called data decomposition, where the dataset is assigned to groups of processors (Commer & Newman, 2008).

2.7.3 Constrained Optimization

This technique considers the solution of both forward and inverse problems simultaneously (Avdeev, 2005). This method is named as the ‘all-at-once approach’ (Haber et al., 2004) and was first proposed by Haber et al. (2000a). Negi et al. (2013) presented a method that reduces the forward model calculations, yet still recovers sharp boundaries. Instead of updating the sensitivity matrix, a smoothness constraint is applied based on the spatial resistivity variation from the previous iteration (Negi et al., 2013).

Chapter 3

Multi-order Vector Finite Element Method

3.1 Introduction

The main problem of 3D EM modeling and inversion is the computational memory and time required to obtain the solutions (Newman, 2014). Thousands of data points are measured, and hundreds or even thousands of forward modeling points are needed to solve the non-linear 3D inverse problem. Both forward and inverse problems consist on solving a system of equations, where the matrix to be inverted is very large. Therefore, the computational memory and time of common desktop computers is not enough to obtain the solutions. This problem has commonly be solved with a parallel framework, and fast preconditioned linear solvers (Avdeev, 2005).

Consequently, a fast, accurate and reliable numerical solution has to be obtained in order to apply it to the inverse problem (Avdeev, 2005; Börner, 2010). According to Avdeev (2005), the goal of forward modeling is to reduce the computational load by obtaining accurate solutions within coarser grids, including anisotropy and complex model geometry (e.g. surface topography).

Han et al. (2009) argued that although FD methods are fast, VFEM obtains more accurate solutions, and can model surface topography and complex boundaries. Only linear-order edge-elements have been applied for MT modeling (Farquharson & Miensoyust, 2011; Mitsuhata & Uchida, 2004; Nam et al., 2007; Shi et al., 2004). Edge-elements of linear-order need really small finite elements to obtain accurate solutions. Consequently, a problem with large number of unknown is obtained, which leads to a large array. Yilmaz & Kuzuoglu (2008) recommended the use of high-order edge-elements for the EM scattering problem, because it is possible to obtain accurate solutions with larger elements. Therefore, the problem will contain less elements than with linear-order, less number of unknowns, and thus a smaller global array. This leads to a problem that uses less computer memory and could be faster than linear-order edge-elements (Yilmaz & Kuzuoglu, 2008).

Although the anisotropy of the medium has an effect on the interpretation of MT data, most forward modeling algorithms consider the subsurface as isotropic (Farquharson & Miensoyust, 2011; Liu et al., 2010; Mackie et al., 1993; Mitsuhata & Uchida, 2004; Nam et al., 2007; Shi et al., 2004; Zyserman & Santos, 2000).

The main objective of this research is to calculate the forward model of 3D MT data including anisotropy and complex geometry, such as topography and subsurface

interfaces. Another objective is the use of high-order edge-elements for the MT problem that has not been previously described in the literature. High-order edge-elements are applied to investigate if accurate results can be obtained with larger elements. A Fortran program is developed with a Multi-order Vector Finite Element Algorithm, called MoVFEM, in order to accomplish the mentioned objectives.

The MT problem is based on the secondary field formulation, where the primary fields are the EM fields propagating in the air. Both the electric field and magnetic field governing equations are programmed in MoVFEM. However, the electric field governing equation is applied in the execution of the program. Once one of the governing equations is solved, and one of the EM fields is obtained, the other is calculated from Maxwell's equations. For example, if the electric field governing equation is used, the magnetic field is obtained from Faraday's Law.

Two boundary conditions are proposed for this modeling problem, Dirichlet and Generalized Perfect Matched Layers (GPML). Three types of Dirichlet boundary conditions are proposed which are: 1) considering the model as a perfect conductor (EM fields tangential to the boundaries are zero), 2) 1D boundary fields of a homogeneous Earth, and 3) 1D boundary fields of a layered Earth. In this case, the model is extended on each direction (x, y, z) to assume that boundaries are far away from inhomogeneities.

Generalized Perfect Matched Layers boundary conditions are applied by defining a layer zone (called Perfect Matched Layer) where the field values will gradually decrease to a zero value on the boundary of the domain (Fang, 1996; Zhou et al., 2012). GPML was first proposed by Fang (1996), and Zhou et al. (2012) modified the GPML equations for MT and CSEM modeling. Both GPML approaches are included in MoVFEM in order to compare their behavior.

Edge-elements are proposed for the linear-order hexahedral (8 nodes), quadratic hexahedral (20 nodes), and Lagrangian hexahedral (27 nodes). Linear-order and quadratic hexahedral elements are those proposed by Kameari (1990). The Lagrangian edge-elements are based on Crowley et al. (1988) and Kameari (1990). By using such basis functions, the problem leads to a global matrix \mathbf{A} which is sparse, and symmetric. To obtain the solution, this matrix is inverted using the MUMPS package which is a parallel direct solver for sparse matrices (Amestoy et al., 2006).

Section 3.2 contains the description of the 3D MT problem, where the secondary field formulation, primary fields, and boundary conditions are discussed. The Vector Finite Element Algorithm is discussed on Section 3.3. This section contains a description of the domain discretization, of edge-elements, and the discretized integrals with global matrix assembly. In Appendix C, a description of MoVFEM implementation is presented together with the work-flow of this algorithm, a description of input and output files, as well as complementary modules of 3D visualization.

3.2 Magnetotelluric Problem

3.2.1 Secondary Field Formulation

Maxwell's Equations For the frequency range that MT Method measures, $\frac{\partial \mathbf{D}}{\partial t} \rightarrow 0$, where \mathbf{D} is the displacement current. Consequently, the quasi-static approximation is applied to the governing equations (Weaver, 1994, Chap.1). The primary field (\mathbf{F}_p) is included as part of the total field as $\mathbf{F} = \mathbf{F}_p + \mathbf{F}_s$, where $\mathbf{F} \in \{\mathbf{E}, \mathbf{H}\}$. The secondary field (\mathbf{F}_s) represents the field behavior in the conducting medium and is the unknown field to be calculated. By using this definition of the total field in Maxwell's equations

it is possible to obtain these equations in terms of the secondary fields:

$$\left. \begin{aligned} \nabla \times \mathbf{E}_s + i\omega \boldsymbol{\mu} \cdot \mathbf{H}_s &= -i\omega \delta \boldsymbol{\mu} \cdot \mathbf{H}_p \\ \nabla \times \mathbf{H}_s - \boldsymbol{\sigma} \cdot \mathbf{E}_s &= \delta \boldsymbol{\sigma} \cdot \mathbf{E}_p \\ \nabla \cdot (\boldsymbol{\mu} \cdot \mathbf{H}_s) &= -\nabla \cdot (\boldsymbol{\mu} \cdot \mathbf{H}_p) \\ \nabla \cdot (\boldsymbol{\varepsilon} \cdot \mathbf{E}_s) &= \delta q - \nabla \cdot (\delta \boldsymbol{\varepsilon} \cdot \mathbf{E}_p) \end{aligned} \right\} \text{Maxwell's Equations}$$

In these equations, the primary field is altered by the model change $(\delta \boldsymbol{\sigma}, \delta \boldsymbol{\varepsilon}, \delta \boldsymbol{\mu}, \delta q)$ from the model of primary fields $(\boldsymbol{\sigma}_p, \boldsymbol{\varepsilon}_p, \boldsymbol{\mu}_p, q_p)$, to the model in study $(\boldsymbol{\sigma}, \boldsymbol{\varepsilon}, \boldsymbol{\mu}, q)$. This is presented in Maxwell's equations as $\delta \boldsymbol{\sigma} = \boldsymbol{\sigma} - \boldsymbol{\sigma}_p$, and similar applies for $\delta \boldsymbol{\varepsilon}$, $\delta \boldsymbol{\mu}$, and δq . The mathematical steps to obtain Maxwell's equations based on the secondary fields are in Appendix B.1.

In this Chapter, $\boldsymbol{\sigma}$, and $\boldsymbol{\mu}$ are defined as 3×3 tensors. For the MT problem, $\boldsymbol{\mu} \approx \mu_0 \mathbf{I}$, where \mathbf{I} is the 3×3 identity matrix.

Governing Equations In order to obtain the secondary field behavior in the sub-surface, Maxwell's equations are decoupled to obtain the governing equations based on one field only, either \mathbf{E}_s or \mathbf{H}_s . This is obtained by applying the decoupling procedure discussed in Section 1.3 to Maxwell's equations based on the secondary field. The electric field governing equation is

$$\nabla \times (\boldsymbol{\mu}^{-1} \cdot \nabla \times \mathbf{E}_s) + i\omega \boldsymbol{\sigma} \cdot \mathbf{E}_s = \mathbf{s}^E, \quad (3.1)$$

with a source (\mathbf{s}^E) defined as

$$\mathbf{s}^E = -i\omega [\delta \boldsymbol{\sigma} \cdot \mathbf{E}_p + \nabla \times (\boldsymbol{\mu}^{-1} \delta \boldsymbol{\mu} \cdot \mathbf{H}_p)]. \quad (3.2)$$

In this case, the problem is solved for the secondary electric field (\mathbf{E}_s) , and the total magnetic field (\mathbf{H}) is calculated from Faraday's Law:

$$\mathbf{E} = \mathbf{E}_p + \mathbf{E}_s \Rightarrow \mathbf{H} = -(\boldsymbol{\mu})^{-1} \nabla \times \mathbf{E} \quad (3.3)$$

For MT modeling $\delta \boldsymbol{\mu} = 0$ because $\boldsymbol{\mu} \approx \mu_0 \mathbf{I}$ for both the primary model and the model in study. Consequently, the term $\nabla \times (\boldsymbol{\mu}^{-1} \delta \boldsymbol{\mu} \cdot \mathbf{H}_p) = 0$ in Equation (3.2), and the source becomes:

$$\mathbf{s}^E = -i\omega \delta \boldsymbol{\sigma} \cdot \mathbf{E}_p \quad (3.4)$$

In the same way, the magnetic field problem is solved for the secondary field

$$\nabla \times \boldsymbol{\sigma}^{-1} \cdot \nabla \times \mathbf{H}_s + i\omega \boldsymbol{\mu} \cdot \mathbf{H}_s = \mathbf{s}^H, \quad (3.5)$$

with a magnetic source

$$\mathbf{s}^H = \nabla \times (\boldsymbol{\sigma}^{-1} \delta \boldsymbol{\sigma} \cdot \mathbf{E}_p), \quad (3.6)$$

and the total electric field (\mathbf{E}) is calculated from Ampere's Law:

$$\mathbf{H} = \mathbf{H}_p + \mathbf{H}_s \Rightarrow \mathbf{E} = \boldsymbol{\sigma}^{-1} \nabla \times \mathbf{H} \quad (3.7)$$

Because of the similarity of these governing equations, a general governing equation can be defined as

$$\nabla \times \boldsymbol{\nu}^{-1} \cdot \nabla \times \mathbf{F}_s + i\omega \boldsymbol{\kappa} \cdot \mathbf{F}_s = \mathbf{s}^F. \quad (3.8)$$

Here, $\boldsymbol{\nu} \in \{\boldsymbol{\mu}, \boldsymbol{\sigma}\}$ and $\boldsymbol{\kappa} \in \{\boldsymbol{\sigma}, \boldsymbol{\mu}\}$ for the electric field problem or the magnetic field problem, respectively. The VFEM procedure is applied to this general equation.

Galerkin Method The Galerkin method presents a governing equation as its inner product with a weighting function \mathbf{w} , such that $\forall \mathbf{w} \in \mathcal{C}(\Omega)$, $\langle \mathbf{w}, D(\mathbf{m})\mathbf{F}_s \rangle = \langle \mathbf{w}, \mathbf{s}^F \rangle$ (see Section 2.5). These inner products for the general MT governing equations are:

$$\begin{aligned} \langle \mathbf{w}, D(\mathbf{m})\mathbf{F}_s \rangle &= \int_{\Omega} [(\nabla \times \mathbf{w}) \cdot \boldsymbol{\nu}^{-1} \cdot (\nabla \times \mathbf{F}_s) + i\omega \mathbf{w} \cdot \boldsymbol{\kappa} \cdot \mathbf{F}_s] d\Omega \\ &\quad - C_{\Gamma} \int_{\Gamma} \mathbf{w} \cdot (\boldsymbol{\nu}^{-1} \cdot \nabla \times \mathbf{F}_s) \times \hat{\mathbf{n}} d\Gamma \\ \langle \mathbf{w}, \mathbf{s}^F \rangle &= \int_{\Omega} \mathbf{w} \cdot \mathbf{s}^F d\Omega \end{aligned} \quad (3.9)$$

In Equation (3.9), the boundary (Γ) integral describes the Neumann boundary condition for tangential fields, as

$$(\boldsymbol{\mu}^{-1} \cdot \nabla \times \mathbf{E}_s) \times \hat{\mathbf{n}} = -i\omega (\mathbf{H}_s + \boldsymbol{\mu}^{-1} \cdot \delta \boldsymbol{\mu} \cdot \mathbf{H}_p) \times \hat{\mathbf{n}} \quad (3.10)$$

for the electric field problem, and

$$(\boldsymbol{\sigma}^{-1} \cdot \nabla \times \mathbf{H}_s) \times \hat{\mathbf{n}} = (\mathbf{E}_s + \boldsymbol{\sigma}^{-1} \cdot \delta \boldsymbol{\sigma} \cdot \mathbf{E}_p) \times \hat{\mathbf{n}} \quad (3.11)$$

for the magnetic field problem.

From the construction of edge-elements in MoVFEM the tangential EM fields are continuous among shared elements, therefore $C_{\Gamma} = 0$ in the local calculation of Equation (3.9) (Farquharson & Miensopust, 2011). On the boundary Γ of the domain, homogeneous Neumann boundary conditions are applied. Hence, $\mathbf{H}_s \times \hat{\mathbf{n}} = 0$ and $\mathbf{H}_p \times \hat{\mathbf{n}} = 0$ in Equation (3.10), and $\mathbf{E}_s \times \hat{\mathbf{n}} = 0$ and $\mathbf{E}_p \times \hat{\mathbf{n}} = 0$ in Equation (3.11). By applying these tangential fields, the boundary integral in Equation (3.9) can be omitted.

3.2.2 Primary Fields

For the MT problem, the source fields (Equation (3.2), or (3.6)) are defined in terms of a primary field \mathbf{E}_p and \mathbf{H}_p .

For the primary EM fields, the domain Ω is considered as air. The following equations describe the primary fields for xy -polarization, where the electric field is in the x direction and the magnetic field in the y direction:

$$\begin{aligned} E_{px} &= E_0 - i\omega B_0 z; & E_0 &= 0 \\ B_{py} &= B_0; & B_0 &= 1 \text{ nT} \end{aligned} \quad (3.12)$$

These primary fields do not consider the geometry of the computational domain, e.g. surface topography, thus it can be used for models with complex geometry.

3.2.3 Boundary Conditions

Two types of boundary conditions are considered in this methodology, and these are Dirichlet and GPML. Dirichlet boundary conditions requires that the boundaries are far away from the inhomogeneities, therefore the model domain is extended several skin-depths to each direction (x, y, z). In this case, the secondary EM fields on the boundaries of the domain will be treated as zero, as EM fields in homogeneous Earth, or EM fields in layered Earth. GPML assumes that the secondary EM fields gradually decreases to zero in the PML zone (Fang, 1996).

Dirichlet: Perfect Conductor In this case, the secondary fields at the boundary are assigned with a value of zero, such as

$$\left. \begin{array}{l} \mathbf{E}_s = 0 \quad \text{for the E field problem} \\ \mathbf{H}_s = 0 \quad \text{for the H field problem.} \end{array} \right\} \Gamma \rightarrow \infty. \quad (3.13)$$

Homogeneous Earth The boundaries are considered as a homogeneous Earth with a conductivity σ_0 , and flat surface topography ($z_0 \equiv 0$), and the secondary EM fields on the boundaries are

$$\left. \begin{array}{l} \mathbf{E}_s = \mathbf{E}^h \quad \text{for the E field problem} \\ \mathbf{H}_s = \mathbf{H}^h \quad \text{for the H field problem.} \end{array} \right\} \Gamma \rightarrow \infty \quad (3.14)$$

According to Weaver (1994), EM fields in the xy -polarization are

$$\begin{aligned} E_x^h &= -2i\omega B_0 f(z) \\ H_y^h &= 2B_0 f'(z)/\mu_0, \end{aligned} \quad (3.15)$$

where $f(z)$ describes the plane wave characteristic (discussed in Appendix B.1.2). The conductivity of the boundary is considered as the background conductivity of the model in study. This boundary condition is applied when the model has a flat topography and the inhomogeneities are within a homogeneous background.

Layered Earth The boundaries of the domain are treated as an Earth with n layers of variable thickness with conductivities $\{\sigma_1, \sigma_2, \dots, \sigma_n\}$, and flat surface topography ($z_0 \equiv 0$). The secondary fields on the boundaries of the domain are

$$\left. \begin{array}{l} \mathbf{E}_s = \mathbf{E}^l \quad \text{for the E field problem} \\ \mathbf{H}_s = \mathbf{H}^l \quad \text{for the H field problem.} \end{array} \right\} \Gamma \rightarrow \infty \quad (3.16)$$

These boundary fields in xy -polarization are defined as

$$\begin{aligned} \left. \begin{array}{l} E_x^l = 2i\omega B_0 [c(\omega) - z] \\ H_y^l = 2B_0/\mu_0 \end{array} \right\} \text{Air}(z < z_0) \\ \left. \begin{array}{l} E_x^l = 2i\omega B_0 c(\omega) e(z) \\ H_y^l = -2B_0 c(\omega) e'(z)/\mu_0 \end{array} \right\} \text{Subsurface}(z \geq z_0) \end{aligned} \quad (3.17)$$

where $c(\omega)$ is the MT transfer function and $e(z)$ describes the plane wave propagation within layers (Weaver, 1994). These functions are described in Appendix B.1.3. The thickness of layers and its conductivity values are the same as the background conductivity structures of the model. Therefore, this boundary condition is applied when the model has a flat surface and the inhomogeneities are embedded in a layered background.

Sometimes is computationally impossible to extend the domain until Dirichlet boundary condition is satisfied. This introduces field reflection from the boundaries back to the inhomogeneities, making the solution to some degree inaccurate.

GPML According to Fang (1996), PML is not effective for evanescent waves and models involving wave propagation in lossy media. Therefore, with PML, significant reflection will be expected on the boundary elements (Fang, 1996). This author suggested a new method, called Generalized Perfect Matched Layer (GPML), to deal with propagating and evanescent waves. MT waves are of evanescent nature, so GPML is implemented in MoVFEM.

The model extension will be the PML Zone where this method is applied, hence, the EM fields on this zone will gradually decrease to a zero value (Figure 3.1). The GPML

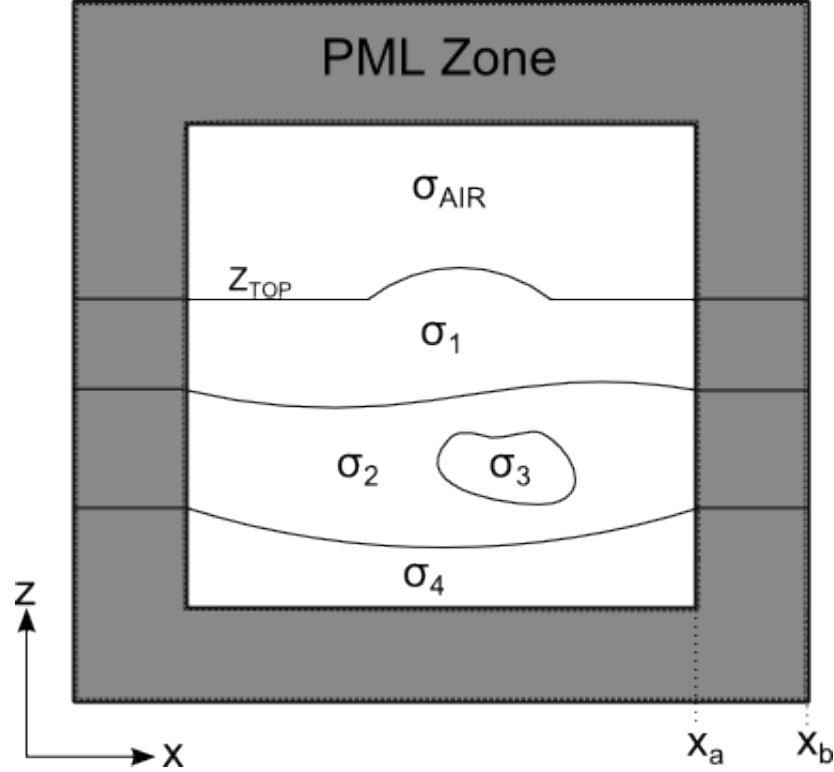


Figure 3.1: Description of the PML zone, x_a is an example of the starting point of the PML zone, and x_b is the end point of the PML zone.

method is implemented by transforming the coordinates into complex coordinates, so that the MT governing equation in complex coordinates is defined as

$$\tilde{\nabla} \times \boldsymbol{\nu}^{-1} \cdot \tilde{\nabla} \times \mathbf{F}_s + i\omega \boldsymbol{\kappa} \cdot \mathbf{F}_s = \tilde{\mathbf{s}}^F. \quad (3.18)$$

The modified Nabla operator $\tilde{\nabla}$ is

$$\tilde{\nabla} = \left(\frac{1}{h_{x_1}} \frac{\partial}{\partial x_1}, \frac{1}{h_{x_2}} \frac{\partial}{\partial x_2}, \frac{1}{h_{x_3}} \frac{\partial}{\partial x_3} \right),$$

and the modified source field $\tilde{\mathbf{s}}^F = h^{(x_1+x_2+x_3)} \mathbf{s}^F$ in Equation (3.18), where $h^{(x_1+x_2+x_3)} = h_{x_1} h_{x_2} h_{x_3}$. In the previous equations, $h_{x_m} = h_{x_m}(x_m)$ is called the stretching factor for the coordinates.

According to Zhou et al. (2012), in the anisotropic case, it is possible to factorize the stretching factors from the partial differentiations into the model tensors, obtaining the MT governing equation with GPML as

$$\nabla \times \tilde{\boldsymbol{\nu}}^{-1} \cdot \nabla \times \mathbf{F}_s + i\omega \tilde{\boldsymbol{\kappa}} \cdot \mathbf{F}_s = \tilde{\mathbf{s}}^F. \quad (3.19)$$

The new model tensors ($\tilde{\boldsymbol{\nu}}, \tilde{\boldsymbol{\kappa}}$) now contain the stretching factors and are defined as

$$\begin{aligned}\tilde{\boldsymbol{\nu}} &= \{\tilde{\nu}_{\gamma m}^{\beta n}\} = \left\{ \nu_{\gamma m} \frac{h^{(x_1+x_2+x_3)}}{h_{x_\beta} h_{x_n}} \right\} \\ \tilde{\boldsymbol{\kappa}} &= h^{(x_1+x_2+x_3)} \boldsymbol{\kappa}.\end{aligned}\quad (3.20)$$

In Equation (3.20) indices (β, m) are related to the derivatives of the curl-curl components, and (γ, n) to the components of $\boldsymbol{\nu}$. Appendix B.1.4 shows the procedure for this factorization. Galerkin method is applied to this MT equation (Equation (3.19)) in order to obtain the secondary field solution with GPML.

Fang (1996) defines the stretching factors as

$$\begin{aligned}h_{x_m}(x_m) &= h_{x_0}(x_m) \left(1 + \frac{b(x_m)}{(i\omega\varepsilon)} \right); \quad \forall x_m \in \text{PML Zone}, m = 1, 2, 3 \\ b(x_m) &= b_0 \sin^2 \left(\frac{\pi |x_m - x_{am}|}{2|x_{bm} - x_{am}|} \right) \\ h_{x_0}(x_m) &= 1 + a_0 \left(\frac{|x_m - x_{am}|}{|x_{bm} - x_{am}|} \right)^n,\end{aligned}\quad (3.21)$$

where x_{am} is the starting point of PML zone, x_{bm} the end point of PML zone (Figure 3.1), and index m stands for the 3 Cartesian coordinates (x_1, x_2, x_3) .

According to Fang (1996), it is necessary to define the best parameters a_0 , b_0 , and n that lead to a smooth increase of the stretching factor $h_{x_m}(x_m)$. Zhou et al. (2012) modified the stretching factors in order to be applied for MT and CSEM forward modeling,

$$h_{x_m}(x_m) = 1 \pm ib(x_m)/(a_0 + i\omega) \quad (3.22)$$

$$\begin{aligned}b(x_m) &= b_0 \left(\frac{|x_m - x_{am}|}{|x_{bm} - x_{am}|} \right)^n \\ a_0 &= (a_{max} - a_{min}) \frac{(f - f_{min})}{(f_{max} - f_{min})} + a_{min}\end{aligned}\quad (3.23)$$

$$b_0 = (b_{min} - b_{max}) \frac{(f - f_{min})}{(f_{max} - f_{min})} + b_{max}.\quad (3.24)$$

In this case, parameters a_0 (Equation 3.23) and b_0 (Equation 3.24) are defined in such a way that $h_{x_m}(x_m)$ increases smoothly for a frequency range $f \in [f_{min}, f_{max}]$ (Zhou et al., 2012). The smoothness of this increase is modified by a_{min} , a_{max} , b_{min} , and b_{max} which are selected according to the frequency range. In both Fang (1996), and Zhou et al. (2012) formulations, the exponent n is usually $1 \leq n \leq 3$ for evanescent waves.

Figure 3.2 shows the magnitude of $h_x(x)$ for a frequency range of $[10^{-5} : 10^2]$ of both stretching factors presented here. The top panel on this figure shows the definition of Fang (1996) for fixed parameters $a_0 = 100$ and $b_0 = 10^{-10}$. Bottom panel show the formulation of Zhou et al. (2012) for fixed parameters $a_{min} = 0$, $a_{max} = 100$, $b_{min} = 10^{-2}$, $b_{max} = 10^6$. Both formulations of $h_x(x)$ depend on the frequency applied. For higher frequencies, the stretching factor increases smoother than for lower frequencies. The selection of the stretching factor parameters is important to obtain a smooth increase for each frequency. However, an analysis of these parameters has not been

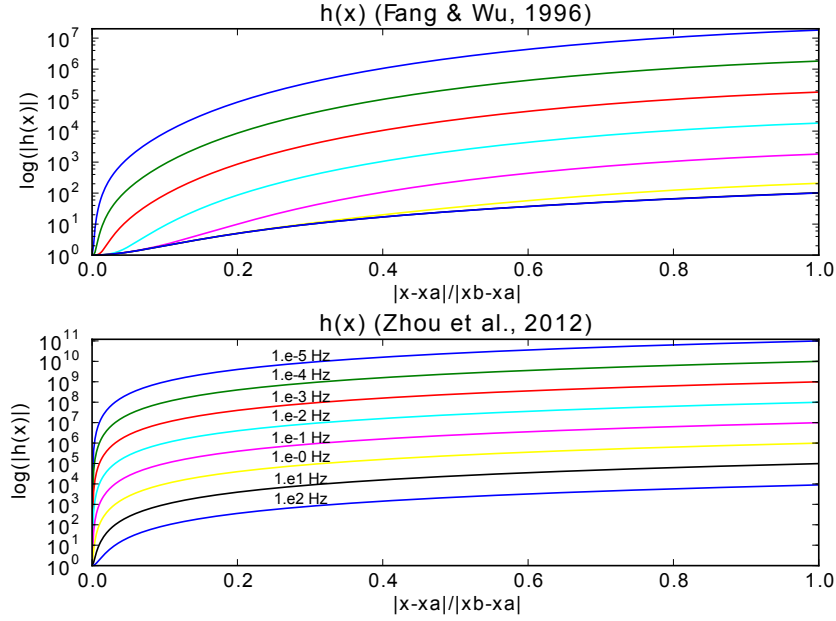


Figure 3.2: Top panel show the magnitude of stretching factor from Fang (1996), for fixed parameters $a_0 = 100$ and $b_0 = 10^{-10}$. Bottom panel show that from Zhou et al. (2012), with $a_{min} = 0$, $a_{max} = 100$, $b_{min} = 10^{-2}$, $b_{max} = 10^6$.

carried out. By applying the stretching factors to the MT governing equations, the problem will decrease to zero as x reaches the end of the boundary. Finally, outside the PML Zone, $h_{x_m}(x_m) \equiv 1$.

3.3 Vector Finite Elements

3.3.1 Domain Discretization

The model domain consists of an input subsurface model. An air domain with height h_{air} is added to this model domain. The symmetric conductivity tensor is defined as $\sigma = \sigma_{re} + i\omega\epsilon_0\mathbf{I}$, where σ_{re} is the real conductivity value, and \mathbf{I} is the 3×3 identity matrix. This definition is applied in order to have an air conductivity of $\sigma_{re} = 0$ S/m. This domain is extended to a distance $\sim 3\delta_{max}$, where δ_{max} is the maximum skin-depth (Equation (1.17)). In this case the maximum skin-depth is calculated with the minimum conductivity of the model and minimum frequency of the frequency range in use. The extension is truncated according to the length of the input model. For example, if the length of the input model is $> \delta_{max}$, then the extension will be of $\sim 2\delta_{max}$. This truncation is applied to not create a big computational grid. The conductivity values on these extension zones will be the values on their respective boundaries of the input model.

The computational domain Ω will be the model domain including its extension zones. This domain is discretized into $N_e = N_x N_y N_z$ hexahedral elements, such that

$$\Omega = \bigcup_{e=1}^{N_e} \Omega_e. \quad (3.25)$$

Let Γ_e be a surface of Ω_e , then $\Gamma_i^e = \Gamma_j^e$, if Ω_i^e and Ω_j^e are adjacent. Each hexahedral

element is defined as

$$\Omega_e = [x_i, x_{i+1}] \times [y_j, y_{j+1}] \times [z_k(x, y), z_{k+1}(x, y)] \\ (1 \leq i \leq N_x, 1 \leq j \leq N_y, 1 \leq k \leq N_z). \quad (3.26)$$

These hexahedral elements will fit any topography and subsurface interfaces by defining $z = z(x, y)$. The surface and interfaces interpolation is applied with a ‘quadratic Shepard method’ that interpolates scattered data by weighted average of data point values (Algorithm 660: QSHEP2D of Renka, 1988). The idea of using this method, is that MoVFEM receives as input arrays the location of topography and subsurface interfaces. In geophysics, these values are usually obtained with GPS locations of receivers (on the surface) or from other geophysical data (for the subsurface). The location of these data are commonly measured in scattered points, because in some study areas is not possible to obtain them on a structured way.

Figure 3.3 shows this discretization approach with its extension zones. The element

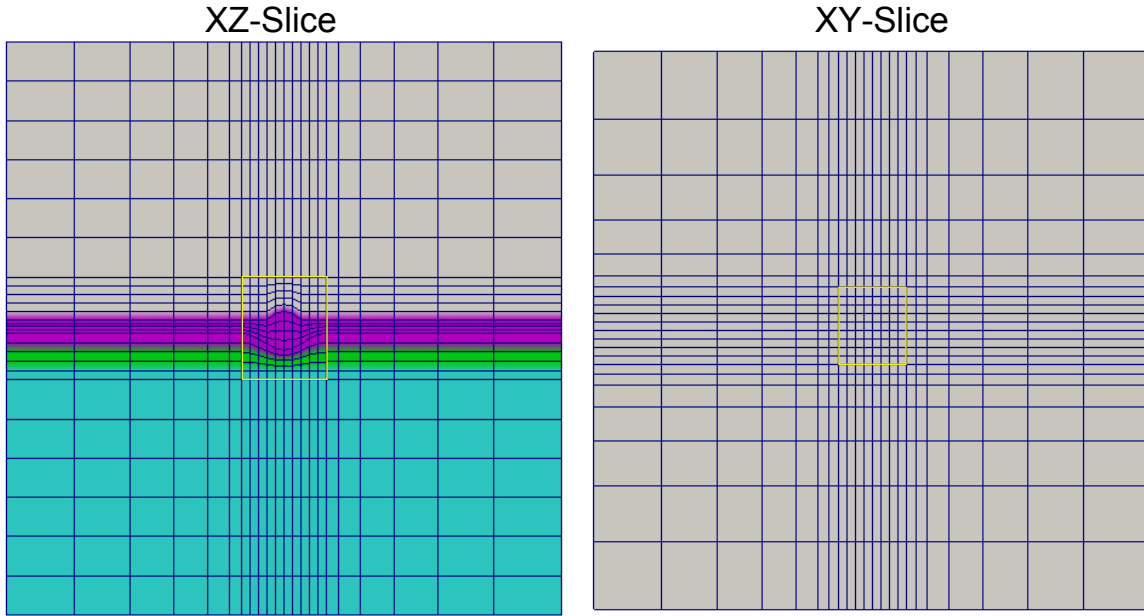


Figure 3.3: Computational domain discretization comprising the model domain with extension zones. Left panel present an example of the (x, z) - or (y, z) -slice, where the discretization among interfaces is shown. Right panel shows the (x, y) -slice. The yellow rectangle shows the location of the inner grid, which is surrounded by the extension zone. In the extension zone, the element size is gradually increased until the boundary of the computational domain.

size is increased on the extension zone, by a factor of 1.3^j , where $j = 1, 2, \dots, n_{ext}$, and n_{ext} is the number of elements in the extension zone.

Each element will have n_e nodes, and these nodes are assigned from the isoparametric coordinates (ξ, η, ζ) . Therefore, the Cartesian coordinates of these nodes will be

$$x = \frac{1}{2} [(x_{i+1} - x_i) \xi + (x_i + x_{i+1})]; \xi \in [-1, 1] \\ y = \frac{1}{2} [(y_{j+1} - y_j) \eta + (y_j + y_{j+1})]; \eta \in [-1, 1] \\ z = \frac{1}{2} [(z_{k+1}(x, y) - z_k(x, y)) \zeta + (z_k(x, y) + z_{k+1}(x, y))]; \zeta \in [-1, 1]. \quad (3.27)$$

Three types of elements are defined according to the numbers of nodes used for each local calculation. These are the linear element, quadratic element, and Lagrangian element. Figure 3.4 shows the location of the nodes used in this methodology. For

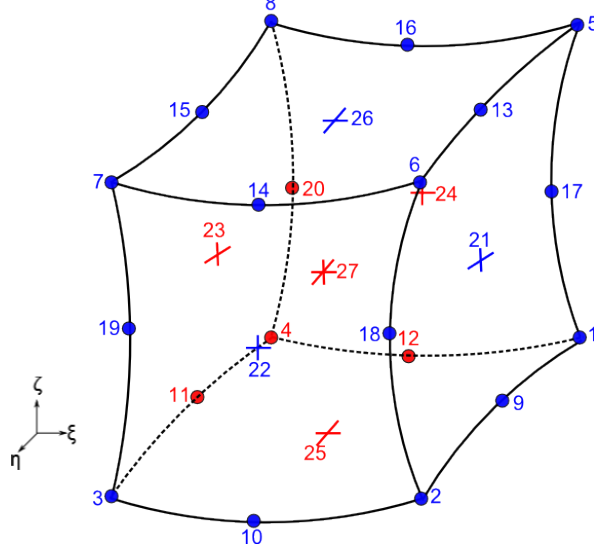


Figure 3.4: Local numbering scheme for nodes on the element.

the linear element, eight corner points of the element are used (nodes 1 to 8 in Figure 3.4). The edge nodes are included for the quadratic element (nodes 1 to 20 in Figure 3.4), and additionally the six face nodes and the center are included for the Lagrangian element (nodes 1 to 27 in Figure 3.4).

3.3.2 Nodal Basis Functions

The nodal basis functions are defined in such a way that $N_i(\boldsymbol{\xi}_j) = \delta_{ij}$, where δ is the Kronecker delta function, $\boldsymbol{\xi}_j = (\xi_j, \eta_j, \zeta_j)$, $i = 1, 2, \dots, n_e$, and $j = 1, 2, \dots, n_e$ (Appendix A.2). These basis functions are used to interpolate known variables, such as conductivity and source fields. These basis functions are constructed with 1D Lagrange polynomials in each direction (Jin, 2002, Chap.4). Let $L_\xi(\xi)$, $L_\eta(\eta)$, and $L_\zeta(\zeta)$ be the Lagrange polynomials in ξ , η , and ζ directions, respectively, then the nodal basis functions are constructed as

$$N_i(\xi, \eta, \zeta) = L_\xi(\xi)L_\eta(\eta)L_\zeta(\zeta).$$

Linear-order Following this construction for each node, the linear element basis functions are defined as

$$N_i = \frac{1}{8}(1 + \xi_i\xi)(1 + \eta_i\eta)(1 + \zeta_i\zeta); \quad i = 1, 2, \dots, 8. \quad (3.28)$$

Quadratic-order For the quadratic element, two types of basis functions are defined. These basis functions are

$$N_i = \begin{cases} \frac{1}{8}(1 + \xi_i\xi)(1 + \eta_i\eta)(1 + \zeta_i\zeta)(\xi_i\xi + \eta_i\eta + \zeta_i\zeta - 2); & i = 1, 2, \dots, 8 \\ \frac{1}{4}(1 - \xi^2)(1 + \eta_i\eta)(1 + \zeta_i\zeta); & i = 10, 12, 14, 16 \end{cases} \quad (3.29)$$

for those nodes in the corners of the element, and for those nodes in the ξ edges of the element, respectively. Appendix B.2 contains the complete nodal basis functions, including those for nodes on η and ζ edges for the quadratic element.

Lagrangian-order In the case of Lagrangian elements, four types of nodal functions are defined. These basis functions are defined as

$$N_i = \begin{cases} \frac{1}{8}(1 + \xi_i\xi)(1 + \eta_i\eta)(1 + \zeta_i\zeta)\xi_i\xi\eta_i\eta\zeta_i\zeta; & i = 1, 2, \dots, 8 \\ \frac{1}{4}(1 - \xi^2)(1 + \eta_i\eta)(1 + \zeta_i\zeta)\eta_i\eta\zeta_i\zeta; & i = 10, 12, 14, 16 \\ \frac{1}{2}(1 + \xi_i\xi)(1 - \eta^2)(1 - \zeta^2)\xi_i\xi; & i = 21, 23 \\ (1 - \xi^2)(1 - \eta^2)(1 - \zeta^2); & i = 27 \end{cases} \quad (3.30)$$

for nodes in the corners of the element, in ξ edges, on (η, ζ) faces, and for the central node of the element, respectively. The complete formulation of these basis functions are in Appendix B.2.

Interpolation A function interpolation with nodal basis is defined as

$$f(\xi, \eta, \zeta) = \sum_{i=1}^{n_e} f_i N_i(\xi, \eta, \zeta),$$

where f_i is the discretized function value on the i^{th} node.

Differentiation The partial differentiation of a function is defined as

$$\frac{\partial f}{\partial x} = \sum_{i=1}^{n_e} \frac{\partial N_i}{\partial x} f_i,$$

where the nodal function partial differentiation is defined in Equation (A.6) in the Appendix.

3.3.3 Vector Basis Functions

As discussed in Section 2.5, a vector basis function \mathbf{v} is defined in the Sobolev space $\mathcal{H}_0(\Omega, \text{curl})$, in order to satisfy the divergence-free condition and to have these basis functions defined on element edges. In addition, these vector functions are defined in such a way that $\mathbf{v}_i(\boldsymbol{\xi}_j) = \delta_{ij}$, where δ_{ij} is the Kronecker delta function.

Covariant Projections Crowley et al. (1988) considered the fields as a projection to the curvilinear basis vectors $\vec{\boldsymbol{\xi}} = \partial \mathbf{r} / \partial \xi$, where $\mathbf{r} = (x, y, z)$, as

$$\mathbf{F}_\xi = \mathbf{F} \cdot \vec{\boldsymbol{\xi}}. \quad (3.31)$$

The field component defined in Equation (3.31) is called the covariant component, and consequently this definition is the so-called covariant projection. According to Crowley et al. (1988), by defining the field components as in Equation (3.31), then the total field is defined as

$$\mathbf{F} = F_\xi \nabla \xi + F_\eta \nabla \eta + F_\zeta \nabla \zeta. \quad (3.32)$$

Appendix B.4 describes the covariant projections in higher details. In Equation (3.32), the gradient of ξ local coordinate is defined as

$$\nabla\xi = \frac{\vec{\eta} \times \vec{\zeta}}{|\mathbf{J}|}, \quad (3.33)$$

where $|\mathbf{J}|$ is the determinant of the Jacobian matrix of transformation. The proof of this definition is in Appendix B.4, where $\nabla\eta$, and $\nabla\zeta$ are also described. These components $(\nabla\xi, \nabla\eta, \nabla\zeta)$ are normal to the surfaces (η, ζ) , (ξ, ζ) , and (ξ, η) of the curvilinear element, respectively, and they define the local basis vectors.

Kameari (1990) obtained the same definition for vector basis functions, i.e. the local basis vectors are $(\nabla\xi, \nabla\eta, \nabla\zeta)$. The vector basis functions are defined with mixed-order polynomials (e.g. N_ξ), that is polynomials of order $(p-1)$ on ξ and order p on the other components (Crowley et al., 1988; Kameari, 1990). The use of mixed-order polynomials will reduce the degrees of freedom from $3n_e$ to the number of edges m_e . Therefore, with a proper numbering scheme for the edges, the field interpolation will be

$$\mathbf{F} = \sum_{i=1}^{m_e} F_i \mathbf{v}_i(\xi, \eta, \zeta), \quad (3.34)$$

and the vector basis function can be defined as (Kameari, 1990):

$$\mathbf{v}_i = \begin{cases} N_{\xi i} \nabla\xi & \text{for edges in } \hat{\xi} \text{ direction} \\ N_{\eta i} \nabla\eta & \text{for edges in } \hat{\eta} \text{ direction} \\ N_{\zeta i} \nabla\zeta & \text{for edges in } \hat{\zeta} \text{ direction.} \end{cases} \quad (3.35)$$

By using mixed-order polynomials, the vector basis functions satisfy the divergence-free condition, so no spurious solution is obtained (Crowley et al., 1988; Jin, 2002). In addition, these vector functions are continuous among shared edges, thus the condition of continuity of tangential EM fields between interfaces is automatically satisfied (Jin, 2002).

Mixed-order polynomials can be obtained from the polynomials used as nodal basis functions by reducing the order on the direction of the edge, and normalizing it with the length of local edge. In this section some polynomials in $\hat{\xi}$ direction will be presented, the complete formulation of these polynomials are in Appendix B.3. Kameari (1990) presented these basis functions for the linear (12 edges) and quadratic (36 edges) elements, these are the edge-elements used in this algorithm. Webb & Miniowitz (1991) presented the covariant projections for the Lagrangian element. In this methodology, the polynomials for the Lagrangian (54 edges) element essentially are the same of Webb & Miniowitz (1991), but modified to have these edges in the formulation of Kameari (1990).

Linear-order The mixed-order polynomial for the i -th basis vector in $\hat{\xi}$ direction in the linear element is

$$N_{\xi i} = \frac{1}{4}(1 + \eta_j \eta)(1 + \zeta_j \zeta). \quad (3.36)$$

Quadratic-order For the quadratic element, two types of mixed-order polynomials are defined, one is defined for basis vectors over the element edges, and the other for basis vectors over element faces:

$$N_{\xi i} = \begin{cases} \frac{1}{8}(1 + \eta_j \eta)(1 + \zeta_j \zeta)(\xi_j \xi + \eta_j \eta + \zeta_j \zeta - 1); & \hat{\xi} - \text{edges} \\ \frac{1}{2}(1 - \eta^2)(1 + \zeta_j \zeta); & (\xi, \eta) - \text{faces.} \end{cases} \quad (3.37)$$

Lagrangian-order In the case of Lagrangian elements, three types of mixed-order polynomials are obtained. The first type is defined for basis vectors over element edges, the second type is defined for basis vectors over element faces, and the last is defined for edge-elements on the center of this element. These polynomials are

$$N_{\xi i} = \begin{cases} \frac{1}{8}(1 + \xi_j \xi)(1 + \eta_j \eta)(1 + \zeta_j \zeta)\eta_j \eta \zeta_j \zeta; & \hat{\xi} - \text{edges} \\ \frac{1}{4}(1 + \xi_j \xi)(1 - \eta^2)(1 + \zeta_j \zeta)\zeta_j \zeta; & (\xi, \eta) - \text{faces} \\ \frac{1}{2}(1 + \xi_j \xi)(1 - \eta^2)(1 - \zeta^2); & \text{central.} \end{cases} \quad (3.38)$$

As it can be noticed, these mixed-order polynomials are defined with nodes (ξ_j, η_j, ζ_j) , in Appendix B.3 the numbering scheme of these edges is presented as well as these nodes defining the edges.

With vector basis functions defined in Equation (3.35), and the field interpolation defined as Equation (3.34), the curl of this function is calculated as

$$\begin{aligned} \nabla \times \mathbf{F} &= \sum_{i=1}^{m_e} F_i \nabla \times \mathbf{v}_i \\ \nabla \times \mathbf{v}_i &= \nabla N_{\xi i} \times \nabla \xi. \end{aligned} \quad (3.39)$$

The proof for this definition is in Appendix B.5.

3.3.4 Local Problem: Numerical Integration

When applying the basis functions in finite elements, the integration is calculated on the isoparametric element and is then transformed into global coordinates,

$$\int_{\Omega_e} f(x, y, z) dx dy dz = \int \int \int_{-1}^1 f(\xi, \eta, \zeta) |\mathbf{J}(\xi, \eta, \zeta)| d\xi d\eta d\zeta, \quad (3.40)$$

where $|\mathbf{J}(\xi, \eta, \zeta)|$ is the determinant of the Jacobian of the transformation. This local integration is calculated numerically as a sum of weighted functions on integration points. Gauss's quadrature is used in MoVFEM, as it is the most common numerical integration applied in finite elements:

$$\begin{aligned} & \int \int \int_{-1}^1 f(\xi, \eta, \zeta) |\mathbf{J}(\xi, \eta, \zeta)| d\xi d\eta d\zeta \\ &= \sum_{i=1}^{n_g} \sum_{j=1}^{n_g} \sum_{k=1}^{n_g} w_i w_j w_k f(\xi_i, \eta_j, \zeta_k) |\mathbf{J}(\xi_i, \eta_j, \zeta_k)|. \end{aligned} \quad (3.41)$$

In this Equation (3.41), n_g is the number of integration points, w_i are the Gaussian quadrature weights, and (ξ_i, η_j, ζ_k) are the Gaussian quadrature points. The number of Gauss's quadrature points are selected according to the order of the respective polynomial, i.e. for linear-order $n_g = 2$, and for quadratic order $n_g = 3$, and so on (Jin, 2002, Chap.4). The polynomials used in this methodology are up to quadratic order, so up to 3 integration points are used for each direction, yielding 27 total points in the element.

The Galerkin formulation of the MT problem (Equation 3.9) is solved on each element, and the boundary integral is ignored ($C_\Gamma = 0$). To solve these integrals, the basis vectors (Equation 3.35) are applied as the weighting function \mathbf{w} in the Galerkin formulation ($\mathbf{w} = \mathbf{v}$). Consequently, three integrals are solved on each element:

$$\begin{aligned} I_1^{(e)} &= \int_{\Omega_e} (\nabla \times \mathbf{v}^{(e)}) \cdot \boldsymbol{\nu}^{-1} \cdot (\nabla \times \mathbf{F}^{(e)}) d\Omega \\ &= \sum_{\alpha=1}^{m_e} \sum_{\beta=1}^{m_e} F_\beta^{(e)} \int_{\Omega_e} (\nabla \times \mathbf{v}_\alpha^{(e)}) \cdot \boldsymbol{\nu}^{-1} \cdot (\nabla \times \mathbf{v}_\beta^{(e)}) d\Omega \end{aligned} \quad (3.42a)$$

$$\begin{aligned} I_2^{(e)} &= \int_{\Omega_e} \mathbf{v}^{(e)} \cdot \boldsymbol{\kappa} \cdot \mathbf{F}^{(e)} d\Omega \\ &= \sum_{\alpha=1}^{m_e} \sum_{\beta=1}^{m_e} F_\beta^{(e)} \int_{\Omega_e} \mathbf{v}_\alpha^{(e)} \cdot \boldsymbol{\kappa} \cdot \mathbf{v}_\beta^{(e)} d\Omega \end{aligned} \quad (3.42b)$$

$$\begin{aligned} I_3^{(e)} &= \int_{\Omega_e} \mathbf{v}^{(e)} \cdot \mathbf{s}_F^{(e)} d\Omega \\ &= \sum_{\alpha=1}^{m_e} \int_{\Omega_e} \mathbf{v}_\alpha^{(e)} \cdot \mathbf{s}_F^{(e)} d\Omega \end{aligned} \quad (3.42c)$$

The integrals (Equations (3.42a) to (3.42c)) can be re-written in matrix form for the finite number of edge-elements. The first integral is

$$\begin{aligned} I_1^{(e)} &= \bar{\mathbf{M}}_1^{(e)} \cdot \bar{\mathbf{F}}^{(e)} \\ \bar{\mathbf{F}}^{(e)} &= \left(\mathbf{F}_1^{(e)}, \mathbf{F}_2^{(e)}, \dots, \mathbf{F}_{m_e}^{(e)} \right)^T \\ \bar{\mathbf{M}}_1^{(e)} &= \left[\mathbf{M}_1^{(e)} \right]_{\alpha, \beta}^{m_e \times m_e}; \quad \mathbf{M}_1^{(e)} \alpha, \beta = \int_{\Omega_e} (\nabla \times \mathbf{v}_\alpha^{(e)}) \cdot \boldsymbol{\nu}^{-1} \cdot (\nabla \times \mathbf{v}_\beta^{(e)}) d\Omega, \end{aligned} \quad (3.43)$$

where $\bar{\mathbf{M}}_1^{(e)}$ is a matrix of size $m_e \times m_e$ that contains the integration of curl-curl components. The local matrix $\bar{\mathbf{M}}_1^{(e)}$ is usually known as the 'stiffness matrix'. The edge components are defined as a local vector $\bar{\mathbf{F}}^{(e)}$ of size m_e .

The second integration contains the integration of the dot-product of basis functions, and is

$$\begin{aligned} I_2^{(e)} &= \bar{\mathbf{M}}_2^{(e)} \cdot \bar{\mathbf{F}}^{(e)} \\ \bar{\mathbf{M}}_2^{(e)} &= \left[\mathbf{M}_2^{(e)} \right]_{\alpha, \beta}^{m_e \times m_e}; \quad \mathbf{M}_2^{(e)} \alpha, \beta = \int_{\Omega_e} \mathbf{v}_\alpha^{(e)} \cdot \boldsymbol{\kappa} \cdot \mathbf{v}_\beta^{(e)} d\Omega. \end{aligned} \quad (3.44)$$

This integration defines a local matrix $\bar{\mathbf{M}}_2^{(e)}$, also of size $m_e \times m_e$ and is usually called as the 'mass matrix'.

The third integral becomes

$$\begin{aligned} I_3^{(e)} &= \bar{\mathbf{b}}_F^{(e)T} \\ \bar{\mathbf{b}}_F^{(e)} &= \left[\mathbf{b}_{F,\alpha}^{(e)} \right]_{m_e \times 1}; \quad \mathbf{b}_{F,\alpha}^{(e)} = \int_{\Omega_e} \mathbf{v}_\alpha^{(e)} \cdot \mathbf{s}_F^{(e)} d\Omega \end{aligned} \quad (3.45)$$

contains the integration of known source, and defines a local vector $\bar{\mathbf{b}}_F^{(e)}$ of size m_e .

Dirichlet boundary condition is implemented by modifying rows of the local matrices and the source components for the edge-elements that belongs to the boundaries. In matrix form, the α component of the source vector is

$$\begin{aligned} \mathbf{b}_{F,\alpha}^{(e)} &= \int_{\Omega_e} \mathbf{v}_\alpha^{(e)} \cdot \mathbf{s}_F^{(e)} d\Omega \\ &\quad - \sum_{\beta=1}^{m_e} F_\beta \left[\int_{\Omega_e} (\nabla \times \mathbf{v}_\alpha^{(e)}) \cdot \boldsymbol{\nu}^{-1} \cdot (\nabla \times \mathbf{v}_\beta^{(e)}) d\Omega \right. \\ &\quad \left. + i\omega \int_{\Omega_e} \mathbf{v}_\alpha^{(e)} \cdot \boldsymbol{\kappa} \cdot \mathbf{v}_\beta^{(e)} d\Omega \right], \forall \mathbf{v}_\alpha^{(e)}, \mathbf{v}_\beta^{(e)} \in \Omega; \mathbf{v}_\alpha^{(e)} \notin \Gamma, \mathbf{v}_\beta^{(e)} \in \Gamma \end{aligned} \quad (3.46)$$

This implementation is described in the second term of Equation (3.46), where F_β is the covariant projection of the Dirichlet EM field on the boundary.

3.3.5 Assembly and Solution

The global matrix assembly is obtained by the sum of the N_e elemental matrices, where N_e is the number of elements in the computational domain. This is described in Equation (3.47) for the stiffness matrix ($\bar{\bar{\mathbf{M}}}_1$), mass matrix ($\bar{\bar{\mathbf{M}}}_2$), source vector ($\bar{\bar{\mathbf{b}}}_F$), and vector of total unknowns ($\bar{\bar{\mathbf{F}}}_s$).

$$\begin{aligned} \bar{\bar{\mathbf{M}}}_1 &= \sum_{e=1}^{N_e} \bar{\mathbf{M}}_1^{(e)}; \quad \bar{\bar{\mathbf{M}}}_2 = \sum_{e=1}^{N_e} \bar{\mathbf{M}}_2^{(e)} \\ \bar{\bar{\mathbf{F}}}_s &= \sum_{e=1}^{N_e} \bar{\mathbf{F}}_s^{(e)}; \quad \bar{\bar{\mathbf{b}}}_F = \sum_{e=1}^{N_e} \bar{\mathbf{b}}_F^{(e)} \end{aligned} \quad (3.47)$$

Consequently, the global system of equations to be solved for the MT forward modeling is defined as

$$\left[\bar{\bar{\mathbf{M}}}_1 + i\omega \bar{\bar{\mathbf{M}}}_2 \right] \cdot \bar{\bar{\mathbf{F}}}_s = \bar{\bar{\mathbf{b}}}_F, \quad (3.48)$$

which is the discretized version of the Galerkin formulation (Equation (3.9)).

In the most general case, this matrix will be of size $M_e \times M_e$, where M_e is the total number of unknown edge-elements on the computational domain. Therefore, to assemble this global matrix, an array \mathbf{G}_{NE} with the indices of global degrees of freedom is defined of size $N_e \times m_e$. Hence, for each unknown vector on each element, a global index will be assigned, taking into consideration that edges shared among elements will have the same global index. Consequently, shared edges are summed in the global assembly process. Appendix B.6 shows a simple example of the assembly process.

This index scheme leads to a sparse matrix, because the integration is calculated locally, and elements that are wide apart will not share any edges on the global matrix.

Therefore, the matrix storage can be reduced by defining an array \mathbf{A} of the non-zero entries of global matrix, such as

$$\mathbf{A} = \left\{ \left[\bar{\mathbf{M}}_1 + i\omega\bar{\mathbf{M}}_2 \right]_{mn} ; \left[\bar{\mathbf{M}}_1 + i\omega\bar{\mathbf{M}}_2 \right]_{mn} \neq 0, \quad m, n \in \{1, 2, \dots, M_e\} \right\}.$$

To assemble the problem in the array \mathbf{A} , another index array is defined with size $N_e \times m_e \times m_e$ named \mathbf{NZ}_A . For each local matrix, \mathbf{NZ}_A will have the indices of entries into the non-zero array, also taking into consideration that shared edges will have the same index. So, the size N_{nz} of array \mathbf{A} will be the maximum index in array \mathbf{NZ}_A . To be able to define the global matrix from the array \mathbf{A} , indices of non-zero components of the global matrix must be stored on two arrays called \mathbf{IA} , and \mathbf{JA} , as

$$\begin{aligned} \mathbf{IA}[\mathbf{NZ}_A(e, i, j)] &= \mathbf{G}_{NE}(e, i), \\ \mathbf{JA}[\mathbf{NZ}_A(e, i, j)] &= \mathbf{G}_{NE}(e, j) \\ i, j &\in \{1, 2, \dots, m_e\}; \quad e \in \{1, 2, \dots, N_e\}. \end{aligned} \quad (3.49)$$

Then, the assembly of the global matrix \mathbf{A} is obtained as

$$\begin{aligned} \mathbf{A}[\mathbf{NZ}_A(e, m, n)] &= \mathbf{A}[\mathbf{NZ}_A(e, m, n)] + \left(\bar{\mathbf{M}}_1^{(e)}(m, n) + i\omega\bar{\mathbf{M}}_2^{(e)}(m, n) \right) \\ \bar{\mathbf{b}}_F[\mathbf{G}_{NE}(e, m)] &= \bar{\mathbf{b}}_F[\mathbf{G}_{NE}(e, m)] + \bar{\mathbf{b}}_F^{(e)}(m) \\ m, n &\in \{1, 2, \dots, m_e\}; \quad e \in \{1, 2, \dots, N_e\}. \end{aligned} \quad (3.50)$$

An example of this storage scheme is in Appendix B.6.

The MT problem leads to a symmetric matrix, so the array of non-zero entries will be reduced in size, because the symmetric part is not calculated in the local integrations. This is done by removing extra zero entries in array \mathbf{A} . In addition, the numbering of \mathbf{NZ}_A is done by element, so index arrays \mathbf{IA} , and \mathbf{JA} will not be in the right order of rows and columns. These arrays are sorted with the Merge Sort algorithm (Knuth, 1998).

The global matrix \mathbf{A} is inverted, and the unknown solution is obtained using MUMPS (Amestoy et al., 2006). This package is a parallel direct solver for sparse matrices, so it solves the linear system of equations as

$$\bar{\mathbf{F}}_s = \left[\bar{\mathbf{M}}_1 + i\omega\bar{\mathbf{M}}_2 \right]^{-1} \cdot \bar{\mathbf{b}}_F.$$

According to Amestoy et al. (2006), this direct solver takes advantage from parallelism of sparsity and dense factorization kernels. This package factorize the symmetric matrix into a matrix of the form \mathbf{LDL}^T , where \mathbf{L} is the lower triangular matrix, and \mathbf{D} is the diagonal matrix. So the solution is obtained by solving the following equations:

$$\begin{aligned} \mathbf{LDy} &= \bar{\mathbf{b}}_F \\ \mathbf{L}^T \bar{\mathbf{F}}_s &= \mathbf{y}, \end{aligned}$$

with forward and backward substitution (Amestoy et al., 2006), where $\bar{\mathbf{b}}_F$ and $\bar{\mathbf{F}}_s$ are the assembled arrays defined in Equation (3.47).

Once the unknown field $\bar{\mathbf{F}}_s$ is obtained, the other EM field is calculated directly from Maxwell's equations (Equation 3.3 or Equation 3.7). For example, if the unknown

field is the secondary electric field, then the total field is $\mathbf{E} = \mathbf{E}_p + \mathbf{E}_s$, and the magnetic field is calculated from Faraday's Law. The solution for the forward model is presented in terms of MT responses (i.e. impedance, apparent resistivity and phase). In order to obtain these responses the problem must be solved for both the xy - and yx -polarizations. This is done by defining these polarizations in the source fields (Equation (3.2) or (3.6)), where xy -polarization denotes an electric field on x direction and a magnetic field on y direction, and yx -polarization denotes an electric field on y direction and a magnetic field on x direction. Then, the impedance is obtained as

$$\mathbf{Z} = \begin{pmatrix} E_{x1} & E_{x2} \\ E_{y1} & E_{y2} \end{pmatrix} \begin{pmatrix} H_{x1} & H_{x2} \\ H_{y1} & H_{y2} \end{pmatrix}^{-1}, \quad (3.51)$$

where the subscript 1 denotes the xy -polarization and subscript 2, the yx -polarization. The apparent resistivity is

$$\rho_{i,j} = \frac{1}{\mu_0 \omega} |Z_{i,j}|^2, \quad (3.52)$$

and the phase:

$$\phi_{i,j} = \tan^{-1} \left(\frac{\Im Z_{i,j}}{\Re Z_{i,j}} \right). \quad (3.53)$$

Appendix C presents the workflow of this MoVFEM program, and a description of the input data files and output files obtained.

Chapter 4

Validation: Homogeneous Earth

4.1 Introduction

In order to validate the MoVFEM algorithm, it must be tested against a model with known MT responses. The validation of MoVFEM is carried out with a homogeneous Earth model. In the solution of this model, the apparent resistivity is $\rho_a = 1/\sigma$, where σ is the conductivity of the half-space and the phase is $\phi = 45^\circ$. Two Earth models will be tested; first, a resistive half-space (0.01 S/m) and second a conductive half-space (5 S/m). Both models are tested with a frequency of 0.1 Hz to show how the model dimension and discretization change for different conductivities.

In this Chapter, the convergence of the solution is analyzed with Dirichlet boundary conditions. The Dirichlet boundary conditions used for the validation of MoVFEM are those of a perfect conductor, in which the EM fields are zero. First, the convergence is analyzed for different spacings (dx), in terms of the skin-depth. This convergence analysis is called ‘h-convergence’. The second convergence analysis is for different edge-element orders, and is known as ‘p-convergence’. The analysis of both ‘h-convergence’ and ‘p-convergence’ is named as ‘hp-convergence’. After carrying out the hp-convergence analysis, the best model is selected to analyze the CPU time, memory usage and accuracy of the solution between different edge-element orders, and for the Dirichlet and GPML boundary conditions. Dirichlet and GPML boundary conditions are compared to understand the effect of these boundaries in the solution, i.e. backward reflections of EM fields from the boundaries of the computational domain. Finally, these Earth models are tested for a frequency range of one decade, to understand the behavior of apparent resistivity and phase over this bandwidth.

These models were run on e-Research, SA, High Performance Computing Resources (Coddington, 2013). The solution for one frequency were tested on the Tizard computer cluster that consist of 48 SGI compute nodes, with 48 cores per node. These cores are 4 AMD 6238 with 12-core of 2.6 GHz CPUs, and with 2.7Gb RAM per core (Coddington, 2013). Models were tested in sequential mode, thus, MUMPS inversion does not use any parallelization. The models over a frequency range were tested on the Corvus computer cluster, which consist of 70 SGI nodes with 2 cores per node. These cores are Intel Colvertown Quadcore processors of 2.66GHz CPUs with 8Gb RAM per core (Coddington, 2013).

4.2 Resistive Earth

4.2.1 Input Model and MT Problem

The input model is 100 km in x and y directions, and has a depth of 50 km, and the resistive half-space has a conductivity of 0.01 S/m. The MT problem is solved with the electric field governing equations, using the Dirichlet boundary conditions of a perfect conductor (zero EM fields).

4.2.2 hp-Convergence Analysis

The convergence is carried out using a frequency of 0.1 Hz, with a corresponding skin-depth of ~ 16 km, and an air height of $h_{air} = 20$ km.

The convergence is presented by the maximum and average relative error percentages (ϵ^{max} , ϵ^{avg} , respectively) from the surface values, because the MT data is measured on the Earth's surface. These errors are presented for both apparent resistivity

$$\begin{aligned}\epsilon_{\rho}^{max} &= \max_{surface} \frac{|\rho_{app} - \rho_a|}{|\rho_a|} \times 100 \\ \epsilon_{\rho}^{avg} &= \frac{1}{N_s} \sum_{i=1}^{N_s} \frac{|\rho_{app}^i - \rho_a|}{|\rho_a|} \times 100\end{aligned}\tag{4.1}$$

and phase

$$\begin{aligned}\epsilon_{\phi}^{max} &= \max_{surface} \frac{|\phi_{app} - \phi|}{|\phi|} \times 100 \\ \epsilon_{\phi}^{avg} &= \frac{1}{N_s} \sum_{i=1}^{N_s} \frac{|\phi_{app}^i - \phi|}{|\phi|} \times 100.\end{aligned}\tag{4.2}$$

In these equations, ρ_{app} and ϕ_{app} are the solution of the MoVFEM program, $\rho_a = 100 \Omega\text{m}$, and $\phi = 45^\circ$. The average error % is obtained from the N_s points on the surface of the model, and the maximum is the maximum ϵ from the error values on the surface.

Figure 4.1 shows the results from the hp-convergence analysis for linear, quadratic and Lagrangian elements.

h-Convergence: Linear In the linear case, the range of the spacing dx is defined in terms of the skin-depth δ , as

$$dx = \left[\frac{1}{2}\delta : \frac{1}{10}\delta \right].$$

The maximum resistivity error ranges from 70% for large elements to 30% for small elements, and it converges oscillating around $\epsilon_{\rho}^{max} \approx 40\%$ from $dx = \frac{1}{5}\delta$ to $dx = \frac{1}{10}\delta$ (Figure 4.1 top left plot). In the case of the phase (Figure 4.1 bottom left plot), maximum error ranges from 40% to 8%, and it converges to $\epsilon_{\phi}^{max} \approx 8\%$ from $dx = \frac{1}{7}\delta$ to finer elements. The maximum errors could represent outlier values of the solution on the surface of the model, i.e. there are few nodes on the surface that have the maximum error, and usually are located at the boundaries of the surface.

The average resistivity error (top right plot on Figure 4.1) ranges from 52% on coarse elements to 10% on fine elements. This error converges to $\epsilon_{\rho}^{avg} \approx 12\%$ from $dx = \frac{1}{7}\delta$ to smaller elements. Bottom right plot in Figure 4.1 shows the average error for ϕ . This error ranges from 30% on large elements to 5% on small elements, and it converges to $\epsilon_{\phi}^{avg} \approx 5\%$ from $dx = \frac{1}{7}\delta$ to $dx = \frac{1}{10}\delta$.

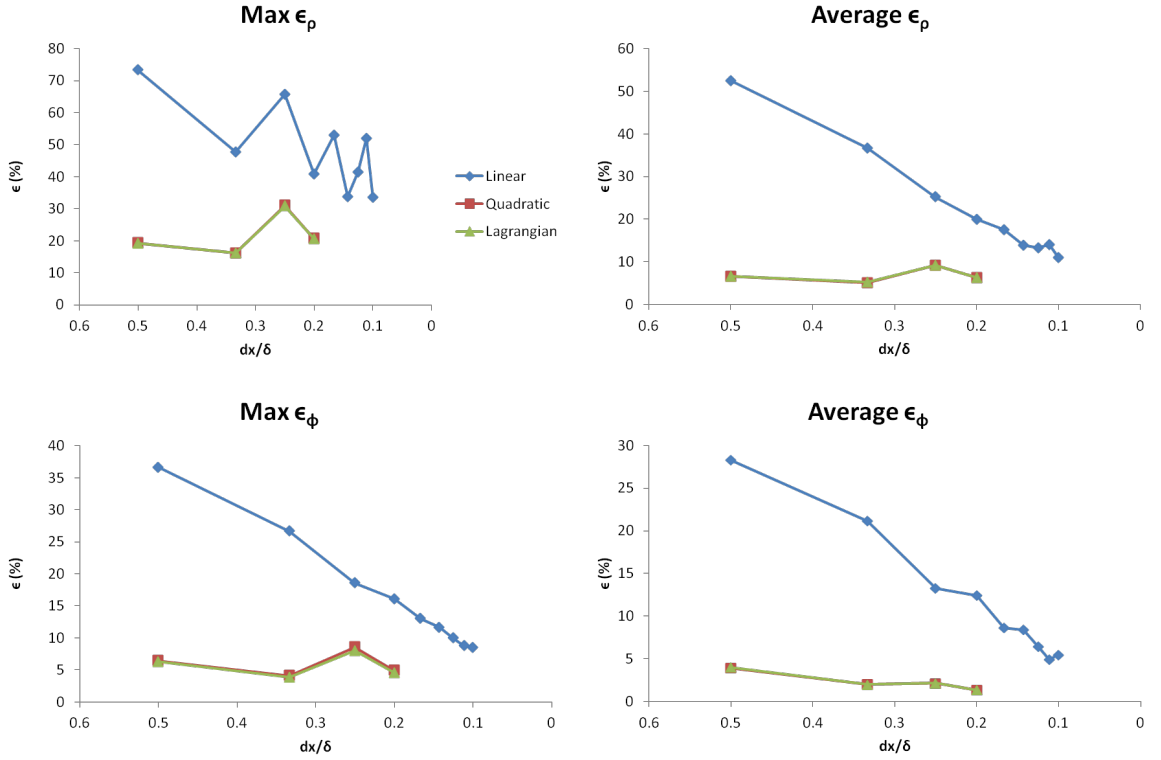


Figure 4.1: hp-Convergence plots for the Resistive Earth model. Top panels show the maximum error (left), and average error (right) for the resistivity. Bottom panels show the maximum error (left) and average error (right) for the phase. In these plots, the linear-order errors are the blue diamonds, quadratic-order are the red-squares, and Lagrangian-order are green triangles.

h-Convergence: Quadratic and Lagrangian Quadratic and Lagrangian elements have the same accuracy, this is shown in Figure 4.1. The interpretation of h-convergence is carried out for both cases together. For these elements, the spacing range is defined as

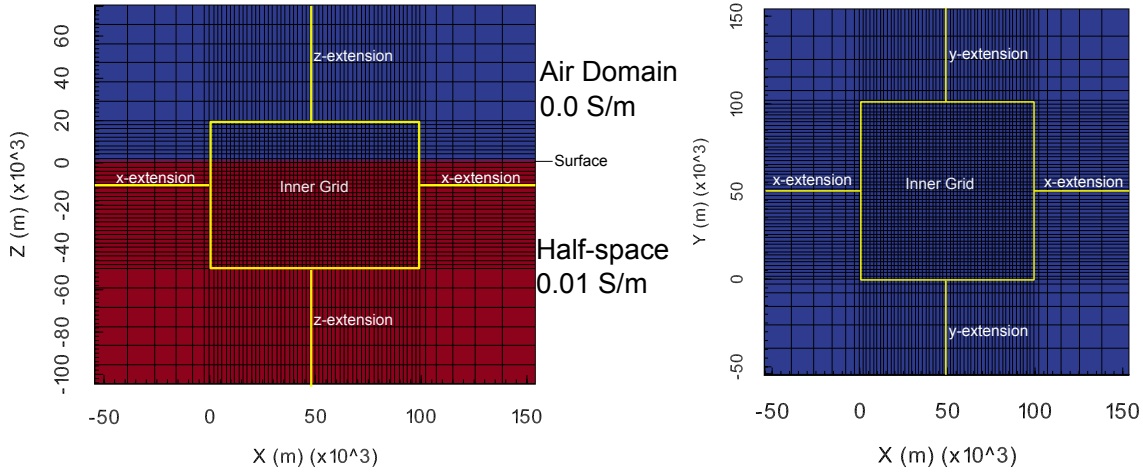
$$dx = \left[\frac{1}{2}\delta : \frac{1}{5}\delta \right].$$

The maximum resistivity error ranges from 30% to 16%, so it converges oscillating around $\epsilon_{\rho}^{max} \approx 25\%$. The maximum phase error ranges from 8% to 4%, and converges to $\epsilon_{\phi}^{max} \approx 5\%$ (Figure 4.1 bottom left plot). Average resistivity error ranges from 9% to 5%, and converges to $\epsilon_{\rho}^{avg} \approx 5.5\%$. The average phase error ranges from 4% for large elements, to 1% for small elements, and it converges to $\sim 1.5\%$.

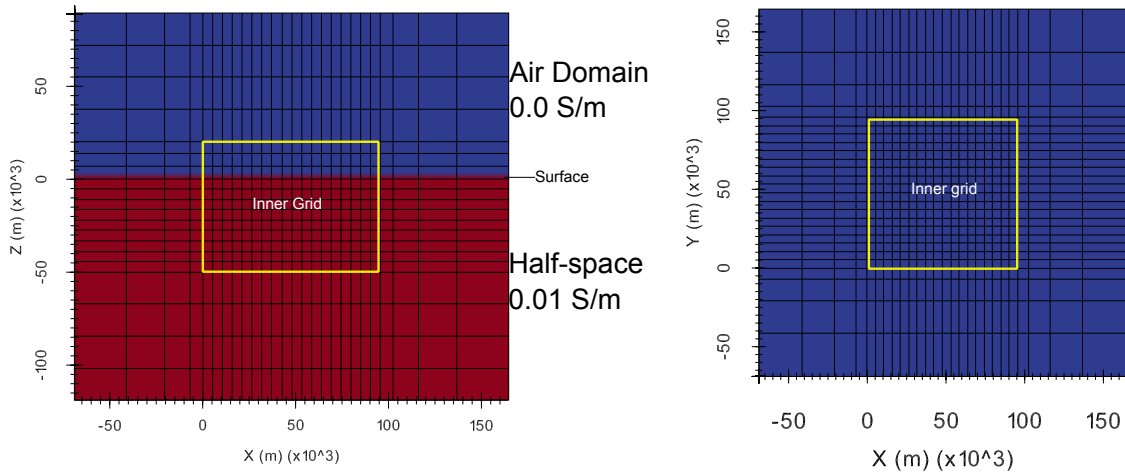
p-convergence The solution with high-order elements had already converged for the spacing range selected (Figure 4.1). Larger spacings were not carried out in order to be able to compare it with the spacings used for the linear elements, and because spacing larger than one skin-depth will not be realistic in real applications. The errors of high-order elements are smaller than those of the linear element for each spacing. Consequently, high-order elements reach a better solution using a coarse grid, than the solution obtained using fine grids with linear elements.

4.2.3 Model Discretization

From the convergence analysis, the optimal spacing to obtain small errors is selected as $dx = \frac{1}{8}\delta$ for the linear case, and $dx = \frac{1}{3}\delta$ for high-order elements. These spacings are selected to show the MT responses obtained from the MoVFEM program, for a frequency of 0.1 Hz. Figures 4.2a and 4.2b show the discretization of this Earth model using the spacings mentioned before.



(a) Discretization using linear elements.



(b) Discretization using quadratic and Lagrangian elements.

Figure 4.2: Domain discretization for the resistive half-space. Left panels: XZ-slice showing the air domain (blue) and half-space (red). YZ-slice shows the same discretization as this slice. Right panels show the XY-slice. Yellow rectangles enclose the inner grid and are surrounded by the extension zones.

Discretization with linear elements: The spacing $dx = 1990$ m is assigned for all directions, so that $dx = dy = dz$ (Figure 4.2a). The air height is 20 km because the model is extended several skin-depths in the air domain. As mentioned in Section 3.3, the extension zone has a thickness $\sim 3\delta$, in which case the extension zone is ~ 55 km. The computational domain dimensions are

$$\Omega = [-104327 : 103827] \times [-104327 : 103827] \times [0 : 178654] \text{ m},$$

and this domain has a total of $N_e = 62 \times 62 \times 47$ linear elements. The coordinates in Figure 4.2a are not the same as those for the computational domain, because these coordinates are scaled in order to be consistent with the input model in the visualization. However, MoVFEM works in the computational dimensions presented in this text.

Discretization with quadratic and Lagrangian elements: Figure 4.2b shows the discretization for high-order elements. In this case, the spacing is $dx = 5300$ m, and the same spacing is assigned to all directions. The air height is also 20 km, and the extension zone in all directions is of ~ 69 km. The extension zone is larger than in the linear case, because of the larger spacing used. The computational domain has a total of $N_e = 26 \times 26 \times 20$ elements, which is less than the elements used in the linear case, compare Figure 4.2b with Figure 4.2a. The computational domain in this case has dimensions of

$$\Omega = [-118900 : 114300] \times [-118900 : 114300] \times [0 : 207800] \text{ meters.}$$

4.2.4 Dirichlet Results

MT responses are analyzed for each element order, from the solution obtained using Dirichlet boundary conditions. Figure 4.3a shows the apparent resistivities (ρ_{xy}) of the three element orders, for the x -line ($y = 0$) of the receiver locations at the Earth's surface. Figure 4.3b shows the phase (ϕ_{xy}) on the same line of receiver locations.

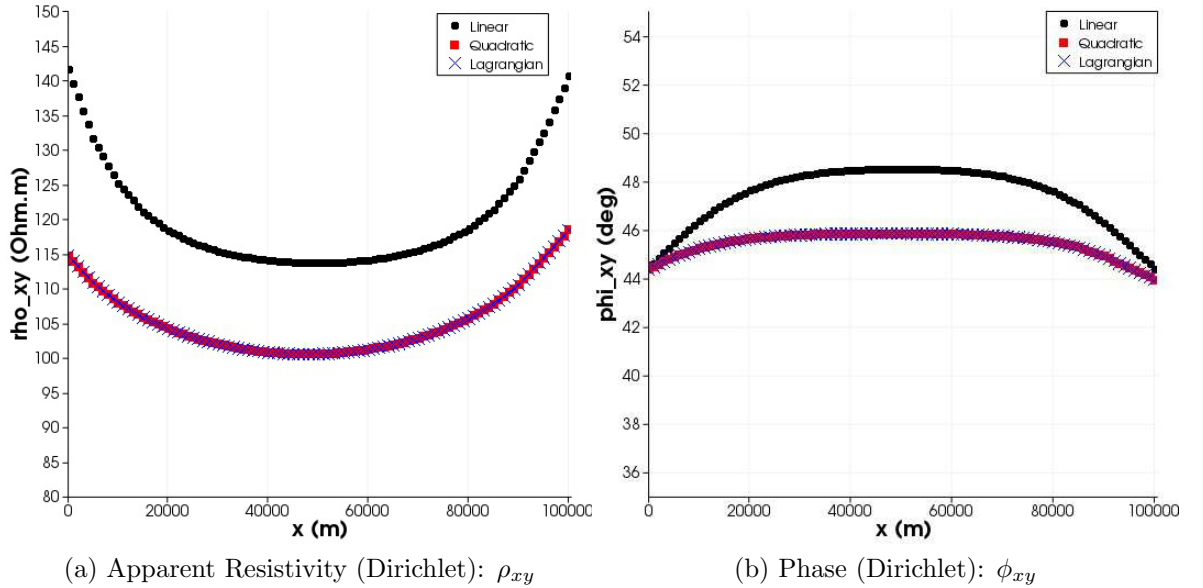


Figure 4.3: Apparent resistivity and phase obtained from solving the MT problem with Dirichlet boundary conditions, for three element orders. MT responses obtained using linear elements are plotted in black circle. Quadratic elements responses are plotted in red squares and Lagrangian elements in blue crosses. The apparent resistivity is plotted in linear scale.

These responses are shown for the x -polarization only, assuming that in the homogeneous (1D) case $\rho_{xy} = \rho_{yx}$. Table 4.1 shows the time and memory used by the MoVFEM program in this case, as well as the average errors on the Earth's surface.

Element	Linear	Quadratic	Lagrangian
Grid N_e	$62 \times 62 \times 47$	$26 \times 26 \times 20$	$26 \times 26 \times 20$
DoF	522831	152088	310896
NNZE	8644803	6060707	15370824
Assembly Time	177.93 s	385.06 s	759.74 s
Total Time	7851.57 s	1891.69 s	3436.97 s
ϵ_{ρ}^{avg}	13.35%	5.20%	5.20%
ϵ_{ϕ}^{avg}	6.44%	2.01%	1.99%

Table 4.1: Time and memory used in MoVFEM with Dirichlet boundary conditions. The memory is shown in terms of the number of elements (Grid), number of unknowns (DoF) and size of the symmetric sparse array in terms of the non-zero array (NNZE). Assembly time, and total time is shown in seconds. Average error percentages for the apparent resistivity and phase are obtained from the surface of the model.

Linear Using linear elements, the problem has 5.2×10^5 unknown edges, and the symmetric sparse array will have around 8.6 million non-zero entries. The assembly of global matrix from all the finite elements took 178 seconds, and the total time for the global matrix inversion and solution took around 8000 seconds \approx 133 min.

The apparent resistivity ranges from 115 Ωm in the center of the model domain, to 140 Ωm on the edges of the domain. This can be seen in Figure 4.3a, where the black cross values show the MT responses for the linear elements. These high resistivity values on the edge of the model domain are the effect of the Dirichlet boundary conditions, i.e. backwards reflections from the boundaries of the computational domain. For the x-polarization the electric field propagates parallel to the x direction, making these boundaries more resistive. Looking at the phase, the values range from $\approx 45^\circ$ on the edge of the domain, to $\sim 50^\circ$ in the center of the domain. This is also due to Dirichlet boundary conditions, and can be seen in Figure 4.3b where the black cross values show the MT phase for linear elements. From Table 4.1, the average resistivity error is 13.35% and the average phase error is 6.44% from the surface values.

Quadratic In this case, the problem is reduced to 1.5×10^5 unknown edges (Table 4.1). The sparse array contains around 6 millions non-zero entries, which is also reduced compared to the linear case. The time used for the assembly of the global array from all finite elements is 385 seconds, which is larger than the linear case because the assembly is done with more operations. However, the time used to invert the global matrix and obtain the solution is around 1900 seconds \approx 31 min, which is clearly less than the time used in the linear case, because the matrix to be inverted is smaller, i.e. less degrees of freedom.

Apparent resistivity values for the receiver line range from 102 Ωm in the center of the line, to around 115 Ωm at the end points of the line (red squares on Figure 4.3a). Although these values are more accurate than in the linear case, it still shows the effect of Dirichlet boundary conditions. On the other hand, the phase shows a more stable solution ranging from 45° at the boundaries to around 46° in the center of the line, but it still shows reflections from the boundaries of the computational domain (red squares in Figure 4.3b). The average resistivity error is reduced to 5.20%, and $\sim 2.0\%$ for the phase. Consequently, more accurate results are obtained using a coarser grid with quadratic elements.

Lagrangian By using Lagrangian elements, the degrees of freedom are increased to 3×10^5 from the quadratic case (Table 4.1). However, this number of unknowns are still less than the degrees freedom of the linear case. The number of non-zero entries on the sparse array is around 15 million, which is clearly larger than both linear and quadratic cases. In addition, the time spent on the assembly of global matrix is 760 seconds ≈ 13 min, which is almost double of the time on the quadratic case. This is because 54 edges must be calculated for each Lagrangian element, so the number of operations is increased from 36 edges used in quadratic elements. The total time used for the inversion and solution is 3437 seconds ≈ 57 min, which is more time than the quadratic case, but still less than the linear case.

Lagrangian elements obtain the same MT responses as quadratic elements, shown in Figures 4.3a and 4.3b. Also, the average error for resistivity and phase is the same (Table 4.1).

The previous results show that Dirichlet boundary conditions have an effect on the boundaries of the inner model. To understand this effect, Figures 4.4a and 4.4b show the apparent resistivities on the surface of the inner model for x -polarization and y -polarization, respectively. For the x -polarization, high resistivities are obtained at

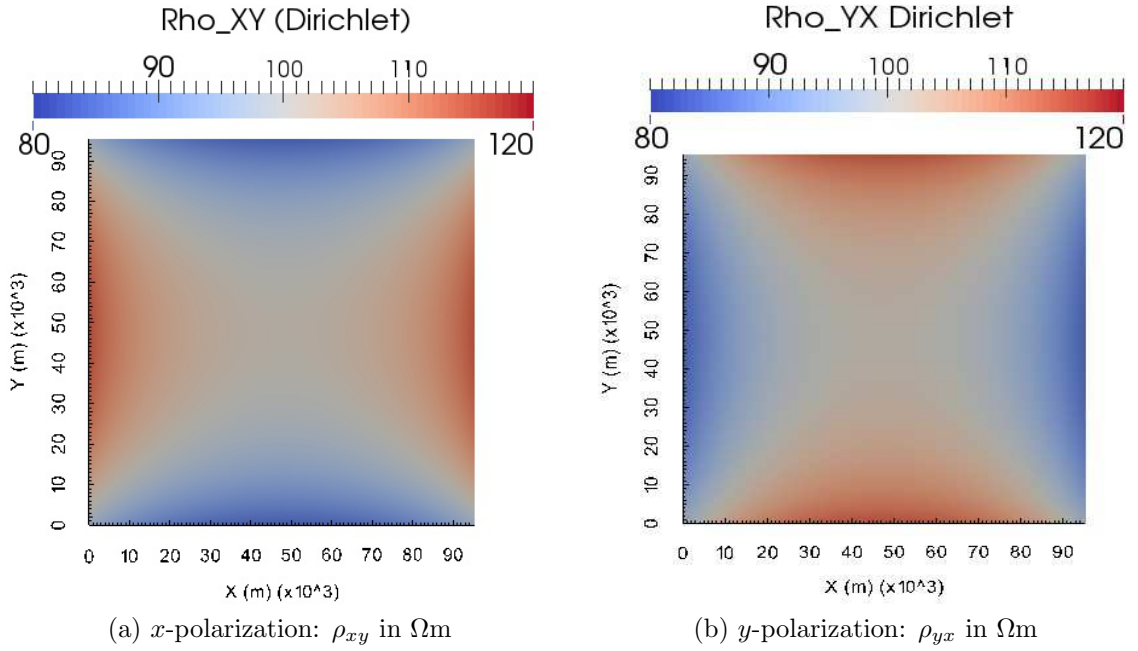


Figure 4.4: Surface plot of apparent resistivity on both polarizations, obtained from solving the MT problem with Dirichlet boundary conditions. The reflections of EM fields from the boundaries of the computational domain are shown at the boundaries of these surface plots.

x boundaries and lower resistivities are obtained at y boundaries, because the electric field propagates parallel to the x direction, so stronger reflections are obtained on these boundaries (Figure 4.4a). This behavior is also shown in Figure 4.3a.

On y -polarization, stronger reflections are obtained on y boundaries, because the electric field propagates parallel to y direction (Figure 4.4b). Therefore, the apparent resistivity plot for a y line of receivers ($x = 0$) will show the same behavior as the apparent resistivities and phase plots shown in Figure 4.3a.

4.2.5 GPML (Fang, 1996) Results

MT responses are shown for both GPML boundary conditions of this MoVFEM program. These are those of Fang (1996), and Zhou et al. (2012). In this section, GPML results from Fang (1996) formulation are presented. An analysis of stretching factor parameters (a_0 , b_0 and n) has not been made, these parameters are assigned as $a_0 = 1$, $b_0 = 1$, and $n = 2$. MT responses are shown in Figures 4.5a and 4.5b, for the x -line ($y = 0$) of the receiver locations on the Earth's surface. These responses are also

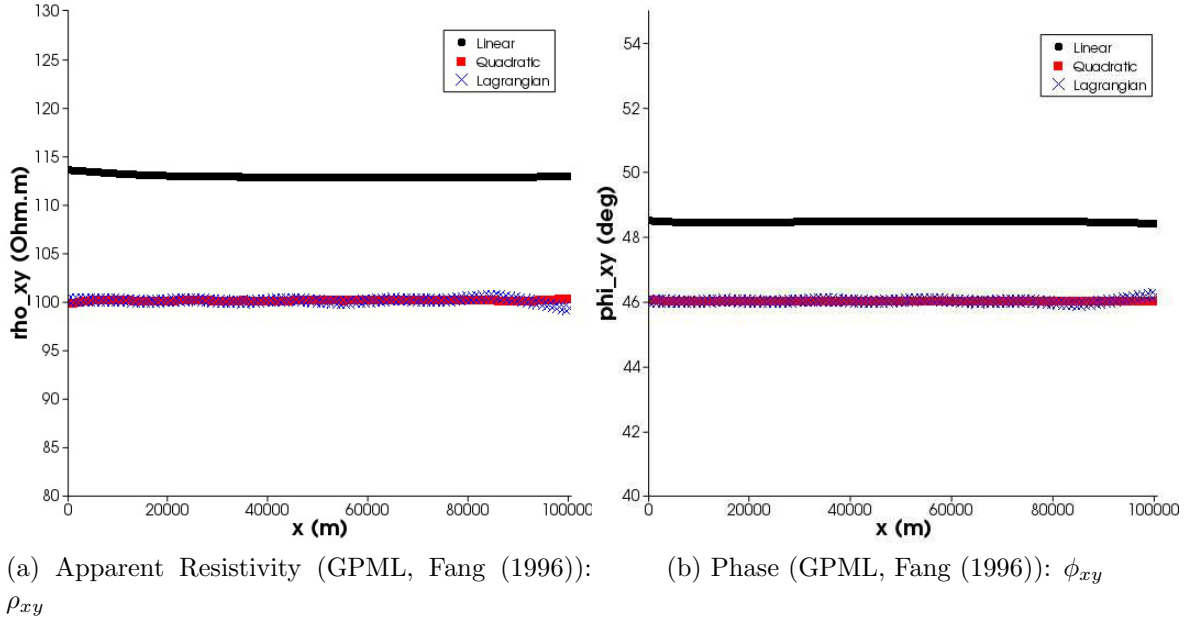


Figure 4.5: Apparent resistivity and phase obtained from solving the MT problem with GPML boundary conditions (Fang, 1996), for all elements order. Black circles in this plots show the MT responses obtained using linear elements. Red squares show the values from quadratic elements, and the values from Lagrangian elements are shown with blue crosses.

from the x -polarization, assuming that $\rho_{xy} = \rho_{yx}$ in the homogeneous case.

Table 4.2 shows the time and memory consumption by solving the model with this GPML boundary condition.

Element	Linear	Quadratic	Lagrangian
Grid N_e	$62 \times 62 \times 47$	$26 \times 26 \times 20$	$26 \times 26 \times 20$
DoF	561519	172680	338352
NNZE	9291615	6979448	17158968
Assembly Time	195.27 s	382.04 s	750.64 s
Total Time	9872.5 s	2104.37 s	3584.95 s
ϵ_{ρ}^{avg}	12.88%	0.23%	0.17%
ϵ_{ϕ}^{avg}	7.37%	2.21%	2.21%

Table 4.2: Time and memory used in MoVFEM with GPML boundary conditions (Fang, 1996). Times are shown in seconds, and the memory is presented in terms of the number of elements, the number of unknowns and the number of non-zero entries for the global array.

Linear By using GPML boundary conditions, the number of degrees of freedom is increased from solving the problem with Dirichlet conditions because the boundary edges are considered unknown in the MT problem, and GPML assumes that the edge values decrease gradually to zero in the PML zone. In this case, 5.6×10^5 unknowns have to be solved (Table 4.2). Consequently, the number of non-zero entries in the sparse array is 9 million. The time spent for the global matrix assembly is 195 seconds, and the matrix inversion and solution took 9872 seconds \approx 164 min.

The apparent resistivity becomes more stable than using Dirichlet boundary conditions, with a value of 115 Ωm (Figure 4.5a). Therefore, there are no backward reflections from the boundaries of the computational domain. The average resistivity error is 12.88% which is less than the error obtained from using Dirichlet boundary conditions. In the case of phase, it also shows a more stable solution, although the value is 48° (Figure 4.5b). The average phase error is 7.37%, which is larger than the error obtained with Dirichlet, compare Table 4.2 with Table 4.1.

The apparent resistivity and phase values are larger than the values of the homogeneous Earth model because of the use of linear-order polynomials with the stretching factor parameters assigned in GPML. An analysis of how these parameters improve the results has not been carried out.

Quadratic Using quadratic elements with GPML will lead to a problem with 1.7×10^5 unknown edges (Table 4.2) which is less than the linear case, because less elements are used. However, it contains more unknowns than solving the problem with Dirichlet boundaries, because boundary edges are unknown. Consequently, the sparse array has 6.9 million non-zero entries, which is less than the linear case. The assembly of the global matrix from finite elements takes 382 seconds. As expected, it takes more time to assemble the matrix because more operations are done when using quadratic elements. The solution of the problem takes around 2100 seconds \approx 35 min which is less than using linear elements (Table 4.2).

MT responses show more accurate results (shown in Figures 4.5a and 4.5b). The apparent resistivity converges to 100 Ωm , the resistivity of half-space. In addition, no boundary effect is present for this response. The average resistivity error is now 0.20%, which is less than the error obtained from Dirichlet boundaries. Therefore, GPML absorbs EM waves on the PML zone without any reflection from the boundaries of the computational domain. The phase converges to 46° , and no boundary effect is present. The average phase error is of 2.20% which is less than the error obtained from using linear elements (Table 4.2).

Lagrangian As expected, when using Lagrangian elements, the problem will have more unknowns than using quadratic elements (Table 4.2). In this case, 3.3×10^5 edge unknowns have to be solved, which again is less than for the linear case. The sparse array has 17 million non-zero entries. As shown with Dirichlet boundaries, this type of elements leads to a sparse array with more non-zero entries than both quadratic and linear elements. The global matrix is assembled after 750 seconds, and the solution is obtained after 3585 seconds \approx 1 hour. Although the sparse array is larger than the linear elements, the time to solve the problem is less, because less unknowns have to be calculated.

Figure 4.5a shows that Lagrangian elements have almost the same accuracy as

quadratic elements. The average resistivity error is 0.17%, which is slightly less than the error obtained from quadratic elements (Table 4.2). The same error is obtained for the phase in Figure 4.5b.

The effect of GPML boundary condition is shown in Figures 4.6a and 4.6b, where the behavior of x - and y -polarizations shown with Dirichlet boundaries are not present in this case. Consequently, the solution with GPML will present the homogeneous

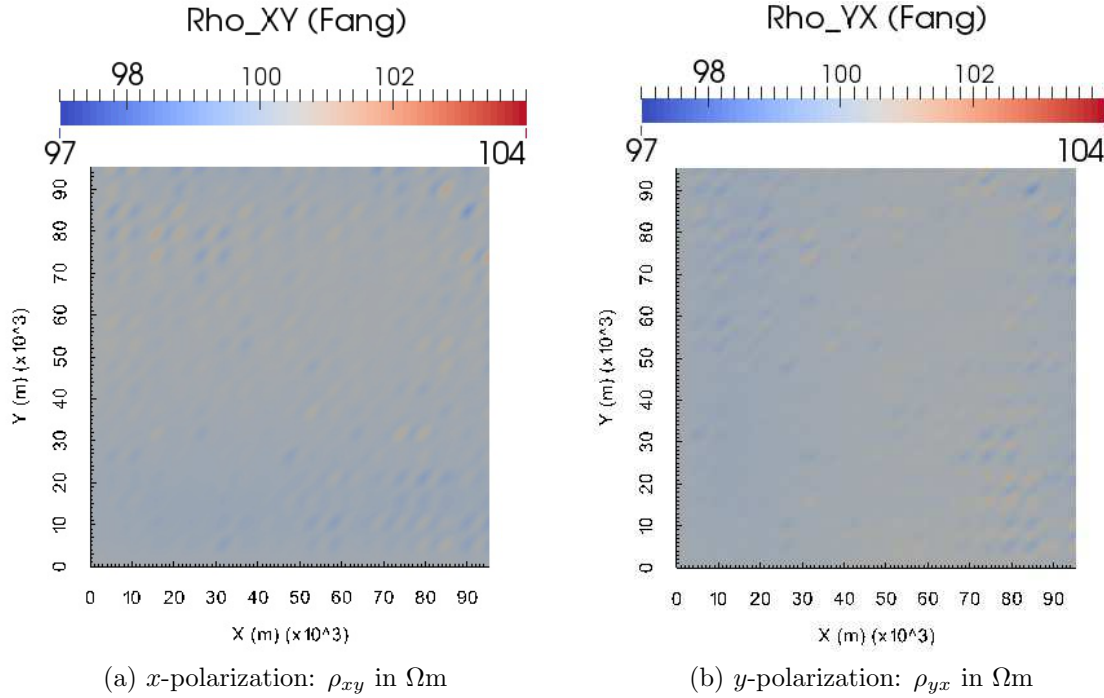


Figure 4.6: Surface plot of apparent resistivity of x and y polarizations, obtained from solving the MT problem with GPML boundary conditions (Fang, 1996). GPML ‘absorbs’ the EM fields at the boundaries, thus these plots do not show reflections from the boundaries of the computational domain, compared with Figures 4.4a and 4.4b.

model exactly as a 1D model, where $\rho_{xy} = \rho_{yx}$. The application of GPML (Fang, 1996) for either linear-order and high-order elements present MT responses that oscillate within a small range of error.

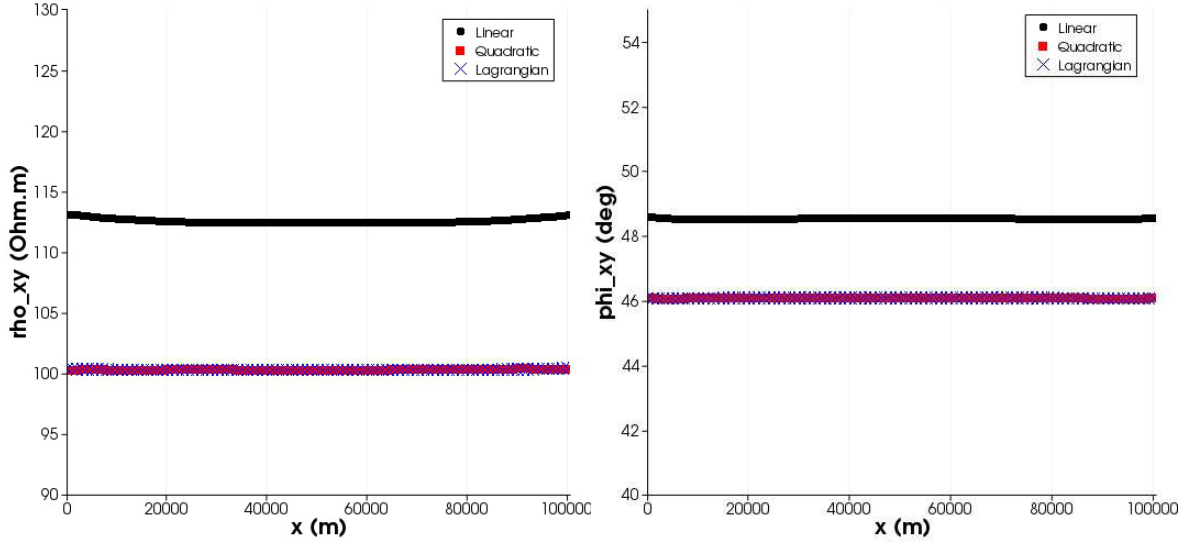
4.2.6 GPML (Zhou et al., 2012) Results

MT responses obtained from solving the MT problem with GPML boundary conditions from Zhou et al. (2012) are presented here. GPML parameters for the stretching factor are assigned as $a_{min} = 0$, $a_{max} = 100$, $b_{min} = 10^{-2}$, $b_{max} = 10^6$, and $n = 2$. MT responses (x -polarization) are shown in Figures 4.7a and 4.7b, for the x -line ($y = 0$) from the receiver locations on the Earth’s surface.

Table 4.3 shows the time and memory consumption by solving the model with this GPML boundary condition.

Linear The MT problem with this GPML boundary has the same degrees of freedom as the Fang (1996) formulation (Table 4.3, 4.2). There is also not much time difference between the solution of the problem compared to the Fang (1996) formulation.

Using linear elements with this GPML formulation, the apparent resistivity converges to $\sim 112 \Omega\text{m}$ (Figure 4.7a), which is slightly better than using the Fang (1996)



(a) Apparent Resistivity (GPML, Zhou et al. (2012)): ρ_{xy} (b) Phase (GPML, Zhou et al. (2012)): ϕ_{xy}

Figure 4.7: Apparent resistivity and phase obtained from solving the MT problem with GPML boundary conditions (Zhou et al., 2012), for all elements order. Black circles in this plots show the MT responses obtained using linear elements. Red squares show the values from quadratic elements, and the values from Lagrangian elements are shown with blue crosses.

Element	Linear	Quadratic	Lagrangian
Grid N_e	$62 \times 62 \times 47$	$26 \times 26 \times 20$	$26 \times 26 \times 20$
DoF	561519	172680	338352
NNZE	9291615	6979448	17158968
Assembly Time	184.55 s	389.12 s	770.37 s
Total Time	8046.82 s	2603.16 s	3877.8 s
ϵ_{ρ}^{avg}	12.77%	0.26%	0.22%
ϵ_{ϕ}^{avg}	3.29%	2.3%	2.3%

Table 4.3: Time and memory used in Multi-order VFEM with GPML boundary conditions (Zhou et al., 2012).

formulation. EM waves are absorbed in the PML zone, hence no boundary reflection is observed for the apparent resistivity along the x -line of receivers. The average surface error in this case is 12.77% (Table 4.3). The phase converges to 48.5° with this GPML formulation (Figure 4.7b). The average phase error is of 3.29%, which is less than the error obtained with previous boundary conditions. As with Fang (1996) formulation, the apparent resistivity and phase obtained with GPML are larger than the homogeneous Earth values.

Quadratic Using quadratic elements with this GPML formulation, the apparent resistivity also fluctuates around $100 \Omega\text{m}$ which is exactly the resistivity of the half-space (Figure 4.7a). The average resistivity error is 0.26% in this case. The phase fluctuates around 46° (Figure 4.7b), and the error is similar to that from Fang (1996) GPML formulation.

Lagrangian Figure 4.7a shows that the solution obtained with these elements is similar to that of the quadratic element solution. The average resistivity error is 0.22% which is a little higher than the error obtained with Fang (1996) GPML formulation. The phase shows a similar behavior to the results for the quadratic elements. In this case the average error is similar to the previous GPML formulation, and the same as with quadratic elements. In order to compare the behavior of this GPML formulation with that of Fang (1996), Figures 4.8a and 4.8b show the surface resistivity values for both polarizations. Comparing these surface plots with Figures 4.6a and 4.6b, it can be

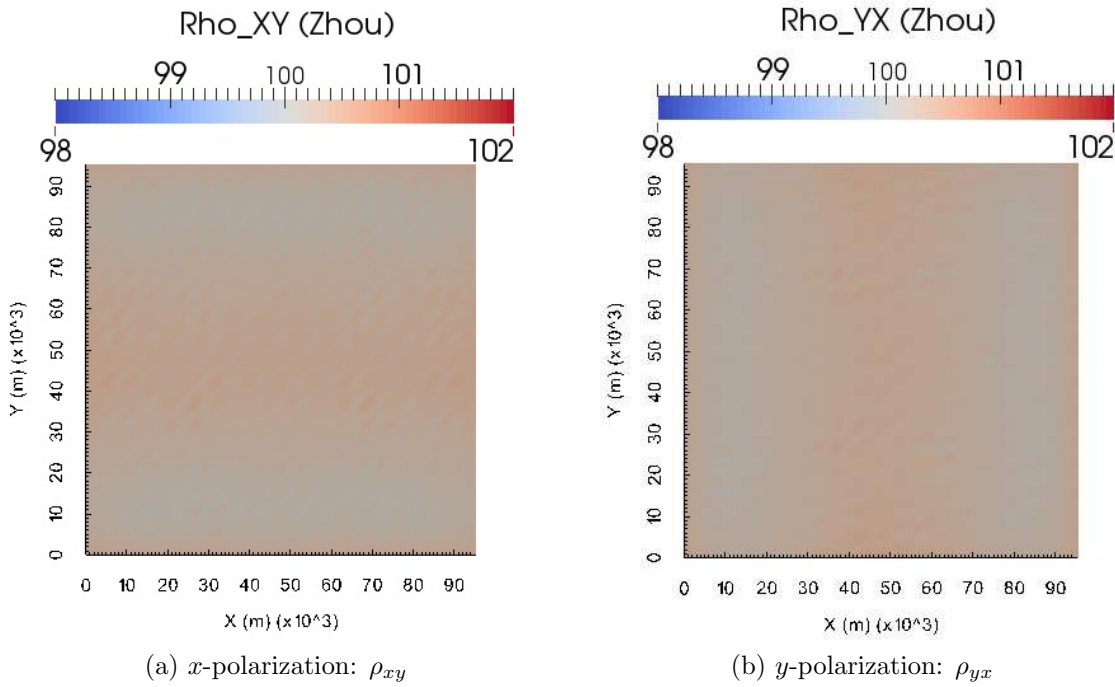


Figure 4.8: Surface plot of apparent resistivity on both polarizations, obtained from solving the MT problem with GPML boundary conditions (Zhou et al., 2012). The surface values do not show reflections from the boundaries of the computational domain, compared with the results obtained with Dirichlet conditions (Figures 4.4a and 4.4b).

seen that in general there is not much difference. The GPML formulation of Zhou et al. (2012) appears more stable than previous GPML formulation. The surface resistivity values using this GPML formulation range from $99.9 \Omega\text{m}$ to $101 \Omega\text{m}$. In comparison, these values range from $98.9 \Omega\text{m}$ to $101 \Omega\text{m}$ when using the formulation of Fang (1996).

4.2.7 Frequency Range Validation

In order to show the behavior of the solution for a frequency range, the resistive model is solved with 5 frequencies in the range from 10^{-2} Hz to 10^{-1} Hz. This bandwidth is selected because for the higher frequencies, the resistivity of $100 \Omega\text{m}$ will lead to a model with small elements, which takes more time and memory to solve. In this case, MT responses are plotted in order to compare the boundary conditions for each element order (Figures 4.9a to 4.11b). These MT responses are obtained from the receiver located at the center of the surface $(x, y) = (0, 0)$.

Linear For this case, the skin-depth ranges from 16 km to 50 km for the frequency range used. The air height is assigned as 10km because the boundary extension is

obtained from the maximum skin-depth. A spacing of 2300 meters is assigned, and the same spacing is used for all frequencies, in order to obtain a solution that can be adequate for the whole frequency range. Figures 4.9a, and 4.9b show the MT responses for the linear case.

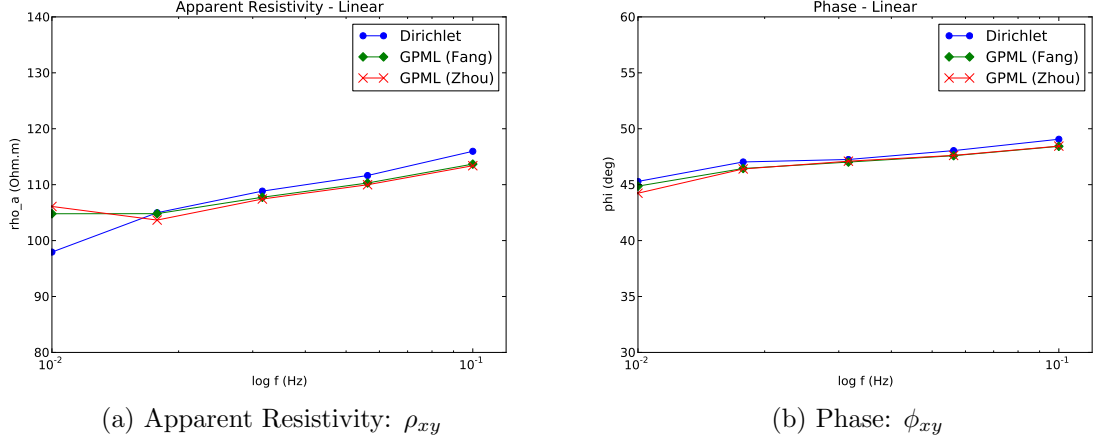


Figure 4.9: Apparent resistivity and phase obtained from solving the MT problem with linear elements for all boundary conditions.

The apparent resistivity obtained with Dirichlet boundaries ranges from $\sim 99 \Omega\text{m}$ for the lowest frequency to $\sim 120 \Omega\text{m}$ for the highest frequency (Figure 4.9a). With both GPML formulations, the apparent resistivities have a similar behavior, ranging from $\sim 105 \Omega\text{m}$ for 10^{-2} Hz to $\sim 117 \Omega\text{m}$ for 10^{-1} Hz. A similar phase behavior is obtained for all boundary conditions. The values range from around 45° for 10^{-2} Hz, up to 50° for 10^{-1} Hz (Figure 4.9b).

Quadratic The spacing used for quadratic elements is $dx = 10$ km. Figures 4.10a, and 4.10b show the MT responses for the quadratic case.

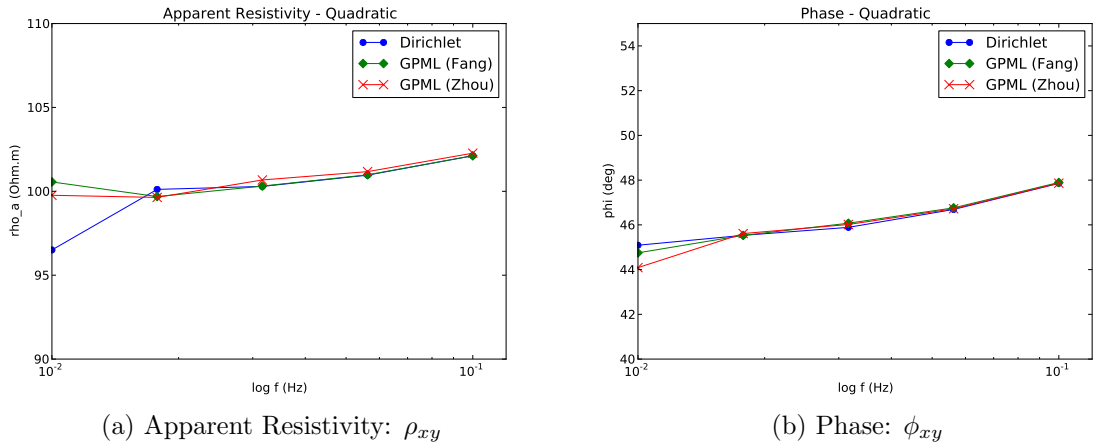


Figure 4.10: Apparent resistivity and phase obtained from solving the MT problem with quadratic elements for all boundary conditions.

Apparent resistivity values obtained from solving the problem with Dirichlet boundary conditions range $\sim 98 \Omega\text{m}$ for 10^{-2} Hz to around $101 \Omega\text{m}$ for the highest frequency (Figure 4.10a). The resistivity values obtained with GPML are more accurate and range from $100 \Omega\text{m}$ to $101 \Omega\text{m}$ for the frequency range of $[10^{-2}, 10^{-1}]$ Hz. The three boundary conditions produce results that converge to the same resistivity values for the higher frequencies, because the boundary reflections do not reach the central receiver on the Dirichlet case. The phase values are similar to the behavior obtained with linear elements for all boundary conditions (Figure 4.10b). These values range from $\sim 45^\circ$ to $\sim 48^\circ$ for the frequency range used.

Lagrangian The behavior and accuracy of MT responses using Lagrangian elements (Figures 4.11a, 4.11b) are very similar to the results obtained with quadratic elements (Figures 4.10a, 4.10b). For higher frequencies the results from all boundary conditions

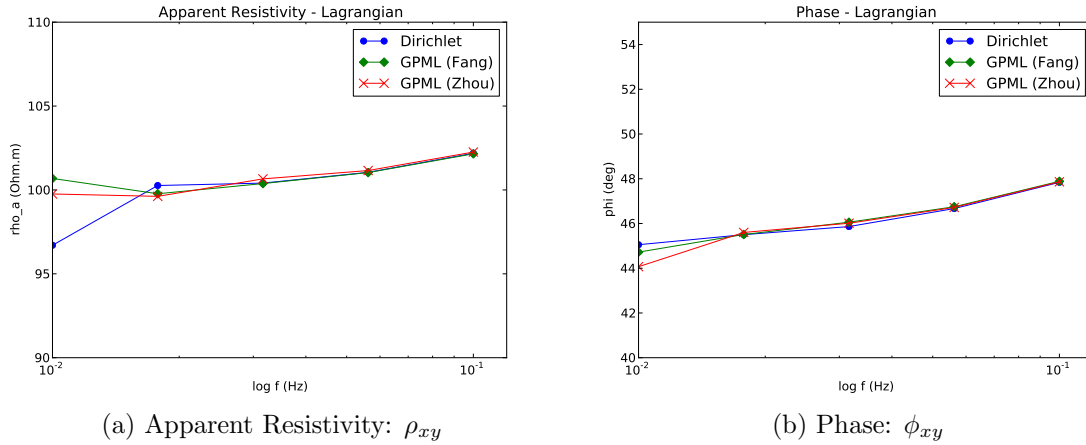


Figure 4.11: Apparent resistivity and phase obtained from solving the MT problem with Lagrangian elements for all boundary conditions.

converge to the same resistivity value of $\sim 101 \Omega\text{m}$ (Figure 4.11a). The phase ranges from $\sim 45^\circ$ for 10^{-2} Hz to $\sim 48^\circ$ for 10^{-1} Hz (Figure 4.11b).

4.3 Conductive Earth

4.3.1 Input Model and MT Problem

This model is presented to show how the dimension, discretization and results change for different conductivity values for the same frequency of 0.1 Hz. The conductive half-space has a conductivity of 5 S/m, thus the skin-depth is reduced to 712 m from the 16 km of the resistive Earth model, for $f = 0.1$ Hz. In consequence, the dimension of this Earth model is reduced to 1 km in x , y and z directions. The MT problem is solved for the electric field, using zero Dirichlet boundary conditions, and the air height is 700 m.

4.3.2 hp-Convergence Analysis

Because of the dimension of this model, it is computationally possible to compare same spacings for all element orders. The range of spacings in terms of skin-depths are

$$\left[\frac{1}{2}\delta : \frac{1}{8}\delta \right].$$

Figure 4.12 shows the convergence in term of relative errors percentage defined in equations (4.1) and (4.2).

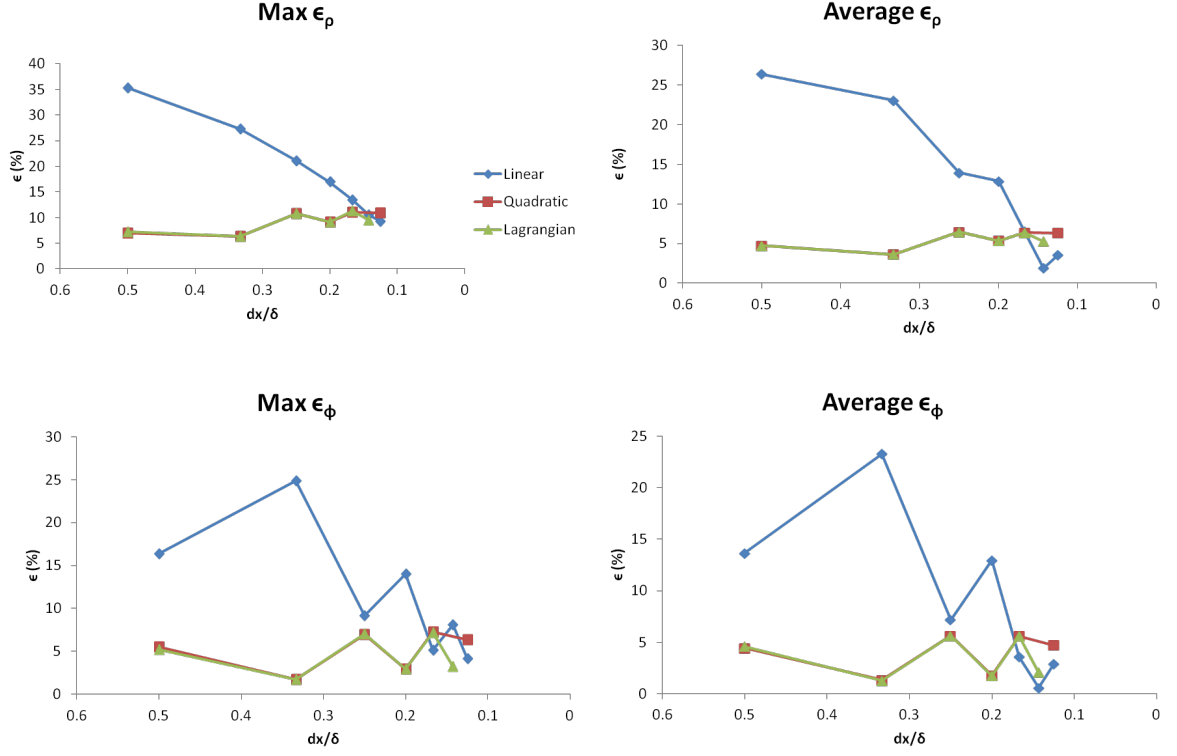


Figure 4.12: Convergence plots, in terms of relative errors, for the conductive half-space.

The convergence of this model behaves similar to the resistive half-space (Figure 4.12). Quadratic and Lagrangian elements produce MT responses with the same convergence and these responses had already converged for the spacing range used. The MT responses obtained with high-order elements converge to a maximum error of 10% for the resistivity and $\sim 5\%$ for the phase. The average errors for high-order elements converge to $\sim 4\%$ for the resistivity, and $\sim 1\%$ for the phase.

The linear case shows a convergence similar to high-order elements when the spacing is $\geq \frac{1}{6}\delta$. In this case, maximum error converges to around 15% for the resistivity and 10% for the phase, and the average error converges to 5% for the resistivity and 3% for the phase.

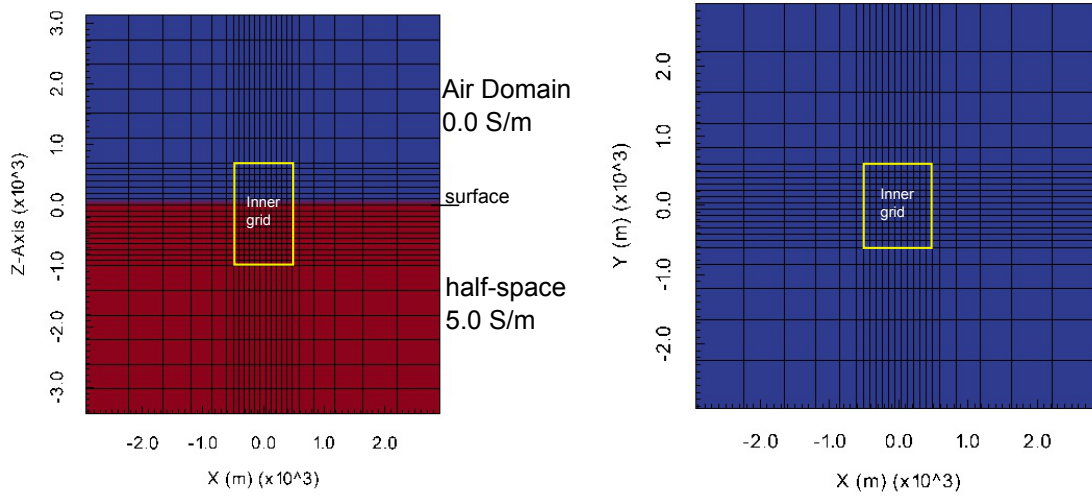
4.3.3 Model Discretization

The same spacing as with the resistive model is chosen for this model, i.e. $\frac{1}{8}\delta$ for linear elements and $\frac{1}{3}\delta$ for high-order elements. Figures 4.13a and 4.13b show the discretized grids with these spacings.

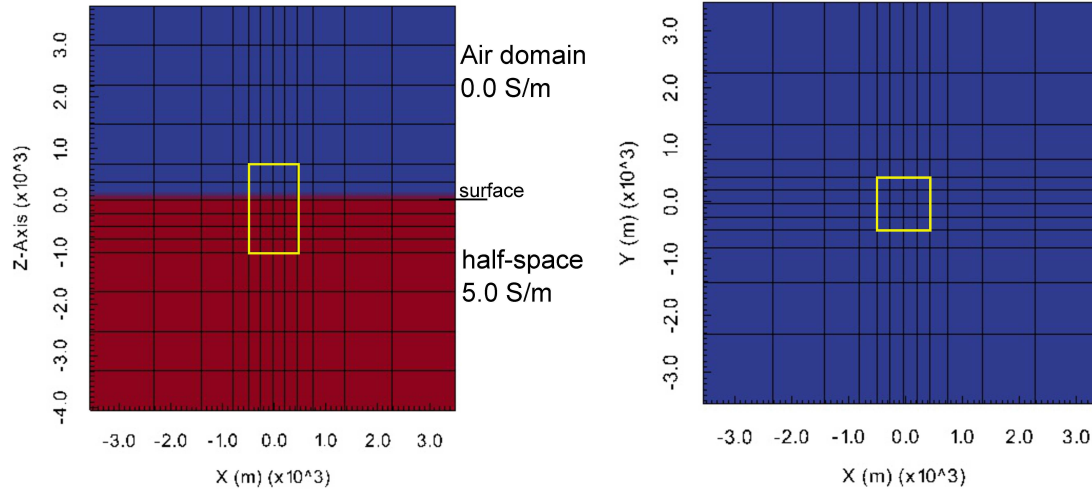
The spacing is 89 meters in all directions, and the extension zone is 2430 meters for linear elements. The computational domain contains $N_e = 23 \times 23 \times 30$ elements, and its dimension is

$$\Omega = [-2929.7 : 2908.7] \times [-2929.7 : 2908.7] \times [0 : 6559.4] \text{ m.}$$

The spacing assigned for high-order elements is 235 m in all directions with an extension zone of 3055 m. The computational domain contains $N_e = 12 \times 12 \times 14$ elements, and



(a) Discretization using linear elements.



(b) Discretization using quadratic and Lagrangian elements.

Figure 4.13: Computational grid for the conductive model. Left panels: XZ-slice showing the air domain (blue) and half-space (red). Right panels: XY-slice. Yellow rectangles enclose the inner grid and is surrounded by the extension zones.

has the following dimensions

$$\Omega = [-3555 : 3495] \times [-3555 : 3495] \times [0 : 7810]\text{m}.$$

4.3.4 Dirichlet Results

Figures 4.14a and 4.14b show MT responses from solving the MT problem with Dirichlet boundaries. In this Figure, the MT responses are taken from the x -line ($y = 0$) of the surface values of this model. Table 4.4 shows the time and memory usage for all element orders in this case.

Same boundary effect is shown for the MT responses, i.e. backwards reflections from boundaries of the computational domain (Figures 4.14a, 4.14b). The errors are smaller than in the resistive model because for the dimensions of this model MoVFEM is more accurate (Table 4.4). As with the resistive model, MoVFEM with linear elements ob-

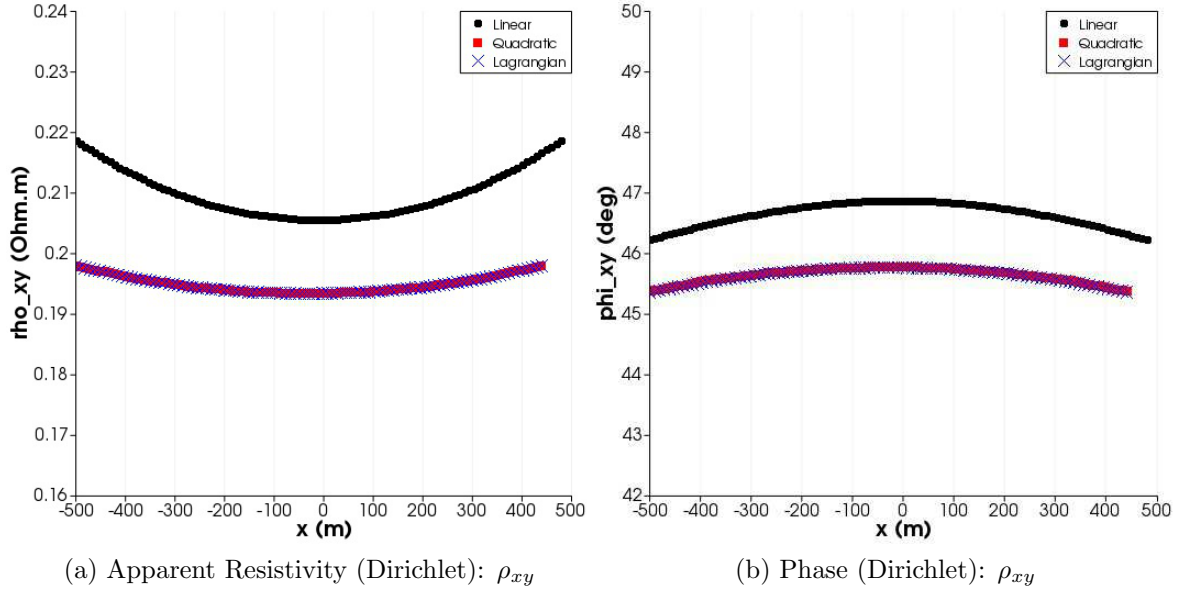


Figure 4.14: Apparent resistivity and phase obtained from solving the MT problem with Dirichlet boundary conditions, for all elements order in the conductive half-space

Element	Linear	Quadratic	Lagrangian
Grid N_e	$23 \times 23 \times 30$	$12 \times 12 \times 14$	$12 \times 12 \times 14$
DoF	43868	21388	44620
NNZE	699710	802538	2087202
Assembly Time	16.33 s	60.22 s	120.17 s
Total Time	1215.25 s	386.79 s	386.38 s
ϵ_{ρ}^{avg}	3.52%	3.62%	3.64%
ϵ_{ϕ}^{avg}	2.87%	1.32%	1.26%

Table 4.4: Time and memory used in MoVFEM with Dirichlet boundary. Assembly time, and total time are shown in seconds. The memory is shown in terms of the number of elements, the number of unknowns (DoF) and size of the symmetric sparse array (NNZE). Average error percentage of apparent resistivity and phase are obtained from the surface of the model.

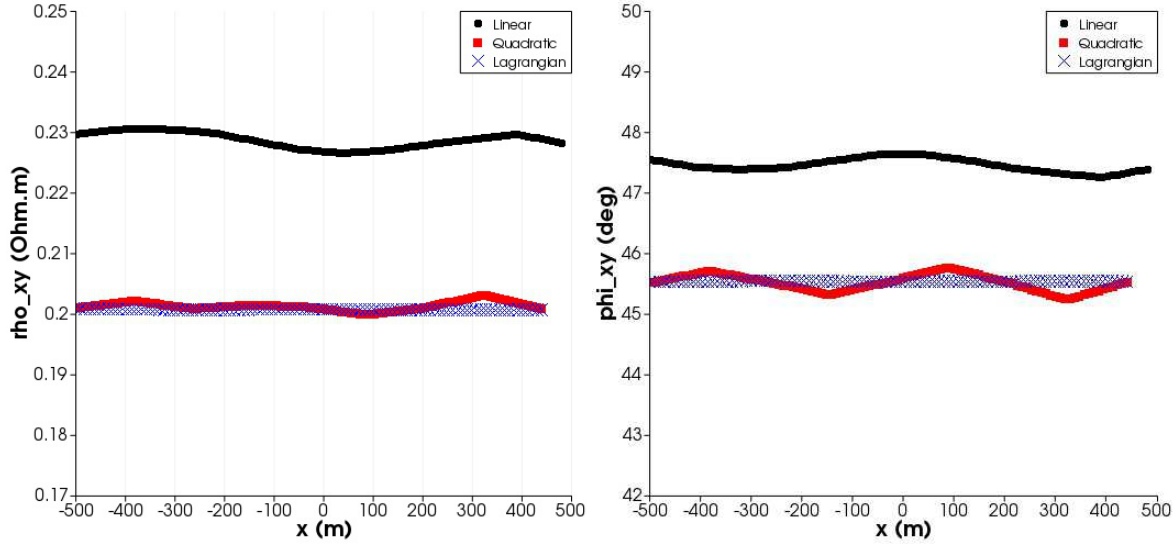
tains larger MT responses than high-order elements. In this case $\rho_a \in [0.20 : 0.22] \Omega\text{m}$, and $\phi \in [46^\circ : 48^\circ]$ with average errors of 3.52%, and 2.87% for the resistivity and phase, respectively.

MoVFEM with high-order elements produces more accurate responses. For both quadratic and Lagrangian elements $\rho_a \in [0.19 : 0.20] \Omega\text{m}$, and $\phi \in [45^\circ : 46^\circ]$ with average errors of $\sim 3.6\%$, and $\sim 1.3\%$ for the resistivity and phase, respectively.

4.3.5 GPML (Fang, 1996) Results

Figures 4.15a and 4.15b show MT responses from solving the MT problem with GPML boundary condition (Fang, 1996). These plots illustrate the surface values of the x -line ($y = 0$) locations. Table 4.5 shows the time and memory usage for all element orders in this case.

The resistivities obtained with linear elements oscillate more around $0.23 \Omega\text{m}$, but the boundaries reflections are absorbed in the PML zone. The same behavior as in the resistive model is shown in Figures 4.15a and 4.15b, i.e. the resistivity and phase



(a) Apparent Resistivity (GPML, Fang (1996)):
 ρ_{xy}

(b) Phase (GPML, Fang (1996)): ϕ_{xy}

Figure 4.15: Apparent resistivity and phase obtained from solving the MT problem with GPML boundary conditions (Fang, 1996), for all elements order with the conductive model.

Element	Linear	Quadratic	Lagrangian
Grid N_e	$23 \times 23 \times 30$	$12 \times 12 \times 14$	$12 \times 12 \times 14$
DoF	51504	27148	52300
NNZE	824718	1051766	2574834
Assembly Time	16.11 s	58.77 s	112.02 s
Total Time	506.56 s	137.15 s	263.3 s
ϵ_{ρ}^{avg}	14.65%	0.71%	0.49%
ϵ_{ϕ}^{avg}	5.56%	1.25%	1.18%

Table 4.5: Time and memory used in Multi-order VFEM with GPML boundary (Fang, 1996) on the conductive model.

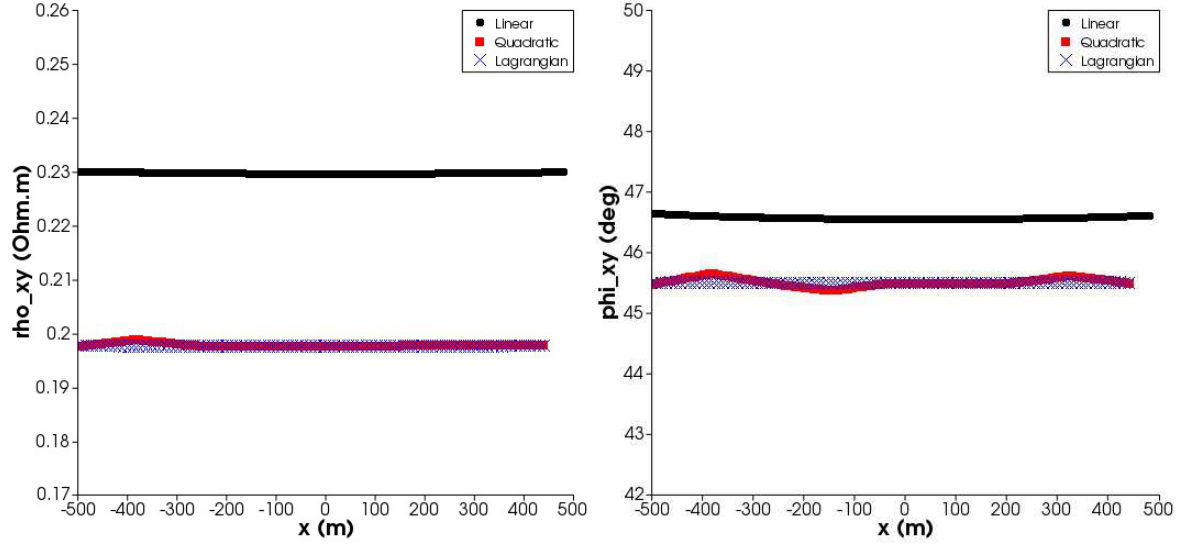
values are higher for linear elements than for high-order elements.

The solution becomes more stable with the use of Lagrangian elements, which have the lowest errors for resistivity and phase (Table 4.5). The solution using high-order elements oscillates around $0.20 \Omega\text{m}$ and the phase oscillates around 45° which are the values of the conductive Earth. This can be seen in the MT plots where MT responses with quadratic elements seem to oscillate more than with Lagrangian elements (Figures 4.15a, 4.15b).

The time used by MoVFEM in this model is less than the time used for the resistive Earth model (Tables 4.2, 4.5). This is because the dimension of this model is smaller than the resistive model, thus less elements are computed. Similar to the resistive model, the assembly time is larger for high-order elements than for linear elements, and the total time is small for the quadratic case compared to the linear and Lagrangian cases. The oscillations of MT responses obtained by applying GPML (Fang, 1996) is clearly shown for all element orders in the conductive Earth.

4.3.6 GPML (Zhou et al., 2012) Results

Figures 4.16a and 4.16b show MT responses from solving the MT problem with GPML boundary condition (Zhou et al., 2012). The MT responses are on from the x -line ($y = 0$) of the surface values in this model.



(a) Apparent Resistivity (GPML, Zhou et al. (2012)): ρ_{xy}

(b) Phase (GPML, Zhou et al. (2012)): ϕ_{xy}

Figure 4.16: Apparent resistivity and phase obtained from solving the MT problem with GPML boundary conditions (Zhou et al., 2012), for all elements order with the conductive model.

Table 4.6 shows the time and memory usage for all element orders in this case.

Element	Linear	Quadratic	Lagrangian
Grid N_e	$23 \times 23 \times 30$	$12 \times 12 \times 14$	$12 \times 12 \times 14$
DoF	51504	27148	52300
NNZE	824718	1051766	2574834
Assembly Time	15.63 s	57.97 s	111.13 s
Total Time	216.07 s	178.18 s	282.70 s
ϵ_{ρ}^{avg}	15.49%	0.99%	1.01%
ϵ_{ϕ}^{avg}	3.55%	1.13%	1.06%

Table 4.6: Time and memory used in Multi-order VFEM with GPML boundary (Zhou et al., 2012).

Solving the MT problem with Zhou et al. (2012) GPML formulation stabilizes the MT responses for the linear case compared to Fang (1996) formulation (Figures 4.16a, 4.16b). The solution becomes more stable for Lagrangian elements than for quadratic elements. In Figures 4.16a, and 4.16b, the solutions with this GPML formulation seem to be more stable than using Fang (1996) formulation, though the error in this case is somewhat higher ($\sim 1\%$ for both ρ_a , and ϕ) (Table 4.6).

4.3.7 Frequency Range Validation

Because of the dimension of the conductive model, a bandwidth containing high frequencies $[0.1, 1]$ Hz is selected, and 5 frequencies within this range are obtained with

equal spacing. In this case the spacings for linear elements are 40 m for all directions, with quadratic elements the spacing is 85 m, and with Lagrangian elements the spacing is increased to 100 m in all directions.

Figures 4.17a and 4.17b show the MT responses for the linear case.

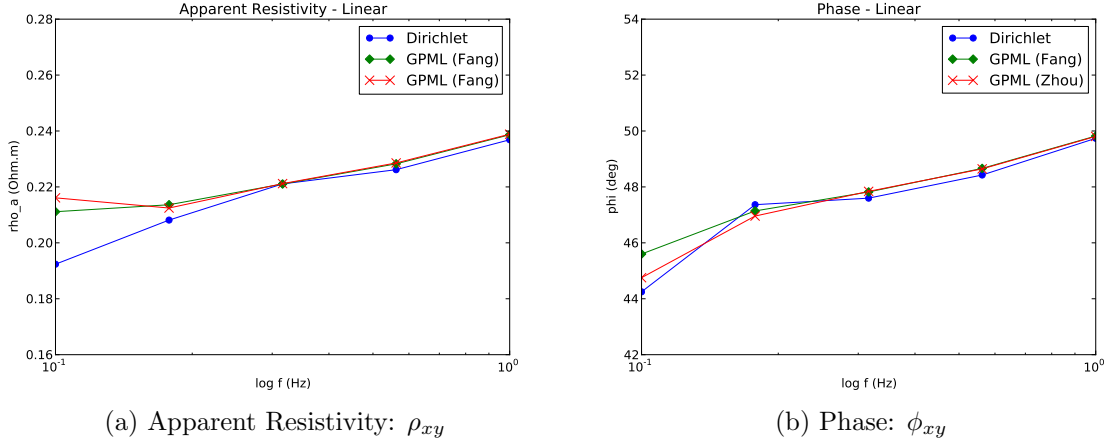


Figure 4.17: Apparent resistivity and phase obtained from solving the MT problem with linear elements for all boundary conditions with the conductive model.

MoVFEM with this conductive model behave similar to the resistive case. The apparent resistivity obtained by using Dirichlet boundary conditions increases from $\sim 19 \Omega\text{m}$ for 0.1 Hz to $\sim 24 \Omega\text{m}$ for 1 Hz. The phase increases from $\sim 45^\circ$ for the lowest frequency to $\sim 50^\circ$ for the highest frequency. Both GPML boundary conditions produces resistivities that range from $\sim 0.22 \Omega\text{m}$ to $\sim 0.24 \Omega\text{m}$ for the frequency range used. The phase values range from $\sim 45^\circ$ to $\sim 50^\circ$, for 0.1 Hz and 1 Hz, respectively. This is also because the values plotted are from the central node on the surface, where no boundary effect is expected for the problem with Dirichlet boundaries.

Figures 4.18a and 4.18b show the MT responses for the quadratic case.

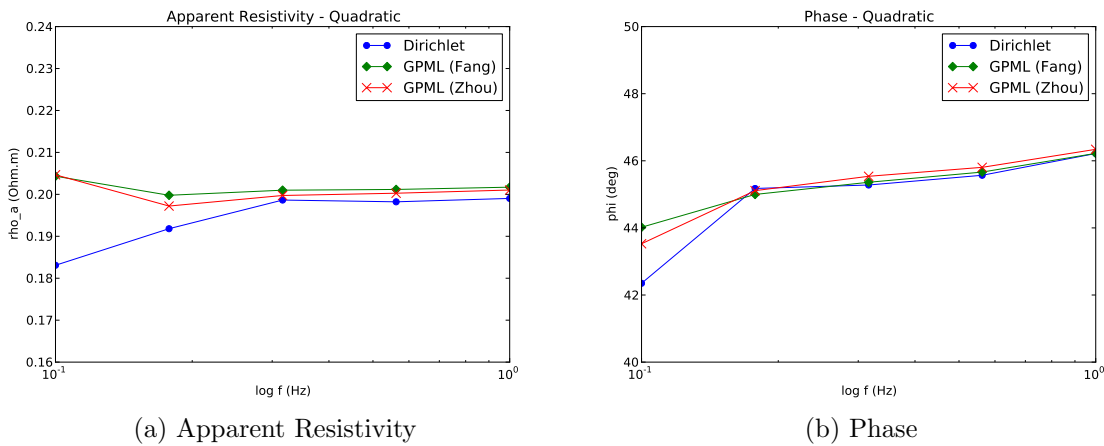


Figure 4.18: Apparent resistivity and phase obtained from solving the MT problem with quadratic elements for all boundary conditions with the conductive model.

In this case the resistivities stabilize more to the real resistivity of the half-space

for all the frequencies, except the Dirichlet solution for 0.1 Hz. The phase curve also becomes more stable, ranging in this case from 43° to 46° .

MT responses obtained with Lagrangian elements are shown in Figures 4.19a and 4.19b.

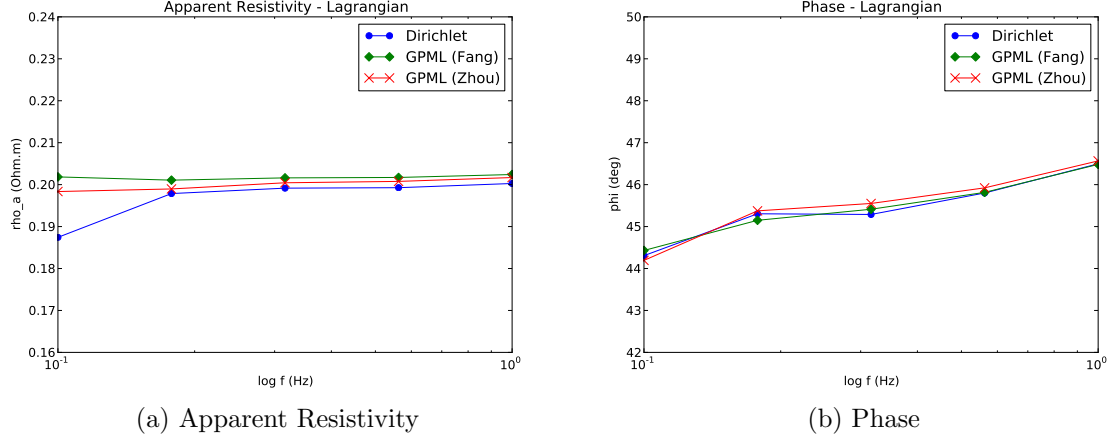


Figure 4.19: Apparent resistivity and phase obtained from solving the MT problem with Lagrangian elements for all boundary conditions with the conductive model.

Using Lagrangian elements with the GPML formulation of Zhou et al. (2012) shows that the resistivities are more accurate and stable than other elements and other boundary conditions. In this case, the resistivity is around $0.20\Omega\text{m}$ for all frequencies. The phase has a similar behavior to the quadratic solution, and ranges from less than 45° to around 46° for the frequency range used.

Zhou et al. (2012) modified the GPML formulation for the MT and CSEM problem, and it obtains better solutions for both resistive (low frequency) and conductive (high frequency) models.

4.4 General Remarks

The skin-depth is inversely proportional to both conductivity and frequency, thus conductive models have smaller skin-depth than resistive models. In consequence, the discretization and dimensions is reduced from the resistive model to conductive models for the same frequency.

High-order edge-elements contain small errors for larger element sizes than linear-order edge-elements. Hence, less elements are used with high-order elements, and the CPU time to obtain the solutions is less than with linear-order elements. However, the assembly time is increased because the number of operations applied in the integration of each element increases for high-order elements. The number of operations in the element integration is $m_e \times m_e \times n_g^3$; for linear elements there are $12 \times 12 \times 8 = 1152$ calculations, for quadratic elements there are $36 \times 36 \times 27 = 34992$ calculations, and for Lagrangian elements there are $54 \times 54 \times 27 = 78732$ calculations.

Dirichlet boundary conditions shows reflections from the boundaries of the computational domain to the boundaries of the inner model (the model without extension zones). This is shown with high resistivity values on the boundaries related to the field polarization.

The application of GPML boundary conditions of Fang (1996) presents MT responses that oscillate within a small range of error. On the other hand, GPML boundary conditions of Zhou et al. (2012), using quadratic and Lagrangian elements, stabilize more the solution to the analytic solution. Linear elements with GPML show higher values of MT responses than the analytic solution, because of the error inherent in linear polynomials and the selection of GPML parameters.

Chapter 5

Applications: Complex Models

5.1 Introduction

The aim of this chapter is to test MoVFEM with established synthetic examples to obtain the forward modeling response for models with complex conductivity structures and geometries, including anisotropy. A discussion of the results obtained is presented in order to describe how the MoVFEM algorithm behaves with each input model.

The first two models are part of the COMMEMI project introduced by Zhdanov et al. (1997) for comparing EM forward modeling responses between international researchers. These models are named 3D-1A and 3D-2 in the COMMEMI project, and the forward modeling results obtained by MoVFEM are compared with the results presented by Zhdanov et al. (1997). Unfortunately, the COMMEMI report does not contain the phase data; thus, the MT responses obtained by MoVFEM with model 3D-1A are also compared with the results of FEM obtained by Mitsuhashi & Uchida (2004). In addition, the modeled responses from the 3D-2 are compared with the results of FD modeling obtained by Mackie et al. (1993).

Topographic effects are investigated by using a homogeneous Earth model including a 2D surface hill, as modeled by Wannamaker et al. (1986) and Nam et al. (2007). The results of MoVFEM are compared with the result of linear-VFEM modeling presented by Nam et al. (2007).

Anisotropic effects are tested with a homogeneous and anisotropic model. The conductivity tensor has only diagonal components to understand the MT responses for a transverse anisotropic model.

Finally, a layered model with topography and subsurface interfaces is modeled firstly with three isotropic layers, and secondly with three layers where the first one is anisotropic.

The results of MoVFEM are chosen from the tests executed for each synthetic example with different frequencies. Hence, different edge-elements orders, and different boundary conditions are applied to each synthetic examples. The results of MoVFEM are shown for the frequency used in previous publications. For models that have not been published, the results of MoVFEM are shown for the frequency related to the skin-depth and dimensions of the input model structures.

The tests carried out were run in parallel with 4 CPUs AMD 6238 of 2.6 GHz on Tizard computer from eResearch, SA (Coddington, 2013). MoVFEM runs the assembly sequentially, thus the parallelization is applied with MUMPS.

5.2 COMMEMI 3D-1A

This model consists of a conductive block ($0.5 \Omega\text{m}$) embedded in a resistive ($100 \Omega\text{m}$) homogeneous background (Figure 5.1). The conductor is of $1 \times 2 \times 2 \text{ km}$, and is 250 m below the surface, and the total dimensions of this input model are $4 \times 4 \times 2.5 \text{ km}$.

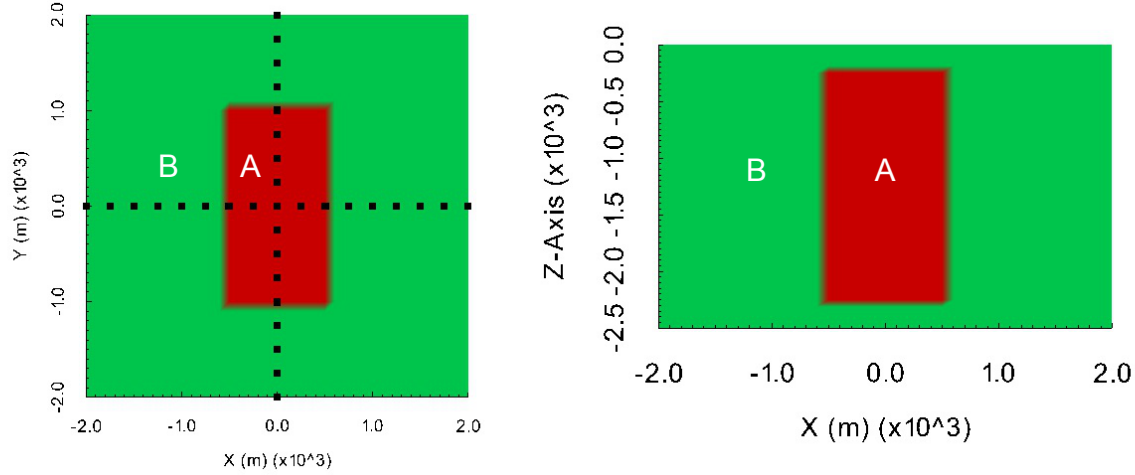


Figure 5.1: Input of COMMEMI 3D-1A model. Left panel shows a xy -slice of this input model, where black squares are the locations of receivers. Right panel shows a xz -slice of this model. Conductive block (A) has a resistivity of $0.5 \Omega\text{m}$, and the resistive background (B) is $100 \Omega\text{m}$.

A model was computed at a frequency of 10 Hz , where the skin-depth ranges from 112 m (for the conductive block) to 1.6 km (for the resistive background). The depth of the input model was increased by 1.5 km , and the air height was 1.5 km , thus the input model (Figure 5.1) is extended vertically from 2.5 km to 5.5 km . The spacing of the model grid is $dx = dy = 200 \text{ m}$, and $dz = 100 \text{ m}$.

Dirichlet boundary conditions were applied, where the boundaries were considered as a homogeneous Earth with a resistivity of $100 \Omega\text{m}$. This inner model is extended 11.7 km in x and y directions, and 5.85 km in the z direction. Consequently, the computational domain for this model is $x = y = [-13.7 : 13.7] \text{ km}$, and $z = [0 : 15.7] \text{ km}$. Quadratic elements were used in this test, and the computational domain contained $38 \times 38 \times 58$ elements. Figure 5.2 shows this computational grid, where the inner model discretization is enclosed by the yellow rectangle. MoVFEM works with a computational grid in which the z coordinates start from zero at the bottom of the subsurface, to z_{max} on top of the air domain.

This problem contains $970180 \approx 10^6$ unknown edges, thus the assembled matrix has a size of $\sim 10^6 \times 10^6$. The assembled matrix contained only $39818017 \approx 4 \times 10^7$ non-zero entries, which is around 0.004% of the global matrix. The assembly process finished in $2852 \text{ s} \approx 47 \text{ min}$. The inversion of the assembled matrix and solutions were obtained in $5982 \text{ s} \approx 99 \text{ min}$. Farquharson & Miensoopust (2011) applied a VFEM algorithm with $70 \times 70 \times 39$ elements; the total CPU time for the VFEM assembly with divergence correction was $\sim 120 \text{ min}$, and the time to obtain the solution with a bi-conjugate gradient method was $\sim 50 \text{ min}$. Therefore, MoVFEM runs the assembly of the global matrix in an acceptable time. However, the direct method used for the inversion of the global matrix in MUMPS is slow compared to the bi-conjugate gradient

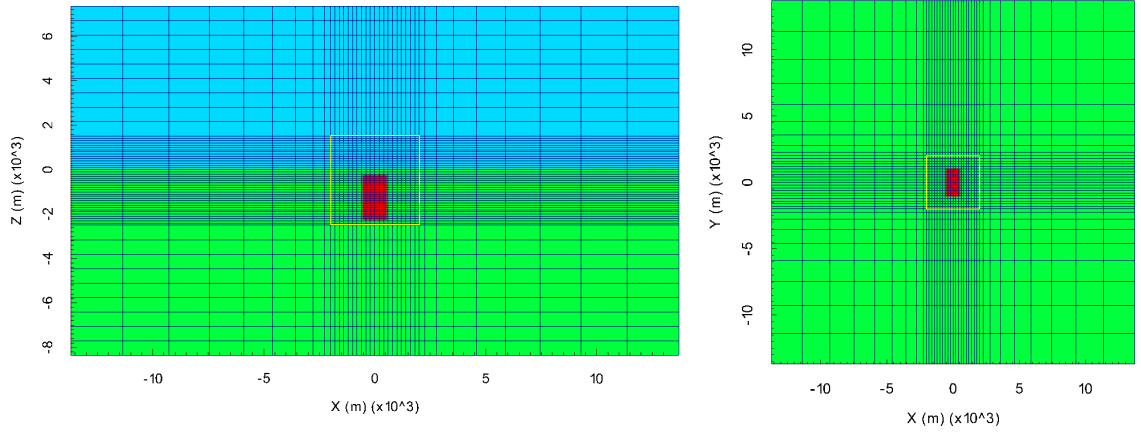


Figure 5.2: Computational grid of COMMEMI 3D-1A model. Left panel: XZ-plane discretization. Right panel: XY-plane discretization. The yellow rectangle in these panels encloses the inner grid, and is surrounded by the extension zones. The blue half-space is the air domain, and the green half-space is the resistive background (B) of the subsurface model.

method used by Farquharson & Miensoopust (2011).

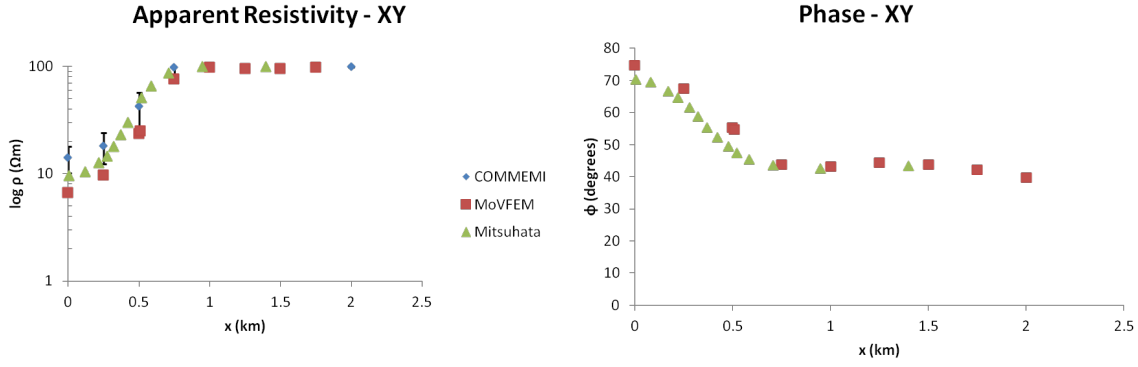
Figures 5.3a, and 5.3b present the forward modeling responses as apparent resistivity and phase obtained from this test. The x-line of receivers is shown on these graphs, and only half of this line is shown because of the symmetry of this model.

In the xy -polarization, the apparent resistivity increases from $6.5 \Omega\text{m}$ on top of the conductive block (A), to $\sim 100 \Omega\text{m}$ through the resistive background (B) (Figure 5.3a). A similar behavior is present in the phase plot, in which ϕ_{xy} decreases from $\sim 75^\circ$ above the conductive block (A) to 40° on the resistive background (B). In this polarization, the contact from the conductive and resistive bodies is clearly shown because the electric field propagates orthogonal to this contact, and from the interface conditions, this field is discontinuous across the contact.

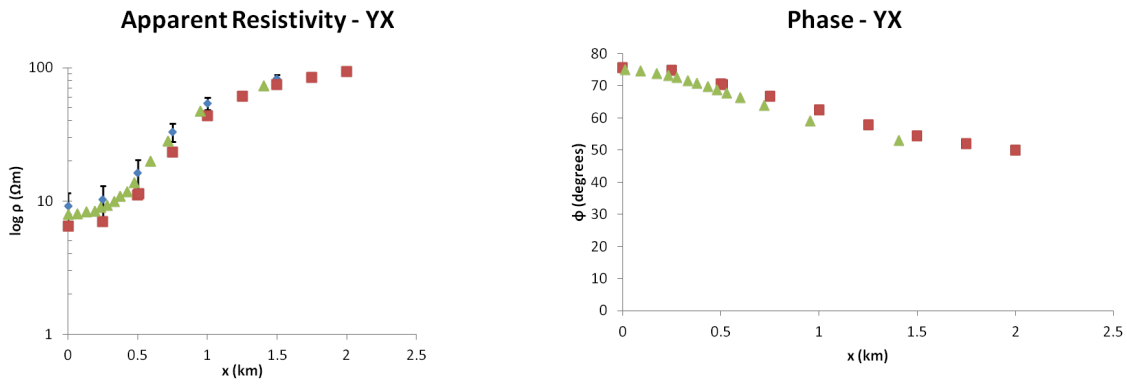
The apparent resistivity and phase curves for the yx -polarization change smoothly from the location of the conductive block (A) ($\rho_{yx} \approx 6.5 \Omega\text{m}$, $\phi_{yx} \approx 75^\circ$) to the resistive background ($\rho_{yx} \approx 100 \Omega\text{m}$, $\phi_{yx} \approx 50^\circ$) (Figure 5.3b). This is because the electric field propagates parallel to the contact of these bodies, and this field is continuous on this contact.

In general, the apparent resistivity curves agree with the respective results presented in the COMMEMI report of Zhdanov et al. (1997), and with the forward model of Mitsuhashi & Uchida (2004). At the center of the model, directly above the conductive block, the resistivity values obtained are smaller than those presented in COMMEMI by $\sim 8 \Omega\text{m}$. Mitsuhashi & Uchida (2004) present similar results, for which resistivities obtained above the conductive block are less than the average values presented by Zhdanov et al. (1997) (Figure 5.3b) by $\sim 5 \Omega\text{m}$. The phase data obtained by MoVFEM presents values slightly higher than the results of Mitsuhashi & Uchida (2004) for both polarizations, by $\sim 4^\circ$ for ϕ_{xy} , and $\sim 1^\circ$ for ϕ_{yx} .

A reason for this discrepancy is that in MoVFEM the spacing is constant over the inner domain, and therefore a grid refinement is not applied on areas of high conductivity gradient, as other forward modeling algorithms do (e.g. Mackie et al., 1994; Mitsuhashi & Uchida, 2004; Nam et al., 2007). Another reason for such discrepancy is due to boundary reflections towards the inner domain. Tests executed with GPML



(a) Apparent Resistivity and Phase on XY-Mode



(b) Apparent Resistivity and Phase on YX-Mode

Figure 5.3: Apparent resistivity (left) and phase (right) from the x -line of receivers for the model COMMEMI 3D-1A at 10 Hz. Blue diamonds are the average results presented in the COMMEMI report, and the error bars are the minimum and maximum results presented by Zhdanov et al. (1997). COMMEMI results does not contain phase data. Red squares are the solution obtained from this MoVFEM algorithm. Green triangles are the solution obtained from the FEM algorithm of Mitsuata & Uchida (2004).

present MT responses that oscillate within the values of each resistive structure, thus the results are not as stable as with Dirichlet boundary conditions.

Figure 5.4 shows the apparent resistivities on the surface of the inner model. In these plots, it can be seen that the inner model does not show strong boundary reflections because the resistivity values appear to be constant across the resistive background (B). In addition, the effect of xy -polarization is shown more clearly, where the contact in the x direction is sharper than the contact in y direction (Figure 5.4, left panel). The same effect is noticed for the yx -polarization, in which the contact of the conductive body and the resistive background is sharper in the y direction than in the x direction (Figure 5.4, right panel).

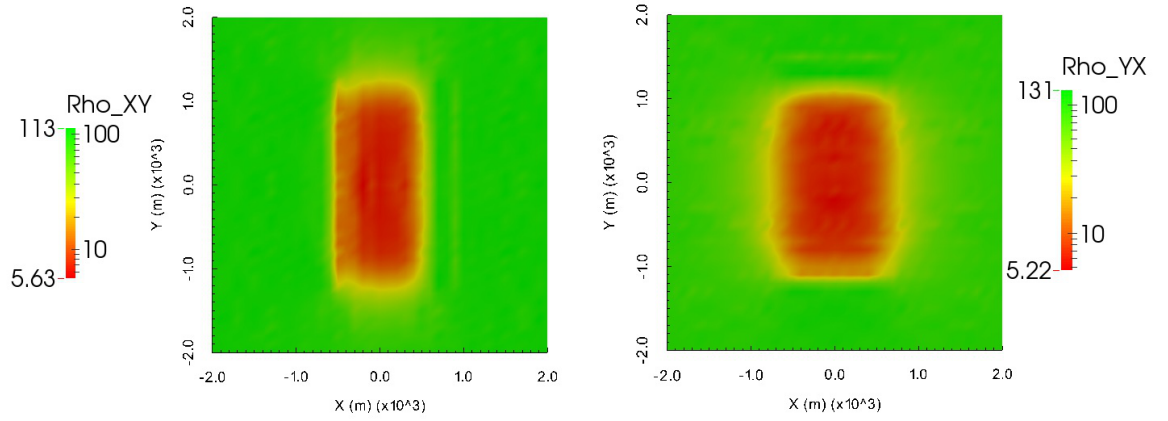


Figure 5.4: Modeled apparent resistivities at 10 Hz across the surface of the inner model for the COMMEMI 3D-1A structures. Left panel shows ρ_{xy} , and right panel shows ρ_{yx} . x and y axes are in meters and the resistivity is plotted with a logarithmic scale.

5.3 COMMEMI 3D-2

Two adjacent rectangular blocks (A, B) with dimensions of $20 \times 40 \times 10$ km are embedded in a horizontally layered background, and located at the center of the top layer (Figure 5.5). These blocks have resistivities of $A = 1 \Omega\text{m}$ and $B = 100 \Omega\text{m}$,

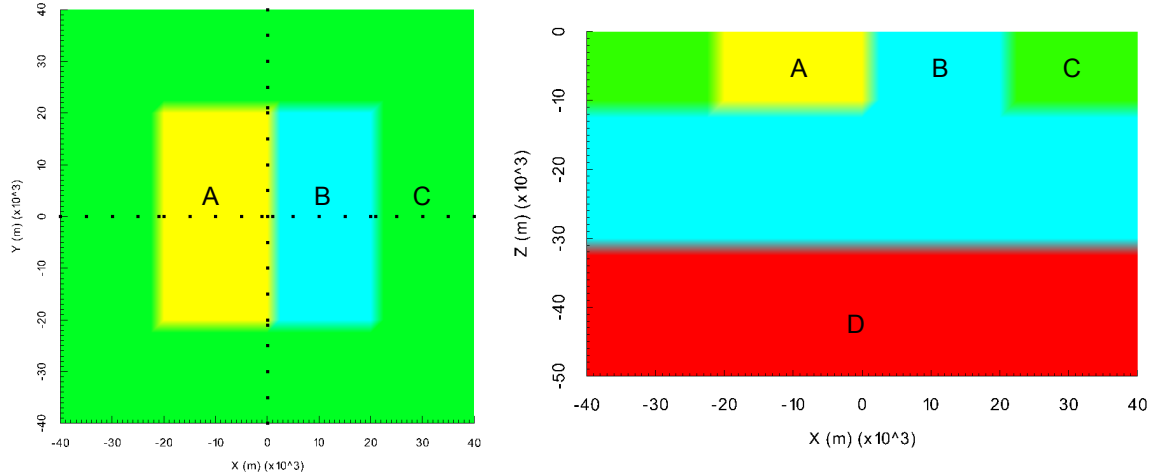


Figure 5.5: Input model of COMMEMI 3D-2. Left panel shows the plane view, where the black squares represents the location of receivers. Right panel shows the xz -slice of this model with the value of resistivities. The resistive bodies are $A = 1 \Omega\text{m}$, $B = 100 \Omega\text{m}$, $C = 10 \Omega\text{m}$, and $D = 0.1 \Omega\text{m}$. The axes are shown in meters.

respectively. The background consist of three layers with resistivities of $C = 10 \Omega\text{m}$, $B = 100 \Omega\text{m}$, and $D = 0.1 \Omega\text{m}$, from surface to bottom, respectively. The thickness of the first two layers are 10 km and 20 km from top to bottom, respectively. This input model has dimensions of $x = y = [-40 : 40]$ km, and $z = [0 : -50]$ km.

A model is presented for a frequency of 0.01 Hz, in which the skin-depth ranges from 5 km (for surface conductor A), to 50 km (for resistor B). Because the model is extended several skin-depths, the air height is set to 10 km. In order to represent the conductive block on the surface, the spacing on this model was of $dx = dy = dz = 3$

km. The inner domain was extended 175.5 km in all directions, and the computational grid had dimensions of $x = y = [-215.5 : 213.5]$ km, and $z = [0 : 411]$ km.

Dirichlet boundary conditions were applied, in which the boundaries were considered as a layered Earth with the same thickness and resistivity of the background of the input model. Several tests were also run with GPML, changing the spacing and extensions of the model; these results showed MT responses that fluctuate around the values of each resistivity structure.

Lagrangian elements were applied in this test, and the computational grid contained $44 \times 44 \times 37$ elements. Although quadratic elements had the same accuracy for the homogeneous Earth, in this case Lagrangian elements showed better MT responses than quadratic elements. In this case, $1677882 \approx 1.7 \times 10^6$ unknown edges needs to be calculated requiring a full matrix of $\sim 2.9 \times 10^{12}$ elements. However, only $85154263 \approx 8.5 \times 10^7$ non-zero entries were stored in the sparse array, which is $\sim 0.003\%$ of the global matrix. Figure 5.6 shows the discretization scheme described here.

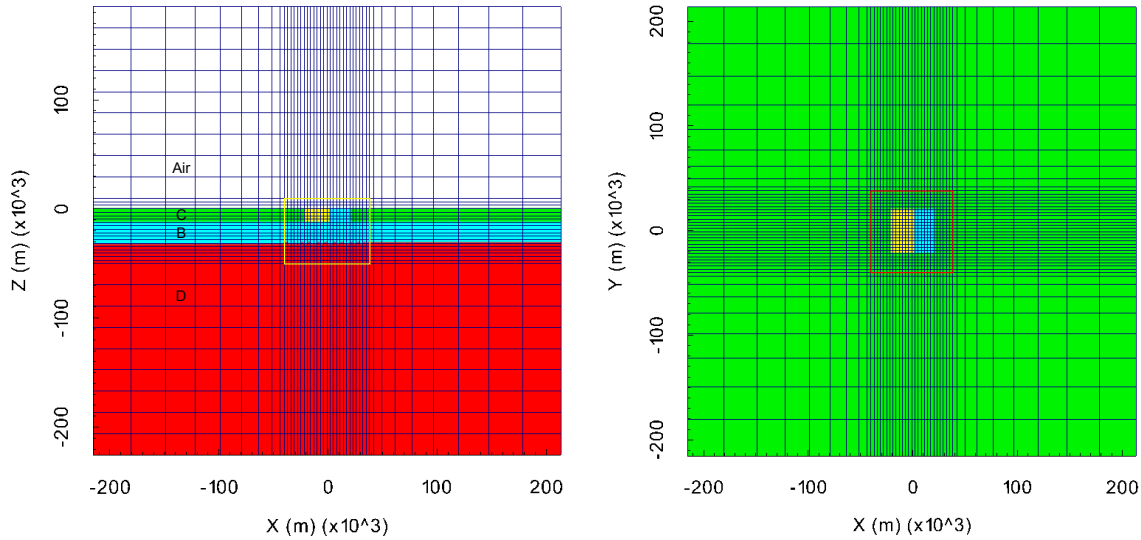


Figure 5.6: Computational grid for the model COMMEMI 3D-2. Left panel: XZ-plane discretization, the white domain on the top is the air domain, and the subsurface structures have the same labels as in the input model. Right panel: XY-plane discretization. The yellow rectangle (on the left panel) and red rectangle (on the right panel) enclose the inner grid and are surrounded by the extension zones. The axes are shown in meters, and are transformed to the coordinates location of the input model.

The assembly process was complete in 4674 seconds ≈ 78 min, and the matrix inversion and solution finished in 11824 seconds ≈ 197 min for both xy - and yx -polarizations. Zyserman & Santos (2000) applied a FEM algorithm with non-conforming vectors (12 edge-elements for the electric field, plus 9 face-vectors for the magnetic field); their algorithm required a model of $54 \times 54 \times 32$ elements, for a total CPU time for one mode (i.e. xy -polarization) of ~ 115 min in sequential mode.

Figures 5.7a, and 5.7b show apparent resistivity and phase plots for the x -line ($y = 0$) of receivers. In this case results from the COMMEMI report (Zhdanov et al., 1997) and from the FD modeling algorithm of Mackie et al. (1994) are shown for comparison. The phase obtained from MoVFEM algorithm can be compared with the

results obtained by Mackie et al. (1994), note that COMMEMI only shows apparent resistivity.

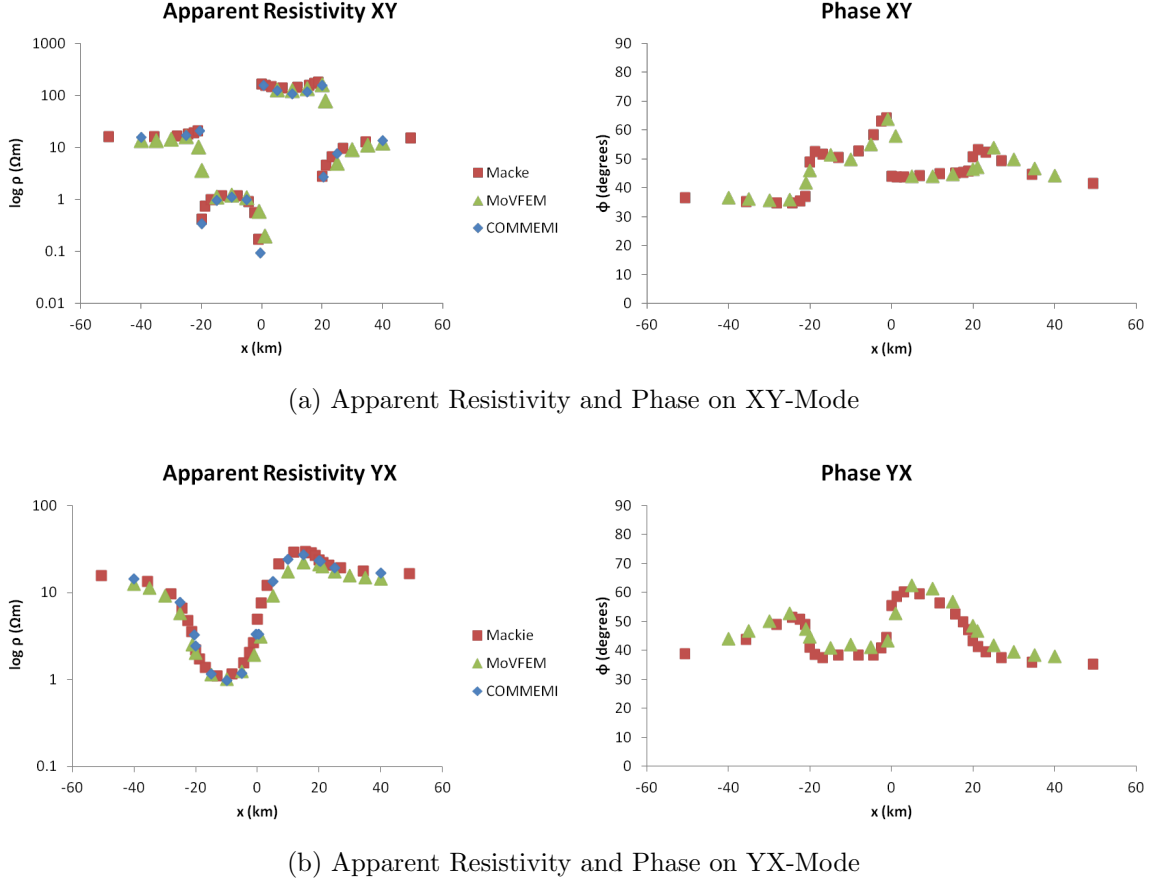


Figure 5.7: Apparent resistivity (left) and phase (right) for a frequency of 0.01 Hz, from the x -line ($y = 0$) of receivers for the model COMMEMI 3D-2. Blue diamonds are the results presented in the COMMEMI report (Zhdanov et al., 1997). Red squares are the solution of Mackie et al. (1994), and green triangles are the solution of this MoVFEM algorithm.

The xy -polarization plots (Figure 5.7a) show how the apparent resistivity changes abruptly from one body to the next in the x direction. This model shows more clearly the effect of an electric field propagating orthogonal to the contact of structures, as the TM mode in 2D structures. Outputs of MoVFEM compare well with the results from Zhdanov et al. (1997) and Mackie et al. (1994), differences are of about $2\ \Omega\text{m}$ and 4° . The largest discrepancies are at the contacts, due to the discretization scheme used in MoVFEM, where no grid refinement takes place.

For the yx -polarization (Figure 5.7b), variations across the blocks are smoother, approximating the TE mode. In this case, the results obtained from MoVFEM have a better fit, although the apparent resistivities are slightly lower than those of Zhdanov et al. (1997) by $\sim 2\ \Omega\text{m}$, and Mackie et al. (1994) by $\sim 3\ \Omega\text{m}$ at the location of the blocks. Phase values obtained from MoVFEM are slightly higher than those of Mackie et al. (1994) by $\sim 3^\circ$. Some of the discrepancy occurs at contacts, due to the discretization scheme applied in MoVFEM. Additionally, the location of the boundaries for Dirichlet boundary conditions may not be sufficient to remove reflections from the top and bottom boundaries of the computational domain.

Figure 5.8 shows surface maps of apparent resistivities in both polarizations. There is no significant reflection from the side boundaries of the computational domain. Also, the xy -polarization (left plane) shows sharp contacts in the x direction, and the yx -polarization (right plane) shows sharp contacts in the y direction. There is a slight asymmetry in the yx responses, probably due to a numerical round off that propagates through the matrix LU decomposition.

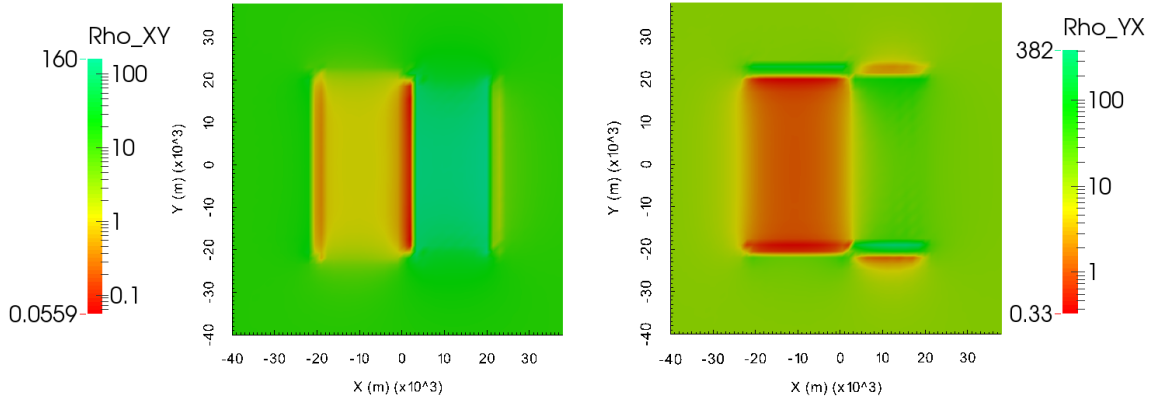


Figure 5.8: Apparent resistivity values on the surface of the inner model. Left plane shows the xy -polarization, and yx -polarization is shown on the right plane. The axes are shown in meters, and the apparent resistivities are presented in logarithmic scale.

5.4 Topography Effect for Homogeneous Earth

The topography effect is investigated with a 2D surface hill model, as used by Wannamaker et al. (1986) and Nam et al. (2007). The hill is 100 m high, and has a width of 2.4 km in the x direction. A homogeneous subsurface has a resistivity of 100 Ωm . The 2D hill extends 10 km in the y direction to not include any significant 3D effect in the solution, as suggested by Nam et al. (2007). The input model dimensions are $4 \times 10 \times 5$ km (Figure 5.9).

To be able to compare these results with the results of Nam et al. (2007), a frequency of 10 Hz was used in this test, for which the skin-depth is 1.6 km. The air domain had a thickness of 2.5 km, and the depth of the input model was increased by 5 km, thus, the input model has a dimension of 12.5 km in the z direction. The spacing for the inner grid was of $dx = 250$ m, $dy = 500$ m, and $dz = 250$ m.

GPML boundary conditions were applied, using the scheme of Zhou et al. (2012). In this case, the stretching factor parameters were the same as in the homogeneous model shown in previous Chapter, which are $a_{min} = 0$, $a_{max} = 100$, $b_{min} = 10^{-2}$, $b_{max} = 10^6$, and $n = 2$. The width of boundary regions surrounding the inner model were 4.9 km in the x and z directions, and 9.75 km in the y direction. This computational grid had dimensions of $x = [-6.9 : 6.9]$ km, $y = [-14.75 : 14.75]$ km, and $z = [0 : 17.35]$ km. Figure 5.10 presents the discretization of this computational grid, and inner model.

This computational grid contained $26 \times 30 \times 40$ Lagrangian elements, with a total of $773152 \approx 7.7 \times 10^5$ unknown edges. Therefore, the assembled matrix includes $\sim 6.0 \times 10^{11}$, where only $39529728 \approx 4 \times 10^7$ non-zero entries were stored ($\sim 0.007\%$ of the global matrix).

Computational time for the matrix assembly was 2070 s ≈ 34 min. The time spent for the matrix inversion and to calculate the solution was 1689 s ≈ 28 min. Nam

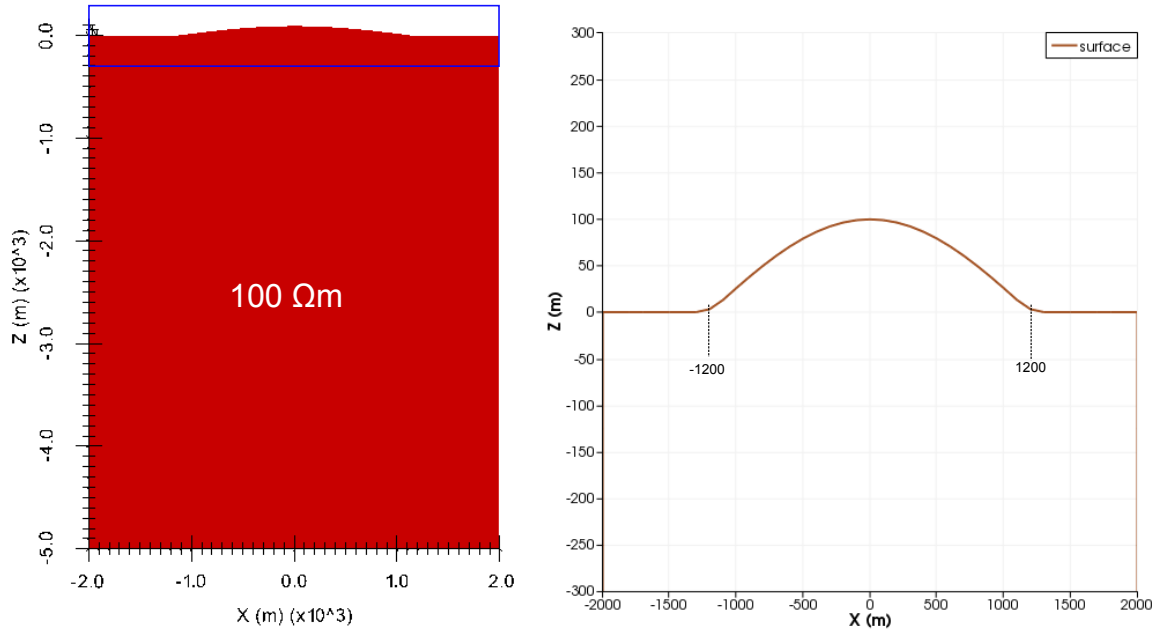


Figure 5.9: Input of the homogeneous model with 2D topography. Left panel shows the xz -plane, where the 2D surface enclosed by the blue rectangle is shown in the right panel. This 2D hill is extended in y direction. The axes are shown in meters.

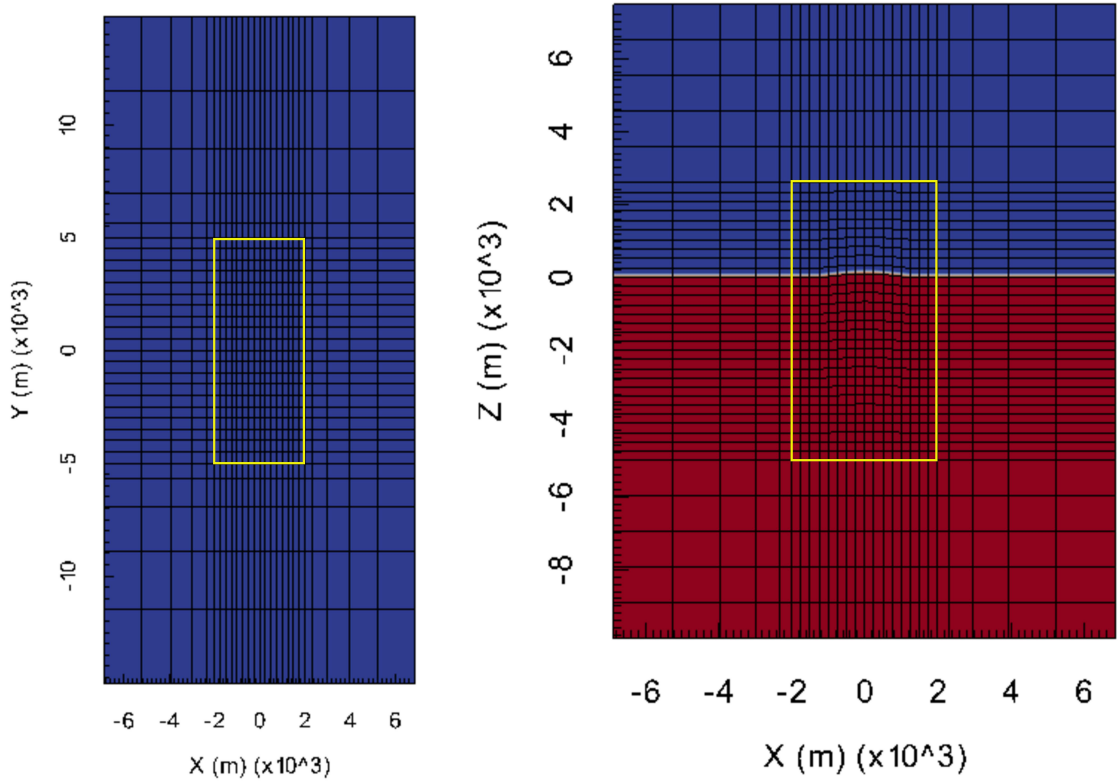


Figure 5.10: Computational grid for the 2D topography model with homogeneous earth. Right panel shows the XZ plane discretization, where blue half-space is the air space, and red is the subsurface. The left panel shows the discretization of the XY plane. The yellow rectangle in each plane describes the location of the inner model. The axes are shown in meters, and are transformed to the coordinate locations of the input model.

et al. (2007) applied linear VFEM to this problem, using $48 \times 48 \times 31$ elements. The total time to obtain a convergence of bi-conjugate gradient was about 5 min in xy -polarization and 4 min in the yx -polarization. MoVFEM uses more time because of the use of Lagrangian elements, and anisotropy, where the isotropic model is stored as the symmetric part of $\sigma \mathbf{I}$ which has 6 components. Consequently, more calculations are made within each element in MoVFEM.

Apparent resistivity and phase plots are shown in Figures 5.11a, and 5.11b for the x -line of receivers. Comparing the results obtained from MoVFEM to those of Nam et al. (2007), it can be seen that the yx -polarization (Figure 5.11b) have a better fit than the xy -polarization, with an average ρ_{yx} difference of $\sim 3 \Omega\text{m}$ and phase difference of $\sim 1^\circ$ (Figure 5.11a). However, the results from both polarizations show a similar pattern to the results from Nam et al. (2007). MoVFEM obtained higher values of

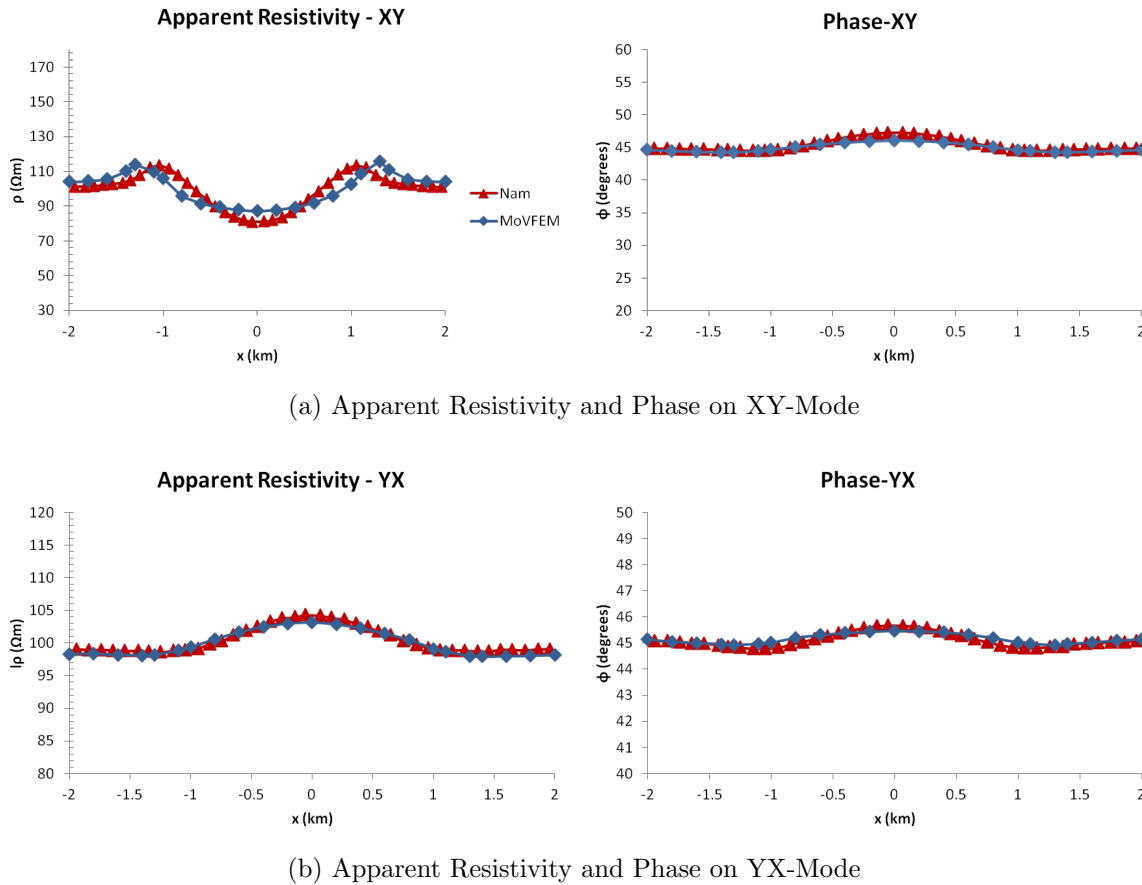


Figure 5.11: Apparent resistivity (left) and phase (right) from the x -line of receivers for the homogeneous model with 2D topography at 10 Hz. Red triangles are the solution from Nam et al. (2007). Blue diamonds are the solution of this MoVFEM algorithm.

ρ_{xy} than Nam et al. (2007) by around $5 \Omega\text{m}$ in the center of the 2D hill, and towards the boundaries these values have a difference of $\sim 2 \Omega\text{m}$. Phases in the center of the hill are lower than Nam et al. (2007) by around 1° . Nam et al. (2007) discretized the domain with a finer grid at the air/subsurface contact while MoVFEM uses the same spacing for the whole inner domain. In addition, the surface interpolation method used in MoVFEM obtains a smoother hill than the input model (Section 3.3), where the break of slope is slightly different than the input surface.

The behavior of the field polarizations are shown on the surface plots (Figure 5.12). In the xy -polarization, the apparent resistivity starts with a value of around $100 \Omega\text{m}$

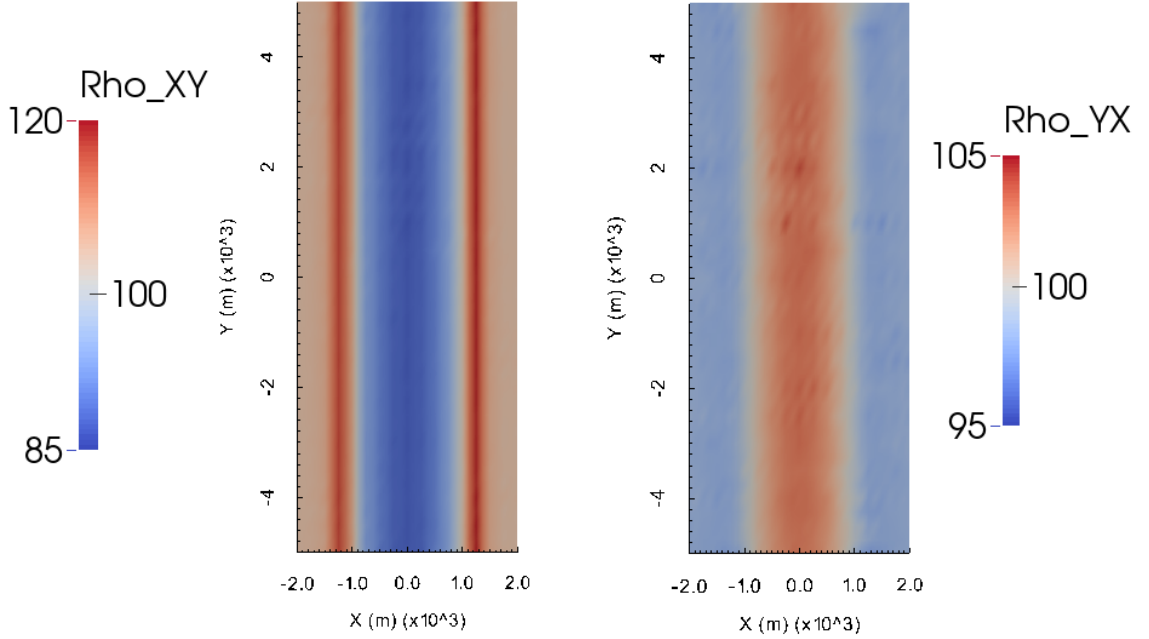


Figure 5.12: Apparent resistivities on the surface of the inner model at 10 Hz. Left plane shows the xy -polarization, and right plane shows the yx -polarization. In both cases the apparent resistivity is plotted on logarithmic scale.

at the boundary where the topography is flat. When the topography starts to change ρ_{xy} takes its higher values and at the center of the hill it reduces to its minimum value. The yx -polarization changes gradually from $97 \Omega\text{m}$ across the boundaries to $104 \Omega\text{m}$ on top of the center of the hill. From these surface plots, it can be noticed that reflections effects from the boundaries of the computational domain are not significant across the inner model. Thus, in this case, GPML boundary conditions work well.

5.5 Anisotropic Homogeneous Earth

The anisotropic homogeneous model has a dimension of $100 \times 100 \times 50 \text{ km}$, and a transverse resistivity tensor

$$\boldsymbol{\rho} = \begin{pmatrix} 100 & 0 & 0 \\ 0 & 50 & 0 \\ 0 & 0 & 1 \end{pmatrix} \Omega\text{m}.$$

Models were computed for various frequencies, the example here is shown at 0.01 Hz, for which the maximum skin-depth is around 50 km and is related to the input model dimensions. This input model was extended 50 km in depth, and the air height was of 10 km. In order to achieve a good solution for all the components of the conductivity tensor, a spacing of $dx = dy = dz = 7 \text{ km}$ was applied.

The extension zone has a width of 191 km for all directions. GPML (Zhou et al., 2012) boundaries were applied with stretching factor parameters of $a_{min} = 0$, $a_{max} = 100$, $b_{min} = 10^{-2}$, $b_{max} = 10^6$, and $n = 2$. With this discretization, the computational grid had dimensions of $x = y = [-241.1 : 239.1] \text{ km}$, and $z = [0 : 442.2] \text{ km}$ (Figure 5.13).

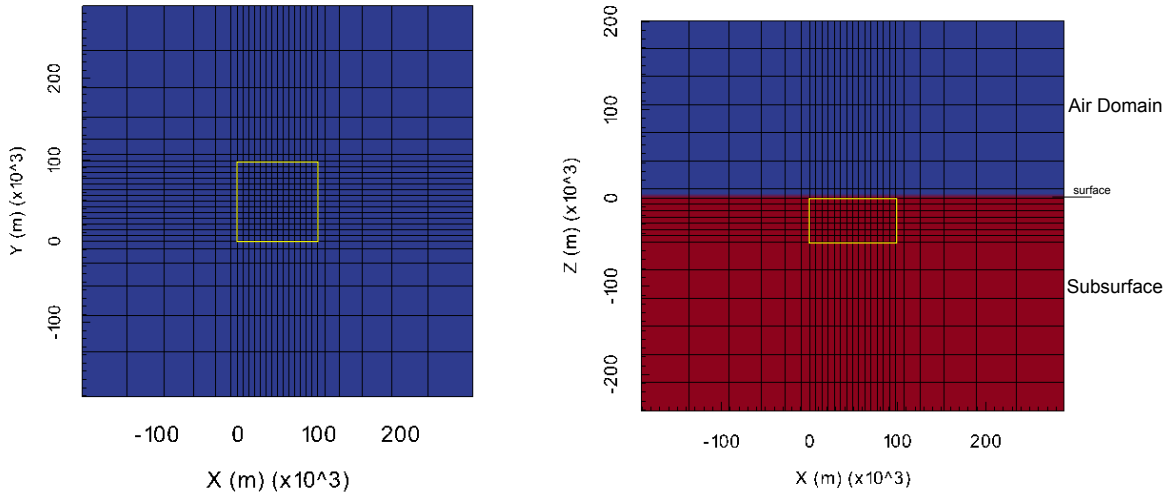


Figure 5.13: Computational grid, showing the discretization of the homogeneous anisotropic Earth model. Blue color corresponds to the air domain, and the red color corresponds to the anisotropic subsurface with the diagonal conductivity tensor. The yellow rectangle on each plane shows the location of the inner grid. The axes are in meters, and the coordinates are transformed to the locations of the input model.

Lagrangian elements were used in this test, and this discretization contained $26 \times 26 \times 20$ elements, thus this problem contained a total of $338352 \approx 3.4 \times 10^5$ edge-elements. The assembled matrix contained only $17158968 \approx 1.7 \times 10^7$ non-zero entries, and the assembly time was $814 \text{ s} \approx 13 \text{ min}$. The time for matrix inversion and solution was $439 \text{ s} \approx 7 \text{ min}$.

Figure 5.14 shows the apparent resistivity and phase plots for both polarization modes. For the xy polarization (blue diamonds on the plots), the apparent resistivity has a constant value of $99.8 \Omega\text{m}$ with an error of $\sim 0.2\%$, and the phase has a constant value of 44.2° , as opposed to 45° expected ($\sim 1.7\%$). For the yx -polarization, the apparent resistivity has a constant value of $49.8 \Omega\text{m}$ with an error of $\sim 0.4\%$, and the phase has a constant value of 45.4° with an error of $\sim 0.88\%$. Consequently, the apparent resistivity in xy polarization obtains the ρ_{xx} component of the input resistivity tensor, and the apparent resistivity in yx -polarization obtains the ρ_{yy} component of the input resistivity tensor.

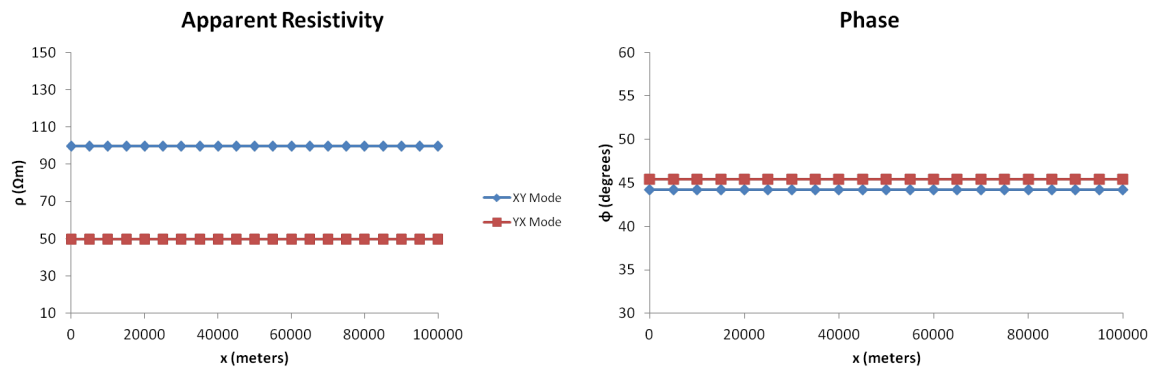


Figure 5.14: Apparent resistivity and phase pots from the x -line of receivers of the anisotropic homogeneous model at 0.01 Hz . Blue diamonds corresponds to the xy -polarization and red squares corresponds to the yx -polarization.

Figure 5.15 shows the apparent resistivity on the surface of the inner model, and it can be noticed that the resistivity values are constant over all the surface. It also can be noticed that no boundary reflection is present on the surface of the inner model.

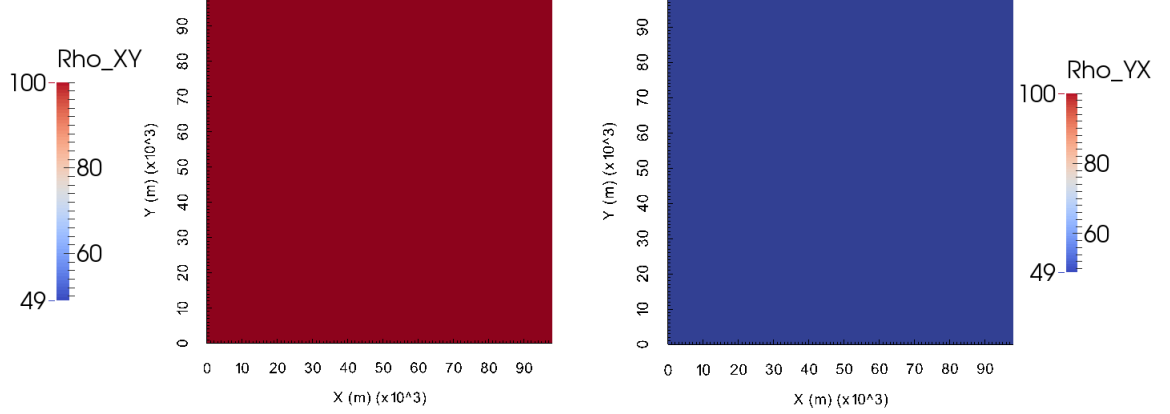


Figure 5.15: Apparent resistivity on the surface of the inner model at 0.01 Hz. Right plane shows ρ_{xy} and left plane shows ρ_{yx} . The axes are in meters, and the resistivity values are in linear scale.

5.6 Three Layers with Complex Interfaces: Isotropic Case

This model consists of three layers with topography and one complex subsurface interface. The topography is a 10 km wide 2D hill in x direction, and with a height of 200 m. The bottom of the top layer resembles a trough and is 20 km wide (in the x direction) and 800 m deep. This interface is located at 3 km depth below the surface at the x boundaries and 3.8 km beneath the hill. Thus, the thickness of the first layer ranges from 3 km to 4 km, and it has a resistivity of 5 Ωm . The thickness of the second layer ranges from 2.2 km at the center of the interface, to 3 km at the boundaries, and has a resistivity of 100 Ωm . The third layer has a resistivity of 500 Ωm . This input model has dimensions of $30 \times 30 \times 10$ km (Figure 5.16).

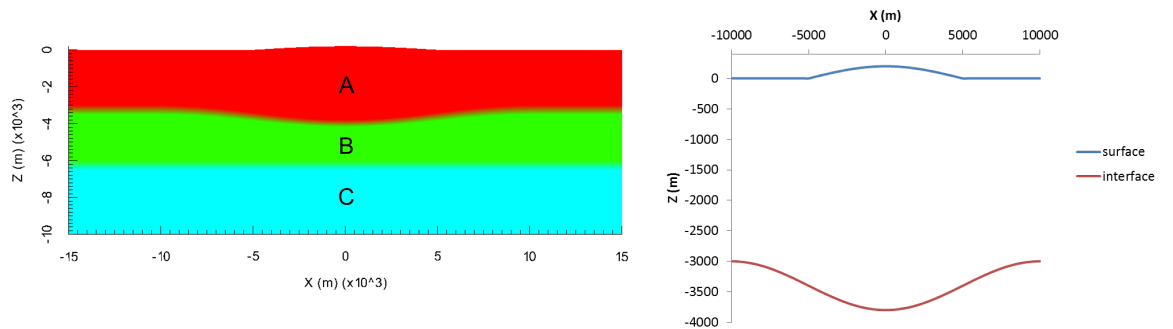


Figure 5.16: Input model representing the three layers with topography and complex interface. The left panel shows a xz -slice with the geometry of these layers, and its resistivity values are $A = 5 \Omega\text{m}$, $B = 100 \Omega\text{m}$, and $C = 500 \Omega\text{m}$. The right panel shows a zoom to the top and bottom 2D surfaces of the first layer. In both panels the axes are presented in meters.

Models were calculated and presented for a frequency of 0.1 Hz, in which the skin-depth ranges from 3.5 km on the surface layer, to 35.5 km in the bottom layer. This

frequency is selected in order to show how the MT responses obtained with MoVFEM behave in relation with the first layer. The air height was 5 km, and the spacing used was $dx = dy = 2000$ m and $dz = 800$ m.

GPML boundary conditions were applied, with the same stretching factor parameters as in Section 5.4. The inner model was extended ~ 203 km in the x and y directions, and ~ 81 km in the z direction. Thus, the computational domain had dimensions of $x = y = [-217.8 : 217.8]$ km, and $z = [0 : 177.44]$ km. Figure 5.17 shows the discretization of this computational grid, where the spacing applied on the inner grid is shown in Figures 5.17c, d.

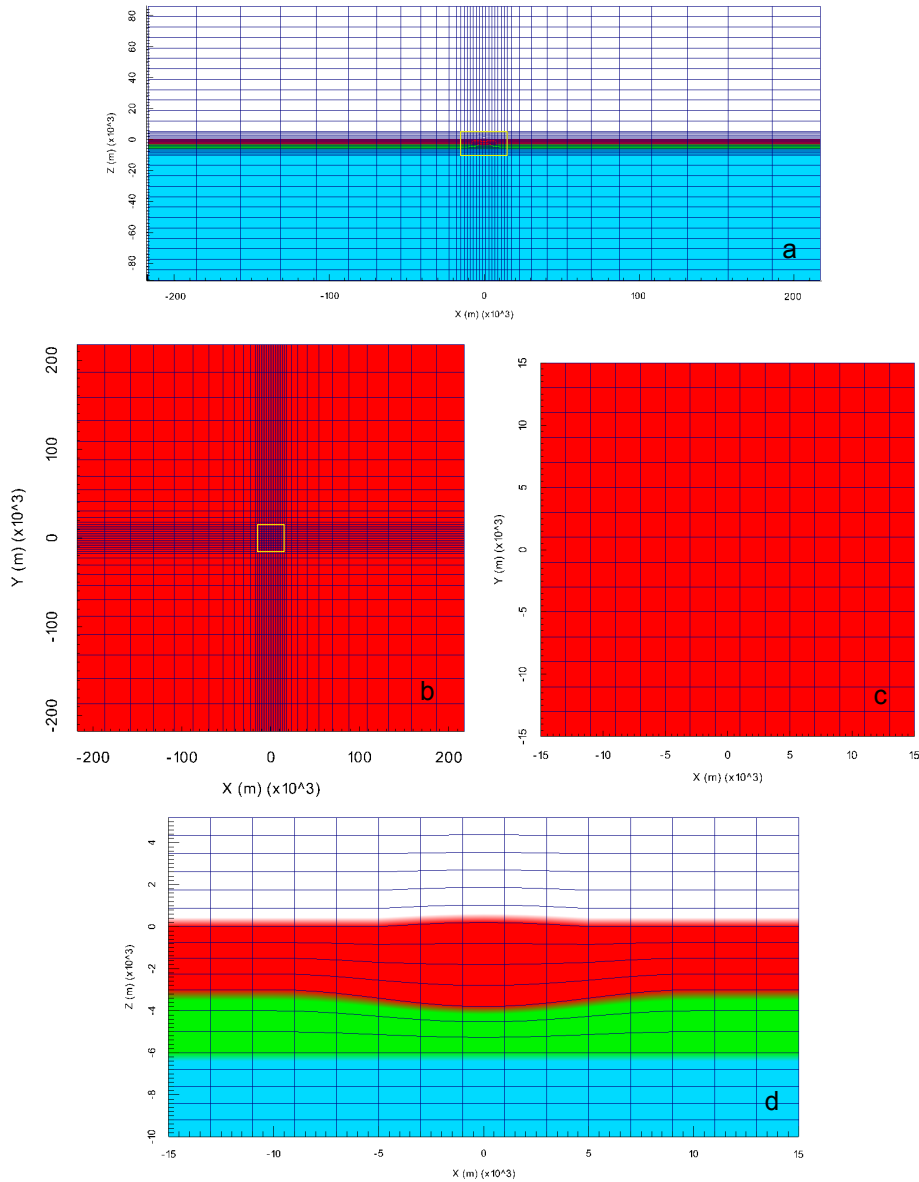
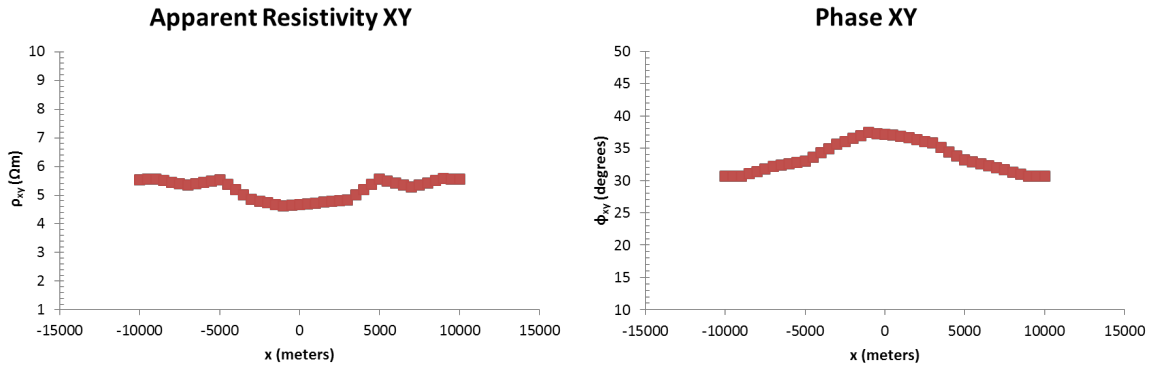


Figure 5.17: Computational grid for the isotropic layered model with complex interfaces. a) XZ slice of the computational domain, where the yellow rectangle encloses the inner grid. b) XY slice of the computational domain. The yellow rectangle encloses the inner grid and is surrounded by the extension zones. c) Zoom to the inner grid in the XY slice. d) Zoom to the inner grid in the XZ slice.

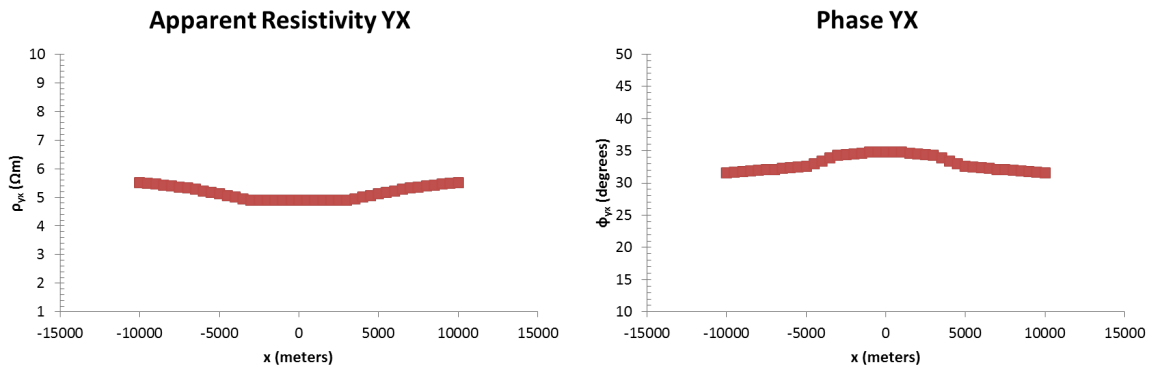
Lagrangian elements were applied, and the computational grid contained $39 \times 39 \times 42$ elements. This problem contained $1571784 \approx 1.5 \times 10^6$ edge-elements, and $80837064 \approx$

8.1×10^7 non-zero entries stored ($\sim 0.003\%$ of the global matrix). The matrix assembly process took 3559 s \approx 59 min, and the matrix inversion and solution finished in 6953 s \approx 115 min.

This model has not been published by other authors, and the purpose of this synthetic example is to show how MoVFEM works with complex geometries. The forward modeling responses from the x -line ($y = 0$) of receivers are shown in Figures 5.18a, and 5.18b. The apparent resistivity of the xy -polarization ranges from 4.6 Ωm to 5.5 Ωm (Figure 5.18a). Comparing these results to the results obtained from a homogeneous Earth with topography (Figure 5.11a in Section 5.4), this curve behaves similarly to the resistivity response obtained in Section 5.4. The effect of the second interface is seen at the center of the curve, where it remains relatively constant around 4.6 Ωm . In this case, the phase values ranges from 31° towards the boundaries, up to 37° at the center of the receivers line. The GPML effect is present in these results, where the MT responses oscillate around the resistivity values at the boundaries and the center of the hill. These oscillations give the impression of a lack of symmetry when plotting the MT responses over the x -line of receivers.



(a) Apparent resistivity and phase on XY-Mode



(b) Apparent resistivity and phase on YX-Mode

Figure 5.18: Apparent resistivity (left) and phase (right) from the x -line of receivers for the isotropic layered model with complex interfaces for a frequency of 0.1 Hz.

In the yx -polarization, the apparent resistivity ranges from 4.8 Ωm to 5.5 Ωm . In this case, the effect of the second interface is seen as a convex resistivity curve, instead of the concave curve of the 2D topography model in Section 5.4 (Figure 5.11b). The phase ranges from 31° around the boundaries to 35° across the center of the line of

receivers. In this case the GPML oscillation is shown in the ϕ_{yx} plot (Figure 5.18b).

Figure 5.19 presents the resistivity values at the surface of the inner model.

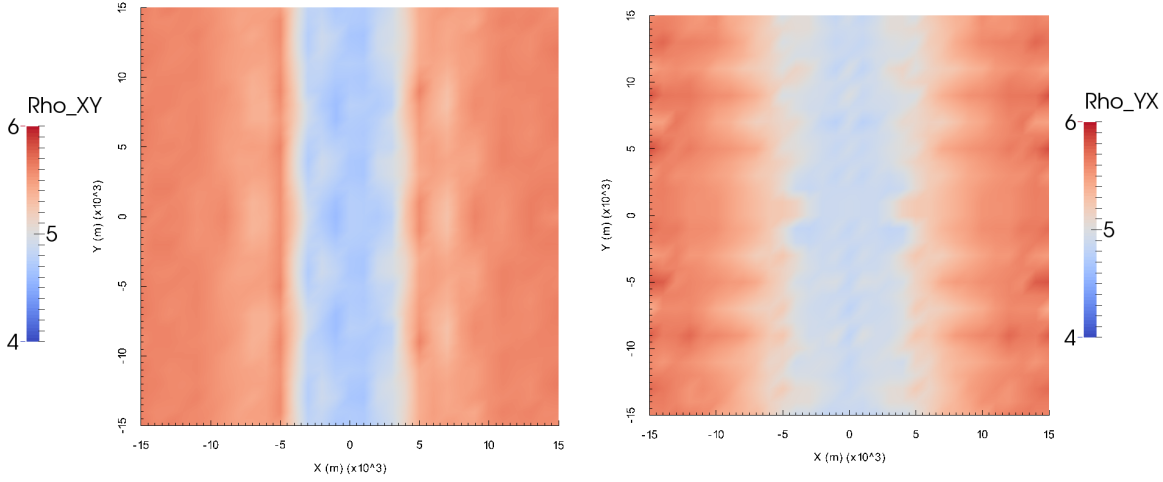


Figure 5.19: Surface resistivity plots for the isotropic layered model with complex interfaces. The resistivity is plotted in linear scale, and the axes are presented in meters with a factor of 10^3 .

The behavior of the apparent resistivities described before, can be seen by comparing the surface resistivity plots with those presented in Section 5.4 (Figure 5.12). Similar to previous models, the apparent resistivity of the xy -polarization shows the location where the topography starts to change (left panel on Figure 5.19). On the other hand, ρ_{yx} presents a smoother variation of resistivities in x direction (right panel on Figure 5.19). The surface maps clearly show the effect of GPML where the apparent resistivity oscillates over the whole surface.

5.7 Three Layers with Complex Interfaces: Anisotropic Case

The input model geometry and dimensions are the same as for the model shown in the previous section (Figure 5.16). In this case, the surface layer has a resistivity tensor of

$$\boldsymbol{\rho} = \begin{pmatrix} 5 & 0 & 0 \\ 0 & 20 & 0 \\ 0 & 0 & 5 \end{pmatrix} \Omega\text{m}.$$

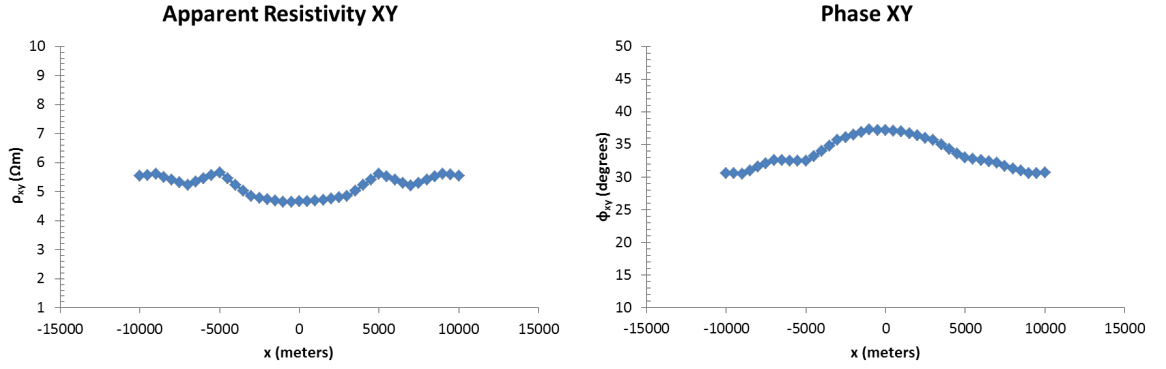
The second and third layers have the same resistivity as in the isotropic case.

This model was also tested with a frequency of 0.1 Hz to show the MT responses for the surface layer because the minimum skin-depth is around 3.5 km. The same spacing, air height, and boundary conditions as in the isotropic case, were applied. Therefore the computational grid is the same as the one presented in Figure 5.17.

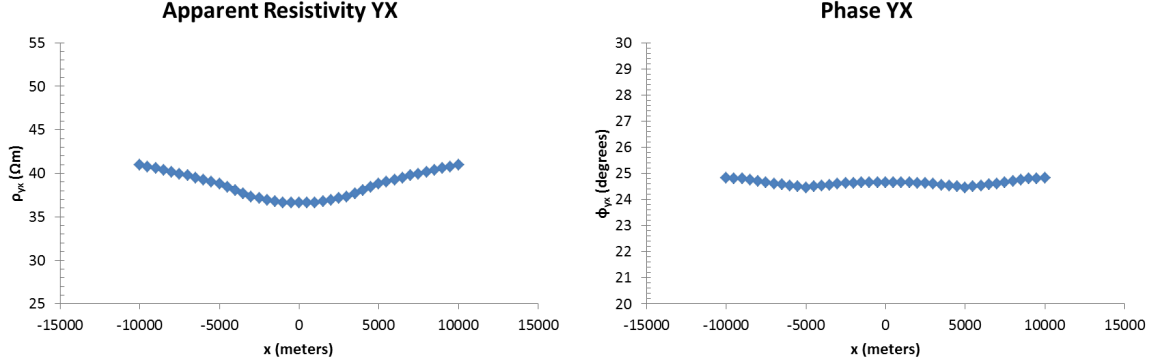
Lagrangian elements were applied, and the problem contained the same amount of elements as described in the previous section. Therefore, this problem contains the same amount of unknown edges, and it was completed in approximately the same time as presented in the isotropic case.

The purpose of this synthetic example is to show how MoVFEM behave for the most general Earth model, i.e. a model with complex geometry and anisotropy. This model has not been published before, thus there is no data to compare with.

The forward modeling responses are shown from the x -line of receivers in Figures 5.20a, and 5.20b. The apparent resistivity of the xy -polarization ranges from $4.6 \, \Omega\text{m}$ to $5.6 \, \Omega\text{m}$ (Figure 5.20a). In this case the phase ranges from 31° around the boundaries, up to 37° at the center of the receivers line. These responses are the same as in the isotropic case, because the xy -polarization is affected by the component ρ_{xx} of the input resistivity tensor. Similar to the isotropic case, the GPML effect is present in these responses where the apparent resistivity oscillates on the boundaries of the line, and the center of hill.



(a) Apparent Resistivity and Phase on XY-Mode



(b) Apparent Resistivity and Phase on YX-Mode

Figure 5.20: Apparent resistivity (left) and phase (right) from the x -line of receivers for the anisotropic layered model with complex interfaces.

The apparent resistivity for the yx -polarization ranges from $36.5 \, \Omega\text{m}$ to $41 \, \Omega\text{m}$ (Figure 5.20b). The phase ranges from 24° on the boundaries to 25° on the center of the line of receivers. These curves follow the same pattern described in the isotropic case. However, the values of the resistivity on this polarization mode describes the component ρ_{yy} of the input resistivity tensor. In addition, these resistivity values are affected by the second layer because the skin-depth of the ρ_{yy} component is of $7 \, \text{km}$, and the maximum thickness of this layer is of $4 \, \text{km}$.

Figure 5.21 presents the resistivity values at the surface of the inner model.

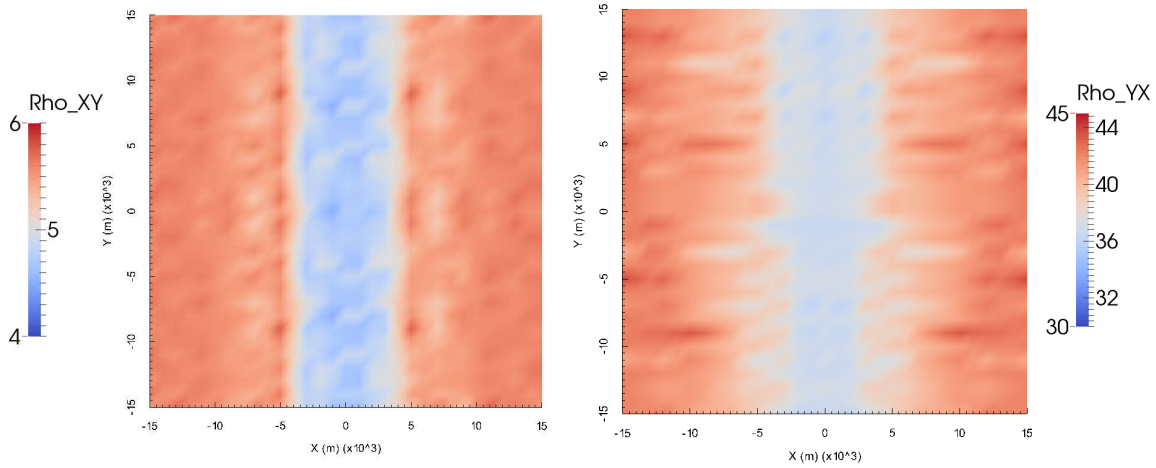


Figure 5.21: Surface resistivity plots for the anisotropic layered model with complex interfaces. The resistivity is plotted in linear scale, and the axes are presented in meters with a factor of 10^3 .

The behavior of the apparent resistivities is similar as in the isotropic case, but the yx -polarization is affected by the component ρ_{yy} of the input resistivity tensor, thus having higher resistivity values. Additionally, the oscillations of GPML are present over the surface in both polarizations.

5.8 General Remarks

In general, MoVFEM works well for models containing complex structures. Most of the discrepancies obtained between MoVFEM forward modeling and other algorithms are located around the contacts of different conductivity structures. The main reason for this is that most of the algorithms applied to MT modeling discretize the domain with fine grid on areas of high conductivity gradient. MoVFEM applies the same spacing values to the whole inner model, and make the grid coarser in the extension zones. Another possible reason for the discrepancies is the location of the boundaries, that still present backwards reflections from the boundaries of the computational domain to the inner domain. Nevertheless, several tests has been done by applying different extensions for the boundary of the domain and still similar results are obtained.

The GPML formulation of Zhou et al. (2012) works well with the homogeneous Earth with topography, and with the anisotropic homogeneous Earth. For the three layers model with complex interfaces (isotropic and anisotropic cases), GPML produces results that resemble the subsurface structures. However, the effect of GPML is present in these models by the oscillation of MT responses over the whole surface.

In the case of models containing complex conductivity structures, Dirichlet boundary conditions were applied. This is because among the several tests with GPML, the values tends to oscillate around a range close to each conductivity value. Consequently, the parameters for the stretching factor needs to be analyzed in order to obtain a stable solution for complex models.

The computational time for the assembly of the global matrix, in which the MoVFEM calculations are executed, is acceptable for FEM algorithms. However, the parallel version of MUMPS is slow compared with the iterative solvers used by other algorithms (Zyserman & Santos, 2000; Nam et al., 2007; Farquharson & Miensopust, 2011).

In the transverse anisotropic case, the MT responses show that the field polarization is decoupled into the TE and TM modes, where the MT responses relate to the

components of the input resistivity tensor. This computational algorithm appears to work well with anisotropy and complex geometries.

Chapter 6

Conclusions

This thesis presented a Multi-order Vector Finite Element (MoVFEM) algorithm programmed in Fortran to model 3D MT data with anisotropy and complex geometry. linear, quadratic and Lagrangian element basis functions have been defined, and implemented. Dirichlet and Generalized Perfect Matched Layers boundary conditions are also included in MoVFEM. This program includes the electric and magnetic field decoupled governing equations to be solved based on the secondary field formulation, but the electric field governing equation is solved in the execution of the program. Outputs are in standard MT response estimations. In the development of this computer program, I programmed all the modules with exemption of MUMPS (Amestoy et al., 2006) and the Shepard Algorithm 660 for surface interpolation (Renka, 1988).

MoVFEM is validated with a homogeneous Earth model. From the convergence analysis, high-order elements obtain a better solution with a coarse grid; linear-order elements need a very fine spacing in order to obtain the same accuracy. This method obtains solutions with a minimum average resistivity error ranging from 3% for linear-order to 0.2% for high-order elements.

Dirichlet boundaries exhibit backwards reflection of the EM field from the boundaries of the domain to the center of the model. However, GPML boundaries stabilize the solution, and no boundary reflection is seen in the inner model. With GPML the solution tends to oscillate within a range of values closer to that of a homogeneous Earth, and the lowest error are obtained with high-order elements. In linear-order elements, the GPML tends to stabilize the solution, but with values higher than the correct value for a homogeneous Earth. However, the selection of stretching factor parameters in GPML depends on the frequency applied and the conductivity, and is difficult to implement for a wide variation of Earth resistivities.

The difference in model dimension and spacing needed to obtain accurate solutions for different conductivities is noticed by comparing the resistive homogeneous Earth model with the conductive homogeneous Earth model, for the same frequency. In this case, the resistive model has a larger skin-depth than the conductive model, thus the spacing used and the model dimension is larger for the resistive model.

In the application of this algorithm to complex resistivity structures, MoVFEM obtained MT responses that agree with the average solutions presented in the COMMEMI project (Zhdanov et al., 1997). The main discrepancy occurred at the boundaries between resistivity structures. These discrepancies are present because in MoVFEM the same spacing is used for the inner grid, and it increases gradually towards the bound-

ary of the computational domain. Other authors implement fine grid in areas of high conductivity gradients or in the location of receivers (Mackie et al., 1994; Mitsuhata & Uchida, 2004; Zhdanov et al., 1997). The COMMEMI models are quite extreme models, much smaller conductivity gradients are likely in the subsurface. Moreover, in a smooth inversion scheme, the gradients are always going to be small.

In the case of topography, this methodology obtains results that are comparable to Nam et al. (2007) in the yx -polarization. In the xy -polarization the resistivity curve differs from the solution of Nam et al. (2007) where the topography changes most rapidly due to grid spacing. Another reason for this discrepancy is the surface interpolation method used in this methodology. The surface interpolation method applied is defined to interpolate scattered data on the surface of the model. This is applied to take into consideration that in the MT application the surface values are usually obtained from the receiver locations in scattered points with a GPS, and not in a structured grid. Therefore, the surface tends to be interpolated in a smooth way.

In general, the boundary extensions are defined to be around three skin-depths from the inner model. In the case of complex resistivity structures, the skin-depths range can be orders of magnitude. Therefore, the extension is defined by a threshold considering the input model size and the maximum skin-depth obtained. The idea behind this is to avoid requiring a large computational grid.

Anisotropic effects were analyzed with a homogeneous-anisotropic Earth with transverse anisotropy, where the conductivity components varies only in the three principal directions. In this case there were no published results to compare with. The MoVFEM solution from anisotropic homogeneous model obtains responses in which the field polarization is related to the conductivity tensor components, i.e. xy -polarization is related to σ_{xx} and yx -polarization to σ_{yy} . Current programs that include anisotropy are for 1D or 2D MT forward modeling and inversion only (Pek & Santos, 2006; Pek et al., 2011). A comparison of the results obtained from MoVFEM (3D forward modeling) with those of a 2D algorithm can be made, but the 3D effects of modeling anisotropic media cannot be described with a 2D algorithm.

In order to analyze the effect of complex geometry, a simple layered model with topography, one subsurface interface and three layers was tested with MoVFEM. This model was tested first with isotropic layers, and second with the first layer being anisotropic. In both models, the MT responses behave similar to the homogeneous with topography case. Calculated apparent resistivities are affected by the second interface in the center of the model. The model with the first anisotropic layer obtained the same behavior as in the anisotropic homogeneous earth.

MoVFEM uses an acceptable CPU time to assemble the global matrix. However, MUMPS uses most of the total computational time to invert the global matrix compared to other methods to solve the linear system of equations (Zyserman & Santos, 2000; Nam et al., 2007; Farquharson & Miensopust, 2011) as discussed in Chapter 5.

6.1 Future Work

In order to improve this algorithm a better discretization scheme could be applied. A discretization with fine grid on areas of high conductivity gradient or on the location of receivers is preferred to improve the solution (e.g. Mackie et al., 1994). A better location of the boundary extension could be calculated to improve the solution for models containing structures with a wide range of conductivity values.

H-adaptive methods have been applied to 2D MT modeling with triangular mesh

(Franke et al., 2007). A h-adaptive method can be applied also to 3D MT modeling with hexahedral mesh, to obtain more accurate results. P-adaptive methods have not been applied for MT modeling, but this approach could be used with MoVFEM because linear and two high-order elements are defined. MoVFEM can also be modified to apply a combination of hp-adaptive methods (e.g. Pardo et al., 2007).

In order to improve the CPU time, a faster method for the inversion of the global matrix could replace MUMPS. Domain decomposition methods have been applied to 3D MT modeling with VFEM (Zyserman & Santos, 2000). In this case the problem is divided into subdomains that can be solved in parallel and be faster than solving the entire computational domain in one go. A domain decomposition scheme can be applied to MoVFEM in order to speed up the assembly process.

An innovative method that can improve the CPU time is the assembly of FEM in parallel using graphic processors (GPUs) (Cecka et al., 2000). Recent researches has been developed to simulate EM field using GPUs (Newman, 2014). NVIDIA's Compute Unified Device Architecture (CUDA) is a new programming interface (in C/C++ and Fortran) developed to use GPUs in parallel, and has been applied for FEM assembly as well as for some linear system of equation solvers (Cecka et al., 2000). In this case, the assembly can be executed in a personal computer containing NVIDIA GPUs. CUDA can be used with MoVFEM for both the assembly process and for the inversion of the global matrix.

MoVFEM can be used with a 3D inversion method of MT data. This can lead to a better understanding of the subsurface model when the area of study has complex topography and subsurface interfaces. It can also be used in 3D inversions to understand the anisotropy of the subsurface structures.

MoVFEM has been developed for MT forward modeling. However, this algorithm can be extended to other geophysical methods by modifying the governing equations and boundary conditions. Consequently, MoVFEM can be modified to be used in the joint inversion of different geophysical data.

Appendix A

Finite Element Method

A.1 Sobolev Space

FEM defines both the problem statement, and the solution on Sobolev spaces. Yilmaz (2007) introduced a detailed description of these spaces and the differential forms used in EM modeling.

A Sobolev space is a vector space of functions with finite norm $f \in \mathcal{L}_p(\Omega)$, and sufficiently many derivatives $f \in \mathcal{C}^k(\Omega)$, where

$$\mathcal{L}_p(\Omega) = \left\{ f \in \mathcal{L}_p(\Omega); \|f\|_p = \left(\int_{\Omega} |f|_p d\Omega \right)^{1/p} < \infty, 1 \leq p < \infty \right\},$$

and

$$\mathcal{C}^k(\Omega) = \{f \in \mathcal{C}^k; D^\alpha f < \infty, 1 \leq \alpha < \infty\}.$$

A Hilbert space $\mathcal{H}(\Omega)$ is a Sobolev space based on the inner product $\mathcal{L}^2(\Omega)$. A basis of the Sobolev space is a set of linearly independent functions that span the space. In EM, these basis can be defined by the differential forms of EM fields, which can be scalars (0-Forms, e.g. EM potentials), vectors that are tangential to interfaces (1-Forms, e.g. Electric field), vectors that are normal to interfaces (2-Forms, e.g. Magnetic Flux), or defined within a volume (3-Forms, e.g. charge density) (Yilmaz, 2007).

Four Hilbert spaces for the EM problem can be obtained, $\mathcal{H}(\Omega, \text{grad})$, $\mathcal{H}(\Omega, \text{curl})$, $\mathcal{H}(\Omega, \text{div})$, and $\mathcal{L}^2(\Omega)$ (Yilmaz, 2007), and are defined as

$$\begin{aligned} \mathcal{H}(\Omega, \text{grad}) &:= \{N \in \mathcal{L}^2(\Omega); \nabla N \in \mathcal{L}^2(\Omega)\} \\ \mathcal{H}(\Omega, \text{curl}) &:= \{\mathbf{v} \in \mathcal{L}^2(\Omega); \nabla \times \mathbf{v} \in \mathcal{L}^2(\Omega)\} \\ \mathcal{H}(\Omega, \text{div}) &:= \{\mathbf{v} \in \mathcal{L}^2(\Omega); \nabla \cdot \mathbf{v} \in \mathcal{L}^2(\Omega)\}. \end{aligned} \tag{A.1}$$

0-Forms basis belongs to $\mathcal{H}(\Omega, \text{grad})$, which are a set of squared integrable functions N with squared integrable gradient. $\mathcal{H}(\Omega, \text{curl})$ contains the 1-Forms basis, and is defined as the set of squared integrable vectors \mathbf{v} with a squared integrable curl, or continuous curl. 2-Forms belongs to $\mathcal{H}(\Omega, \text{div})$, which are the set of vectors \mathbf{v} with squared norm, and with a continuous divergence. 3-Forms are just a set of scalars.

To satisfy the boundary Γ conditions, these basis are defined on Hilbert spaces $\mathcal{H}_0(\Omega, \text{grad})$, $\mathcal{H}_0(\Omega, \text{curl})$, and $\mathcal{H}_0(\Omega, \text{div})$ (Yilmaz, 2007), as

$$\begin{aligned} \mathcal{H}_0(\Omega, \text{grad}) &:= \{\phi \in \mathcal{H}(\Omega, \text{grad}); \phi = 0 \text{ on } \Gamma\} \\ \mathcal{H}_0(\Omega, \text{curl}) &:= \{\mathbf{v} \in \mathcal{H}(\Omega, \text{curl}); \mathbf{v} \times \hat{\mathbf{n}} = 0 \text{ on } \Gamma\} \\ \mathcal{H}_0(\Omega, \text{div}) &:= \{\mathbf{v} \in \mathcal{H}(\Omega, \text{div}); \mathbf{v} \cdot \hat{\mathbf{n}} = 0 \text{ on } \Gamma\}. \end{aligned} \tag{A.2}$$

Therefore, 0-forms are the basis of $\mathcal{H}(\Omega, \text{grad})$, such that the function $\phi = 0$ on Γ . 1-forms satisfy the condition of zero tangential fields on Γ , and 2-Forms satisfy the condition of zero normal fields to Γ .

Depending on which set of basis functions is used in FEM, different FEM approaches are obtained (Yilmaz, 2007). 0-Form basis functions define the classic Nodal-FEM procedure. 1-Forms basis define the Vector-FEM (edge-elements), and are usually called curl-conforming elements. 2-Forms are constructed as facet elements (vectors normal to the elements faces), sometimes are falsely named edge-elements, but this basis is defined by div-conforming elements. 3-Forms results on volume elements, from which the Finite Volume Method is developed.

The de Rham complex relates these differential forms with the differential operator used $(\nabla, \nabla \times, \nabla \cdot)$ (Figure A.1) For example, when applying a curl operator $(\nabla \times)$ to

$$\mathcal{H}(\Omega, \text{grad}) \xrightarrow{\nabla} \mathcal{H}(\Omega, \text{curl}) \xrightarrow{\nabla \times} \mathcal{H}(\Omega, \text{div}) \xrightarrow{\nabla \cdot} \mathcal{L}^2(\Omega)$$

Figure A.1: The de Rham complex defined as a cochain of Hilbert Spaces and differential operators, from Yilmaz (2007).

basis functions on the $\mathcal{H}(\Omega, \text{curl})$ space, a set of functions on the $\mathcal{H}(\Omega, \text{div})$ space are obtained. Therefore, by using edge-elements (curl-conforming elements) in FEM for the EM problem, the divergence free condition is automatically satisfied, when the de Rham complex is considered in relation to \mathcal{H}_0 (Yilmaz, 2007).

Moreover, Maxwell's equations can be viewed in terms of the de Rham complex by a 'Tonti Diagram' (Figure A.2) (Tonti, 2001; Yilmaz, 2007). For example, taking

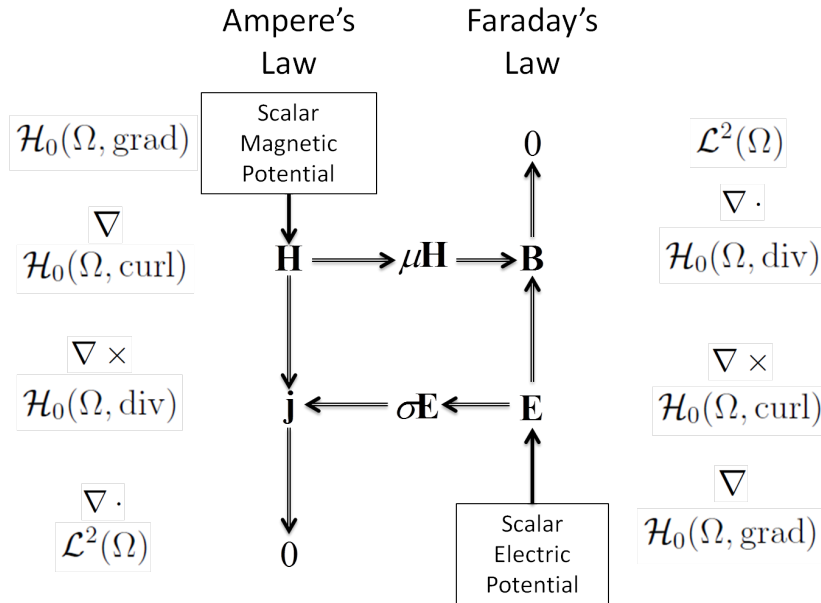


Figure A.2: Tonti's Diagram that relates the de Rham complex with Maxwell's equations, simplified version of Yilmaz (2007).

the curl of the magnetic field in Ampere's Law, a set of functions on $\mathcal{H}_0(\Omega, \text{div})$ are obtained, and these are the current densities. Consequently, by defining the basis functions as 1-Forms in FEM, the divergence condition is automatically satisfied in the EM problem.

A.2 Isoparametric Elements

In FEM the basis functions are defined on each element, such that the integration of the problem is calculated locally, and assembled into a global matrix to get the solution. When the domain Ω does not have any complex geometry, i.e. a rectilinear mesh, then it is possible to define basis functions on their respective Hilbert Space with Cartesian (or Global) coordinates (x, y, z) . However, when the domain has complex geometry, i.e. when the discretization is made with curvilinear elements (Figure A.3a), the generation of these basis functions becomes difficult using Cartesian coordinates. Therefore, it is necessary to define the problem in a rectilinear element (Figure A.3b)

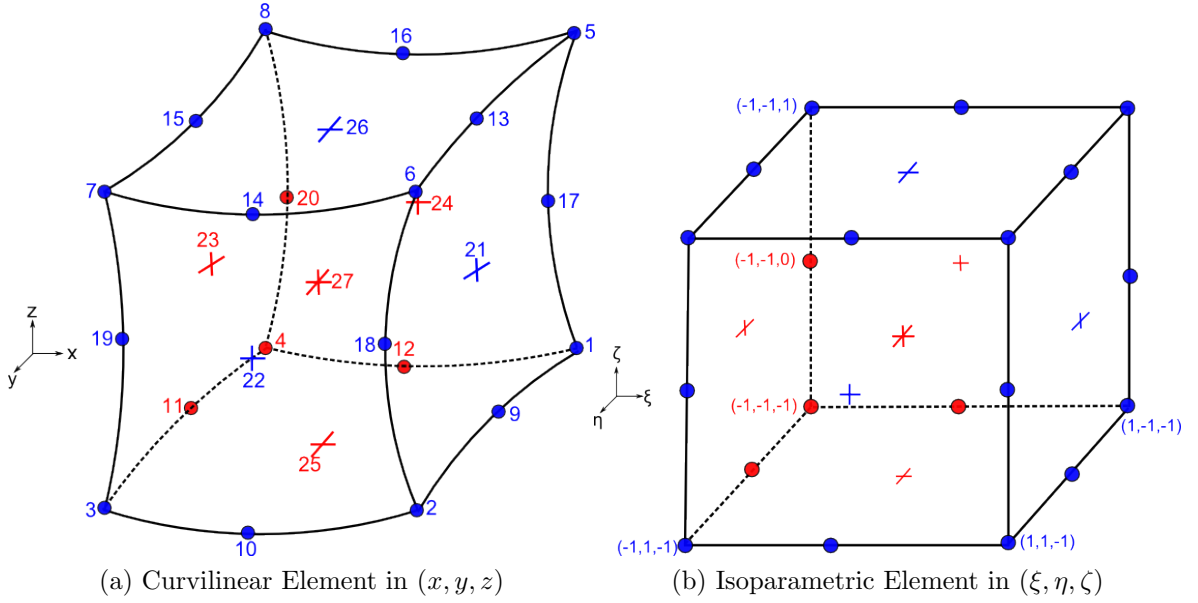


Figure A.3: Curvilinear and Isoparametric Hexahedra used in FEM. The Curvilinear element contains the nodal numbering scheme commonly used in unstructured grids. The Isoparametric element is defined as a cube in $[-1, 1]^3$

with isoparametric (or local) coordinates (ξ, η, ζ) , to then transform the problem back to Cartesian coordinates (Carrillo-Ledesma et al., 2008). In the case of hexahedral elements, the so called isoparametric element will be a rectangular brick with coordinates in the range of $[-1, 1]^3$, and the nodal basis functions are defined on these coordinates $N(\xi, \eta, \zeta)$.

A.2.1 Coordinate Transformation

As mentioned in Section 2.5, the approximation of a function on a point $\mathbf{r} = (x, y, z)$ is made in terms of the nodal basis function N_i , as

$$f(\mathbf{r}) = \sum_{i=1}^{n_e} N_i(\boldsymbol{\xi}) f_i, \quad (\text{A.3})$$

where $i = 1, 2, \dots, n_e$, and n_e is the number of nodes in the element. The nodal basis function is defined with polynomials in local coordinates $\boldsymbol{\xi} = (\xi, \eta, \zeta)$, such that $N_i(\boldsymbol{\xi}_j) = \delta_{ij}$, where $j = 1, 2, \dots, n_e$ (Carrillo-Ledesma et al., 2008). The Kronecker delta function δ_{ij} is

$$\delta_{ij} = \begin{cases} 1 & i = j \\ 0 & \text{otherwise} \end{cases}, \quad (\text{A.4})$$

and means that the nodal function N_i will have a value of 1 on the node ξ_i , and zero on other nodes. Consequently, n_e basis functions are defined on the isoparametric element.

If a function can be interpolated with these basis functions, then a coordinate transformation must exist between (x, y, z) and (ξ, η, ζ) . Any point $\mathbf{r} = (x, y, z)$ is obtained in the same way as with the function approximation:

$$\mathbf{r} = \sum_{i=1}^{n_e} N_i(\xi, \eta, \zeta) \mathbf{r}_i, \quad (\text{A.5})$$

for a location ξ in the isoparametric element.

A function derivative in x direction is obtained as $\partial_x f(\mathbf{r}) = \partial_x N_i(\xi) f_i$. Implicit summation over $i = 1, 2, \dots, n_e$ nodes is considered through this section. Global derivatives of the local nodal function are obtained by the chain rule as

$$\frac{\partial N_i}{\partial x} = \frac{\partial N_i}{\partial \xi} \frac{\partial \xi}{\partial x} + \frac{\partial N_i}{\partial \eta} \frac{\partial \eta}{\partial x} + \frac{\partial N_i}{\partial \zeta} \frac{\partial \zeta}{\partial x}.$$

In matrix form, these derivative are expressed as

$$\begin{pmatrix} \frac{\partial N_i}{\partial x} \\ \frac{\partial N_i}{\partial y} \\ \frac{\partial N_i}{\partial z} \end{pmatrix} = \begin{pmatrix} \frac{\partial \xi}{\partial x} & \frac{\partial \eta}{\partial x} & \frac{\partial \zeta}{\partial x} \\ \frac{\partial \xi}{\partial y} & \frac{\partial \eta}{\partial y} & \frac{\partial \zeta}{\partial y} \\ \frac{\partial \xi}{\partial z} & \frac{\partial \eta}{\partial z} & \frac{\partial \zeta}{\partial z} \end{pmatrix} \begin{pmatrix} \frac{\partial N_i}{\partial \xi} \\ \frac{\partial N_i}{\partial \eta} \\ \frac{\partial N_i}{\partial \zeta} \end{pmatrix}. \quad (\text{A.6})$$

The matrix $\mathbf{J}^{-1} = \frac{\partial(\xi, \eta, \zeta)}{\partial(x, y, z)}$ in Equation (A.6), is the inverse of the Jacobian matrix of transformation. The Jacobian matrix is

$$\begin{aligned} \mathbf{J} &= \frac{\partial(x, y, z)}{\partial(\xi, \eta, \zeta)} \\ &= \begin{pmatrix} x_i \frac{\partial N_i}{\partial \xi} & y_i \frac{\partial N_i}{\partial \xi} & z_i \frac{\partial N_i}{\partial \xi} \\ x_i \frac{\partial N_i}{\partial \eta} & y_i \frac{\partial N_i}{\partial \eta} & z_i \frac{\partial N_i}{\partial \eta} \\ x_i \frac{\partial N_i}{\partial \zeta} & y_i \frac{\partial N_i}{\partial \zeta} & z_i \frac{\partial N_i}{\partial \zeta} \end{pmatrix}. \end{aligned} \quad (\text{A.7})$$

In order to obtain a complete transformation $\xi \rightarrow \mathbf{r}$, \mathbf{J} must be non-singular, i.e. the Jacobian matrix must be invertible (Carrillo-Ledesma et al., 2008).

Using this transformation, the integration is calculated locally, and transformed into the global coordinates by using $dxdydz = |\mathbf{J}|d\xi d\eta d\zeta$. Then, the numerical integration of a function f is approximated with Gaussian Quadrature:

$$\int_{\Omega} f(\mathbf{r}) dxdydz \approx \sum_{i=1}^{p_1} \sum_{j=1}^{p_2} \sum_{k=1}^{p_3} w_i w_j w_k f(\xi_i, \eta_j, \zeta_k) |\mathbf{J}_{ijk}|$$

where (p_1, p_2, p_3) are the number of Gauss quadrature points in each direction, w_i are the Gauss's quadrature weights, (ξ_i, η_j, ζ_k) are the Gauss quadrature points, and $|\mathbf{J}_{ijk}| = \det(\mathbf{J}(\xi_i, \eta_j, \zeta_k))$.

Appendix B

MoVFEM Algorithm

B.1 MT Problem

B.1.1 Maxwell's Equations with Secondary Field Formulation

The secondary field is defined as $\mathbf{F}_s = \mathbf{F} - \mathbf{F}_p$, where $\mathbf{F} \in \{\mathbf{E}, \mathbf{H}\}$. Applying this definition to Maxwell's equations (1.1a) to (1.1d), the following equations are obtained:

$$\begin{aligned}\nabla \times \mathbf{E} - \nabla \times \mathbf{E}_p &= i\omega\boldsymbol{\mu}_p \cdot \mathbf{H}_p - i\omega\boldsymbol{\mu} \cdot \mathbf{H} \\ \nabla \times \mathbf{H} - \nabla \times \mathbf{H}_p &= \boldsymbol{\sigma} \cdot \mathbf{E} - \boldsymbol{\sigma}_p \cdot \mathbf{E}_p \\ \nabla \cdot (\boldsymbol{\mu} \cdot \mathbf{H}) - \nabla \cdot (\boldsymbol{\mu}_p \cdot \mathbf{H}_p) &= 0 \\ \nabla \cdot (\varepsilon \mathbf{E}) - \nabla \cdot (\varepsilon_p \mathbf{E}_p) &= q - q_p\end{aligned}$$

Maxwell's equations with the primary fields describe the field behavior on a primary model $(\boldsymbol{\sigma}_p, \boldsymbol{\mu}_p, \varepsilon_p)$. Substituting the total field (e.g. $\mathbf{F} = \mathbf{F}_p + \mathbf{F}_s$) into previous equations, then

$$\begin{aligned}\nabla \times (\mathbf{E}_p + \mathbf{E}_s) - \nabla \times \mathbf{E}_p &= i\omega\boldsymbol{\mu}_p \cdot \mathbf{H}_p - i\omega\boldsymbol{\mu} \cdot (\mathbf{H}_p + \mathbf{H}_s) \\ \nabla \times (\mathbf{H}_p + \mathbf{H}_s) - \nabla \times \mathbf{H}_p &= \boldsymbol{\sigma} \cdot (\mathbf{E}_p + \mathbf{E}_s) - \boldsymbol{\sigma}_p \cdot \mathbf{E}_p \\ \nabla \cdot (\boldsymbol{\mu} \cdot (\mathbf{H}_p + \mathbf{H}_s)) - \nabla \cdot (\boldsymbol{\mu}_p \cdot \mathbf{H}_p) &= 0 \\ \nabla \cdot (\varepsilon(\mathbf{E}_p + \mathbf{E}_s)) - \nabla \cdot (\varepsilon_p \mathbf{E}_p) &= q - q_p\end{aligned}$$

Subtracting similar terms, and using $\delta\boldsymbol{\nu} = \boldsymbol{\nu} - \boldsymbol{\nu}_p$ for $\boldsymbol{\nu} \in \{\boldsymbol{\sigma}, \boldsymbol{\mu}, \varepsilon, q\}$, then Maxwell's equations based on secondary fields are obtained:

$$\begin{aligned}\nabla \times \mathbf{E}_s + i\omega\boldsymbol{\mu} \cdot \mathbf{H}_s &= -i\omega\delta\boldsymbol{\mu} \cdot \mathbf{H}_p \\ \nabla \times \mathbf{H}_s - \boldsymbol{\sigma} \cdot \mathbf{E}_s &= \delta\boldsymbol{\sigma} \cdot \mathbf{E}_p \\ \nabla \cdot (\boldsymbol{\mu} \cdot \mathbf{H}_s) &= -\nabla \cdot (\boldsymbol{\mu} \cdot \mathbf{H}_p) \\ \nabla \cdot (\varepsilon \mathbf{E}_s) &= \delta q - \nabla \cdot (\varepsilon \mathbf{E}_p).\end{aligned}$$

B.1.2 Homogeneous Earth

As discussed in Section 1.3, EM fields within a homogeneous Earth will have a sinusoidal variation that decays exponentially with depth. Therefore, EM fields for a homogeneous Earth will have a function $f(z)$ describing this behavior (Weaver, 1994,

Chap.2), as

$$\begin{aligned} f(z) &= \frac{1}{\alpha\sqrt{i}} \begin{cases} 1 - z\alpha\sqrt{i} & (-h < z < 0) \\ e^{-z\alpha\sqrt{i}} & (z > 0) \end{cases} \\ f'(z) &= \begin{cases} 1 & (-h < z < 0) \\ e^{-z\alpha\sqrt{i}} & (z > 0) \end{cases}. \end{aligned} \quad (\text{B.1})$$

Earth's surface is located at $z_0 \equiv 0$, the air space will have a height $-h$, and the subsurface ($z > 0$) will have an initial conductivity σ_0 . On this equation, $\alpha = \sqrt{\omega\mu_0\sigma_0}$, where ω is the angular frequency, and μ_0 is the magnetic permeability of free-space.

B.1.3 Layered Earth

In the case of layered Earth, the EM fields are obtained with a transfer function $c(\omega) \equiv c_1$ on the surface ($z_0 \equiv 0$). This transfer function is obtained from Wait's Recursion formula, which calculates the transfer function at the top of n -th layer, from the transfer function at the top of layer $n+1$ (Weaver, 1994, Chap.2). The subsurface has N layers, with conductivities $\{\sigma_1, \sigma_2, \dots, \sigma_N\}$ and thickness $\{d_1, d_2, \dots, d_N\}$, where $d_n = z_{n+1} - z_n$, and $z_{N+1} = \infty$. Then, Wait's recursion formula are as

$$c_n = \frac{1 - r_n e^{(-2\gamma_n d_n)}}{\gamma_n [1 + r_n e^{(-2\gamma_n d_n)}]}; \quad r_n = \frac{1 - \gamma_n c_{n+1}}{1 + \gamma_n c_{n+1}} \quad (\text{B.2a})$$

$$c_N = \frac{1}{\gamma_N}. \quad (\text{B.2b})$$

In these equations, $\gamma_n = \alpha_n \sqrt{i}$, where $\alpha_n = \sqrt{\omega\mu_0\sigma_n}$. The transfer function on the top of N -th layer is (B.2b), and recursion is done with $n = N-1, N-2, \dots, 1$.

In order to obtain the EM fields in the subsurface, a function $e(z)$ is defined which describes a plane wave propagation within a layer n , i.e. $z_n < z < z_{n+1}$, as

$$e(z) = \frac{e_n}{2} \left(1 + \frac{1}{c_n \gamma_n} \right) (1 - r_n e^{-2\gamma_n(z_{n+1}-z)}) e^{-\gamma_n(z-z_n)} \quad (\text{B.3a})$$

$$\begin{aligned} e'(z) &= \frac{-e_n}{2} \left(\gamma_n + \frac{1}{c_n} \right) (1 + r_n e^{-2\gamma_n(z_{n+1}-z)}) e^{-\gamma_n(z-z_n)} \\ e_{n+1} &= \frac{e_n c_{n+1} (1 + c_n \gamma_n)}{c_n (1 + c_{n+1} \gamma_n)} e^{-\gamma_n d_n}. \end{aligned} \quad (\text{B.3b})$$

After calculating the transfer functions, the parameter e_n is obtained by iterating with $n = 2, 3, \dots, N$, where $e_1 = 1$, and e_{n+1} is in equation (B.3b).

B.1.4 MT Governing Equations with GPML

In GPML the MT governing equation is modified by the stretching factors (h_1, h_2, h_3) which transform the coordinate system into complex coordinates. Through this Section, subscripts 1, 2, 3 stands for the 3D coordinates (x, y, z). The modified governing equation is

$$\tilde{\nabla} \times \boldsymbol{\nu}^{-1} \cdot \tilde{\nabla} \times \mathbf{F}_s + i\omega \boldsymbol{\kappa} \cdot \mathbf{F}_s = \tilde{\mathbf{s}}^F, \quad (\text{B.4})$$

and the modified nabla operator is defined as

$$\tilde{\nabla} = \left(\frac{1}{h_1} \frac{\partial}{\partial_1}, \frac{1}{h_2} \frac{\partial}{\partial_2}, \frac{1}{h_3} \frac{\partial}{\partial_3} \right).$$

The curl-curl of Equation (B.4) gives:

$$\begin{aligned} \tilde{\nabla} \times \boldsymbol{\nu}^{-1} \cdot \tilde{\nabla} \times \mathbf{F}_s = & \left(\begin{aligned} & \frac{1}{h_2} \partial_2 \left[\nu_{31} \left(\frac{1}{h_2} \partial_2 F_3 - \frac{1}{h_3} \partial_3 F_2 \right) + \nu_{32} \left(\frac{1}{h_3} \partial_3 F_1 - \frac{1}{h_1} \partial_1 F_3 \right) + \nu_{33} \left(\frac{1}{h_1} \partial_1 F_2 - \frac{1}{h_2} \partial_2 F_1 \right) \right] \\ & \frac{1}{h_3} \partial_3 \left[\nu_{11} \left(\frac{1}{h_2} \partial_2 F_3 - \frac{1}{h_3} \partial_3 F_2 \right) + \nu_{12} \left(\frac{1}{h_3} \partial_3 F_1 - \frac{1}{h_1} \partial_1 F_3 \right) + \nu_{13} \left(\frac{1}{h_1} \partial_1 F_2 - \frac{1}{h_2} \partial_2 F_1 \right) \right] \\ & \frac{1}{h_1} \partial_1 \left[\nu_{21} \left(\frac{1}{h_2} \partial_2 F_3 - \frac{1}{h_3} \partial_3 F_2 \right) + \nu_{22} \left(\frac{1}{h_3} \partial_3 F_1 - \frac{1}{h_1} \partial_1 F_3 \right) + \nu_{23} \left(\frac{1}{h_1} \partial_1 F_2 - \frac{1}{h_2} \partial_2 F_1 \right) \right] \end{aligned} \right) - \\ & \left(\begin{aligned} & \frac{1}{h_3} \partial_3 \left[\nu_{21} \left(\frac{1}{h_2} \partial_2 F_3 - \frac{1}{h_3} \partial_3 F_2 \right) + \nu_{22} \left(\frac{1}{h_3} \partial_3 F_1 - \frac{1}{h_1} \partial_1 F_3 \right) + \nu_{23} \left(\frac{1}{h_1} \partial_1 F_2 - \frac{1}{h_2} \partial_2 F_1 \right) \right] \\ & \frac{1}{h_1} \partial_1 \left[\nu_{31} \left(\frac{1}{h_2} \partial_2 F_3 - \frac{1}{h_3} \partial_3 F_2 \right) + \nu_{32} \left(\frac{1}{h_3} \partial_3 F_1 - \frac{1}{h_1} \partial_1 F_3 \right) + \nu_{33} \left(\frac{1}{h_1} \partial_1 F_2 - \frac{1}{h_2} \partial_2 F_1 \right) \right] \\ & \frac{1}{h_2} \partial_2 \left[\nu_{11} \left(\frac{1}{h_2} \partial_2 F_3 - \frac{1}{h_3} \partial_3 F_2 \right) + \nu_{12} \left(\frac{1}{h_3} \partial_3 F_1 - \frac{1}{h_1} \partial_1 F_3 \right) + \nu_{13} \left(\frac{1}{h_1} \partial_1 F_2 - \frac{1}{h_2} \partial_2 F_1 \right) \right] \end{aligned} \right) \end{aligned}$$

Multiplying the left hand side of Equation (B.4) by $h_1 h_2 h_3$, and factorizing the terms related to F_1 , F_2 , and F_3 separately, we have

$$\begin{aligned} h_1 h_2 h_3 [\tilde{\nabla} \times \boldsymbol{\nu}^{-1} \cdot \tilde{\nabla} \times \mathbf{F}_s + i\omega \boldsymbol{\kappa} \cdot \mathbf{F}_s] = & \left(\begin{aligned} & (h_1 \nu_{32} + h_1 \nu_{23}) \partial_{23} F_1 - \frac{h_1 h_3}{h_2} \nu_{33} \partial_{22} F_1 - \frac{h_1 h_2}{h_3} \nu_{22} \partial_{33} F_1 + i\omega h_1 h_2 h_3 \kappa_{11} F_1 \\ & h_3 \nu_{33} \partial_{12} F_1 - h_2 \nu_{32} \partial_{13} F_1 - h_1 \nu_{13} \partial_{23} F_1 + \frac{h_1 h_2}{h_3} \nu_{12} \partial_{33} F_1 + i\omega h_1 h_2 h_3 \kappa_{21} F_1 \\ & h_2 \nu_{22} \partial_{13} F_1 - h_3 \nu_{23} \partial_{12} F_1 + \frac{h_1 h_3}{h_2} \nu_{13} \partial_{22} F_1 - h_1 \nu_{12} \partial_{23} F_1 + i\omega h_1 h_2 h_3 \kappa_{31} F_1 \end{aligned} \right) + \\ & \left(\begin{aligned} & h_3 \nu_{33} \partial_{12} F_2 - h_2 \nu_{23} \partial_{13} F_2 - h_1 \nu_{31} \partial_{23} F_2 + \frac{h_1 h_2}{h_3} \nu_{21} \partial_{33} F_2 + i\omega h_1 h_2 h_3 \kappa_{12} F_2 \\ & (h_2 \nu_{13} + h_2 \nu_{31}) \partial_{13} F_2 - \frac{h_2 h_3}{h_1} \nu_{33} \partial_{11} F_2 - \frac{h_1 h_2}{h_3} \nu_{11} \partial_{33} F_2 + i\omega h_1 h_2 h_3 \kappa_{22} F_2 \\ & h_1 \nu_{11} \partial_{23} F_2 - h_3 \nu_{13} \partial_{12} F_2 + \frac{h_2 h_3}{h_1} \nu_{23} \partial_{11} F_2 - h_2 \nu_{21} \partial_{13} F_2 + i\omega h_1 h_2 h_3 \kappa_{32} F_2 \end{aligned} \right) + \\ & \left(\begin{aligned} & h_2 \nu_{22} \partial_{13} F_3 - h_3 \nu_{32} \partial_{12} F_3 - h_1 \nu_{21} \partial_{23} F_3 + \frac{h_1 h_3}{h_2} \nu_{31} \partial_{22} F_3 + i\omega h_1 h_2 h_3 \kappa_{13} F_3 \\ & h_1 \nu_{11} \partial_{23} F_3 - h_3 \nu_{31} \partial_{12} F_3 + \frac{h_2 h_3}{h_1} \nu_{32} \partial_{11} F_3 - h_2 \nu_{12} \partial_{13} F_3 + i\omega h_1 h_2 h_3 \kappa_{23} F_3 \\ & (h_3 \nu_{21} + h_3 \nu_{12}) \partial_{12} F_3 - \frac{h_2 h_3}{h_1} \nu_{22} \partial_{11} F_3 - \frac{h_1 h_3}{h_2} \nu_{11} \partial_{22} F_3 + i\omega h_1 h_2 h_3 \kappa_{33} F_3 \end{aligned} \right). \end{aligned}$$

The source term becomes

$$\begin{aligned} \tilde{\mathbf{s}} = h_1 h_2 h_3 & \begin{cases} -i\omega \delta \boldsymbol{\sigma} \cdot \mathbf{E}_p & \text{For E-PDE} \\ \tilde{\nabla} \times (\boldsymbol{\sigma}^{-1} \delta \boldsymbol{\sigma} \cdot \mathbf{E}_p) & \text{For H-PDE} \end{cases} \\ = & \begin{cases} -i\omega h_1 h_2 h_3 \delta \boldsymbol{\sigma} \cdot \mathbf{E}_p & \text{For E-PDE} \\ \left(\begin{aligned} & h_1 h_3 \partial_2 (\boldsymbol{\sigma}^{-1} \delta \boldsymbol{\sigma} \cdot \mathbf{E}_p)_3 - h_1 h_2 \partial_3 (\boldsymbol{\sigma}^{-1} \delta \boldsymbol{\sigma} \cdot \mathbf{E}_p)_2 \\ & h_1 h_2 \partial_3 (\boldsymbol{\sigma}^{-1} \delta \boldsymbol{\sigma} \cdot \mathbf{E}_p)_1 - h_2 h_3 \partial_1 (\boldsymbol{\sigma}^{-1} \delta \boldsymbol{\sigma} \cdot \mathbf{E}_p)_3 \\ & h_2 h_3 \partial_1 (\boldsymbol{\sigma}^{-1} \delta \boldsymbol{\sigma} \cdot \mathbf{E}_p)_2 - h_1 h_3 \partial_2 (\boldsymbol{\sigma}^{-1} \delta \boldsymbol{\sigma} \cdot \mathbf{E}_p)_1 \end{aligned} \right) & \text{For H-PDE} \end{cases}. \end{aligned}$$

Consequently, the stretching factors in Equation (B.4) can be factorized, to obtain the MT governing equation with GPML:

$$\nabla \times \tilde{\boldsymbol{\nu}}^{-1} \cdot \nabla \times \mathbf{F}_s + i\omega \tilde{\boldsymbol{\kappa}} \cdot \mathbf{F}_s = \tilde{\mathbf{s}}^F. \quad (\text{B.5})$$

The modified model tensors are

$$\tilde{\nu} = \{\tilde{\nu}_{\gamma m}^{\beta n}\} = \left\{ \nu_{\gamma m} \frac{h^{(x_1+x_2+x_3)}}{h_\beta h_n} \right\} \quad (\text{B.6})$$

$$\begin{aligned} \tilde{\kappa} &= h^{(x_1+x_2+x_3)} \kappa \\ h^{(x_1+x_2+x_3)} &= h_1 h_2 h_3, \end{aligned} \quad (\text{B.7})$$

where indices (β, n) are related to the partial derivatives in the curl-curl components, and (γ, m) to the corresponding tensor component.

B.2 Complete Nodal Basis Functions

This section contains the formulation of nodal basis functions for all nodes on the three element schemes. Figure 3.4 shows the local numbering scheme of elements' nodes with index i in the following equations.

Linear Element: 8 Nodes

$$N_i = \frac{1}{8}(1 + \xi_i \xi)(1 + \eta_i \eta)(1 + \zeta_i \zeta) \quad i = \{1, 2, 3, 4, 5, 6, 7, 8\}$$

Quadratic Element: 20 Nodes

$$N_i = \begin{cases} \frac{1}{8}(1 + \xi_i \xi)(1 + \eta_i \eta)(1 + \zeta_i \zeta)(\xi_i \xi + \eta_i \eta + \zeta_i \zeta - 2) & i = \{1, 2, 3, 4, 5, 6, 7, 8\} \\ \frac{1}{4}(1 - \xi^2)(1 + \eta_i \eta)(1 + \zeta_i \zeta) & i = \{10, 12, 14, 16\} \\ \frac{1}{4}(1 + \xi_i \xi)(1 - \eta^2)(1 + \zeta_i \zeta) & i = \{9, 11, 13, 15\} \\ \frac{1}{4}(1 + \xi_i \xi)(1 + \eta_i \eta)(1 - \zeta^2) & i = \{17, 18, 19, 20\} \end{cases}$$

Lagrangian Element: 27 Nodes

$$N_i = \begin{cases} \frac{1}{8}(1 + \xi_i \xi)(1 + \eta_i \eta)(1 + \zeta_i \zeta)\xi_i \xi \eta_i \eta \zeta_i \zeta & i = \{1, 2, 3, 4, 5, 6, 7, 8\} \\ \frac{1}{4}(1 - \xi^2)(1 + \eta_i \eta)(1 + \zeta_i \zeta)\eta_i \eta \zeta_i \zeta & i = \{10, 12, 14, 16\} \\ \frac{1}{4}(1 + \xi_i \xi)(1 - \eta^2)(1 + \zeta_i \zeta)\xi_i \xi \zeta_i \zeta & i = \{9, 11, 13, 15\} \\ \frac{1}{4}(1 + \xi_i \xi)(1 + \eta_i \eta)(1 - \zeta^2)\xi_i \xi \eta_i \eta & i = \{17, 18, 19, 20\} \\ \frac{1}{2}(1 + \xi_i \xi)(1 - \eta^2)(1 - \zeta^2)\xi_i \xi & i = \{21, 23\} \\ \frac{1}{2}(1 - \xi^2)(1 + \eta_i \eta)(1 - \zeta^2)\eta_i \eta & i = \{22, 24\} \\ \frac{1}{2}(1 - \xi^2)(1 - \eta^2)(1 + \zeta_i \zeta)\zeta_i \zeta & i = \{25, 26\} \\ (1 - \xi^2)(1 - \eta^2)(1 - \zeta^2) & i = 27 \end{cases}$$

B.3 Complete Multi-Order Vector Basis Functions

The formulation of mixed-order polynomials for all vector basis functions will be presented here. On each element case, a figure with the local edge numbering scheme is shown. These are, Figure B.1 for the linear element, Figure B.2 for the quadratic element, and Figure B.3 for the Lagrangian element. On these equations, index i belongs to the edge number, and index j belongs to the nodal number defining the edge as in Figure 3.4.

Linear element: 12 Edges

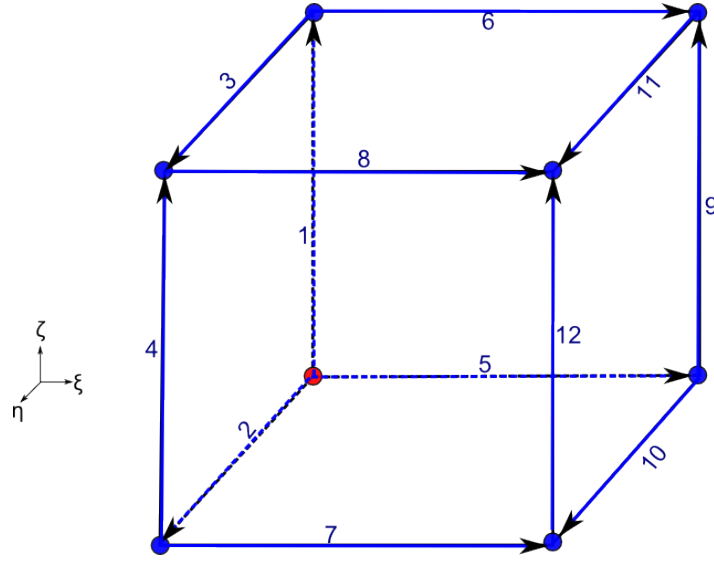


Figure B.1: Numbering scheme for 12 vector basis functions of linear element.

Vector basis on element edges:

$$\mathbf{v}_i = \begin{cases} \frac{1}{4}(1 + \eta_j\eta)(1 + \zeta_j\zeta)\nabla\xi & i = \{5, 6, 7, 8\} & j = \{4, 8, 3, 7\} \\ \frac{1}{4}(1 + \xi_j\xi)(1 + \zeta_j\zeta)\nabla\eta & i = \{2, 3, 10, 11\} & j = \{4, 8, 1, 5\} \\ \frac{1}{4}(1 + \xi_j\xi)(1 + \eta_j\eta)\nabla\zeta & i = \{1, 4, 9, 12\} & j = \{4, 3, 1, 2\} \end{cases}$$

Quadratic element: 36 Edges

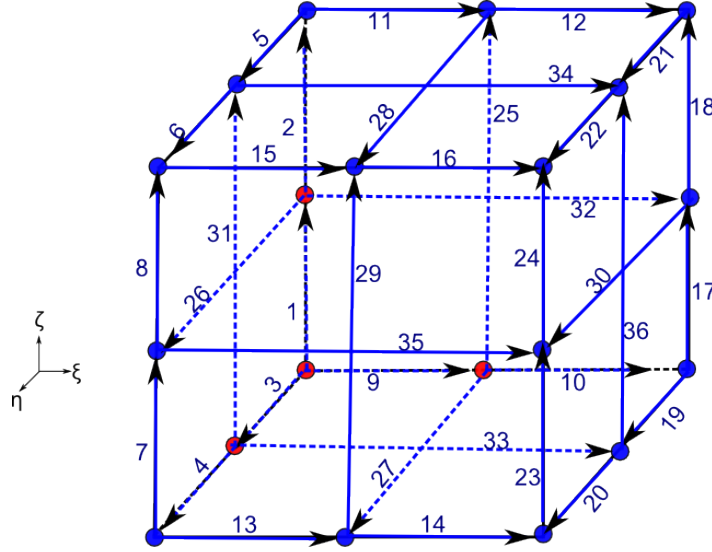


Figure B.2: Numbering scheme for 36 vector basis functions of quadratic element.

Vector basis on element edges:

$$\mathbf{v}_i = \begin{cases} \frac{1}{8}(1 + \eta_j\eta)(1 + \zeta_j\zeta)(\xi_j\xi + \eta_j\eta + \zeta_j\zeta - 1)\nabla\xi & i = \{9, 10, 11, 12, 13, 14, 15, 16\} \\ & j = \{4, 1, 8, 5, 3, 2, 7, 6\} \\ \frac{1}{8}(1 + \xi_j\xi)(1 + \zeta_j\zeta)(\xi_j\xi + \eta_j\eta + \zeta_j\zeta - 1)\nabla\eta & i = \{3, 4, 5, 6, 19, 20, 21, 22\} \\ & j = \{4, 1, 8, 5, 3, 2, 7, 6\} \\ \frac{1}{8}(1 + \xi_j\xi)(1 + \eta_j\eta)(\xi_j\xi + \eta_j\eta + \zeta_j\zeta - 1)\nabla\zeta & i = \{1, 2, 7, 8, 17, 18, 23, 24\} \\ & j = \{4, 8, 3, 7, 1, 5, 2, 6\} \end{cases}$$

Vector basis on the (ξ, η) faces of the element:

$$\mathbf{v}_i = \begin{cases} \frac{1}{2}(1 - \eta^2)(1 + \zeta_j\zeta)\nabla\xi & i = \{33, 34\} \quad j = \{11, 15\} \\ \frac{1}{2}(1 - \xi^2)(1 + \zeta_j\zeta)\nabla\eta & i = \{27, 28\} \quad j = \{12, 16\} \end{cases}$$

Vector basis on the (ξ, ζ) faces of the element:

$$\mathbf{v}_i = \begin{cases} \frac{1}{2}(1 + \eta_i\eta)(1 - \zeta^2)\nabla\xi & i = \{32, 35\} \quad j = \{20, 19\} \\ \frac{1}{2}(1 - \xi^2)(1 + \eta_j\eta)\nabla\zeta & i = \{25, 29\} \quad j = \{12, 10\} \end{cases}$$

Vector basis on the (η, ζ) faces of the element:

$$\mathbf{v}_i = \begin{cases} \frac{1}{2}(1 + \xi_j\xi)(1 - \zeta^2)\nabla\eta & i = \{26, 30\} \quad j = \{20, 17\} \\ \frac{1}{2}(1 + \xi_j\xi)(1 - \eta^2)\nabla\zeta & i = \{31, 36\} \quad j = \{11, 9\} \end{cases}$$

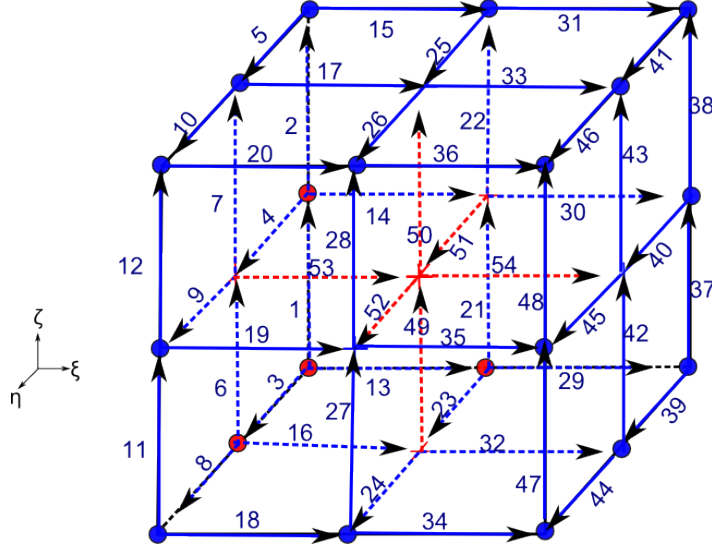
Lagrangian element: 54 Edges

Figure B.3: Numbering scheme for 54 vector basis functions of Lagrangian element.

Vector basis on element edges:

$$\mathbf{v}_i = \begin{cases} \frac{1}{8}(1 + \xi_j \xi)(1 + \eta_j \eta)(1 + \zeta_j \zeta) \eta_j \eta \zeta_j \zeta \nabla \xi & i = \{13, 15, 18, 20, 29, 31, 34, 36\} \\ & j = \{4, 8, 3, 7, 1, 5, 2, 6\} \\ \frac{1}{8}(1 + \xi_j \xi)(1 + \eta_j \eta)(1 + \zeta_j \zeta) \xi_j \xi \zeta_j \zeta \nabla \eta & i = \{3, 5, 8, 10, 39, 41, 44, 46\} \\ & j = \{4, 8, 3, 7, 1, 5, 2, 6\} \\ \frac{1}{8}(1 + \xi_j \xi)(1 + \eta_j \eta)(1 + \zeta_j \zeta) \xi_j \xi \eta_j \eta \nabla \zeta & i = \{1, 2, 11, 12, 37, 38, 47, 48\} \\ & j = \{4, 8, 3, 7, 1, 5, 2, 6\} \end{cases}$$

Vector basis on the (ξ, η) faces of the element:

$$\mathbf{v}_i = \begin{cases} \frac{1}{4}(1 + \xi_j \xi)(1 - \eta^2)(1 + \zeta_j \zeta) \zeta_j \zeta \nabla \xi & i = \{16, 17, 32, 33\} \quad j = \{11, 15, 9, 13\} \\ \frac{1}{4}(1 - \xi^2)(1 + \eta_j \eta)(1 + \zeta_j \zeta) \zeta_j \zeta \nabla \eta & i = \{23, 24, 25, 26\} \quad j = \{12, 10, 16, 14\} \end{cases}$$

Vector basis on the (ξ, ζ) faces of the element:

$$\mathbf{v}_i = \begin{cases} \frac{1}{4}(1 + \xi_j \xi)(1 + \eta_j \eta)(1 - \zeta^2) \eta_j \eta \nabla \xi & i = \{14, 19, 30, 35\} \quad j = \{20, 19, 17, 18\} \\ \frac{1}{4}(1 - \xi^2)(1 + \eta_j \eta)(1 + \zeta_j \zeta) \eta_j \eta \nabla \zeta & i = \{21, 22, 27, 28\} \quad j = \{12, 16, 10, 14\} \end{cases}$$

Vector basis on the (η, ζ) faces of the element:

$$\mathbf{v}_i = \begin{cases} \frac{1}{4}(1 + \xi_j \xi)(1 + \eta_j \eta)(1 - \zeta^2) \xi_j \xi \nabla \eta & i = \{4, 9, 40, 45\} \quad j = \{20, 19, 17, 18\} \\ \frac{1}{4}(1 + \xi_j \xi)(1 - \eta^2)(1 + \zeta_j \zeta) \xi_j \xi \nabla \zeta & i = \{6, 7, 42, 43\} \quad j = \{11, 15, 9, 13\} \end{cases}$$

Vector basis on the center of element:

$$\mathbf{v}_i = \begin{cases} \frac{1}{2}(1 + \xi_j \xi)(1 - \eta^2)(1 - \zeta^2) \nabla \xi & i = \{53, 54\} \quad j = \{23, 21\} \\ \frac{1}{2}(1 - \xi^2)(1 + \eta_j \eta)(1 - \zeta^2) \nabla \eta & i = \{51, 52\} \quad j = \{24, 22\} \\ \frac{1}{2}(1 - \xi^2)(1 - \eta^2)(1 + \zeta_i \zeta) \nabla \zeta & i = \{49, 50\} \quad j = \{25, 26\} \end{cases}$$

B.4 Covariant Basis Vectors

Covariant Projections Crowley (1988) defined the field as a projection to some curvilinear basis vector. On this section, a discussion of how these basis vectors are defined by (Crowley, 1988) will be shown.

A Cartesian point is defined with the unit vectors

$$(\vec{e}_1, \vec{e}_2, \vec{e}_3) = \begin{pmatrix} 1 & 0 & 0 \\ 0 & 1 & 0 \\ 0 & 0 & 1 \end{pmatrix}, \quad (\text{B.8})$$

as $\vec{r} = x_1 \vec{e}_1 + x_2 \vec{e}_2 + x_3 \vec{e}_3$. Through this Section, indices $i = \{1, 2, 3\}$ stands for the coordinates (x, y, z) in x_i , and for the isoparametric coordinates (ξ, η, ζ) in ξ_i . From this definition, the field in Cartesian coordinates is defined as $\vec{F} = F_1 \vec{e}_1 + F_2 \vec{e}_2 + F_3 \vec{e}_3$.

Then, a new basis can be defined from the Cartesian unit vectors as

$$\vec{\xi}_\nu = \mathbf{J}_{\nu k} \vec{e}_k \quad (\text{B.9})$$

where $\nu = \{1, 2, 3\}$, and \mathbf{J} is the Jacobian matrix of transformation

$$\mathbf{J} = \begin{pmatrix} \frac{\partial x_1}{\partial \xi_1} & \frac{\partial x_2}{\partial \xi_1} & \frac{\partial x_3}{\partial \xi_1} \\ \frac{\partial x_1}{\partial \xi_2} & \frac{\partial x_2}{\partial \xi_2} & \frac{\partial x_3}{\partial \xi_2} \\ \frac{\partial x_1}{\partial \xi_3} & \frac{\partial x_2}{\partial \xi_3} & \frac{\partial x_3}{\partial \xi_3} \end{pmatrix} = \begin{pmatrix} \vec{\xi}_1 \\ \vec{\xi}_2 \\ \vec{\xi}_3 \end{pmatrix}. \quad (\text{B.10})$$

In equation (B.9), implicit summation over $k = \{1, 2, 3\}$ will define the curvilinear basis vector as

$$\vec{\xi}_\nu = \frac{\partial x_1}{\partial \xi_\nu} \vec{e}_1 + \frac{\partial x_2}{\partial \xi_\nu} \vec{e}_2 + \frac{\partial x_3}{\partial \xi_\nu} \vec{e}_3.$$

Consequently, the curvilinear basis vectors are defined with ν constant, as

$$\vec{\xi}_1 = \frac{\partial \vec{r}}{\partial \xi_1}; \quad \vec{\xi}_2 = \frac{\partial \vec{r}}{\partial \xi_2}; \quad \vec{\xi}_3 = \frac{\partial \vec{r}}{\partial \xi_3}. \quad (\text{B.11})$$

These vectors are parallel to surfaces of constant ξ_1 , ξ_2 , and ξ_3 , respectively, and define a non-orthogonal curvilinear basis system (Crowley, 1988). With these basis, the field covariant projections are defined as $F_{\xi_\nu} = \mathbf{F} \cdot \vec{\xi}_\nu$.

If a complete coordinate transformation exist, then the inverse mapping will be

$$\vec{e}_k = \mathbf{J}_{k\nu}^{-1} \vec{\xi}_\nu \quad (\text{B.12})$$

$$\mathbf{J}^{-1} = \begin{pmatrix} \frac{\partial \xi_1}{\partial x_1} & \frac{\partial \xi_2}{\partial x_1} & \frac{\partial \xi_3}{\partial x_1} \\ \frac{\partial \xi_1}{\partial x_2} & \frac{\partial \xi_2}{\partial x_2} & \frac{\partial \xi_3}{\partial x_2} \\ \frac{\partial \xi_1}{\partial x_3} & \frac{\partial \xi_2}{\partial x_3} & \frac{\partial \xi_3}{\partial x_3} \end{pmatrix}. \quad (\text{B.13})$$

In this case, implicit summation over $\nu = \{1, 2, 3\}$ will define the vector (\vec{e}_k) as

$$\vec{e}_k = \frac{\partial \xi_1}{\partial x_k} \frac{\partial \vec{r}}{\partial \xi_1} + \frac{\partial \xi_2}{\partial x_k} \frac{\partial \vec{r}}{\partial \xi_2} + \frac{\partial \xi_3}{\partial x_k} \frac{\partial \vec{r}}{\partial \xi_3}.$$

Crowley (1988) defined a reciprocal basis as

$$\begin{aligned}\nabla \xi_1 &= (1/|\mathbf{J}|)(\vec{\xi}_2 \times \vec{\xi}_3) \\ \nabla \xi_2 &= (1/|\mathbf{J}|)(\vec{\xi}_3 \times \vec{\xi}_1) \\ \nabla \xi_3 &= (1/|\mathbf{J}|)(\vec{\xi}_1 \times \vec{\xi}_2)\end{aligned}\tag{B.14}$$

$$|\mathbf{J}| = \vec{\xi}_1 \cdot (\vec{\xi}_2 \times \vec{\xi}_3).\tag{B.15}$$

which are vectors normal to surface of constant ξ_1 , ξ_2 , and ξ_3 , respectively. The reciprocal basis and the curvilinear basis are orthogonal: $\nabla \xi_\nu \cdot \vec{\xi}_\gamma = \delta_{\nu\gamma}$, where δ is the Kronecker delta function. In consequence, the reciprocal basis vectors define the inverse of the Jacobian, as

$$\mathbf{J}^{-1} = (\nabla \xi_1, \nabla \xi_2, \nabla \xi_3).\tag{B.16}$$

This reciprocal basis allows the field to be defined in terms of covariant projections (Crowley, 1988), therefore the total field is defined as

$$\mathbf{F} = F_{\xi_1} \nabla \xi_1 + F_{\xi_2} \nabla \xi_2 + F_{\xi_3} \nabla \xi_3.$$

B.5 Curl of Basis Vector

Nam et al. (2007) defined the curl of linear basis vector on $\hat{\xi}$ direction, as

$$\begin{aligned}\nabla \times \mathbf{v}_i &= \frac{1}{4} [\eta_j \nabla \eta \times \nabla \xi + \zeta_j \nabla \zeta \times \nabla \xi + \eta_j \zeta_j \nabla(\eta \zeta) \times \nabla \xi], \\ \nabla(\eta \zeta) &= \left(\eta \frac{\partial \zeta}{\partial x} + \zeta \frac{\partial \eta}{\partial x} \right) \hat{\mathbf{i}} + \left(\eta \frac{\partial \zeta}{\partial y} + \zeta \frac{\partial \eta}{\partial y} \right) \hat{\mathbf{j}} + \left(\eta \frac{\partial \zeta}{\partial z} + \zeta \frac{\partial \eta}{\partial z} \right) \hat{\mathbf{k}}\end{aligned}\tag{B.17}$$

This equation can be factorized as

$$\nabla \times \mathbf{v}_i = \frac{1}{4} [\eta_j \nabla \eta + \zeta_j \nabla \zeta + \eta_j \zeta_j \nabla(\eta \zeta)] \times \nabla \xi.$$

In order to proof that the definition of the curl is $\nabla \times \mathbf{v}_i = \nabla N_{\xi i} \times \nabla \xi$,

$$\nabla N_{\xi i} = \frac{1}{4} [\eta_j \nabla \eta + \zeta_j \nabla \zeta + \eta_j \zeta_j \nabla(\eta \zeta)]\tag{B.18}$$

has to be demonstrated. By the chain rule of differentiation the gradient of this polynomial is obtained as:

$$\begin{aligned}\nabla N_{\xi i} &= \left(\frac{\partial N_{\xi i}}{\partial \xi} \frac{\partial \xi}{\partial x} + \frac{\partial N_{\xi i}}{\partial \eta} \frac{\partial \eta}{\partial x} + \frac{\partial N_{\xi i}}{\partial \zeta} \frac{\partial \zeta}{\partial x} \right) \hat{\mathbf{i}} \\ &+ \left(\frac{\partial N_{\xi i}}{\partial \xi} \frac{\partial \xi}{\partial y} + \frac{\partial N_{\xi i}}{\partial \eta} \frac{\partial \eta}{\partial y} + \frac{\partial N_{\xi i}}{\partial \zeta} \frac{\partial \zeta}{\partial y} \right) \hat{\mathbf{j}} \\ &+ \left(\frac{\partial N_{\xi i}}{\partial \xi} \frac{\partial \xi}{\partial z} + \frac{\partial N_{\xi i}}{\partial \eta} \frac{\partial \eta}{\partial z} + \frac{\partial N_{\xi i}}{\partial \zeta} \frac{\partial \zeta}{\partial z} \right) \hat{\mathbf{k}}.\end{aligned}$$

The linear mixed-order polynomial on $\hat{\xi}$ direction is defined as

$$N_{\xi i} = \frac{1}{4}(1 + \eta_j - \eta)(1 + \zeta_j \zeta), \quad (\text{B.19})$$

and its partial derivatives over local coordinates are

$$\frac{\partial N_{\xi i}}{\partial \xi} = 0 \quad (\text{B.20})$$

$$\frac{\partial N_{\xi i}}{\partial \eta} = \frac{1}{4}\eta_j(1 + \zeta_j \zeta) \quad (\text{B.21})$$

$$\frac{\partial N_{\xi i}}{\partial \zeta} = \frac{1}{4}\zeta_j(1 + \eta_j \eta). \quad (\text{B.22})$$

The $\hat{\mathbf{i}}$ -th component of the gradient is

$$\nabla N_{\xi i} \hat{\mathbf{i}} = \frac{1}{4} \left[\eta_j(1 + \zeta_j \zeta) \frac{\partial \eta}{\partial x} + \zeta_j(1 + \eta_j \eta) \frac{\partial \zeta}{\partial x} \right].$$

Multiplying the terms in this component, and factorizing the terms with η_j , ζ_j , and $\eta_j \zeta_j$, then

$$\nabla N_{\xi i} \hat{\mathbf{i}} = \eta_j \frac{\partial \eta}{\partial x} + \zeta_j \frac{\partial \zeta}{\partial x} + \eta_j \zeta_j \left(\eta \frac{\partial \zeta}{\partial x} + \zeta \frac{\partial \eta}{\partial x} \right).$$

Applying the same procedure to $\hat{\mathbf{j}}$, and $\hat{\mathbf{k}}$ components:

$$\begin{aligned} \nabla N_{\xi i} \hat{\mathbf{j}} &= \eta_j \frac{\partial \eta}{\partial y} + \zeta_j \frac{\partial \zeta}{\partial y} + \eta_j \zeta_j \left(\eta \frac{\partial \zeta}{\partial y} + \zeta \frac{\partial \eta}{\partial y} \right) \\ \nabla N_{\xi i} \hat{\mathbf{k}} &= \underbrace{\eta_j \frac{\partial \eta}{\partial z}}_1 + \underbrace{\zeta_j \frac{\partial \zeta}{\partial z}}_2 + \underbrace{\eta_j \zeta_j \left(\eta \frac{\partial \zeta}{\partial z} + \zeta \frac{\partial \eta}{\partial z} \right)}_3. \end{aligned}$$

From the three terms on previous equations, it can be concluded that the gradient of mixed-order polynomial can be defined as in Equation (B.18). Consequently, the curl of the vector basis function can be defined as

$$\nabla \times \mathbf{v}_i = \nabla N_{\xi i} \times \nabla \xi.$$

Same applies to basis vectors on other directions. The advantage of this definition is that its implementation is easy for high-order elements.

B.6 Assembly

The global assembly procedure is done by summing all the elements on the domain. Shared edges between elements are summed into the same component of the global matrix, according to the index of global degree of freedom (\mathbf{G}_{NE}). A sparse matrix is obtained because not all the edges of each element are shared with all the elements in the domain. For example, consider 2 elements with 5 edges, their respective local matrices of $[5 \times 5]$, and three shared edges. The local matrix for each element i is

$$\bar{\mathbf{M}}^{(i)} = \begin{pmatrix} m_{11}^i & m_{12}^i & m_{13}^i & m_{14}^i & m_{15}^i \\ m_{21}^i & m_{22}^i & m_{23}^i & m_{24}^i & m_{25}^i \\ m_{31}^i & m_{32}^i & m_{33}^i & m_{34}^i & m_{35}^i \\ m_{41}^i & m_{42}^i & m_{43}^i & m_{44}^i & m_{45}^i \\ m_{51}^i & m_{52}^i & m_{53}^i & m_{54}^i & m_{55}^i \end{pmatrix}, \quad (\text{B.23})$$

and their global degrees of freedom are

$$\mathbf{G}_{NE}(1) = \{3, 4, 5, 6, 7\}; \quad \mathbf{G}_{NE}(2) = \{4, 6, 7, 8, 9\}. \quad (\text{B.24})$$

Shared edges have global indices of $\{4, 6, 7\}$.

Then, the global matrix for these two elements is

$$\begin{aligned} \bar{\mathbf{M}} &= \bar{\mathbf{M}}^{(1)} + \bar{\mathbf{M}}^{(2)} \\ &= \begin{pmatrix} \text{DoF} & 3 & 4 & 5 & 6 & 7 & 8 & 9 & \dots \\ 3 & m_{11}^1 & m_{12}^1 & m_{13}^1 & m_{14}^1 & m_{15}^1 & 0 & 0 & \\ 4 & m_{21}^1 & m_{22}^1 + m_{11}^2 & m_{23}^1 & m_{24}^1 + m_{12}^2 & m_{25}^1 + m_{13}^2 & m_{14}^2 & m_{15}^2 & \\ 5 & m_{31}^1 & m_{32}^1 & m_{33}^1 & m_{34}^1 & m_{35}^1 & 0 & 0 & \\ 6 & m_{41}^1 & m_{42}^1 + m_{21}^2 & m_{43}^1 & m_{44}^1 + m_{22}^2 & m_{45}^1 + m_{23}^2 & m_{24}^2 & m_{25}^2 & \\ 7 & m_{51}^1 & m_{52}^1 + m_{31}^2 & m_{53}^1 & m_{54}^1 + m_{32}^2 & m_{55}^1 + m_{33}^2 & m_{34}^2 & m_{35}^2 & \\ 8 & 0 & m_{41}^2 & 0 & m_{42}^2 & m_{43}^2 & m_{44}^2 & m_{45}^2 & \\ 9 & 0 & m_{51}^2 & 0 & m_{52}^2 & m_{53}^2 & m_{54}^2 & m_{55}^2 & \\ \vdots & & & & & & & & \end{pmatrix} \end{aligned}$$

In order to store only the non-zero components of the global matrix, an index array called \mathbf{NZ}_A contains the indices of the non-zero entries of the global matrix for each element, also taking into consideration shared edges. For the example shown previously, global indices for the non-zero entries on each element are

$$\mathbf{NZ}_A^{(1)} = \begin{pmatrix} 1 & 2 & 3 & 4 & 5 \\ 6 & 7 & 8 & 9 & 10 \\ 11 & 12 & 13 & 14 & 15 \\ 16 & 17 & 18 & 19 & 20 \\ 21 & 22 & 23 & 24 & 25 \end{pmatrix}; \quad \mathbf{NZ}_A^{(2)} = \begin{pmatrix} 7 & 9 & 10 & 26 & 27 \\ 17 & 19 & 20 & 28 & 29 \\ 22 & 24 & 25 & 30 & 31 \\ 32 & 33 & 34 & 35 & 36 \\ 37 & 38 & 39 & 40 & 41 \end{pmatrix}.$$

Then, the global matrix with these indices is

$$\bar{\mathbf{M}}_{NZ} = \begin{pmatrix} \text{DoF} & 3 & 4 & 5 & 6 & 7 & 8 & 9 & \dots \\ 3 & 1 & 2 & 3 & 4 & 5 & 0 & 0 & \\ 4 & 6 & 7 & 8 & 9 & 10 & 26 & 27 & \\ 5 & 11 & 12 & 13 & 14 & 15 & 0 & 0 & \\ 6 & 16 & 17 & 18 & 19 & 20 & 28 & 29 & \\ 7 & 21 & 22 & 23 & 24 & 25 & 30 & 31 & \\ 8 & 0 & 32 & 0 & 33 & 34 & 35 & 36 & \\ 9 & 0 & 37 & 0 & 38 & 39 & 40 & 41 & \\ \vdots & & & & & & & & \end{pmatrix}.$$

The sparse array (\mathbf{A}) will have a size of [41] in this example. As it can be noticed from $\bar{\mathbf{M}}_{NZ}$, the arrays \mathbf{IA} and \mathbf{JA} with indices (i, j) of the global matrix will not be in the proper order of rows and columns. This is because the numbering of non-zero entries is done per elements, and that is why a sorting algorithm is used to arrange these entries in their correct rows and columns order.

Appendix C

Fortran Program

This program is described by the flow of operations contained in Figures C.1 to C.2b. The steps of these flowcharts will be described, with emphasis on the input/output files used in MoVFEM.

Global Flowchart Figure C.1 describes the process of the complete Fortran program. Two input files are used in this program, 3DEM_FEM.INP and PARAM.INP.

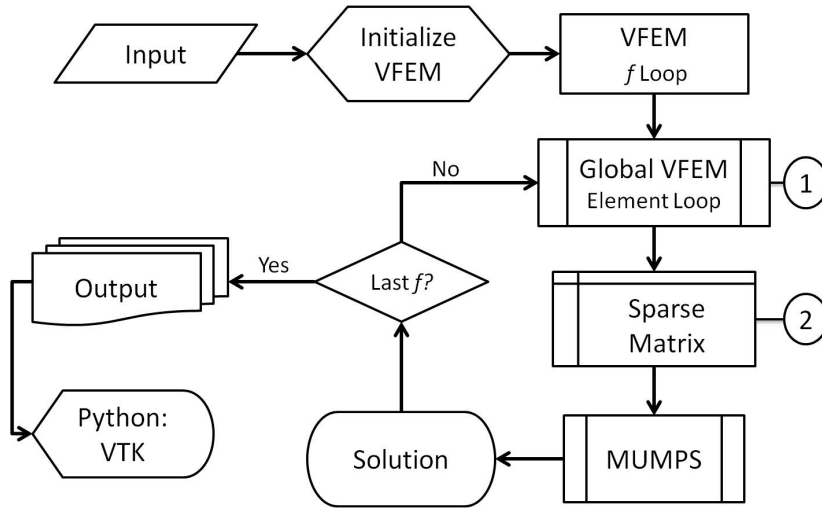


Figure C.1: Flowchart of the complete Fortran program.

File PARAM.INP contains information about the problem to be solved. It allows the user to choose the governing equation, select the primary field model, select boundary conditions, and input the frequency range.

A complementary Fortran program called ‘INPUT’ produce the 3DEM_FEM.INP file from the input parameters assigned in this program. This file is described in the following outline, where each item describes a line on this file:

3DEM_FEM.INP File

- Spacing, air high, depth, and nodes per elements

$$dx, dy, dz, h_{air}, h_{depth}, n_e$$

- Receivers

N_{rx} (Number of receivers)

$i, X_{rx}, Y_{rx}, Z_{rx} \ (i = 1, 2, \dots, N_{rx})$

- Interfaces and surface topography

M_{int} (Number of interfaces plus surface topography)

$N_1, N_2, \dots, N_{M_{int}}$ (Number of points per interface)

Bottom interface M_{int}

$i, X_{M_{int}}, Y_{M_{int}}, Z_{M_{int}}, i = 1, 2, \dots, N_{M_{int}}$

Interface $M_{int} - 1$

$i, X_{M_{int}-1}, Y_{M_{int}-1}, Z_{M_{int}-1}, i = 1, 2, \dots, N_{M_{int}-1}$

...

Surface Topography 1

$i, X_1, Y_1, Z_1, i = 1, 2, \dots, N_1$

- Input Model

Number of tensor components for $\boldsymbol{\mu}$, and $\boldsymbol{\sigma}$: $n_\mu = 0$ (on MT $\boldsymbol{\mu} = \mu_0 \mathbf{I}$),
 $n_\sigma = 1, 2, \dots$, or 6 (symmetric components)

Number of points of input model: M_x, M_y, M_z

SIGMA ij (Index of tensor components, e.g. 11, 22, 33 for $n_\sigma = 3$)

Coordinates X and Y

x_1, x_2, \dots, x_{M_x}

y_1, y_2, \dots, y_{M_y}

Coordinates Z

$z_{11}, z_{12}, \dots, z_{1M_y}$

to $z_{M_x 1}, z_{M_x 2}, \dots, z_{M_x M_y}$

SIGMA ij for each ij .

$\sigma_{11}, \sigma_{12}, \dots, \sigma_{1M_y}$

to $\sigma_{M_x 1}, \sigma_{M_x 2}, \dots, \sigma_{M_x M_y}$

Initialize VFEM: In this part of the program, these input files are read. It initialize the program modules according to the input parameters, such as governing equation, primary fields, boundary condition, and nodal and vector basis from the type of hexahedral element. In this step, the domain is discretized, and the index arrays for the global assembly are defined.

VFEM: Starts the loop over all frequencies, because a problem is solved for each frequency.

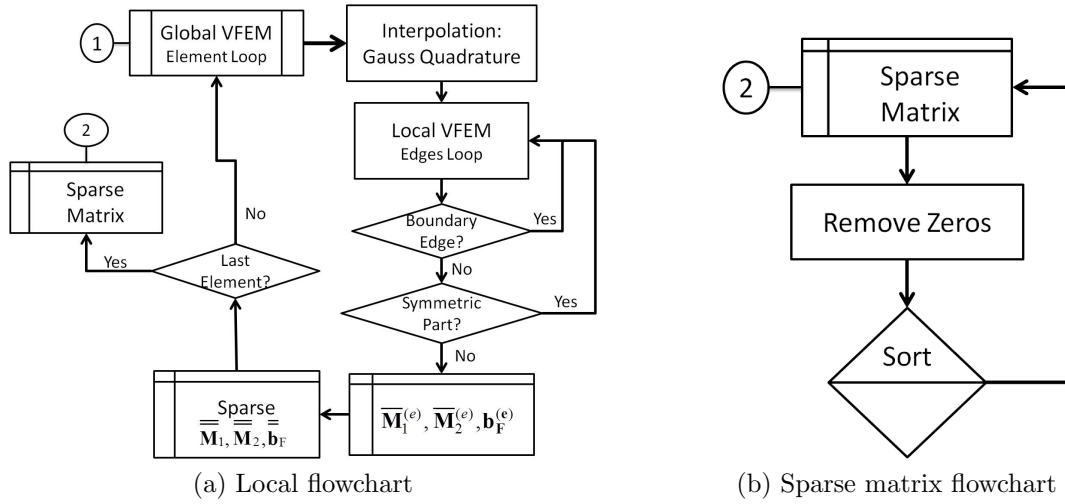


Figure C.2: a) Flowchart of local (elements) computations. b) Flowchart of sparse assembly processing.

Global VFEM Figure C.2a shows the flowchart of VFEM operations. First the sparse index arrays \mathbf{IA} , and \mathbf{JA} are defined from global degrees of freedom array \mathbf{G}_{NE} . Then, it starts the loop over all the elements on the domain, and calculates the source fields on element nodes. It also interpolates this source, the conductivity, (m_e) vector basis, and GPML stretching factors over integration points.

Local VFEM: In this step the integrations are computed. The first loops are over $m_e \times m_e$ edges to obtain the local matrix. In this case the program skips the integrations of boundary edges and symmetric part of local matrix. The second loop is over m_e edges, and calculates the integrations for the local source vector. In this step the local matrix and source vectors are assigned to the global arrays as:

$$\begin{aligned} \mathbf{A}[\mathbf{NZ}_\mathbf{A}(e, i, j)] &= \mathbf{A}[\mathbf{NZ}_\mathbf{A}(e, i, j)] + \mathbf{M}_{ij}^{(e)} \\ \mathbf{b}[\mathbf{G}_{NE}(e, i)] &= \mathbf{b}[\mathbf{G}_{NE}(e, i)] + \mathbf{b}_i^{(e)}. \end{aligned}$$

Sparse Assembly After running over all the elements, the sparse arrays are obtained. Figure C.2b shows the steps to process this matrix before inverting it for the solution. First it remove extra zeros on the array (such as the symmetric part) by searching over all entries. Then, the index arrays (\mathbf{IA}, \mathbf{JA}) will be sorted into a rows/columns order with the array \mathbf{A} .

MUMPS: Arrays \mathbf{A} , \mathbf{IA} , \mathbf{JA} , and \mathbf{b} are the entries to MUMPS package, and the unknown secondary field solution is obtained in array \mathbf{b} .

Solution: After obtaining the secondary field (e.g. \mathbf{E}_s), the total field is the sum of this solution with the primary field used in the program. The other EM field (e.g. \mathbf{H}) is obtained directly from Maxwell's equations. These EM fields are obtained for both xy -, and yz -polarizations. With these fields, the impedance (\mathbf{Z}), apparent resistivity (ρ_a), and phase (ϕ) are calculated for the model domain (i.e. the computational domain without extension zones and without air space). The solution on the receiver locations is interpolated from the solution on the surface of the model.

Output: Five output files are obtained from this program, and these are:

1. GEOMETRY.OUT

Contains the location of receivers and interfaces on the computational domain, and the unstructured grid for this domain and for the model domain. The unstructured grid is defined by the coordinates array $\mathbf{R} = (x, y, z)$ and the global index of these coordinates locations for each element node (linear, quadratic or Lagrangian). It also contains the conductivity model for the computational domain and model domain.

2. PROBLEM.OUT

Contains the primary EM fields and source field (on both polarizations) for the primary model used in the program. These fields are written for all the nodes of the model domain and for each frequency.

3. SOLUTION.OUT

Contains the EM fields solution (on both polarizations), the impedances, apparent resistivities and phase for all nodes in the model domain, and for each frequencies.

The electric field has units of $[\mu V/m]$, the magnetic field is presented in terms of the magnetic flux density (\mathbf{B}) with units of $[nT]$. With these units of EM fields, the impedance will have units of $[km/s]$. Apparent resistivity has units of $[\Omega m]$, and the phase has units of degrees.

4. SURFACE.OUT

Contains these solutions for the surface nodes of the model domain, and for each frequency.

5. RECEIVERS.OUT

Contains these solutions interpolated on receiver locations from the surface values, for each frequency.

Python/VTK Interface A python program called ‘Solution_VTK’ is programmed and contains various python classes to produce the data for 3D visualization. This 3D data is produced with the ‘Visualization Toolkit (VTK) ©’ which is an open-source for C/C++ with a python interface to create 3D data from unstructured grids, in this case using hexahedral elements. In addition, VTK output can be obtained for 2D surface data like for the receiver data.

Visualization Software The VTK files are visualized with Paraview ©, which is an open-source software for data analysis and visualization. This application is used to create the figures presenting 3D models in this thesis.

References

- Alumbaugh, D. L., Newman, G., Prevost, L., & Shadid, J. N., 1996. Three-dimensional wideband electromagnetic modeling on mamassive parallel ccomputer, *Radio Science*, **31**, 1–23.
- Alvarez-Aramberri, J., Pardo, D., & Barucq, H., 2014. Automatically Adapted Perfectly Matched Layers for Problems with High Contrast Materials Properties, *Procedia Computer Science*, **29**, 970–979.
- Amestoy, P. R., Guermouche, A., L’Excellent, J. Y., & Pralet, S., 2006. Hybrid scheduling for the parallel solution of linear systems, *Parallel Computing*, **32**(2), 136–156.
- Avdeev, D. B., 2005. Three-dimensional electromagnetic modelling and inversion from theory to application, *Surveys in Geophysics*, **26**(6), 767–799.
- Avdeev, D. B. & Avdeeva, A. D., 2006. A rigorous three-dimensional magnetotelluric inversion, *Progress in Electromagnetics Research, PIER*, **62**, 41–48.
- Bahr, K., 1988. Interpretation of the magnetotelluric impedance tensor: regional induction and local telluric distortion, *Journal of Geophysics*, **62**, 119–127.
- Berenger, J. P., 1994. A perfectly matched layer for the absorption of electromagnetic waves, *Journal of Computational Physics*, **114**, 185–200.
- Boerner, D. E., 1992. Controlled source electromagnetic deep sounding: Theory, results and correlation with natural source results, *Surveys in Geophysics*, **13**(4), 435–488.
- Börner, R., 2010. Numerical modelling in geo-electromagnetics: Advances and challenges, *Surveys in Geophysics*, **31**(2), 225–245.
- Cagniard, L., 1953. Basic theory of the magneto-telluric method of geophysical prospecting, *Geophysics*, **18**(3), 605–635.
- Caldwell, T. G., Bibby, H. M., & Brown, C., 2004. The magnetotelluric phase tensor, *Geophysical Journal International*, **158**(2), 457–469.
- Carey, G. & Oden, J., 1983. *Finite Elements, A Second Course*, vol. II, chap. 4.5 The Boundary Element Method, pp. 200–207, Prentice-Hall, New Jersey.
- Carrillo-Ledesma, A., Herrera-Revilla, I., & Yates-Smith, R., 2008. *Método de Elementos Finitos (Finite Elements Method, course notes)*, Mathematical and Computational Modelling Group, Geophysics Institute, National Autonomous University of Mexico, Mexico DF.

- Cecka, C., Lew, A. J., & Darve, E., 2000. Assembly of Finite Element Methods on Graphics Processors, *International Journal for Numerical Methods in Engineering*, **85**, 640–669.
- Chave, A. D. & Jones, A. G., 2012. *The Magnetotelluric Method, Theory and Practice*, Cambridge University Press, New York, USA.
- Chave, A. D. & Smith, J. T., 1994. On electric and magnetic galvanic distortion tensor decompositions, *Journal of Geophysical Research*, **99**(B3), 4669–4682.
- Coddington, P., 2013. High Performance Computing (HPC) user guides, *eResearch SA*, Available: https://www.ersa.edu.au/hpc_guides. Last accessed on January, 2013.
- Commer, M. & Newman, G. A., 2008. New advances in three-dimensional controlled-source electromagnetic inversion, *Geophysical Journal International*, **172**(2), 513–535.
- Constable, S. C., Parker, R. L., & Constable, C. G., 1987. Occam's inversion: A practical algorithm for generating smooth models from electromagnetic sounding data, *Geophysics*, **52**(3), 289–300.
- Crowley, C. W., 1988. *Mixed Order Covariant Projection Finite Elements for Vector Fields*, Ph.D. thesis, Department of Electrical Engineering, McGill University.
- Crowley, C. W., Silvester, P. P., & Hurwitz Jr., H., 1988. Covariant projection elements for 3D vector field problems, *IEEE Transactions on Magnetics*, **24**, 397–400.
- de la Kethulle de Ryhove, S., Morten, J. P., & Kumar, K., 2013a. Efficient 3D MT Inversion Using Finite-difference Time-domain Modelling, in *75-th EAGE Conference and Exhibition incorporating SPE EUROPEC, London UK*.
- deGroot Hedlin, C., 1991. Removal of static shift in two dimensions by regularized inversion, *Geophysics*, **56**(12), 2102–2106.
- Fang, J. & Wu, Z., 1996. Generalized Perfectly Matched Layer for the Absorption of Propagating and Evanescent Waves in Lossless and Lossy Media, *IEEE Transaction on Microwave Theory and Techniques*, **44**, 2216–2222.
- Farquharson, C. G. & Miensoopust, M. P., 2011. Three-dimensional finite-element modelling of magnetotelluric data with divergence correction, *Journal of Applied Geophysics*, **75**, 699–710.
- Fischer, G. & Masero, W., 1994. Rotational properties of the magnetotelluric impedance tensor: the example of the Araguinha impact crater, Brazil, *Geophysical Journal International*, **119**, 548–560.
- Franke, A., Börner, R., & Spitzer, K., 2007. Adaptive unstructured grid finite element simulation of two-dimensional magnetotelluric fields for arbitrary surface and seafloor topography, *Geophysical Journal International*, **171**, 71–86.

- Greenhalgh, S. A., Zhou, B., & Green, A., 2006. Solutions, algorithms and inter-relations for local minimization search geophysical inversion, *Journal of Geophysics and Engineering*, **3**(2), 101–113.
- Groom, R. & Bahr, K., 1992. Corrections for near surface effects: decomposition of the magnetotelluric impedance tensor and scaling corrections for regional resistivities: a tutorial, *Surveys in Geophysics*, **13**, 341–379.
- Groom, R. & Bailey, R., 1989. Decomposition of magnetotelluric impedance tensor in the presence of local three-dimensional galvanic distortion, *Journal of Geophysical Research*, **94**, 1913–1925.
- Groom, R. W. & Bailey, R. C., 1991. Analytic investigations of the effects of near-surface three-dimensional galvanic scatterers on MT tensor decompositions, *Geophysics*, **56**(4), 496–518.
- Haber, E. & Heldmann, S., 2007. An octree multigrid method for quasi-static Maxwell's equations with highly discontinuous coefficients., *SIAM Journal on Scientific Computing*, **223**, 1943–1961.
- Haber, E., Ascher, U., Arulia, D., & Oldenburg, D., 2000a. On Optimisation Techniques for Solving Nonlinear Inverse Problems, *Inverse Problems*, **16**, 1263–1280.
- Haber, E., Ascher, U. M., Aruliah, D. A., & Oldenburg, D. W., 2000b. Fast Simulation of 3D Electromagnetic Problems Using Potentials, *Journal of Computational Physics*, **163**, 150–171.
- Haber, E., Ascher, U., & Oldenburg, D., 2004. Inversion of 3D Electromagnetic Data in Frequency and Time Domain Using an Inexact All-at-Once Approach., *Geophysics*, **69**, 1216–1228.
- Han, H., Nam, M. J., Kim, H. J., Song, Y., & Suh, J. H., 2009. A comparison of accuracy and computation time of three-dimensional magnetotelluric modelling algorithms, *Journal of Geophysics and Engineering*, **6**(2), 136–145.
- Hano, M., 1984. Finite-Element Analysis of Dielectric-Loaded Waveguides, *IEEE Transactions on Microwave Theory and Techniques*, **MTT-32**, 1275–1279.
- Hohmann, G. W., 1975. Three-Dimensional Induced Polarization and Electromagnetic Modeling, *Geophysics*, **40**(2), 309–324.
- Hohmann, G. W., 1983. Three-dimensional EM modeling, *Surveys in Geophysics*, **6**(1), 27–53.
- Jin, J., 2002. *The Finite Element Method in Electromagnetics*, John Wiley & Sons, Inc., 2nd edn.
- Jones, F. & Pascoe, L., 1972. The perturbation of alternating geomagnetic fields by three-dimensional conductivity inhomogeneities., *Geophysical Journal of the Royal Astronomical Society*, **27**, 479–485.

-
- Kameari, A., 1990. Calculation of transient 3D eddy current using edge-elements, *IEEE Transactions on Magnetics*, **26**, 466–469.
- Key, K. & Oval, J., 2011. A parallel goal-oriented adaptive finite element method for 2.5-D electromagnetic modelling, *Geophysical Journal International*, **186**, 137–154.
- Key, K. & Weiss, C., 2006. Adaptive finite-element modeling using unstructured grids: The 2D magnetotelluric example, *Geophysics*, **71**(6), G291–G299.
- Knuth, D., 1998. *The Art of Computer Programming.*, vol. 3, chap. 5.2.4: Sorting by Merging., pp. 158–168, Addison-Wesley, 2nd edn.
- Ledo, J., 2005. 2-D Versus 3-D MMagnetotelluric Data Interpretation, *Surveys in Geophysics*, **26**, 511–543.
- Li, Y. & Key, K., 2007. 2D marine controlled-source electromagnetic modelling: Part 1 – An adaptive finite-element algorithm, *Geophysics*, **72**, WA51–WA62.
- Liu, C., Yu, Y., Ren, Z., & Wu, Q., 2010. 3-D Magnetotelluric Adaptive Finite-Element Modeling, in *Advances in Computation and Intelligence*, Lecture Notes in Computer Science, pp. 465–473, Springer Berlin Heidelberg.
- Mackie, R., Smith, J., & Madden, T., 1994. Three-dimensional electromagnetic modelling using finite difference equations: The Magnetotelluric example, *Radio Sciences*, **29**, 923–935.
- Mackie, R., Rodi, W., & Watts, M., 2001. 3-D Magnetotelluric Inversion for Resource Exploration, in *71st Annual International Meeting, SEG*, pp. 1501–1504.
- Mackie, R. L., Madden, T. R., & Wannamaker, P. E., 1993. Three-dimensional magnetotelluric modeling using difference equations – Theory and comparisons to integral equation solutions, *Geophysics*, **58**(2), 215–226.
- Madden, T. R. & Mackie, R. L., 1989. Three-dimensional magnetotelluric modeling and inversion, *Proceedings of the IEEE*, **77**(2), 318–333.
- Martí, A., 2014. The Role of Electrical Anisotropy in Magnetotelluric Responses: From Modelling and Dimensionality Analysis to Inversion and Interpretation, *Surveys in Geophysics*, **35**, 179–218.
- Martí, A., Queralt, P., & Ledo, J., 2009. WALDIM: A code for the dimensionality analysis of magnetotelluric data using the rotational invariants of the magnetotelluric tensor, *Computers and Geosciences*, **35**, 2295–2303.
- Mitsuhata, Y. & Uchida, T., 2004. 3D magnetotelluric modeling using the T- Ω finite-element method, *Geophysics*, **69**(1), 108–119.
- Mogi, T., 1996. Three-dimensional modeling of magnetotelluric data using finite element method, *Journal of Applied Geophysics*, **35**, 185–189.
- Nam, M., Kim, H., Song, Y., Lee, T., Son, J., & Suh, J., 2007. 3D magnetotelluric modelling including surface topography, *Geophysical Prospecting*, **55**, 277–287.

- Nédélec, J., 1980. Mixed Finite Elements in R3, *Numerische Mathematik*, **35**, 315–341.
- Negi, T., Mizunaga, H., Asamori, K., & Umeda, K., 2013. Three-dimensional magnetotelluric inversion using a heterogeneous smoothness-constrained least-squares method, *Exploration Geophysics*, **44**, 145–155.
- Newman, G., 2014. A Review of High-Performance Computational Strategies for Modeling and Imaging of Electromagnetic Induction Data, *Surveys in Geophysics*, **35**, 85–100.
- Newman, G. & Alumbaugh, D. L., 1997. 3D Electromagnetic Modeling Using Staggered Finite Differences, *IEEE International*, **2**, 929–932.
- Newman, G., Recher, S., Tezkan, B., & Neubauer, F., 2003. 3D Inversion of a Scalar Radio Magnetotelluric Field Data Set, *Geophysics*, **68**, 791–802.
- Newman, G. A. & Alumbaugh, D. L., 2000. Three-dimensional magnetotelluric inversion using non-linear conjugate gradients, *Geophysical Journal International*, **140**(2), 410–424.
- Ogawa, Y., 2002. On Two-Dimensional Modeling of Magnetotelluric Field Data, *Surveys in Geophysics*, **23**, 251–272.
- Pardo, D., Demkowicz, L., Torres-Verdn, C., & Paszynski, M., 2007. A self-adaptive goal-oriented hp-finite element method with electromagnetic applications. part ii: Electrodynamics, *Computer Methods in Applied Mechanics and Engineering*, **196**, 3585–3597.
- Parkinson, W., 1959. Directions of rapid geomagnetic variations, *Geophysical Journal of the Royal Astronomical Society*, **2**, 1–14.
- Pek, J. & Santos, F. A. M., 2006. Magnetotelluric inversion for anisotropic conductivities in layered media, *Physics of the Earth and Planetary Interiors*, **158**(2-4), 139–158.
- Pek, J., Santos, F. A. M., & Li, Y., 2011. Non-Linear Conjugate Gradient Magnetotelluric Inversion for 2-D Anisotropic Conductivities, in *24 Schmicker-Weidelt-Kolloquium, Nustadt and der Weinstraße, 19–23 September*.
- Puzyrev, V., Koldan, J., de la Puente, J., Houzeaux, G., Vázquez, M., & Cela, J., 2013. A parallel finite-element method for three-dimensional controlled-source electromagnetic forward modelling, *Geophysical Journal International*, **193**, 678–693.
- Reddy, I., Rankin, D., & Phillips, R., 1977. Three-dimensional modelling in magnetotelluric and magnetic variational sounding, *Geophysical Journal International*, **51**, 313–325.
- Ren, Z., Kalscheuer, T., Greenhalgh, S., & Maurer, H., 2013. A goal-oriented adaptive finite-element approach for plane wave 3-D electromagnetic modelling, *Geophysical Journal International*, pp. 1–19.

-
- Renka, R., 1988. Algorithm 660: QSHEP2D: Quadratic Shepard Method for Bivariate Interpolation of Scattered Data, *ACM Transactions on Mathematical Software (TOMS)*, **14**, 149–150.
- Rodi, W. & Mackie, R., 2012. *The Magnetotelluric Method, Theory and Practice*, chap. 8. The Inverse Problem, pp. 347–420, Cambridge University Press.
- Rodi, W. & Mackie, R. L., 2001. Nonlinear conjugate gradients algorithm for 2-D magnetotelluric inversion, *Geophysics*, **66**(1), 174–187.
- Romo, J. M., Gómez-Treviño, E., & Esparza, F. J., 2005. Series and parallel transformations of the magnetotelluric impedance tensor: theory and applications, *Physics of the Earth and Planetary Interiors*, **150**, 63–83.
- Schmucker, U., 1973. Regional induction studies: a review of methods and results, *Physics of the Earth and Planetary Interiors*, **7**, 365–378.
- Shi, X., Utada, H., Wang, J., & Wu, W., 2004. Three dimensional magnetotelluric forward modeling using vector finite element method combined with divergence corrections (VFE++), in *17th IAGA WG 1.2 Workshop on Electromagnetic Induction in the Earth*, October 18–23, Hyderabad, India.
- Simpson, F. & Bahr, K., 2005. *Practical Magnetotellurics*, Cambridge University Press, United Kingdom.
- Siripunvaraporn, W. & Egbert, G., 2000. An efficient data subspace inversion method for 2-D magnetotelluric data, *Geophysics*, **65**(3), 791–803.
- Siripunvaraporn, W., Egbert, G., Lenbury, Y., & Uyeshima, M., 2005. Three-dimensional magnetotelluric inversion: data-space method, *Physics of the Earth and Planetary Interiors*, **150**(1-3), 3–14.
- Smith, J. & Booker, J., 1991. Rapid inversion of two- and three-dimensional magnetotelluric data, *Journal of Geophysical Research*, **96**, 3905–3922.
- Stratton, J. A., 2007. *Electromagnetic Theory*, IEEE Press Series on Electromagnetic Wave Theory.
- Swift, C. J., 1967. *A magnetotelluric investigation of an electrical conductivity anomaly in the southwestern United States*, Ph.D. thesis, MIT, Massachusetts, USA.
- Szarka, L. & Menvielle, M., 1997. Analysis of rotational invariants of the magnetotelluric impedance tensor, *Geophysical Journal International*, **129**, 133–142.
- Tikhonov, A., 1950. On Determining Electrical Characteristics of Deep Layers of the Earth's Crust, *Proceedings of Academy of Sciences (USSR) Doklady*, **83**(2), 295–297.
- Tikhonov, A. & Arsenin, V., 1977. *Solutions of Ill-posed Problems*, Wiley, New York.
- Tonti, E., 2001. Finite Formulation of the Electromagnetic Field, *Progress In Electromagnetics Research*, **32**, 1–44.

- Torres-Verdín, C. & Bostick, F., 1992. Principles of spatial surface electric field filtering in magnetotellurics: Electromagnetic array profiling (EMAP), *Geophysics*, **57**, 603–622.
- Tournerie, B., Chouteau, M., & Marcotte, D., 2007. Magnetotelluric static shift: Estimation and removal using the cokriging method, *Geophysics*, **72**(1), F25–F34.
- Tumanski, S., 2007. Induction coil sensors – a review, *Measurement Science and Technology*, **18**, R31–R46.
- Utada, H. & Munekane, H., 2000. On galvanic distortion of regional three-dimensional magnetotelluric impedances, *Geophysical Journal International*, **140**(2), 385–398.
- Viljanen, A., 2012. Description of the magnetospheric/ionospheric source, in *The Magnetotelluric Method, Theory and Practice*, eds Chave, A. D. & Jones, A. G., Cambridge University Press, New York, USA.
- Vozoff, K., 1972. The Magnetotelluric Method in the Exploration of Sedimentary Basins, *Geophysics*, **37**(1), 98–141.
- Vozoff, K., 1991. The magnetotelluric method, in *Electromagnetic Methods in Applied Geophysics - Application*, vol. 2, pp. 641–711, ed. Nabighian, M. N., Society of Exploration Geophysicists, Tulsa.
- Wait, J. R., 1954. On the relation between telluric currents and the earth's magnetic field, *Geophysics*, **19**, 281–289.
- Wang, T. & Fang, S., 2001. 3-D electromagnetic anisotropy modeling using finite differences, *Society of Exploration Geophysics*, **66**, 1386–1398.
- Wannamaker, P. E., 1991. Advances in three-dimensional magnetotelluric modeling using integral equations, *Geophysics*, **56**(11), 1716–1728.
- Wannamaker, P. E., Stodt, J. A., & Rijo, L., 1986. Two-dimensional topographic responses in magnetotellurics modeled using finite elements, *Geophysics*, **51**, 2131–2144.
- Ward, S. & Hohmann, G., 1988. 4. Electromagnetic Theory for Geophysical Applications, in *Electromagnetic Methods in Applied Geophysics*, ed. Nabighian, M. N., Society of Exploration Geophysicists.
- Weaver, J., 1994. *Mathematical methods for geo-electromagnetic induction*, John Wiley & Sons, Inc., New York-Toronto-Singapore.
- Weaver, J. T., Agarwal, A. K., & Lilley, F. E. M., 2000. Characterization of the magnetotelluric tensor in terms of its invariants, *Geophysical Journal International*, **141**, 321–336.
- Webb, J. P. & Miniowitz, R., 1991. Analysis of 3-D Microwave Resonators using Covariant-projection elements, *IEEE Transactions on Microwave Theory and Techniques*, **39**, 1895–1899.

-
- Weidelt, P., 1972. The inverse problem of geomagnetic induction, *Zeitschrift für Geophysik*, **38**, 257–289.
- Weiss, C. & Constable, S., 2006. Mapping thin resistors and hydrocarbons with marine EM methods, Part II Modeling and analysis in 3D, *Geophysics*, **71**, G321–G332.
- Weiss, C. & Newman, G., 2002. Electromagnetic Induction in a Fully 3-D Anisotropic Earth, *Geophysics*, **67**, 1104–1114.
- Weiss, C. & Newman, G., 2003. Electromagnetic induction in a generalized 3D anisotropic earth, Part : The LIN preconditioner, *Geophysics*, **68**(3), 922–930.
- Yee, K., 1966. Numerical solution of initial boundary problems involving Maxwell's equations in isotropic media, *IEEE Transactions on Antennas and Propagation*, **14**, 302–309.
- Yilmaz, A. E., 2007. *Finite Element Modeling of Electromagnetic Scattering Problems via Hexahedral Edge Elements*, Ph.D. thesis, Electrical and electronics Engineering Department, Middle East Technical University, Turkey.
- Yilmaz, A. E. & Kuzuoglu, M., 2008. Comparison of linear and quadratic hexahedral edge elements in electromagnetic scattering problems, *AEU - International Journal of Electronics and Communications*, **62**, 582–587.
- Zhang, P., Chouteau, M., Mareschal, M., Kurtz, R., & Hubert, C., 1995. High-frequency magnetotelluric investigation of crustal structure in northern central Abitibi, Quebec, Canada, *Geophysical Journal International*, **120**, 406–418.
- Zhdanov, M., Fang, S., & Hursan, G., 2000. Electromagnetic Inversion using Quasi-Linear Approximation, *Geophysics*, **65**, 1501–1513.
- Zhdanov, M., Lee, S., & Yoshioka, K., 2006. Integral equation method for 3D modeling of electromagnetic fields in complex structures with inhomogeneous background conductivity, *Geophysics*, **71**, G333–G345.
- Zhdanov, M. S., Varentsov, I. M., Weaver, J. T., Golubev, N. G., & Krylov, V. A., 1997. Methods for modelling electromagnetic fields. Results from COMMEMI - the international project on comparison of modelling methods for electromagnetic induction, *Journal of Applied Geophysics*, **37**, 133–271.
- Zhou, B., Greenhalgh, M., & Greenhalgh, S. A., 2009. 2.5-D/3-D resistivity modelling in anisotropic media using Gaussian quadrature grids, *Geophysical Journal International*, **176**(1), 63–80.
- Zhou, B., Heinson, G., Rivera-Rios, A., & Patten, C., 2012. 3D Geo-Electromagnetic Modelling with Subdomain Chebyshev Spectral Method, in *21st EM Induction Workshop*, Darwin, Australia, July 25–31.
- Zyserman, F. & Santos, J., 2000. Parallel finite element algorithm with domain decomposition for three-dimensional magnetotelluric modelling, *Journal of Applied Geophysics*, **44**, 337–351.